METABOLIC MODELING OF GROWTH AND POLY-β-HYDROXYBUTYRATE (PHB) PRODUCTION IN *ALCALIGENES EUTROPHUS* H16

Thesis by

Christopher James Guske

In Partial Fulfillment of the Requirements

for the Degree of

Doctor of Philosophy

Department of Chemical Engineering

California Institute of Technology

Pasadena, California, USA

1990

(Submitted April 2, 1990)

To my wife, Becky,

and my family

ACKNOWLEDGEMENTS

There have been a number of people who have helped shape and mold this experience called Caltech. Without them I would have been utterly lost, not to mention pretty bored.

I don't think there is anyone in this world like Mike "Mr. Science" Loewenberg. Never have I known anyone who could at one moment be so completely silly and then in the blink of an eye lapse into a world of higher intelligence frequented only by the inhabitants of the eighth dimension. Mike, you're one special guy.

And then there's Robin "Mr. P&G" Horrell. Well, we never really did that well at softball, well, not as well as we thought we should have. Thanks for all the special things you did for me. I look forward to seeing the announcement recognizing you as the world's greatest entrepreneur. Watch out, Donald Trump!

Of course there's "The World's Greatest Roommate" aka Hung Nguyen. Hung, you put up with me through the good and bad times. And to think that we didn't kill each other in the process (or is that you didn't kill me?). I can only thank you for putting up with me, Hung; I hope that you find someone who will truly appreciate you and all that you have to offer.

Then there's my family doing all the things that families are supposed to do. Thanks for all the prayers and thanks for always believing in me, particularly when I didn't believe in myself.

If there was only one thing that I could say about my advisor, Dr. J.E. Bailey, it would be that he was always fair. Jay, I thank you for all the benefits of the doubt and chances you gave — more than I rightfully deserved. If I had to do it all over again, I don't think there would be anyone for whom I would rather work. Of course, I would change a lot of things. . . . I hope for your sake that no one steps up to fill my shoes.

If there was anyone who deserved a medal, it would have to be my wife. Being married to a graduate (or is that gradual?) student is no-o-o-o fun. Thanks for hanging in there and loving me through all this, even though there were many times when I know you wanted to toss in the towel or strangle me. I look forward to starting our "new lives" together in San Diego.

And finally, the highest honor and praise goes to Him who blessed me with the talents and the abilities which enabled me to be here.

ABSTRACT

A physiologically based metabolic model for growth and poly-β-hydroxybutyrate (PHB) production in *Alcaligenes eutrophus* H16 has been formulated. The model is based upon *A. eutrophus*' five major heterotrophic metabolic pathways: an overall biosynthesis pathway, respiration, glycolysis, the citric acid cycle, and PHB polymerization. Beginning with microscopic intracellular balances, intracellular phenomena such as pathway flux activities and intracellular balances on acetyl-CoA, ATP and NADH are related to the macroscopic time evolutions of fructose concentration, cell dry weight concentration, PHB concentration, carbon dioxide evolution rate, and oxygen consumption rate.

Using the derived model framework, *Alcaligenes eutrophus* H16's metabolic responses to different medium fructose, ammonium and oxygen concentrations as well as nutrient limitations and exhaustions were determined in a well-controlled, fully monitored bioreactor. Ammonium exhaustion led to the highest observed PHB synthesis rates, while the PHB polymerization rates correlated with the severity of ammonium and oxygen limitations. Surprisingly, fructose limitation led to an increase in intracellular PHB levels. Glycolysis, citric acid cycle and repiration activities were very sensitive to short-term fluctuations during fructose-limited feeding, while biosynthesis and PHB polymerization responses were sluggish. Fructose exhaustion PHB depolymerization occurred at a small

absolute rate relative to polymerization during periods of fructose sufficiency. High intracellular PHB levels appeared to inhibit cell growth.

Using *in vitro* kinetic study data, model metabolic pathway responses were compared with the regulatory properties of the key regulatory enzymes. Glucose-6-phosphate NADH-regulation appears weaker than that exerted on isocitrate dehydrogenase as evidenced by increased ammonium-limited glycolysis activity and presumed elevated NADH levels. Increased NADH levels sharply correlated with increased PHB polymerization activity. Along this line, culture fluorescence was used as a sensitive indicator of NAD(P)H level changes. Culture fluorescence was a good indicator of metabolic shifts, particularly at the onset of increased PHB polymerization. Increases in specific culture fluorescence correlated strongly with intracellular PHB levels.

From the pathway-associated intracellular balances, average metabolic parameters for the ATP yield coefficient, Y_{ATP}^{max}, the oxidative phosphorylation ratio, P/O, and the ATP maintenance coefficient, $m_{ATP,e}$, were determined of 0.34 C-mol biomass/mol ATP, 2.9 mol ATP/mol H_2O, and 9.8 mmol ATP/((g biomass)(hr)), respectively, which agree favorably with other work. Use of the constant metabolic parameters and the closed intracellular balances predicted balanced growth conditions well but deviated under ammonium limitation conditions. Also, the metabolic parameters seemed to shift to lower values as during the growth/PHB storage phase transition.

Incorporation of kinetic expressions for biosynthesis and PHB polymerization activities mimicked balanced growth conditions very well while deviating from ammonium limitation and ammonium exhaustion conditions.

TABLE OF CONTENTS

LIST OF FIGURES

LIST OF TABLES

CHAPTER 1

INTRODUCTION

Alcaligenes eutrophus H16 first attracted scientific investigation because of its ability to grow on completely inorganic nutrients. Using molecular hydrogen, *Alcaligenes eutrophus* H16 can derive metabolic-reducing power via two dehydrogenases that reduce NAD(P) for use in respiration and biosynthetic processes.[1-4] In an atmosphere of hydrogen, oxygen, carbon dioxide, inorganic nitrogen and trace minerals, *A. eutrophus'* hydrogen-reducing mechanism accomplishes carbon dioxide fixation through the Calvin cycle in the first step of biosynthetic precursor formation as well as synthesis of poly-β-hydroxybutyrate (PHB).[5-10] For these reasons an intensive effort was made to completely elucidate the intrinsic autotrophic details of this organism.

Understandably, culturing *A. eutrophus* under a hydrogen and oxygen atmosphere has practical drawbacks. Heterotrophic growth investigations with *A. eutrophus* were also pursued, particularly regarding mixotrophic studies aimed at understanding regulatory interactions between autotrophic and heterotrophic enzyme systems.[11-16] During this work it was discovered that although capable of metabolizing a wide range of carbon sources, wild-type *A. eutrophus* was able to grow on only a few carbohydrates, one of which is fructose.[17-19] Studies suggested that the mechanism for glucose metabolism through the Entner-Doudoroff pathway was available but not utilized because of the absence of the necessary glucose active transport mechanism.[20,21] Under an atmosphere containing hydrogen and in the presence of fructose, *A. eutrophus'* heterotrophic enzyme system is repressed and is not highly expressed.[22] Also, it was found

that the heterotrophic enzymes are inducible.[17] Under heterotrophic growth conditions, autotrophic enzymes are expressed, *e.g.*, Calvin cycle enzymes, but their activity is highly repressed.[14,15] This makes sense from an energetic standpoint since carbon dioxide fixation is an energy-intensive process.[22] In these studies of heterotrophic growth, *A. eutrophus*' pathways have been identified and elucidated with isolation and kinetic characterization of key regulatory enzymes *in vitro*.[23–36]

Recently there has been increased interest in the production of PHB and the unique properties possessed by this polymer of D(-)3-hydroxybutyrate.[37,38] As a biocompatible, biodegradable, thermoplastic, PHB may ultimately find uses in a number of varied applications.[39] The genes responsible for PHB production in *A. eutrophus*, most notably the key regulatory element β-ketothiolase, have been cloned, transformed, and expressed in *E. coli*.[40] Other enzymes in the PHB polymerization pathway have also been studied intensively and cloned in *E. coli*.[41,42]

Our interest in PHB as it pertains to *Alcaligenes eutrophus* H16 lies in the cellular metabolic regulation of its production relative to prevailing fermentation conditions. Generally it is known that PHB production occurs constitutively at low levels under balanced growth conditions; PHB production increases substantially under conditions of nutrient limitation and exhaustion in the presence of excess carbon source levels. Although a considerable amount of work has been applied to understanding *A. eutrophus*'s intrinsic metabolic pathways, surprisingly, none of this wealth of metabolic information and experimental observations has ever been analyzed mathematically in a manner reflective of *A. eutro-*

phus's known metabolism. To date, the best representative model of *A. eutrophus*'s growth and metabolism was constructed on a structured, semi-empirical basis devoid of intrinsic metabolic pathway information.[43]. It is the desire of this work to construct a physiologically based model framework based on *A. eutrophus*' known metabolism, which will be useful for quantifying pathway fluxes and elucidating regulation within the cell.

Beginning in Chapter 2, the important major facets of *Alcaligenes eutrophus* H16' metabolism are identified and described. From this information, a metabolic pathway network structure is formulated and subsequently translated into a mathematical structure. Application of this model allows quantification of the identified pathway fluxes under varying fermentation conditions, given the time course of specific macroscopic fermentation variables. Serving as a simple, initial example, this metabolic model is applied to the case of heterotrophic growth and nitrogen (ammonium) exhaustion, demonstrating the physiologically useful information this structure can provide.

In Chapters 3 through 6, the influences of nitrogen, oxygen, fructose, phosphate, and intracellular PHB on growth and PHB polymerization are investigated, highlighting the unique metabolic influences these species exert over *A. eutrophus*. Initially, nitrogen, oxygen and fructose concentration effects are investigated in Chapter 3, followed by an examination of the effects of cell growth and PHB polymerization under conditions of ammonium limitation. In Chapter 4 the focus is shifted to the effects of oxygen limitation and the cell's response to the relaxation of from oxygen limitation following an extended limitation period. Chapter 5 examines cellular responses to a wide range of fructose growth

conditions, including fructose limitation and exhaustion, as well as short-time-scale metabolic shifts between different fructose metabolic regimes. In Chapter 6 the effects of phosphate concentration, limitation, and exhaustion are examined, followed by a brief investigation of a high intracellular PHB concentration's influence on cellular metabolism.

Although NAD(P)H is difficult to assay chemically, culture fluorescence provides a nonevasive tool, allowing investigation of intracellular NAD(P)H level shifts. Using the experiments examined in the previous chapters, changes in NAD(P)H levels are correlated with *Alcaligenes eutrophus* H16's metabolic response to differing fermentation conditions, correlating an understanding of changes in NAD(P)H levels with the associated influence these level shifts have on various key regulatory enzymes. This is pursued in Chapter 7.

Finally, in Chapter 8, the metabolic model derived in Chapter 2 is inverted, so to speak, through the use of the pathway-associated intracellular balances and is utilized as a predictive and simulatory tool. After identifying approximate average values for the intracellular metabolic parameters, this model framework is tested for its sufficiency and adequacy in predicting *A. eutrophus*'s metabolism in fermentations similar to those extensively investigated. This provides an opportunity to evaluate the usefulness of this model technique as well as to validate the original model structure.

REFERENCES

1. Schneider, K., Cammack, R., and Schlegel, H.G., *Biochim. Biophys. Acta*, **578**, 445 (1979).
2. Schneider, K., and Schlegel, H.G., *Biochim. Biophys. Acta*, **452**, 66 (1976).
3. Schink, B., and Schlegel, H.G., *Biochemie*, **60**, 297 (1978).
4. Schink, B., and Schlegel, H.G., *Biochim. Biophys. Acta*, **567**, 315 (1979).
5. Abdelal, A.T.H., and Schlegel, H.G., *Biochem. J.*, **139**, 481 (1974).
6. Siebert, K., Schobert, P., Bowien, B., *Biochim. Biophys. Acta*, **658**, 35 (1981).
7. Gottschalk, G., *Arch. Mikrobiol.*, **47**, 236 (1964).
8. Kuehn, G.D., and McFadden, B.A., *Biochem.*, **8**, 2394 (1969).
9. Kuehn, G.D., and McFadden, B.A., *Biochemistry.*, **8**, 2403 (1969).
10. Abdelal, A.T.H., and Schlegel, H.G., *J. Bacteriol.*, **120**, 304 (1974).
11. Cook, D.W., Tischer, R.G., and Brown, L.R., *Can. J. Microbiol.*, **13**, 701 (1967).
12. DeCicco, B.T., and Stukus, P.E., *J. Bacteriol.*, **95**, 1469 (1968).
13. Schink, B., and Schlegel, H.G., *Arch. Microbiol.*, **117**, 123 (1978).
14. Stukus, P.E., and DeCicco, B.T., *J. Bacteriol.*, **101**, 339 (1970).
15. Friedrich, C.G., Friedrich, B., and Bowien, B., *J. Gen. Microbiol.*, **122**,

69 (1981).

16. Friedrich, C.G., Bowien, B., and Friedrich, B., *J. Gen. Microbiol.*, **115**, 185 (1979).

17. Gottschalk, G., Eberhardt, U., and Schlegel, H.G., *Arch. Mikrobiol.*, **48**, 95 (1964).

18. Wilde, E., *Arch. Mikrobiol.*, **43**, 109 (1962).

19. Schlegel, H.G., and Gottschalk, C., *Biochem. Z.*, **341**, 249 (1965).

20. Schlegel, H.G., *Adv. Comp. Physiol. Biochem.*, **2**, 185 (1965).

21. Entner, N., and Doudoroff, M., *J. Biol. Chem.*, **196**, 853 (1952).

22. Lehninger, A.L., *Principles of Biochemistry*, Worth Publisher, Inc., New York, New York (1982).

23. Heinzle, E., and Lafferty, R.M., *Eur. J. Appl. Microbiol.*, **11**, 8 (1980).

24. Srienc, F., Dissertation, Universität Graz, Graz(1980).

25. Blackkolb, F., and Schlegel, H.G., *Arch. Microbiol.*, **63**, 177 (1968).

26. Tunail, N., and Schlegel, H.G., *Biochem. Biophys. Comm.*, **49**, 1554 (1972).

27. Wilke, D., and Schlegel, H.G., *Arch. Microbiol.*, **105**, 109 (1975).

28. Glaeser, H., and Schlegel, H.G., *Arch. Microbiol.*, **86**, 327 (1972).

29. Oeding, V., and Schlegel, H.G., *Biochem. J.*, **134**, 239 (1973).

30. Senior, P.J., and Dawes, E.A., *Biochem. J.*, **134**, 225 (1973).

31. Saito, T., Fukui, T., Ikeda, F., Tanaka, Y. and Tomita, K., *Arch. Microbiol.*, **114**, 211 (1977).

32. Abdelal, A.T.H., and Schlegel, H.G., *Biochem. J.*, **139**, 481 (1974).

33. Bowien, B., Cook, A.M., and Schlegel, H.G., *Arch. Microbiol.*, **97**, 273 (1974).

34. Haywood, G.W., Anderson, A.J., Chu, L., and Dawes, E.A., *FEMS Microbiol. Lett.*, **52**, 91 (1988).

35. Haywood, G.W., Anderson, A.J., Chu, L., and Dawes, E.A., *FEMS Microbiol. Lett.*, **52**, 259 (1988).

36. Haywood, G.W., Anderson, A.J., and Dawes, E.A., *FEMS Microbiol. Lett.*, **57**, 1 (1989).

37. Byrom, D., *TIBTECH*, **3**, 246 (1987).

38. Pool, R., *Science*, **245**, 1187 (1989).

39. Holmes, P.A., *Phys. Technol.*, **16**, 32 (1985).

40. Slater, S. and Dennis, D., *Abstr. Annu. Meet. Am. Soc. Microbiol.*, **87**, 160 (1987).

41. Slater, S.C., Voige, W.H., and Dennis, D.E., *J. Bacteriol.*, **170**, 4431 (1988).

42. Schubert, P., Steinbüchel, A., and Schlegel, H.G., *J. Bacteriol.*, **170**, 5837 (1988).

43. Heinzle, E. and Lafferty, R.M., *Eur. J. Appl. Microbiol.*, **11**, 8 (1980).

CHAPTER 2

EXPERIMENTAL MODEL DEVELOPMENT

2.1 INTRODUCTION

When a host organism is transformed with a foreign plasmid or when a foreign DNA fragment is incorporated into the host's genome, it is not always clear how this foreign DNA's presence will impact the rest of the cell's metabolic machinery. Questions regarding the impact on the cell's replication system, effects of gene dosage, foreign protein degradation, inhibition or overburdening of key pathways, and foreign proteins that can be switched on or off can create a complicated modeling scenario. In other words, the host organism's known metabolism has been complicated by an additional metabolic component whose contributions and interactions may not be completely defined or understood. Under such circumstances, an empirical approach to modeling the system is initially necessary until more detailed investigations can be made to better understand the metabolic additions or complications introduced by these new cellular components.

Unlike genetically engineered organisms, there exist a number of wild-type systems that can serve as models for understanding regulation of a desired product. Understanding such metabolic models may provide useful regulatory information which can be extended to other systems. Since the metabolic machinery is native to the organism of interest, interactions caused by unknown factors or components are avoided. Since, in general, the key metabolic pathways are understood to some degree, we have a basis upon which to further the under-

standing of regulation and metabolic interactions. By exploiting this basis we can establish a foundation upon which to further advance our knowledge.

In the case of *Alcaligenes eutrophus* H16, the organism's metabolism has been clearly elucidated; key metabolic pathways have been identified and characterized. Unlike a number of genetically engineered organisms in which the impact of product synthesis is sometimes unclear since the product is not native to the organism, *A. eutrophus*' ability to produce poly-β-hydroxybutyrate (PHB) is a natural, native function of the cell. PHB is constitutively produced at low levels during balanced growth; enhanced PHB production occurs when growth is unbalanced or has ceased in the presence of excess carbon source. As a native component of *A. eutrophus*' metabolism, the PHB polymerization pathway is influenced directly by other pathways within the cell. This is most highly evident during the so-called "switch mechanism" that occurs during the transition between growth and nongrowth regimes.

The purpose of this chapter is to describe in detail a physiologically based experimental model for studying *A. eutrophus*' metabolism. The basis for this model differs from the vast majority of prior attempts at modeling this system, which have incorporated empirical and semi-empirical approaches. By focusing upon selected, major metabolic pathways, we will be able to elucidate the organism's responses via changes in pathway activities under a broad range of fermentation conditions. It will be shown that this approach allows us to expand upon the "single-case" limitation of previously proposed empirical models.

2.2 PREVIOUS MODELING WORK

2.2.1 Siegel and Ollis Model

One of the few empirical models for *A. eutrophus* was proposed by Siegel and Ollis.[1] The purpose of the model was to describe the cellular response of *A. eutrophus* to varying concentrations of hydrogen and oxygen in an autotrophic, continuous fermentation. Using Monod kinetic forms, expressions were developed for the influence of hydrogen and oxygen on the specific growth rate, μ. Calculations also included determinations of the yield and maintenance coefficients with respect to hydrogen and oxygen. No attempt was made to correlate PHB production with hydrogen and oxygen concentrations other than to note that the PHB concentration decreased linearly with increasing growth rate.

2.2.2 Heinzle and Lafferty Model

Heinzle and Lafferty[2] proposed a semi-empirical, structured model for batch growth and PHB production under autotrophic conditions. The model incorporated active and passive ammonium assimilation in its formulation for the specific growth rate in the growth equation. Also, the mathematical formulation for PHB production was divided into two parts — one term to account for constitutive production during growth and one term to account for increased PHB production during nongrowth periods. The second portion of the PHB production expression included inhibitory effects of ammonium and PHB (*i.e.*,

PHB inhibits its own production) as well as a biomass-associated production element.

Specifically, Heinzle and Lafferty described the concentration time evolutions of residual biomass, R, cell dry weight, X, PHB, P, and ammonium, S, in the following manner:

$$X = P + R \tag{2.1}$$

$$\frac{dR}{dt} = r_R = \mu R, \tag{2.2}$$

where

$$\mu = \mu_1 + \mu_2 \tag{2.3}$$

$$= \mu_{m,1}\frac{S}{K_{S,1} + S} + \mu_{m,2}\frac{(S/K_{S,2})^n}{1 + (S/K_{S,2})^n} \tag{2.4}$$

$$\frac{dS}{dt} = r_S = -\frac{1}{Y_{R/S}} r_R \tag{2.5}$$

$$\frac{dP}{dt} = r_P = r_{P,1} + r_{P,2}, \tag{2.6}$$

where

$$r_{P,1} = Y_{P/R} \cdot r_R \tag{2.7}$$

$$r_{P,2} = (k_2 R - k_1 P)\frac{K_I}{K_I + S}. \tag{2.8}$$

The specific growth rate, μ, is divided into an active transport term, μ_1, and a passive transport term, μ_2 (Eqs. (2.3) and (2.4)); μ is a function of the prevailing ammonium concentration. Furthermore, the decrease in the ammonium concentration is directly related through the ammonium yield coefficient, $Y_{R/S}$, to the increase in residual biomass (Eq. (2.5)). Finally, the change in the PHB concentration (Eq. (2.6)) is considered to be the sum of a growth-associated

or constituitive term, $r_{P,1}$ (Eq. (2.7)), and a nongrowth associated term, $r_{P,2}$ (Eq. (2.8)). $r_{P,2}$ is comprised of an ammonium inhibition component with inhibition constant K_I, a first-order biomass concentration component, k_2R, and a first-order PHB self-inhibition component, k_1P.

The system of model equations simulated the experimental data very well. Unfortunately, the equations were restricted to the specific ammonium exhaustion fermentation conditions of the paper as dictated by the data-fitting modeling approach typical of empirical formulations. Although several very inventive attempts were made to include physiologically significant information (*i.e.*, active and passive ammonium assimilation, constituitive and unbalanced growth PHB synthesis), the model shed little new light on the understanding of the intrinsic metabolic interactions of the known pathways that ultimately lead to the observed fermentation behavior. Therefore, the Heinzle and Lafferty model, while a very ingeniously developed model for the specific case of autotrophic growth and PHB production under conditions of changing ammonium concentration and ammonium exhaustion, is limited in scope for the biochemical engineer seeking a model framework capable of describing to a wide range of fermentation scenerios.

2.3 MODEL

2.3.1 Purpose

In light of the previously mentioned empirical models, it is the purpose

of this work to propose a phenomenologically based reaction pathway framework through which heterotrophic fermentation experimental data can be analyzed by inferring *Alcaligenes eutrophus* H16's metabolic response to varying conditions of fructose, ammonium and dissolved oxygen concentrations. Ultimately, this same framework will be used for simulating the microorganism's metabolism.

The goals of this model are to provide a more detailed, quantitative insight into *A. eutrophus*' metabolism scheme and to examine the manifestation of metabolic control as indicated by observed pathway interactions under carefully defined and controlled conditions. Once this framework is validated, the model reaction network can be extended by the incorporation of individual regulatory kinetic expressions for each pathway. With a satisfactory phenomenologically based simulation model, more intelligent decisions with regard to fermentation optimization and potential genetic manipulations can be proposed and the implications of those decisions understood.

2.3.2 Model Framework

The foundation of this model is grounded in the five major metabolic pathways of *A. eutrophus*: glycolysis, citric acid cycle, PHB polymerization, respiration, and biosynthesis. The first four pathways have been studied in varying degrees in the literature. Of particular note is the branching of the glycolytic pathway into the citric acid cycle and the PHB polymerization pathway. This is highlighted in Figure 2.1. Also highlighted are the known regulatory enzymes

and the intracellular species that exert control at these points. Figure 2.2 delineates the simplified network model employed in this work and indicates the relationship of each pathway to one another. In the following paragraphs descriptions of the five major reaction pathways along with pathway stoichiometry are presented.

2.3.2.1 Glycolysis, v_1. Unlike a wide range of aerobic organisms that utilize the EMP pathway for glycolysis, *Alcaligenes eutrophus* H16 catabolizes fructose[18] via the Entner-Doudoroff pathway.[19] The Entner-Doudoroff pathway is very similar to the EMP pathway except for the formation of 2-keto-3-desoxy-6-phosphogluconate, which ultimately splits to form pyruvate and glyceraldehyde-3-phosphate (see Figure 2.1). Although metabolically capable of consuming glucose, *A. eutrophus* lacks the necessary active transport mechanism for glucose.[20] As a matter of fact, fructose is one of the few carbohydrates which *A. eutrophus* can actively metabolize.[21,22] The overall stoichiometry for the glycolytic pathway is:

$$\text{Fructose} + (\text{ADP} + \text{P}_\text{i}) + \text{NADP} + 3\text{NAD} + 2\text{CoASH} \rightarrow$$
$$2(\text{Acetyl-CoA}) + \text{CO}_2 + \text{NADPH} + 3\text{NADH} + \text{ATP}. \quad (2.9)$$

Following the simplifing nomenclature suggested by Grosz *et al.*[23] (*e.g.*, NADH is assumed to be balanced on the other side of the reaction by NAD, and NADH $\equiv$ NADPH), the above equation can be written in the following simplified form:

$$\text{Fructose} \rightarrow 2(\text{Acetyl-CoA}) + 2\text{CO}_2 + 4\text{NADH} + \text{ATP}. \quad (2.10)$$

Figure 2.1: Detail of glycolytic, citric acid cycle and PHB polymerization pathways in *Alcaligenes eutrophus* H16. Calvin cycle is included for completeness. Based on Srienc with modifications.[3] Metabolic regulation is denoted by $\longrightarrow$; $\oplus$ denotes positive regulation and $\ominus$ denotes negative regulation. Regulated enzymes: [1], glucose-6-phosphate dehydrogenase;[4,5] [2], pyruvate kinase;[6] [3], isocitrate dehydrogenase;[7] [4], β-ketothiolase;[8–12] [5], acetacetyl-CoA reductase;[12–14] [6], β-hydroxybutyrate dehydrogenase;[9] [7] phosphoribulokinase;[15] [8], ribulose-1,5-diphosphate carboxylase;[16] [9], PHB-synthase.[12,17] Abbreviations: AcAc, acetacetate; AcAcCoA, acetacetyl-CoA; AMP, adenosine 5'-monophosphate; ADP, adenosine 5'-diphosphate; ATP, adenosine 5'-triphosphate; F6P, fructose-6-phosphate; FUM, fumarate; GAP, glyceraldehyde-3-phosphate; G6P, glucose-6-phosphate; HB, β-hydroxybutryate; HB-A-I, β-hydroxybutryate-A-I; HBCoA, β-hydroxybutryate-CoA; ISOC, isocitrate; KDPG, 2-keto-3-desoxy-6-phosphogluconate; KGL, α-ketoglutarate; MAL, malate; NADH, nicotinamide adenine dinucleotide (reduced); OxAx, oxaloacetate; P_i, inorganic phosphate; PEP, phosphoenolpyruvate; 6PG, 6-phosphogluconate; 3PGA, phosphoglycerate; R5P, ribose-5-phosphate; RuDP, ribulose-1,5-diphosphate; Ru5P, ribulose-5-phosphate; SUCC, succinate.

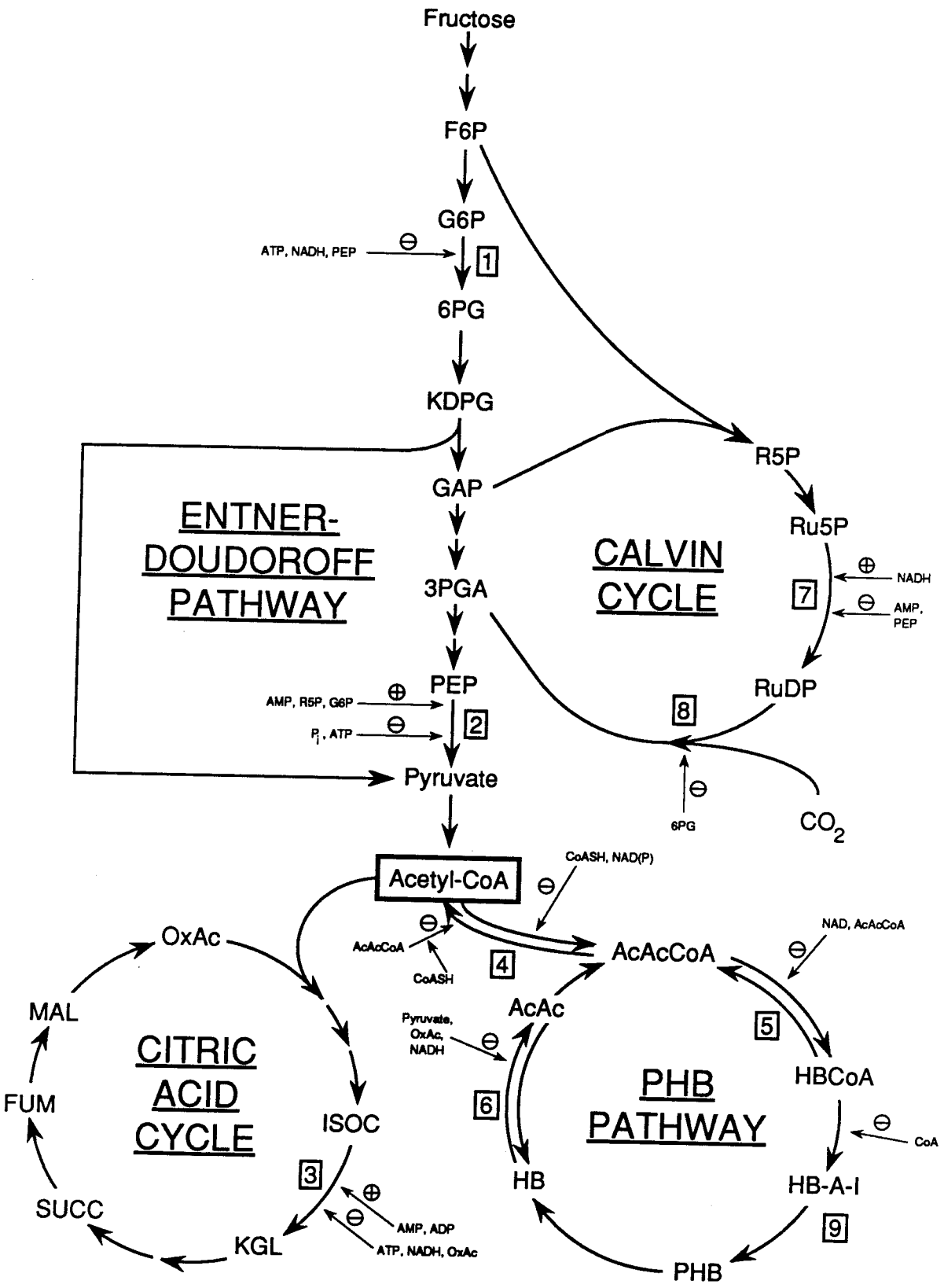
Fructose
F6P
G6P
ATP, NADH, PEP
1
6PG
KDPG
GAP
3PGA
PEP
AMP, R5P, G6P
P_i, ATP
2
Pyruvate
ENTNER-DOUDOROFF PATHWAY
R5P
Ru5P
NADH
AMP, PEP
7
RuDP
8
6PG
CO_2
CALVIN CYCLE
Acetyl-CoA
CoASH, NAD(P)
AcAcCoA
CoASH
4
AcAcCoA
NAD, AcAcCoA
5
HBCoA
CoA
HB-A-I
9
PHB
PHB PATHWAY
AcAc
Pyruvate, OxAc, NADH
6
HB
OxAc
ISOC
3
AMP, ADP
ATP, NADH, OxAc
KGL
SUCC
FUM
MAL
CITRIC ACID CYCLE

Figure 2.1

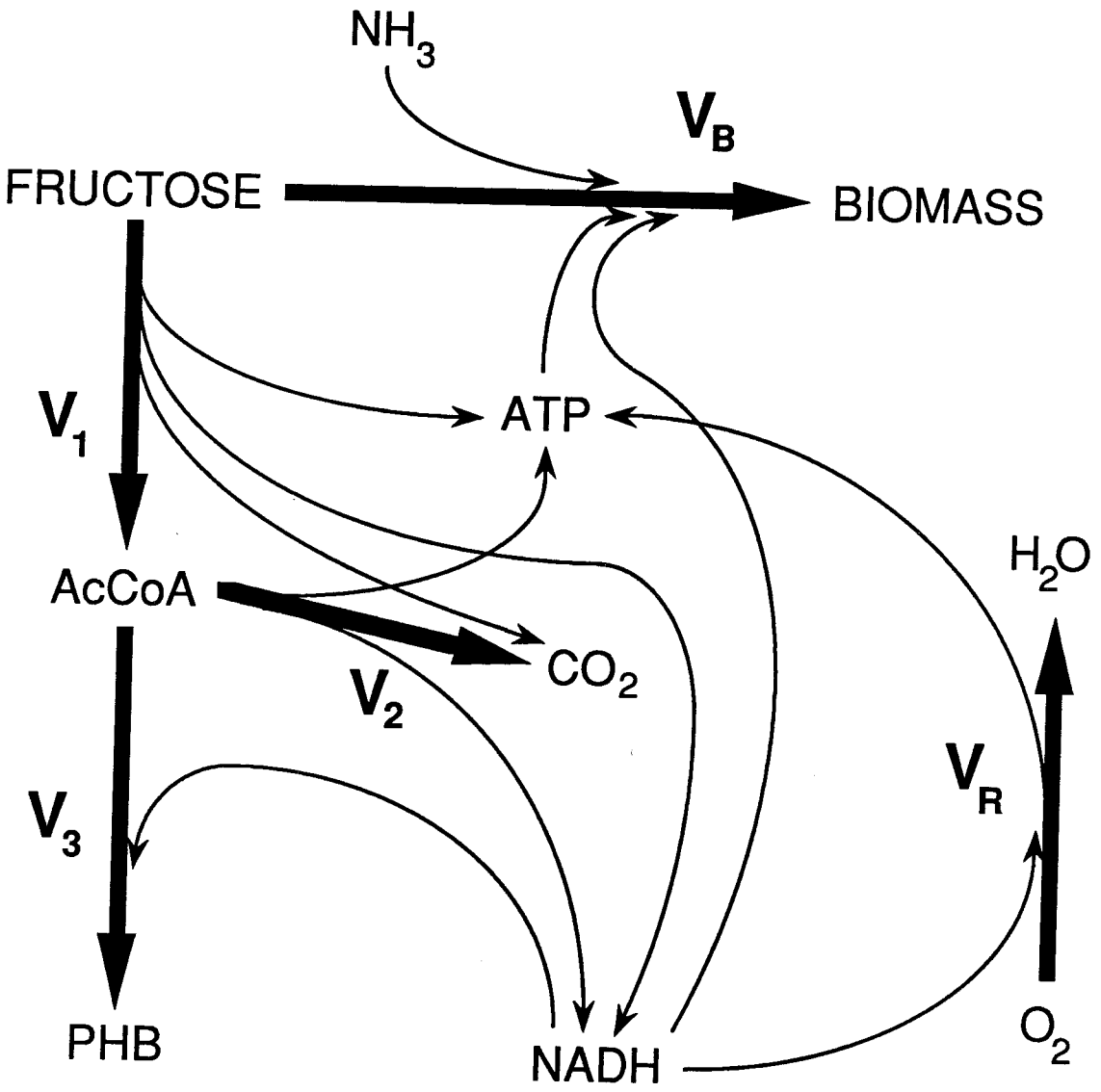

Figure 2.2: Reaction pathway flux network denoting simplified representations of glycolysis (Entner-Doudoroff pathway[19]), $\mathbf{v}_1$, citric acid cycle, $\mathbf{v}_2$, PHB polymerization, $\mathbf{v}_3$, biosynthesis, $\mathbf{v}_B$, and respiration, $\mathbf{v}_R$. The $\mathbf{v}_i$ represent the rate at which product of the i^{th} pathway is formed, *e.g.*, $\mathbf{v}_1 \equiv$ C-mol AcCoA formed in the glycolytic pathway per gram biomass per hour. Cofactor participation in each pathway is also included.

2.3.2.2 Citric Acid Cycle, v_2. In earlier work it was believed that the citric acid cycle did not exist in *A. eutrophus*, but this was later found to be in error.[24] Serving as the major provider of reducing power in the model, the citric acid cycle provides the largest amounts of NADH and NADPH of all five pathways per fructose molecule catabolized. Enzyme activity assays have suggested higher citric acid pathway activity in the presence of simple carbon sources such as acetate, succinate and malate[25], indicating that the need for greater amounts of reducing energy for biosynthesis precurser formation is satisfied by the citric acid cycle. Citric acid cycle stoichiometry is as follows:

$$\begin{aligned}(\text{Acetyl-CoA}) + 3\text{NAD} + \text{FAD} + (\text{GDP} + \text{P}_\text{i}) \rightarrow \\ \text{CoASH} + 2\text{CO}_2 + 3\text{NADH} + \text{FADH} + \text{GTP}.\end{aligned} \tag{2.11}$$

Following the method suggested by Grosz *et al.*[23], the above expression simplifies to:

$$(\text{Acetyl-CoA}) \rightarrow 2\text{CO}_2 + 4\text{NADH} + \text{ATP}. \tag{2.12}$$

2.3.2.3 PHB Polymerization, v_3. The pathway of PHB polymerization was originally elucidated by Shindler.[26] The first reaction step involves the β-ketothiolase-catalyzed condensation of two acetyl-CoA molecules:[8–12]

$$2(\text{Acetyl-CoA}) \rightarrow (\text{Acetoacetyl-CoA}) + \text{CoASH}. \tag{2.13}$$

The next step calls for an acetacetyl-CoA reductase-catalyzed internal rearrangement requiring consumption of NAD(P)H:[12–14]

$$(\text{Acetoacetyl-CoA}) + \text{NAD(P)H} \rightarrow (\beta\text{-hydroxybutyryl-CoA}) + \text{NAD(P)}. \tag{2.14}$$

The final step in the polymerization process catalyzed by PHB-synthase[12,17] is not well understood but is believed to involve an intermediate, A-I, in the following manner:[27]

$$(\beta\text{-hydroxybutyryl-CoA})+(\text{A-I}) \rightarrow$$

$$(\beta\text{-hydroxybutyryl-A-I}) + \text{CoASH} \quad (2.15a)$$

$$(\beta\text{-hydroxybutyryl-A-I}) + \text{PHB}_n \rightarrow \text{PHB}_{n+1} + (\text{A-I}). \quad (2.15b)$$

Simplifying results in:

$$2(\text{Acetyl-CoA}) + \text{NADH} + \text{PHB}_n \rightarrow \text{PHB}_{n+1}. \quad (2.16)$$

Within the cell PHB functions as a carbon and energy reserve.[28] PHB can support biosynthesis in the presence of all necessary biosynthesis nutrients other than a carbon source.

2.3.2.4 Respiration, v_R. *A. eutrophus*' respiratory chain has been studied fairly thoroughly. The presence of four oxidative phosphorylation sites have been identified in *A. eutrophus*[29]; Drozd *et al.*[30] suggest an oxidative phosphorylation ratio, P/O, of approximately 3.85 in the presence of sufficient iron. If less optimal amounts of iron are available, less than four sites are used. In simplified form, the respiration pathway may be stoichiometrically represented as follows:

$$\text{NADH} + \frac{1}{2}\text{O}_2 \rightarrow \text{NAD} + \text{H}_2\text{O} + (\text{P/O})\text{ATP}. \quad (2.17)$$

2.3.2.5 Biosynthesis, v_B. Because biosynthesis incorporates a multitude of varied, individual reactions, this pathway will be lumped into one

single, stoichiometric equation. Since there are no reports of *A. eutrophus*' biomass composition reported in the literature except for one that is effectively unavailable[31], an elemental analysis of *A. eutrophus*'s residual biomass (= cell dry weight − PHB) was conducted for carbon, nitrogen and hydrogen. The results from the compositional analysis of whole cells were corrected for PHB content. After accounting for carbon, nitrogen, and hydrogen content, the remainder was attributed to oxygen and ash. Assuming that the residual biomass contained *ca* 7% ash[32], we assigned a single carbon formula of $CH_{1.66}O_{0.43}N_{0.25}$. The nitrogen content is in close agreement with another reported value.[33] We then propose the following biosynthesis equation:

$$\frac{1}{6}\text{Fructose} + 0.25NH_3 + \frac{1}{(Y_{ATP}^{max})_{th}}ATP + \frac{1}{(Y_{NADH}^{max})_{th}}NADH \rightarrow CH_{1.66}O_{0.43}N_{0.25} + 0.57H_2O, \quad (2.18)$$

where $(Y_i^{max})_{th}$ is the theoretical yield coefficient of i (mol biomass/mol i). Applying a reductive balance[22] to the fructose/biomass system results in a calculation of *ca* 40 (mol biomass)/(mol NADH) for $(Y_{NADH}^{max})_{th}$.

As Figure 2.2 and the above stoichiometric equations indicate, ATP, NADH, and acetyl-CoA are produced and consumed by all five pathways. Figure 2.1 depicts how these intracellular species contribute to the inhibition or enhancement of the pathway activities of the glycolytic, citric acid cycle and PHB polymerization pathways. It is quite apparent that we need to consider the responses of these components to understand regulation of *A. eutrophus* pathways.

2.3.3 Mass Balances

To infer the individual pathway rates of the model experimentally, we must be able to relate these microscopic pathway rates to macroscopic fermentation parameters. We begin with an intracellular microscopic species balance on non-transported species i:

$$\frac{d\mathbf{c}_i}{dt} = \mathbf{r}_{f,i} - \frac{1}{\mathbf{x}}\frac{d\mathbf{x}}{dt}\mathbf{c}_i, \tag{2.19}$$

where $\mathbf{c}_i \equiv$ mol i per unit weight biomass, mol/g

$\mathbf{x} \equiv$ weight of biomass, g

$\mathbf{r}_{f,i} \equiv$ rate of formation of i, mol/g/hr.

In the above microscopic balance we imagine our control volume enveloping a single cell but excluding PHB granules within the cell. In other words we are performing our balance on the entire mass of a cell minus the PHB contribution. This effectively defines the portion of the cell mass that we choose to call the (residual) biomass.

We note next that $\mathbf{r}_{f,i}$ consists of two components. The first component accounts for the formation of i through the direct creation of biomass. The second component accounts for the formation of i through nonbiosynthetic reactions (See Figure 2.2). In mathematical form this can be represented as follows:

$$\mathbf{r}_{f,i} = \sum_j \nu_{ij}\mathbf{v}_j + \alpha_i \mathbf{r}_\mathbf{g}, \tag{2.20}$$

where $\alpha_i \equiv$ fraction of i in biomass, g_i/g biomass

$\nu_{ij} \equiv$ stoichiometric coefficient of i in the j^{th} pathway, mol/mol

$\mathbf{v_j}$ $\equiv$ rate through the j^{th} pathway, mol product/g/hr

$\mathbf{r_g}$ $\equiv$ rate of biomass synthesis per unit weight biomass, mol/g/hr.

With a little thought we realize that

$$\frac{1}{\mathbf{x}}\frac{d\mathbf{x}}{dt}\mathbf{c}_i = \alpha_i \mathbf{r_g}, \tag{2.21}$$

and our intracellular microscopic balance given in Eq. (2.19) simplifies to:

$$\frac{d\mathbf{c}_i}{dt} = \sum_j \nu_{ij}\mathbf{v}_j. \tag{2.22}$$

This expression, therefore, allows us to estimate fluctuations in intracellular pools or directly relate pathway rates to one another by imposing quasi-steady-state assumptions on any or all the intracellular balances.

To relate fermentation observables to the reaction pathways of interest, we perform a macroscopic species balance on species i over the entire fermenter volume (Figure 2.3). Applying a general macroscopic balance, we start with the following equation:

$$\frac{d(\bar{\mathbf{V}}\cdot\bar{\mathbf{C}}_i)}{dt} = \left\{ \begin{matrix} net\ rate\ of\ i \\ into\ system \end{matrix} \right\} + \bar{\mathbf{V}}\cdot\bar{\mathbf{R}}_{f,i}, \tag{2.23}$$

where $\bar{\mathbf{V}}$ $\equiv$ total fermenter volume, l

$\bar{\mathbf{C}}_i$ $\equiv$ volume-averaged concentration of i, mol/l

$\bar{\mathbf{R}}_{f,i}$ $\equiv$ volume-averaged rate of formation of i, mol/l/hr.

The first term on the right-hand side of Eq. (2.23) accounts for convective transport of species i into and out of the fermenter, *e.g.*, gas sparging, or direct addition of species i, *e.g.*, liquid nutrient addition.

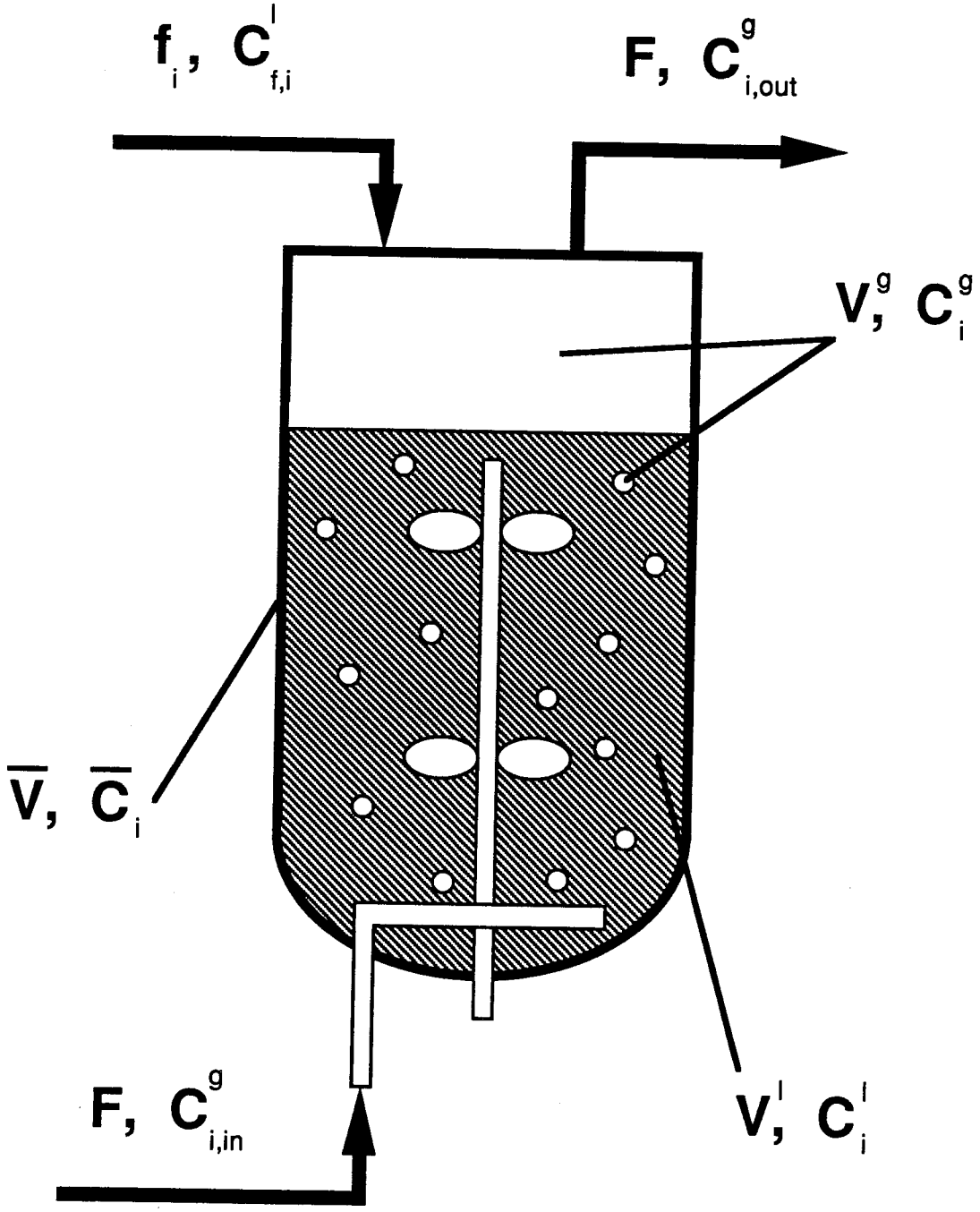

Figure 2.3: Description of the mass balance over fermenter system. $\bar{\mathbf{V}}$ and $\bar{\mathbf{C}}_i$ are the total reactor volume and volume-averaged concentration of species i, respectively. $\mathbf{F}$ is the gas volumetric flow rate through the reactor. $\mathbf{V}^l$ and $\mathbf{V}^g$ are the nonaerated liquid and gas volumes, respectively. $\mathbf{C}_i^l$ and $\mathbf{C}_i^g$ are the liquid and gas volume-averaged concentrations of i, respectively. $\mathbf{f}_i$ and $\mathbf{C}_{f,i}^l$ are the volumetric nutrient feed rate and the concentration of nutrient feed of species i, respectively. $\mathbf{C}_{i,in}^g$ and $\mathbf{C}_{i,out}^g$ are the inlet and outlet gas concentrations of species i, respectively.

In Figure 2.3 the total fermenter volume has been partitioned into two parts: the nonaerated liquid volume, $\mathbf{V}^l$, and the gas volume, $\mathbf{V}^g$. Therefore,

$$\bar{\mathbf{V}} = \mathbf{V}^l + \mathbf{V}^g. \tag{2.24}$$

For species i, the volume-averaged concentration can be related to the concentration of i in the liquid phase, $\mathbf{C}_i^l$, and the volume-averaged concentration of i in the gas phase, $\mathbf{C}_i^g$, through the following relationship:

$$\bar{\mathbf{C}}_i\bar{\mathbf{V}} = \mathbf{C}_i^l\mathbf{V}^l + \mathbf{C}_i^g\mathbf{V}^g. \tag{2.25}$$

Both gas and liquid phases are assumed to be well mixed and approximated by CSTRs. In like manner, the volume-averaged rate of formation of species i can be decomposed into a liquid-phase component, $\mathbf{R}_{f,i}^l$, and and gas-phase component, $\mathbf{R}_{f,i}^g$. These three are related by their volume portions as shown:

$$\bar{\mathbf{R}}_{f,i}\bar{\mathbf{V}} = \mathbf{R}_{f,i}^l\mathbf{V}^l + \mathbf{R}_{f,i}^g\mathbf{V}^g. \tag{2.26}$$

Since no reaction occurs in the gas phase,

$$\bar{\mathbf{R}}_{f,i}\bar{\mathbf{V}} = \mathbf{R}_{f,i}^l\mathbf{V}^l. \tag{2.27}$$

We can relate the liquid phase rate of formation of species i and the various pathway rates, $\mathbf{v}_j$, through the following equation:

$$\mathbf{R}_{f,i}^l = \mathbf{X} \cdot \sum_j \gamma_{ij}\mathbf{v}_j, \tag{2.28}$$

where $\mathbf{X}$ $\equiv$ weight biomass-per-unit liquid volume, g/l

γ_{ij} $\equiv$ stoichiometric coefficient of production of i in the j^{th} pathway, mol/g/hr.

Substituting Eq. (2.25) into the left side of Eq. (2.23), substituting Eq. (2.27) into the right side of Eq. (2.23) with subsequent substitution of Eq. (2.28), and explicitly defining the convective transport terms, the generalized macroscopic balance reduces to:

$$\frac{d\left(\mathbf{C}_i^l\mathbf{V}^l + \mathbf{C}_i^g\mathbf{V}^g\right)}{dt} = \mathbf{V}^l\left(\mathbf{X}\cdot\sum_j \gamma_{ij}\mathbf{v}_j\right) + \mathbf{F}\left[\mathbf{C}_{i,in}^g - \mathbf{C}_{i,out}^g\right] + \mathbf{f}_i\mathbf{C}_{f,i}^l, \quad (2.29)$$

where $\mathbf{F}$ $\equiv$ gas volumetric flow rate, l/hr

$\mathbf{f}_i$ $\equiv$ nutrient feed rate of i, l/hr

$\mathbf{C}_{f,i}^l$ $\equiv$ nutrient feed concentration of i, mol/l

$\mathbf{C}_{i,in}^g$ $\equiv$ inlet gas concentration of i, mol/l

$\mathbf{C}_{i,out}^g$ $\equiv$ outlet gas concentration of i, mol/l.

Following rearrangement, Eq. (2.29) is then applied to the fermentation observables fructose, biomass, NH_3, CO_2, O_2, and PHB:

$$\frac{d\mathbf{C}_{Fruc}^l}{dt} = \mathbf{X}\left[-\frac{3}{2}\mathbf{v}_1 - \mathbf{v}_B\right] - \frac{\mathbf{C}_{Fruc}^l}{\mathbf{V}^l}\frac{d\mathbf{V}^l}{dt} + \frac{\mathbf{f}_{Fruc}}{\mathbf{V}^l}\mathbf{C}_{f,Fruc}^l \quad (2.30)$$

$$\frac{d\mathbf{C}_{Bio}^l}{dt} = \mathbf{X}\mathbf{v}_B - \frac{\mathbf{C}_{Bio}^l}{\mathbf{V}^l}\frac{d\mathbf{V}^l}{dt} \quad (2.31)$$

$$\frac{d\mathbf{C}_{NH_3}^l}{dt} = -0.25\mathbf{X}\mathbf{v}_B - \frac{\mathbf{C}_{NH_3}^l}{\mathbf{V}^l}\frac{d\mathbf{V}^l}{dt} + \frac{\mathbf{f}_{NH_3}}{\mathbf{V}^l}\mathbf{C}_{f,NH_3} \quad (2.32)$$

$$\frac{d\mathbf{C}^l_{CO_2}}{dt} = \frac{\mathbf{F}}{\mathbf{V}^l}\left[\mathbf{C}^g_{CO_2,in} - \mathbf{C}^g_{CO_2,out}\right] + \mathbf{X}\left[\frac{1}{2}\mathbf{v}_1 + \mathbf{v}_2\right] - \frac{\mathbf{C}^l_{CO_2}}{\mathbf{V}^l}\frac{d\mathbf{V}^l}{dt} \quad (2.33)$$
$$- \left(\frac{\mathbf{V}^g}{\mathbf{V}^l}\frac{d\mathbf{C}^g_{CO_2}}{dt} + \frac{\mathbf{C}^g_{CO_2}}{\mathbf{V}^l}\frac{d\mathbf{V}^g}{dt}\right)$$

$$\frac{d\mathbf{C}^l_{O_2}}{dt} = \frac{\mathbf{F}}{\mathbf{V}^l}\left[\mathbf{C}^g_{O_2,in} - \mathbf{C}^g_{O_2,out}\right] - \frac{\mathbf{X}}{2}\mathbf{v}_R - \frac{\mathbf{C}^l_{O_2}}{\mathbf{V}^l}\frac{d\mathbf{V}^l}{dt} \quad (2.34)$$
$$- \left(\frac{\mathbf{V}^g}{\mathbf{V}^l}\frac{d\mathbf{C}^g_{O_2}}{dt} + \frac{\mathbf{C}^g_{O_2}}{\mathbf{V}^l}\frac{d\mathbf{V}^g}{dt}\right)$$

$$\frac{d\mathbf{C}^l_{PHB}}{dt} = \mathbf{X}\mathbf{v}_3 - \frac{\mathbf{C}^l_{PHB}}{\mathbf{V}^l}\frac{d\mathbf{V}^l}{dt}. \quad (2.35)$$

The intracellular balances for acetyl-CoA, ATP, and NADH from Eq. (2.22) take the form

$$\frac{d\mathbf{c}_{AcCoA}}{dt} = \frac{1}{2}\left[\mathbf{v}_1 - \mathbf{v}_2 - \mathbf{v}_3\right] \quad (2.36)$$

$$\frac{d\mathbf{c}_{ATP}}{dt} = \frac{1}{4}\mathbf{v}_1 + \frac{1}{2}\mathbf{v}_2 - \frac{1}{\mathrm{Y_{ATP}}}\mathbf{v}_B + (\mathrm{P/O})\mathbf{v}_R \quad (2.37)$$

$$\frac{d\mathbf{c}_{NADH}}{dt} = \mathbf{v}_1 + 2\mathbf{v}_2 - \frac{1}{4}\mathbf{v}_3 - \mathbf{v}_R - \frac{1}{\mathrm{Y_{NADH}}}\mathbf{v}_B, \quad (2.38)$$

where $$\frac{1}{\mathrm{Y}_i} \equiv \frac{1}{\mathrm{Y}_i^{\max}} + \frac{\mathrm{m}_{i,e}}{\mu} \quad (2.39)$$

$$\equiv \frac{1}{(\mathrm{Y}_i^{\max})_{\mathrm{th}}} + \mathrm{m}_{i,g} + \frac{\mathrm{m}_{i,e}}{\mu} \quad (2.40)$$

$\mathrm{P/O} \equiv$ oxidative phosphorylation ratio, mol ATP/mol $\mathrm{H_2O}$.

The concept of a yield coefficient for ATP expressed as in Eq. (2.39) was proposed by Stouthamer and Bettenhaussen.[34] Later this formulation was expanded[35] to that shown in Eq. (2.40) when experimental observations indicated that calculated values of $\mathrm{Y}_{\mathrm{ATP}}^{\max}$ for a number of different organisms were too

high and varied with growth rate. Essentially, using the case of ATP, Eq. (2.40) suggests that there is a critical amount of ATP required simply to chemically synthesize biomass. The constant $m_{i,g}$ accounts for the ATP expended to support biosynthesis activities, *e.g.*, energy required to sustain biosynthetic protein turnover. The constant $m_{i,e}$ accounts for any nonbiosynthetic maintenance requiring expenditure of ATP. For completeness, we have drawn a yield coefficient parallel for NADH, although NADH maintenance is largely ignored in most metabolic model formulations.

To solve for the various pathway rates, $\mathbf{v}_i$, we simply rearrange the macroscopic balance equations (Eqs. (2.30)–(2.35)) to the following forms:

$$\mathbf{v}_B = \frac{1}{\mathbf{X}}\left[\frac{d\mathbf{C}^l_{Bio}}{dt} + \frac{\mathbf{C}^l_{Bio}}{\mathbf{V}^l}\frac{d\mathbf{V}^l}{dt}\right] \tag{2.41}$$

$$= -\frac{4}{\mathbf{X}}\left[\frac{d\mathbf{C}^l_{NH_3}}{dt} + \frac{\mathbf{C}^l_{NH_3}}{\mathbf{V}^l}\frac{d\mathbf{V}^l}{dt} + \frac{\mathbf{f}_{NH_3}}{\mathbf{V}^l}\mathbf{C}^l_{f,NH_3}\right] \tag{2.42}$$

$$\mathbf{v}_R = \frac{2}{\mathbf{X}}\left[\frac{\mathbf{F}}{\mathbf{V}^l}\left(\mathbf{C}^g_{O_2,in} - \mathbf{C}^g_{O_2,out}\right) - \frac{d\mathbf{C}^l_{O_2}}{dt} - \frac{\mathbf{C}^l_{O_2}}{\mathbf{V}^l}\frac{d\mathbf{V}^l}{dt} - \left(\frac{\mathbf{V}^g}{\mathbf{V}^l}\frac{d\mathbf{C}^g_{O_2}}{dt} + \frac{\mathbf{C}^g_{O_2}}{\mathbf{V}^l}\frac{d\mathbf{V}^g}{dt}\right)\right] \tag{2.43}$$

$$\mathbf{v}_1 = -\frac{2}{3\mathbf{X}}\left[\frac{d\mathbf{C}^l_{Fruc}}{dt} + \frac{\mathbf{C}^l_{Fruc}}{\mathbf{V}^l}\frac{d\mathbf{V}^l}{dt} - \frac{\mathbf{f}^l_{Fruc}}{\mathbf{V}^l}\mathbf{C}^l_{f,Fruc}\right] - \frac{2}{3}\mathbf{v}_B \tag{2.44}$$

$$\mathbf{v}_2 = \frac{1}{\mathbf{X}}\left[\frac{1}{3}\left(\frac{d\mathbf{C}^l_{Fruc}}{dt} + \frac{\mathbf{C}^l_{Fruc}}{\mathbf{V}^l}\frac{d\mathbf{V}^l}{dt} - \frac{\mathbf{f}_{Fruc}}{\mathbf{V}^l}\mathbf{C}^l_{f,Fruc}\right)\right. \tag{2.45}$$
$$+ \frac{\mathbf{F}}{\mathbf{V}^l}\left(\mathbf{C}^g_{CO_2,out} - \mathbf{C}^g_{CO_2,in}\right) - \left(\frac{\mathbf{V}^g}{\mathbf{V}^l}\frac{d\mathbf{C}^g_{CO_2}}{dt} + \frac{\mathbf{C}^g_{CO_2}}{\mathbf{V}^l}\frac{d\mathbf{V}^g}{dt}\right)$$
$$\left. + \frac{d\mathbf{C}^l_{CO_2}}{dt} + \frac{\mathbf{C}^l_{CO_2}}{\mathbf{V}^l}\frac{d\mathbf{V}^l}{dt}\right] + \frac{1}{3}\mathbf{v}_B$$

$$\mathbf{v}_3 = \frac{1}{\mathbf{X}}\left[\frac{d\mathbf{C}^l_{PHB}}{dt} + \frac{\mathbf{C}^l_{PHB}}{\mathbf{V}^l}\frac{d\mathbf{V}^l}{dt}\right]. \tag{2.46}$$

Employing a series of varying fermentation conditions, the above equations lend a framework through which experimental data can be analyzed and interpreted, thereby elucidating the cell's metabolic response and metabolic activity during each fermentation. Through the intracellular balances, the unknown metabolic parameters Y_i^{max}, $m_{i,e}$ and P/O can be investigated. A simple extension of this model is accomplished by returning to the earlier macroscopic balances for each observed species (Eqs. (2.30)–(2.35)) and substituting an appropriate kinetic expression for each $\mathbf{v}_i$ in terms of the metabolite and medium components included in the model. One might envision a wide spectrum of derived expressions beginning with simple Michaelis-Menten kinetics relationships and ultimately extending to mathematical formulations utilizing the results of kinetic studies of rate-limiting, regulatory enzymes in each pathway. In this way one could simulate the *A. eutrophus* fermentation system with varying degrees of complexity using a physiologically based model framework as opposed to mathematically fitting data with an empirical model.

2.4 MATERIALS AND METHODS

2.4.1 Organism

Alcaligenes eutrophus H16 (ATCC 17699) was stored on nutrient broth slants with 0.5% fructose added to retain induction of the fructose catabolism enzyme system;[20] cells were restreaked every two months. During liquid cultivation, *A. eutrophus* was grown heterotrophically on media described by Schlegel *et al.*[36] and micronutrient supplement described by Pfennig and Lippert.[37] Cells were grown at 31°C and pH 6.8.

2.4.2 Analytical Methods

2.4.2.1 Off-line. Fructose concentrations were determined spectrophotometrically with the Boehringer Mannheim GMBH Glucose/Fructose assay kit (Cat. No. 139106). PHB was determined after the method of Braunegg *et al.*[38] Ammonium, determined as ammonium chloride, was measured by an ammonium probe (Ingold Electrodes, Inc., Series 7500). Dry weight determinations were made via the membrane-filtration technique. Biomass was calculated from the difference between the cell dry weight and PHB concentrations.

2.4.2.2 On-line. The dissolved oxygen concentration was determined with an Instrumentation Laboratories (IL) 531 Industrial Dissolved Oxygen monitor and an Ingold Electrodes, Inc. polarographic oxygen-sensing probe. Optical density was determined at 420 nm with a Spectronic 20 (Baush and

Lomb) modified to accept the flow cell described by Lee and Lim.[39] A Cole-Parmer pH controller (Model 5997-20) was used to measure and maintain the pH in conjunction with two Masterflex peristaltic pumps for the addition of sodium hydroxide and phosphoric acid. Off-gas carbon dioxide and oxygen concentrations were monitored with an Infrared Industries, Inc. (Santa Barbara, CA) Model # 703-075 carbon dioxide gas detector and a Leeds and Northrup 7863 thermomagnetic oxygen analyzer, respectively.

2.4.3 Fermentation System

Fermentations were conducted in an 18 liter Bioengineering AG Laboratory Fermenter L1523. The fermenter off-gas first passed through a condensing column chilled to *ca* $-5°C$ with a Haake A80 recirculation bath and an ethanol/water solution (1:1) and then through a drying column filled with Drierite before entering the off-gas analyzers.

The data acquisition system supplied as part of the FluroMeasure System^{TM} (BioChem Technology, Inc., Malvern, PA) data logged fluorescence (data presented elsewhere), optical density, off-gas oxygen, off-gas carbon dioxide, pH, and dissolved oxygen. Data were collected at intervals of two points per minute over the course of the fermentation.

2.4.4 Post-fermentation Data Manipulations

2.4.4.1 On-line Data Processing. Preliminary data manipulations were performed on an IBM PC-AT. Further manipulations of on-line observables

occurred on a VAX 11/780 or MicroVax 3500. First, each on-line parameter was checked against a rejection tolerance. Following spurious data-point checking and elimination, the data were subjected to a three-point box-car average. Using the method of Savitzky and Golay[40] with corrections by Steiner *et al.*,[41] the data were smoothed and derivatives calculated. This technique is equivalent to a linear regression fit for a single point, given the nature of the surrounding points and the desired weighting function. A 25 point grouping size was used for both smoothing and derivative determinations. Smoothing was accomplished using a cubic weighting function, and derivatives were calculated with a quadratic derivative weighting function. Every fifth point (every fifteenth point of the raw data) was selected for later pathway rate calculations. Since the culture volume was known at each sampling time via back-calculation, the volume and volume changes between sampling times were approximated by a linear expression.

2.4.4.2 Off-line Data Processing. To make the off-line fructose, ammonium, PHB and dry weight data suitable for calculation with the on-line data, a number of adjustments and interpolations were necessary. In the case of fructose and ammonium chloride, additions of concentrated feed solutions had to be accounted for in the model. Also, since a fed-batch system was employed, PHB and dry weight concentrations were effectively diluted because of feed solution and pH control additions, as also were the fructose and ammonium chloride concentrations.

To incorporate the effects of nutrient feeding, pH control additions, and the associated volume changes, a computational tool was developed, beginning with the previously presented general macroscopic balance (Eq. (2.23)), simplified for

nongaseous liquid phase components only. The "l" superscript has been dropped and all concentrations, volumes and rates of formation will be assumed to be liquid phase only. For a fed-batch reactor:

$$\frac{d(\mathbf{V}\cdot\mathbf{C}_i)}{dt} = \mathbf{f}_i\cdot\mathbf{C}_{f,i} + \mathbf{V}\cdot\mathbf{R}_{f,i}, \tag{2.47}$$

where $\mathbf{V}$ $\equiv$ liquid culture volume, l

$\mathbf{C}_i$ $\equiv$ mol i per unit liquid volume, mol/l

$\mathbf{C}_{f,i}$ $\equiv$ mol i per unit liquid volume in the feed, mol/l

$\mathbf{R}_{f,i}$ $\equiv$ rate of formation of i, mol/l/hr

$\mathbf{f}_i$ $\equiv$ volumetric feed rate of i, l/hr.

Differentiating, dividing by $\mathbf{V}$, and rearranging Eq. (2.47) lead to

$$\frac{d\mathbf{C}_i}{dt} + \frac{\mathbf{C}_i}{\mathbf{V}}\frac{d\mathbf{V}}{dt} - \frac{\mathbf{f}_i}{\mathbf{V}}\mathbf{C}_{f,i} = \mathbf{R}_{f,i}. \tag{2.48}$$

This equation clearly demonstrates that unlike a constant volume batch fermentation in which $\mathbf{R}_{f,i}$ can be determined directly from the change in the concentration of i (the second and third terms on the left-hand side are zero), we need to be aware of volume changes as well as feed additions in a fed-batch fermentation.

For the sake of mathematical convenience let us define Φ_i such that the derivative of Φ_i equals the left side of Eq. (2.48):

$$\frac{d\Phi_i}{dt} = \frac{d\mathbf{C}_i}{dt} + \frac{\mathbf{C}_i}{\mathbf{V}}\frac{d\mathbf{V}}{dt} - \frac{\mathbf{f}_i}{\mathbf{V}}\mathbf{C}_{f,i}. \tag{2.49}$$

Φ_i is, therefore, related to $\mathbf{R}_{f,i}$ through the following relationship:

$$\Phi_i = \int \mathbf{R}_{f,i}dt + \Theta_i, \tag{2.50}$$

where Θ_i is an arbitrary constant. Effectively, Φ_i is a pseudoconcentration; the derivative of Φ_i gives $\mathbf{R}_{f,i}$. As Eq. (2.49) suggests, Φ_i allows consolidation of all three effects of concentration change, volume change, and nutrient feed addition and effectively replaces these three terms in Eqs. (2.41), (2.42), (2.44), (2.45), and (2.46). The remainder of this derivation is reserved to Appendix 1.

At this point the question of why we have proceeded in this manner may arise. Simply put, it is much better, computationally speaking, to integrate the data, fit the pseudoconcentration, Φ_i, with a smooth function for interpolation and calculation of derivatives than to try to fit and interpolate the actual concentration data and assume a linear profile for feed additions. The latter method introduces larger uncertainties in the derivative calculations simply because the concentration of species i may fluctuate up and down from sample to sample throughout the fermentation, giving both positive and negative slopes. With the pseudoconcentration method, calculation of derivatives is dramatically improved since the pseudoconcentration is almost always monotonically increasing or decreasing.

Psuedoconcentrations as well as observed cell dry weight and PHB concentrations were smoothed and interpolated, using IMSL cubic spline routines ICSSCU or ICSSCV; interpolations and derivative calculations were made at time points corresponding to the selected on-line data points.

2.5 EXPERIMENTAL WORK

2.5.1 Application of Model

The previously described network model was applied to a fermentation similiar in nature to that used by Heinzle and Lafferty.[2] We chose a run similiar to the one used by Heinzle and Lafferty to demonstrate the usefulness of this approach as well as to highlight the physiological information provided by this model structure. In this application the metabolic implication of ammonium exhaustion clearly manifests itself in the dramatic shift in pathway activities.

Alcaligenes eutrophus H16 was grown heterotrophically on a salts medium, with ammonium chloride serving as the nitrogen source and fructose serving as the carbon source. The cells were allowed to grow exponentially until the ammonium became exhausted. The initial concentration of NH_4Cl was 0.92 g/l, and the air flow rate was 2.3 l/min. Agitation began at 600 rpm for the first 10.5 hours of the fermentation, followed by an increase to 700 rpm for the duration of the experiment. The fructose concentration was maintained by constant addition of a fructose solution (*ca* 500 g/l), beginning at 10 hours. The fructose feed addition rate was gradually increased during growth and decreased after ammonium exhaustion as dictated by periodic measurements of the fructose concentration; the fructose concentration averaged 5 g/l throughout most of the experiment.

2.5.2 Experimental Run Results

2.5.2.1 Monitored Fermentation Parameters. Figure 2.4a describes the time course of the cell dry weight, biomass, PHB and ammonium (as ammonium chloride). As Heinzle and Lafferty observed,[2] biomass and cell dry weight increase exponentially until the ammonium source is exhausted at approximately 12.5 hours. Beginning at ammonium exhaustion, biosynthesis ceases; the cell dry weight continues to increase but at a distinctly slower rate. The PHB concentration remains at a low level during growth, followed by a dramatic increase in concentration upon cessation of growth. The PHB concentration continues to increase strongly through the end of the fermentation. Separate fermentations that temporally extend further into the PHB storage phase confirm Heinzle and Lafferty's observation of diminishing increases in PHB concentration with increasing time (Figure 2.5). Clearly, the continued rise in the cell dry weight concentration is directly attributable to the increase in the PHB concentration.

Figure 2.4b depicts the temporal evolution of the off-gas carbon dioxide and oxygen concentrations. In both cases the growth-phase concentration changes are exponential in nature, increasing exponentially in the case of carbon dioxide and decreasing exponentially, *i.e.*, $O_2(t) \approx 20.946\% - \beta e^{\mu t}$, in the case of oxygen. At the cessation of growth, trajectories of both gas concentrations dramatically reverse and eventually stabilize at values roughly 40 percent of their pre-ammonium exhaustion maxima. As time progresses, these concentrations continue to shift gradually towards the direction of their normal air values.

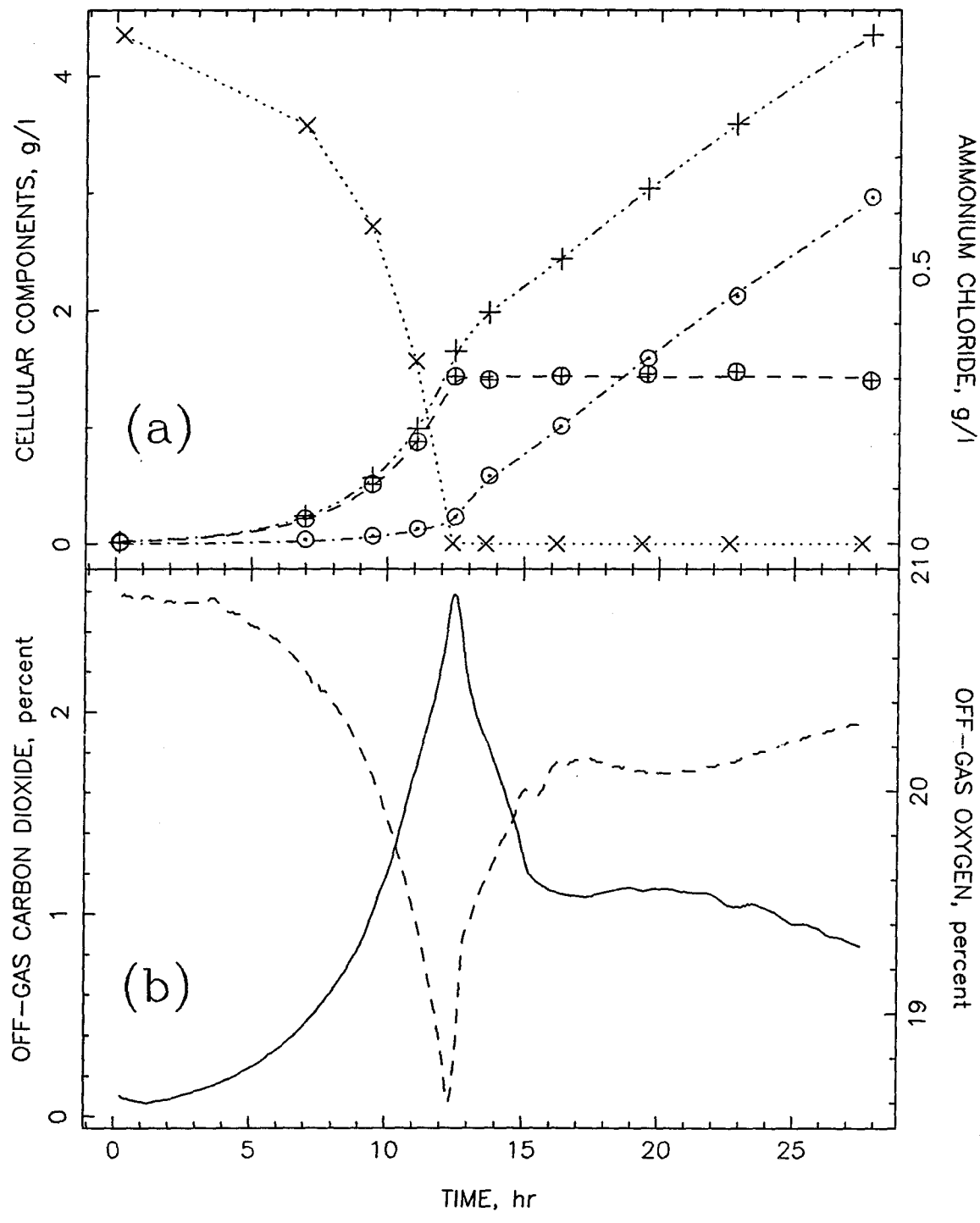

Figure 2.4: Ammonium exhaustion experiment: raw data. **(a)** Cell dry weight, + ; biomass, ⊕ ; PHB, ⊙ ; ammonium chloride, × . **(b)** Off-gas carbon dioxide, —— ; off-gas oxygen, – – – .

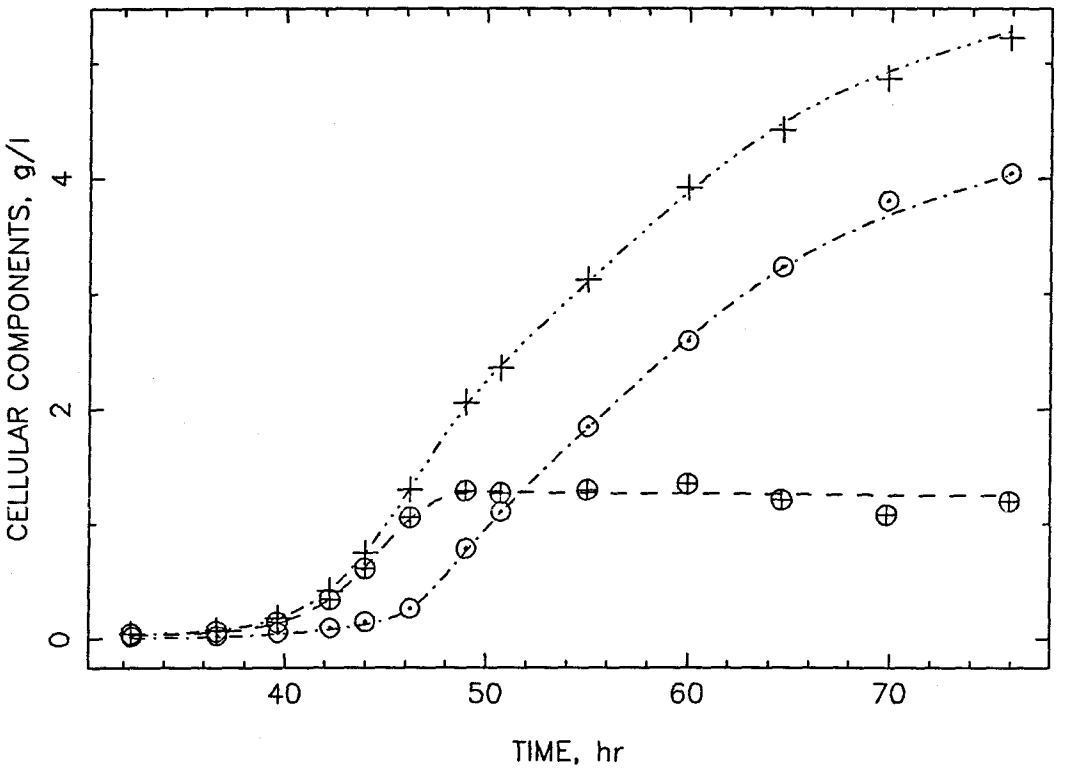

Figure 2.5: Extended PHB storage: raw data. Cell dry weight, + ; biomass, $\oplus$; PHB, $\odot$.

Figure 2.6a shows the time course of the back-calculated (to be discussed), time-integrated fructose production rate, or, equivalently, the pseudofructose concentration, Φ_{Fruc}, as defined by Eq. (2.50). As the combination of Eqs. (2.48) and (2.49) suggest, the negative slope of this curve indicates the rate at which fructose is being consumed. Up to 12 hours the slope of the solid line decreases exponentially, indicating an exponentially increasing demand for fructose consumption that is due to biosynthesis. When biosynthesis stops, fructose consumption decreases markedly, and remains fairly constant throughout the rest of the run. Figure 2.6a also indicates the fermenter fructose concentration level throughout the course of the experment. The initial decrease in fructose concentration is counteracted by the initiation of fructose feeding beginning at *ca* 10 hours.

Similiarly, Figure 2.6b depicts the time course of the integrated ammonium production rate, or, equivalently, the pseudoammonium chloride concentration, $\Phi_{\mathrm{NH_4Cl}}$. As with the pseudofructose concentration, the slope decreases exponentially, indicating an increasing rate of ammonium consumption until exhaustion is encountered; thereafter, the slope is zero, indicating no consumption of ammonium chloride. The similarity between this curve and the fermenter ammonium concentration in Figure 2.4a is not surprising considering that changes in volume that are due to nutrient feed and pH control additions are very small. Effectively, this fermentation is very similiar to a batch fermentation.

2.5.2.2 Pathway Calculations. In calculating the pathway rates for this and several other experiments, a consistent 10% average of the consumed

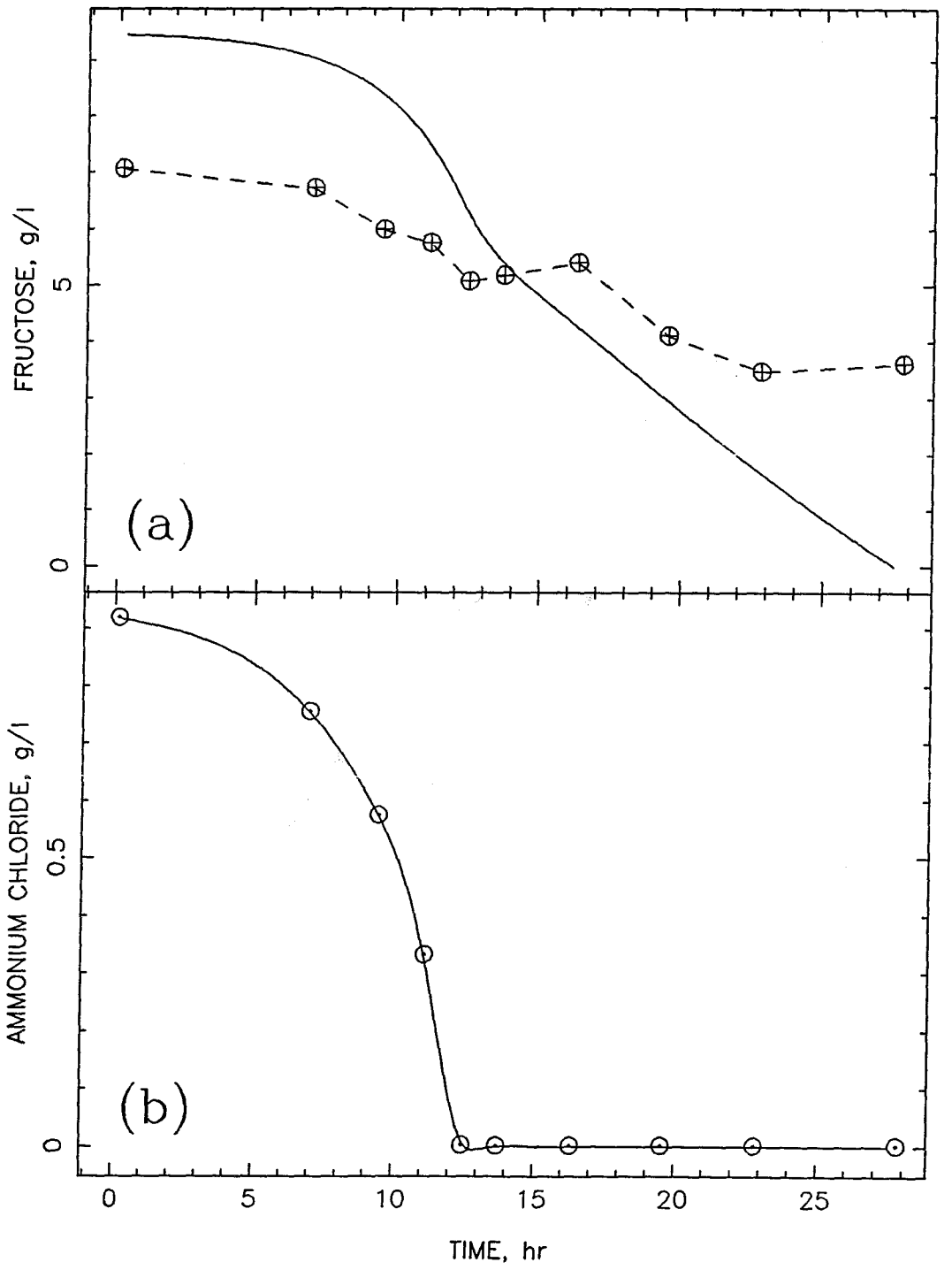

Figure 2.6: Ammonium exhaustion experiment: nutrient concentrations. **(a)** Pseudofructose concentration ($\equiv \Phi_{\mathrm{Fruc}}$) or time integral of fructose production rate, —— ; fructose concentration in the fermenter, $\oplus$. **(b)** Pseudoammonium chloride concentration ($\equiv \Phi_{\mathrm{NH_4Cl}}$) or time integral of ammonium chloride production rate, —— .

fructose could not be accounted for as biomass, PHB, carbon dioxide or excreted metabolites. An extensive reevaluation of the experimental system and techniques confirmed the reliability of the overall experimental procedure.

Reevaluation of the experimental data strongly suggested that the presence of a sizeable foam layer served a capacitorlike function, retaining significant amounts of nutrient feed and pH control solutions added through the fermenter headplate. Evidence of the foam layer's influence manifested itself in the delayed culture broth pH response to pH corrective action as well as the overshoot of the pH setpoint, once pH corrective action ceased. Also, at the cessation of growth, the foam layer quickly disintegrated; simultaneously, the fermenter pH increased rapidly. The details of this analysis are discussed extensively in Appendix 2.

Ignoring the missing fructose in the foam layer led to nonphysiological pathway rates for the citric acid cycle, $\mathbf{v}_2$. As Eq. (2.45) indicates, $\mathbf{v}_2$ relies heavily on the consumption rate of fructose. The (negative) fructose contribution to $\mathbf{v}_2$ is counterbalanced by the (positive) carbon dioxide evolution contribution. Proceeding with the uncorrected carbon balance calculation led typically to small or negative citric acid pathway rates. In the interest of correcting this problem, the fructose consumption rate was back-calculated by closing the intracellular acetyl-CoA balance (setting the time derivative equal to zero) shown in Eq. (2.36). This effectively remedied the negative or low citric acid cycle pathway rates and therefore was deemed a suitable solution to this experimental anomaly.

As depicted in Figure 2.7a, the biosynthesis pathway rate, $\mathbf{v}_B$, during the growth phase of this fermentation averages approximately 13.6 C-mmol

biomass/((g biomass)(hr)). Assuming a single carbon biomass formula weight of *ca* 26, this is equivalent to a specific growth rate of 0.35 hr^{-1}. A plot of the natural logarithm of biomass versus time yields a linear plot during the growth phase, indicating that the growth is indeed exponential (not shown). Beginning at 12 hours, $\mathbf{v}_B$ declines sharply as the ammonium concentration rapidly approaches zero (Figure 2.4a). Thereafter, $\mathbf{v}_B$ is zero.

The respiratory pathway rate, $\mathbf{v}_R$, shown also in Figure 2.7a, averages 17.5 mmol H_2O/((g biomass)(hr)) through the growth phase. Unlike $\mathbf{v}_B$, $\mathbf{v}_R$ drops less dramatically at the onset of ammonium exhaustion. After an initial short drop, $\mathbf{v}_R$ tails off as the PHB storage rate gradually declines; the growth-phase to PHB storage-phase shift incurs a 70% decrease in $\mathbf{v}_R$.

Like the respiratory pathway rate, the citric acid pathway rate (Figure 2.7b), $\mathbf{v}_2$, is also relatively constant at 6.2 mmol CO_2/((g biomass)(hr)) through the growth phase but drops sharply before a subtle increase and subsequent tailing into the PHB storage phase. Unlike $\mathbf{v}_R$, $\mathbf{v}_2$ decreases over 90% after ammonium exhaustion.

Initially the glycolytic pathway, $\mathbf{v}_1$, begins at 8.2 C-mmol AcCoA/((g biomass)(hr)) through the growth phase. But rather than dropping sharply as in the case of $\mathbf{v}_R$ and $\mathbf{v}_2$, $\mathbf{v}_1$ experiences an upward spike to 11 C-mmol AcCoA/((g biomass)(hr)) and subsequently drops to the relatively high plateau of 6.3 C-mmol AcCoA/((g biomass)(hr)) at the onset of ammonium exhaustion. As PHB storage phase continues, $\mathbf{v}_1$ declines gradually. Clearly, $\mathbf{v}_1$ is reacting in concert with the increased activity of the PHB polymerization pathway. The overall shift in $\mathbf{v}_1$ from growth to PHB storage is a decrease of almost 30%.

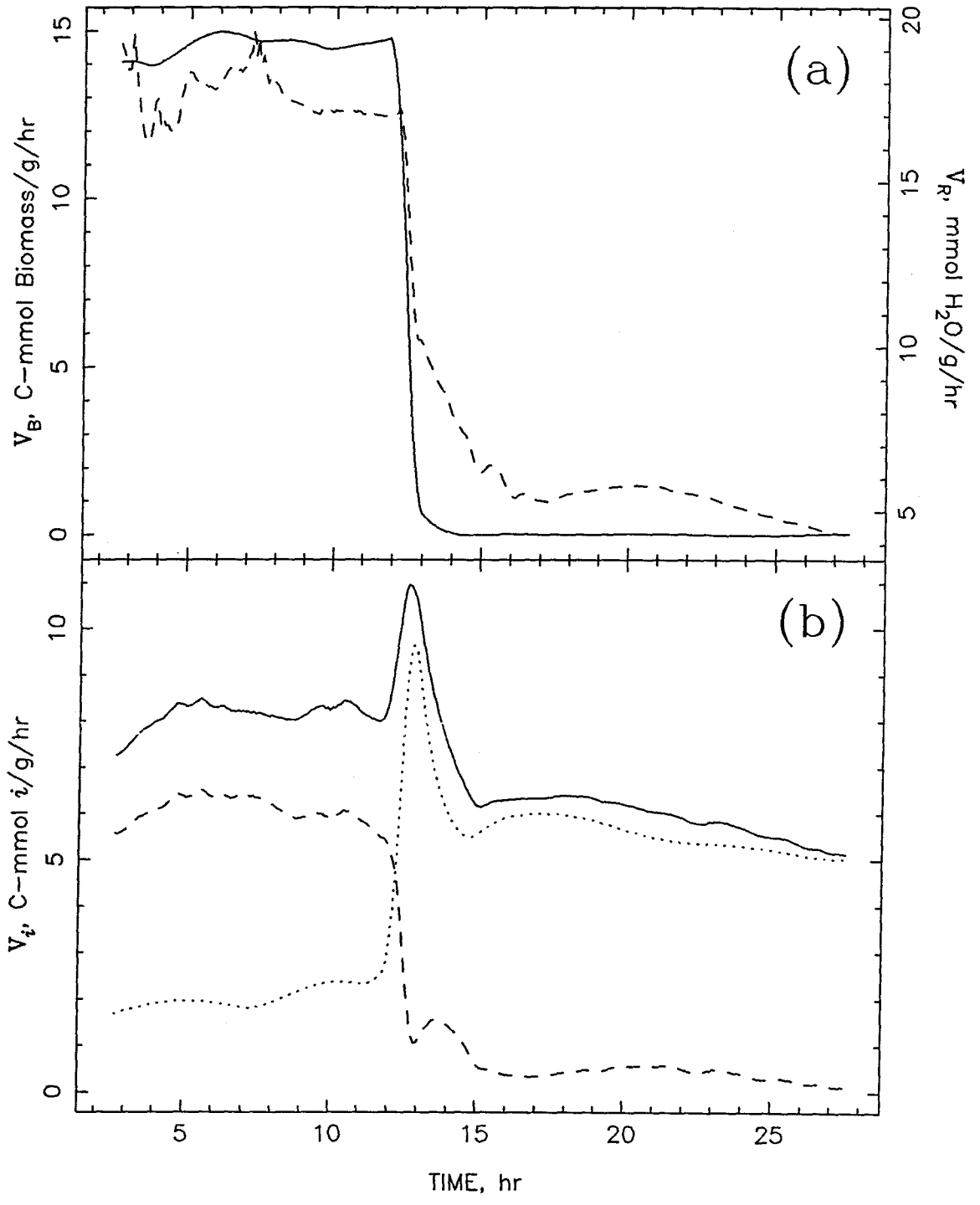

Figure 2.7: Ammonium exhaustion experiment: pathway fluxes. **(a)** Biosynthesis activity ($\mathbf{v}_B$), ——— ; respiration activity ($\mathbf{v}_R$), – – – . **(b)** Glycolysis activity ($\mathbf{v}_1$), ——— ; citric acid cycle activity ($\mathbf{v}_2$), – – – ; PHB polymerization activity ($\mathbf{v}_3$), ····· .

During growth, the PHB polymerization pathway activity, v_3, in Figure 2.7b initially begins at 1.8 C-mmol PHB/((g biomass)(hr)) with a perceptible increase in activity as ammonium exhaustion approaches. Beginning at 12 hours, PHB polymerization increases dramatically to a high of 9.5 C-mmol PHB/((g biomass)(hr)) before settling down to a plateau of about 6 C-mmol PHB/((g biomass)(hr)) and declining to 5 C-mmol PHB/((g biomass)(hr)) at the end of the experiment. The overall increase in v_3 is 300%.

2.5.2.3 Discussion of Experimental Results. The cessation of growth upon ammonium exhaustion is clearly an abrupt metabolic change within the cell. Apparently the cells are capable of actively producing biomass at a high rate nearly up to the point of ammonium exhaustion. The immediate implication, therefore, is that ammonium concentration effects are small. Unfortunately this analysis is not conclusive on this point. In Heinzle and Lafferty's investigation of *A. eutrophus* autotrophic growth, they were able to detect the influence of ammonium concentration on cell growth rate (Eq. (2.4)). However, under the heterotrophic conditions employed here, the specific growth rate was roughly 75% higher than Heinzle and Lafferty observed under autotrophic conditions. Also, the heterotrophically grown cells derive their energy from the complex fructose carbon source, while autotrophically grown cells require hydrogen gas to create reducing power for fixation of carbon dioxide,[42-51] a very energy-intensive process. Therefore, the effects of ammonium concentration coupled with a lower growth rate are more easily discernible under batch autotrophic conditions, particularly if increasing amounts of energy are required for active ammonium transport,[52,53] than faster growing, more energy-efficient

heterotrophically grown cells. The main point of consensus, however, is that exhaustion of ammonium brings a complete and abrupt halt to biosynthesis, as has been clearly illustrated.

The initial drop and subsequent tailing in $\mathbf{v}_R$ have been observed in a number of different fermentations of this same type. Serving as the major ATP generating pathway, it is not surprising that the activity of this pathway drops at the cessation of ATP-demanding biosynthesis. Unlike $\mathbf{v}_B$, however, the drop in activity at the growth/PHB storage-phase transition is initially smaller in magnitude, followed by an asymptotic approach to its final value. As time progresses, $\mathbf{v}_R$ does gradually decrease. The semi-gradual switch from growth to PHB storage suggests that the cells require ATP energy to facilitate the metabolic shift. One possibility is that cessation of biosynthesis is followed by a brief period of enzyme degradation aimed at constructing enzymes more appropriate to PHB synthesis and accumulation as well as cell-maintenance activities. A second possibility is that the cell may still have a number of biosynthetic precursors available within the cell, requiring further ATP consumption to finish any non-nitrogen-dependent biosynthetic manipulations. Given the stoichiometry of the model as indicated by the ATP intracellular balance (Eqs. (2.37) and (2.39)), all of the ATP demand during the PHB synthesis phase supports cell maintenance.

As the major producer of NADH and NADPH, the citric acid cycle provides much of the needed reducing power for biosynthesis as well as NADH for the respiratory pathway. Whereas the respiratory pathway flux first drops sharply and then gradually tails off, the citric acid cycle pathway rate initially drops nearly to its PHB storage level before making a small rebound. The slight

rebound in $\mathbf{v}_2$ occurs just as glycolysis and PHB polymerization activties drop from their respective transition peaks. The implication is that NADH demand is temporarily met by the brief, sharp increase in $\mathbf{v}_1$. $\mathbf{v}_2$ takes up the slack, so to speak, as $\mathbf{v}_1$ falls. The regulatory control mechanisms in Figure 2.1 suggest inhibitory regulation of isocitrate dehydrogenase (IDH) by increased levels of NADH.[7] If biosynthesis and respiration drop sharply, NADH and NADPH demand drops presumably, leading to an abrupt accumulation of these species, thereby strongly attenuating citric acid cycle activity. Subsequently, respiration continues to consume NADH, part of which is supplied by glycolysis. (PHB consumption of NADH is small relative to glycolysis NADH production.) As $\mathbf{v}_1$ drops, tight regulation of IDH is partially relieved, resulting in a brief increase in $\mathbf{v}_2$.

The increase in glycolysis activity at the transition between growth and PHB synthesis has been observed in several other ammonium exhaustion experiments. From a regulatory standpoint this implies a change in glycolytic regulatory control. As will be evident shortly, this rise in $\mathbf{v}_1$ is necessary to accommodate increased activity in the PHB pathway. It is at this point that the glycolytic pathway switches its function from providing the majority of its carbon to the citric acid cycle to the PHB polymerization pathway.

It is interesting to observe that the shift in PHB polymerization activity at the growth/PHB production transition reacts in the manner of a damped step change — first overshooting and then damping out to a new plateau value. As is evident in Figure 2.5, $\mathbf{v}_3$, as directly related to the slope of the PHB

curve, does gradually drop in activity as PHB accumulates. After initially increasing at a linear rate for approximately 10–15 hours, the rate of increase in PHB diminishes with increasing time. Heinzle and Lafferty characterized this as PHB self-inhibition and incorporated this concept into their modeling equations (Eq. (2.8)).

The sudden increase in glycolysis and PHB polymerization activties poses a very interesting regulatory scenario. During growth, the levels of acetyl-CoA to CoASH and NADH to NAD are low because of high citric acid cycle and respiration consumption rates of these species, respectively.[8,9] This metabolic environment attenuates PHB polymerization activity, predominantly because of inhibition of β-ketothiolase by CoASH.[8–12] Under these conditions, it appears that glycolysis is rate-limiting since the acetyl-CoA concentration is low, although it is not improbable that the citric acid cycle and glycolysis are simultaneously under strict regulatory control. Because pyruvate kinase (PK) has a high sensitivity to ATP,[6] a high ATP level (energy charge *ca* 0.8 under autotrophic growth[54]) may dominate the regulation of PK with the subsequent feedback inhibition of glucose-6-phosphate dehydrogenase (G6PDH) by ATP and accumulated phosphoenolpyruvate (PEP) (Figure 2.1).[5]

At the onset of ammonium exhaustion, the regulation scheme shifts abruptly. Reductions in biosynthesis and respiration activities reduce demand for NADH and NADPH. *In vitro* studies of IDH suggest that NADH inhibition of IDH is more sensitive to lower levels of NADH than is G6PDH.[4,7] Therefore, the citric acid cycle activity drops sharply with a quick increase in NADH. This

is confirmed by a sharp increase in the specific culture fluorescence (see Chapter 7). Studies with autotrophically grown cells indicate a decrease in ATP levels of nearly 50% between growth and ammonium exhaustion conditions.[6] Therefore, ATP inhibition of PK is relieved commensurate with increased consumption of PEP; PEP and ATP inhibition of G6PDH is then relieved, allowing increased glycolysis activity. Low citric acid cycle activity and high glycolysis activity shift the acetyl-CoA/CoASH ratio to higher values. Simultaneously, CoASH inhibition of β-ketothiolase[8-12] and NAD inhibition of acetacetyl-CoA reductase[13,14] are relieved, and PHB polymerization increases dramatically. This suggests one probable mechanism for explaining the dramatically increased levels of glycolysis and PHB synthesis activities.

The subsequent sudden decrease in glycolysis and PHB polymerization activities is somewhat more difficult to rationalize. Perhaps PEP regulation of G6PDH is once again imposed in concert with PHB polymerization feedback inhibition at the acetacetyl-CoA reductase level.[14] If PEP accumulates because of high glycolysis activity and inhibits G6PDH, it is possible that acetyl-CoA availability is reduced further by the brief, small increase in citric cycle activity. This would lead to an increase in the CoASH level and attenuate PHB polymerization. Or, chronologically reordering these events, the brief rise in citric acid activity attenuates PHB synthesis by raising the CoASH level enough to allow reestablishment of the PEP regulation of G6PDH. Having reduced PHB polymerization activity, PHB synthesis continues at a nearly constant rate until a gradual increase in NADH finally influences G6PDH activity, or else some PHB self-inhibition mechanism is activated.

Clearly, the present model framework provides a more intimate understanding of *Alcaligenes eutrophus* H16's metabolism than any presented previously. However, up to now the applicability of the intracellular balances, or more explicitly, the choice of metabolic parameters, has not been investigated. Addressing the ATP and NADH intracellular balances in Eqs. (2.37) and (2.38), the estimates of the rate of intracellular accumulation of ATP and NADH (left side of each equation) are shown in Figure 2.8. Drozd and Jones[30] estimated Y_{ATP}^{max} as 13.0 (g biomass)/(mol ATP). This value was reached on the basis of the procedure suggested by Stouthamer and Bettenhaussen[34], assuming a P/O ratio of 3.85 and ignoring substrate-level phosphorylation. From their discussion, definition of the components of the cell considered as biomass is unclear. It is quite plausible that no delineation between what we define as biomass and PHB was made and that an elemental composition including PHB was considered. If this is indeed true, their calculated value of Y_{ATP}^{max} is overestimated. Using Drozd and Jones' calculated value for Y_{ATP}^{max} and the metabolic framework assumed in this work, we can "correct" Y_{ATP}^{max} by assuming complete oxidation of fructose, thereby estimating the contribution of substrate-level phosphorylation and appropriately scaling Y_{ATP}^{max}; this yields a value of 12.2 (g biomass)/(mol ATP).

In calculating the rate of accumulation of ATP within the cell, values of $Y_{ATP}^{max} = 12.2$ (g biomass)/(mol ATP), $m_{ATP,e} = 0$, and P/O = 3.85 were assumed. As observed with the pathway rates, the rate of intracellular accumulation of ATP as calculated with the above parameters shifts noticeably between growth and PHB storage. As ammonium exhaustion approaches, there

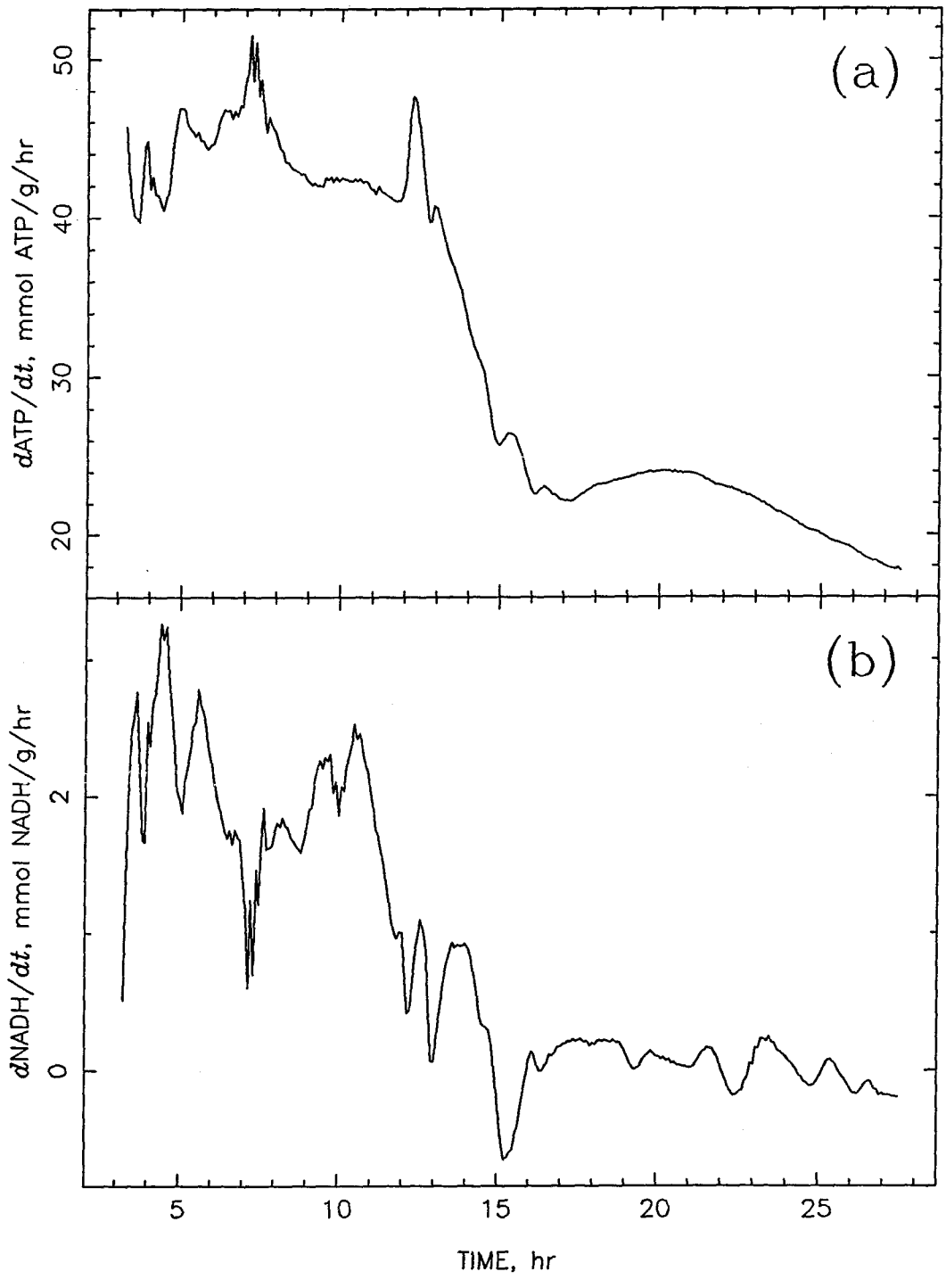

Figure 2.8: Ammonium exhaustion intracellular rates of accumulation. **(a)** Time derivative of the intracellular ATP concentration. **(b)** Time derivative of the intracellular NADH concentration.

is a hint of a reduction in $\frac{dc_{ATP}}{dt}$. From a theoretical standpoint, this observation suggests, assuming a constant growth rate and P/O, an increase in $m_{ATP,g}$ as defined in Eq. (2.40) because of the increased energy requirements of active ammonium transport.[2,52,53] The drop in $\frac{dc_{ATP}}{dt}$ after ammonium exhaustion suggests a shift in ATP's role from an energy-intensive growth regime to a maintenance-intensive regime. During storage phase, $\frac{dc_{ATP}}{dt}$ declines, indicating either a change in $m_{ATP,e}$ or P/O. Under autotrophic conditions, *A. eutrophus* contains an ATP/ADP/AMP total pool of *ca* 6 mmol/l.[54] Assuming similar concentrations under heterotrophic growth, $\frac{dc_{ATP}}{dt}$ values calculated predict short-term saturation of ATP under both growth and PHB storage conditions, leading to the conclusion that reevaluation of the metabolic parameters is required.

In calculating $\frac{dc_{NADH}}{dt}$ the results appear to be much more encouraging; the metabolic parameter values were $(Y_{ATP}^{max})_{th} = 40$ (C-mol biomass)/(mol NADH), $m_{NADH,g} = 0$, and $m_{NADH,e} = 0$. Both the growth and PHB storage phases are constant but shifted. Since the calculated growth rate is also constant, this would suggest that we can calculate $m_{NADH,g}$ and $m_{NADH,e}$ explicitly. This is investigated later in Chapter 8. With regard to the PHB storage phase portion of the NADH balance, there appears to be no net accumulation nor net consumption of NADH. This suggests that $m_{NADH,e}$ is either very small or zero, although culture fluorescence measurements (data presented elsewhere) indicate a net accumulation of NADH. From an order-of-magnitude standpoint, the model implies that the net accumulation of NADH is negligible relative to glycolysis and citric acid cycle production and respiratory pathway consumption

of NADH. Assuming an NADH/NAD total pool of 2.5 mmol/l,[16], calculation of $\frac{dc_{NADH}}{dt}$ also indicates rapid saturation under growth conditions. Therefore, $m_{NADH,g}$ cannot be zero.

2.6 CONCLUSIONS

Clearly, the transition between growth and PHB synthesis invokes a dramatic shift or "switch" in *Alcaligenes eutrophus* H16's metabolic regime. While Heinzle and Lafferty's model gives the same qualitative information, the metabolic model framework proposed here provides a much more fundamental understanding of the metabolic ramifications and implications imposed on *A. eutrophus* by such a change in the cell's exogenous environment.

As an interesting side note, the presented model framework can, in fact, enhance the Heinzle and Lafferty model. Imposing quasi-steady-state assumptions on all three of the intracellular balances and using the proper values for the intracellular balance parameters, three of the five pathway rates can be determined relative to any two explicitly defined pathways. Therefore, we can use the Heinzle and Lafferty expressions for biosynthesis and PHB synthesis to calculate the other three pathways. This, in turn, would allow us to simulate fructose and oxygen consumption and carbon dioxide production. This line of thought will be employed in later theoretical simulation investigations.

2.7 NOMENCLATURE

2.7.1 Heinzle and Lafferty Model:

k_i	PHB synthesis rate constant, $i = 1$ or 2 (Eq. (2.8)), l/g/hr
K_I	PHB synthesis inhibition constant (Eq. (2.8)), g/l $(NH_4)_2 SO_4$
$K_{S,1}$	active transport Michaelis-Menten constant (Eq. (2.4)), g/l $(NH_4)_2 SO_4$
$K_{S,2}$	passive transport Michaelis-Menten constant (Eq. (2.4)), g/l $(NH_4)_2 SO_4$
n	exponent, passive transport term (Eq. (2.4))
P	PHB concentration, g/l
r_i	reaction rate of i (i = X, R, P, (P,1), (P,2), or S), g/l/hr
R	residual biomass concentration (R = X − P), g/l
S	$(NH_4)_2 SO_4$ concentration; limiting nutrient, g/l
X	cell dry weight concentration, g/l
$Y_{P/R}$	PHB yield coefficient, g PHB/ g biomass
$Y_{R/S}$	$(NH_4)_2 SO_4$ yield coefficient, g biomass/g $(NH_4)_2 SO_4$
μ	specific growth rate of residual biomass, hr^{-1}
$\mu_{m,1}$	maximum active transport specific growth rate (Eq. (2.3)), hr^{-1}
$\mu_{m,2}$	maximum passive transport specific growth rate (Eq. (2.3)), hr^{-1}
μ_1	active transport specific growth rate (Eq. (2.3)), hr^{-1}
μ_2	passive transport specific growth rate (Eq. (2.3)), hr^{-1}

2.7.2 Microscopic/Macroscopic Balances:

$\mathbf{c}_i$	mol i per unit weight biomass, mol/g
$\mathbf{C}^g_{i,j}$	gas concentration of i in inlet ($j = in$) or outlet ($j = out$), mol/l
$\mathbf{C}^l_{f,i}$	nutrient feed concentration of i, mol/l
$\mathbf{C}^l_i$	liquid concentration of i, mol/l
$\bar{\mathbf{C}}_i$	fermenter volume-averaged concentration of i, mol/l
$\mathbf{f}_i$	nutrient feed volumetric flow rate, l/hr
$\mathbf{F}$	gas volumetric flow rate, l/hr
$\mathrm{m}_{i,e}$	nongrowth-associated maintenance coefficient, mol i/mol biomass
$\mathrm{m}_{i,g}$	growth-associated maintenance coefficient, mol i/mol biomass
P/O	oxidative phosphorylation ratio, mol ATP/mol H_2O
$\mathbf{r}_{f,i}$	rate of formation of i, mol/g/hr
$\mathbf{r_g}$	rate of biomass synthesis per unit weight biomass, mol/g/hr
$\mathbf{R}^g_{f,i}$	gas-phase rate of formation of i, mol/l/hr
$\mathbf{R}^l_{f,i}$	liquid-phase rate of formation of i, mol/l/hr
$\bar{\mathbf{R}}_{f,i}$	fermenter volume-averaged rate of formation of i, mol/l/hr
$\mathbf{v}_j$	rate through the j^{th} pathway, j = B (biosynthesis), R (respiration), 1 (glycolysis), 2 (citric acid cycle), and 3 (PHB polymerization), mol product/g/hr
$\mathbf{V}^i$	liquid ($i = l$) or gas ($i = g$) volume, l
$\bar{\mathbf{V}}$	total fermenter volume, l
$\mathbf{x}$	weight of biomass, g
$\mathbf{X}$	(residual) biomass concentration, g/l

Y_i	yield coefficient of i, mol biomass/mol i
Y_i^{max}	maximum yield coefficient of i, mol biomass/mol i
$(Y_i^{max})_{th}$	maximum theoretical yield coefficient of i, mol biomass/mol i
α_i	fraction of i in biomass, g_i/g biomass
$\gamma_{i,j}$	stoichiometric coefficient of i in the j^{th} pathway, mol/g/hr
ν_{ij}	stoichiometric coefficient of i in the j^{th} pathway, mol/mol
Φ_i	pseudoconcentration of i, mol/l
Θ_i	pseudoconcentration arbitrary constant, mol/l

2.8 REFERENCES

1. Siegel, R.S., and Ollis, D.F., *Biotechnol. Bioeng.*, **26**, 764 (1984).
2. Heinzle, E., and Lafferty, R.M., *Eur. J. Appl. Microbiol.*, **11**, 8 (1980).
3. Srienc, F., Dissertation, Universität Graz, Graz (1980).
4. Blackkolb, F., and Schlegel, H.G., *Arch. Mikrobiol.*, **63**, 177 (1968).
5. Tunail, N., and Schlegel, H.G., *Biochem. Biophys. Comm.*, **49**, 1554 (1972).
6. Wilke, D., and Schlegel, H.G., *Arch. Microbiol.*, **105**, 109 (1975).
7. Glaeser, H., and Schlegel, H.G., *Arch. Mikrobiol.*, **86**, 327 (1972).
8. Oeding, V., and Schlegel, H.G., *Biochem. J.*, **134**, 239 (1973).
9. Senior, P.J., and Dawes, E.A., *Biochem. J.*, **134**, 225 (1973).
10. Haywood, G.W., Anderson, A.J., Chu, J., and Dawes, E.A., *FEMS Microbiol. Lett.*, **52**, 91 (1988).
11. Slater, S.C., Voige, W.H., Dennis, D.E., *J. Bacteriol.*, **170**, 4431 (1988).
12. Schubert, P., Steinbüchel, A., and Schlegel, H.G., *J. Bacteriol.*, **170**, 5837 (1988).
13. Saito, T., Fukui, T., Ikeda, F., Tanaka, Y. and Tomita, K., *Arch. Microbiol.*, **114**, 211 (1977).
14. Haywood, G.W., Anderson, A.J., Chu, J., and Dawes, E.A., *FEMS Micro-*

biol. Lett., **52**, 259 (1988).

15. Abdelal, A.T.H., and Schlegel, H.G., *Biochem. J.*, **139**, 481 (1974).

16. Bowien, B., Cook, A.M., and Schlegel, H.G., *Arch. Microbiol.*, **97**, 273 (1974).

17. Haywood, G.W., Anderson, A.J., and Dawes, E.A., *FEMS Microbiol. Lett.*, **57**, 1 (1989).

18. Bowien, B., and Schlegel, H.G., *Ann. Rev. Microbiol.*, **35**, 405 (1981).

19. Entner, N., and Doudoroff, M., *J. Biol. Chem.*, **196**, 853 (1952).

20. Gottschalk, G., Eberhardt, U., and Schlegel, H.G., *Arch. Mikrobiol.*, **48**, 95 (1964).

21. König, C., Sammler, I., Wilde, E., and Schlegel, H.G., *Arch. Mikrobiol.*, **67**, 51 (1969).

22. Cook, D.W., Tischer, R.G., and Brown, L.R., *Can. J. Microbiol.*, **13**, 701 (1967).

23. Grosz, R., Stephanopoulos, G., and San,K.-Y., *Biotechnol. Bioeng.*, **26**, 1198 (1984).

24. Trüper, H. G., *Biochim. Biophys. Acta*, **111**, 565 (1965).

25. Glaeser, H., and Schlegel, H.G., *Arch. Mikrobiol.*, **86**, 315 (1972).

26. Shindler, J., *Arch. Mikrobiol.*, **49**, 236 (1964).

27. Griebel, R.J., and Merrick, J.M., *J. Bacteriol.*, **108**, 782 (1971).

28. Dawes, E.A., and Senior, P.J., *Adv. Microb. Physiolog.*, **10**, 135 (1973).

29. Edwards, C., Spode, J.A., and Jones, C.W., *Biochem. J.*, **172**, 253 (1978).

30. Drozd, J.W., and Jones, C.W., *Biochem. Soc. Trans.*, **2**, 529 (1974).

31. Kesler, T.G., Dissertation [in Russian], Institute of Microbiology, Moscow (1974).

32. Erickson, L.E., *Biotechnol. Bioeng.*, **22**, 457 (1980).

33. Volova-Kesler, T.G., and Gladchenko, I.A, *Microbiology*, **48**, 212 (1979).

34. Stouthamer, A.H., and Bettenhaussen, C., *Biochim. Biophys. Acta*, **301**, 53 (1973).

35. Stouthamer, A.H., and Bettenhaussen, C.W., *Arch. Microbiol.*, **111**, 21 (1976).

36. Schlegel, H.G., Gottschalk, G., and Bartha, R., *Nature*, **191**, 463 (1961).

37. Pfennig, N., and Lippert, K.D., *Arch. Mikrobiol.*, **55**, 245 (1966).

38. Braunegg, G., Sonnleitner, B., and Lafferty, R.M., *Appl. Microbiol. Biotech.*, **6**, 29 (1978).

39. Lee, C., and Lim, H., *Biotechnol. Bioeng.*, **22**, 639 (1980).

40. Savitzky, A., and Golay, M.J.E., *Anal. Chem.*, **36**, 1627 (1964).

41. Steiner, J., Termonia, Y., and Deltour, J., *Anal. Chem.*, **44**, 1906 (1972).

42. Schneider, K., Cammack, R., and Schlegel, H.G., *Biochim. Biophys. Acta*, **578**, 445 (1979).

43. Schneider, K., and Schlegel, H.G., *Biochim. Biophys. Acta*, **452**, 66 (1976).

44. Schink, B., and Schlegel, H.G., *Biochemie*, **60**, 297 (1978).

45. Schink, B., and Schlegel, H.G., *Biochim. Biophys. Acta*, **567**, 315 (1979).

46. Abdelal, A.T.H., and Schlegel, H.G., *Biochem. J.*, **139**, 481 (1974).

47. Siebert, K., Schobert, P., Bowien, B., *Biochim. Biophys. Acta*, **658**, 35 (1981).

48. Gottschalk, G., *Arch. Mikrobiol.*, **47**, 236 (1964).

49. Kuehn, G.D., and McFadden, B.A., *Biochem.*, **8**, 2394 (1969).

50. Kuehn, G.D., and McFadden, B.A., *Biochemistry.*, **8**, 2403 (1969).

51. Abdelal, A.T.H., and Schlegel, H.G., *J. Bacteriol.*, **120**, 304 (1974).

52. Kleiner, D., *FEMS Microbiol. Rev.*, **32**, 87 (1985).

53. Jahns, T., Kaltwasser, H., and Kleiner, D., *Arch. Microbiol.*, **145**, 306 (1986).

54. Cook, A.M., Urban, E., and Schlegel, H.G., *Anal. Biochem.*, **72**, 191 (1976).

CHAPTER 3

AMMONIUM EFFECTS

3.1 INTRODUCTION

In the previous chapter, a simple metabolic model was proposed, based upon the known major metabolic pathways of *A. eutrophus* that dominate under heterotrophic growth. The three major pathways of interest are the Entner-Doudoroff pathway (glycolysis),[25] the citric acid cycle, and the PHB polymerization pathway. Of particular interest is the branch point at the end of the Entner-Doudoroff pathway at which the cell must regulate what fraction of acetyl-CoA to channel to either the citric acid cycle or PHB polymerization. The model is completed with the addition of a lumping of the various biosynthetic pathways and the inclusion of the oxidative phosphorylation electron transfer chain.

The purpose of this model is to furnish us with a mathematical tool through which the kinetics and regulatory properties of *A. eutrophus*'s metabolism under transient, fed-batch conditions can be investigated. Using a range of varying fermentation conditions, predominantly different nutrient limitations and nutrient exhaustions, we wish to explore in this chapter and the following three chapters the metabolic decisions made by the cell as evidenced by the changes in pathway fluxes under balanced and varying unbalanced growth conditions. It is the purpose of this metabolic model to provide a framework upon which a regulatory simulation model can be ultimately proposed and constructed.

In this chapter we wish first to establish balanced growth benchmarks for

various metabolic parameters against which all unbalanced growth cases can be compared and evaluated. Second, we briefly address *A. eutrophus'* metabolic response to the effects of low, nonzero nutrient concentrations. Finally, the effects of ammonium limitation, ammonium exhaustion, and the release from ammonium exhaustion or PHB storage phase are investigated. In the following three chapters, the effects of oxygen, fructose, phosphate, and intrinsic PHB content are addressed.

As a necessary component to the formation of amino acids, DNA, and other biomolecules, nitrogen is a nutrient critical to cell growth and replication. By controlling its availability, we can directly influence biosynthesis processes within the cell. Aside from ATP energy required for active ammonium transport at low concentrations,[1,16] manipulation of ammonium availability does not directly perturb any other pathway functions. Consequently, we can observe changes in the regulated responses of the nonbiosynthetic pathway activities that are due directly to ammonium-mediated manipulation of biosynthesis activity.

3.2 MATERIALS AND METHODS

3.2.1 Organism

Alcaligenes eutrophus H16 (ATCC 17699) was stored on nutrient broth slants with 0.5% fructose added to retain induction of the fructose catabolism enzyme system;[2] cells were restreaked every two months. During liquid cultivation, *A. eutrophus* was grown heterotrophically on media described by Schlegel

et al.[3] and micronutrient supplement described by Pfennig and Lippert.[4] Cells were grown at 31°C and pH 6.8. Agitation and aeration rates, fructose and ammonium chloride concentrations varied between experiments. In the case of ammonium-limited growth, a concentrated ammonium chloride solution was pumped into the fermenter at a constant flow rate.

3.2.2 Analytical Methods

Fructose concentrations were determined spectrophotometrically with the Boehringer Mannheim GMBH Glucose/Fructose assay kit (Cat. No. 139106). PHB was determined after the method of Braunegg *et al.*[5] Ammonium, determined as ammonium chloride, was measured by an ammonium probe (Ingold Electrodes, Inc., Series 7500). Dry weight determinations were made through the membrane filtration technique. Biomass was calculated from the difference between the dry weight and PHB concentrations.

Dissolved oxygen concentrations were determined with an Instrumentation Laboratories (IL) 531 Industrial Dissolved Oxygen monitor and an Ingold Electrodes, Inc. polarographic oxygen-sensing probe. Dissolved carbon dioxide was measured with an Ingold carbon dioxide monitor (Model 1230) using an Ingold dissolved carbon dioxide probe (Model 780). Optical density was determined at 420 nm with a Spectronic 20 (Bausch and Lomb) modified to accept the flow-cell described by Lee and Lim.[6] A Cole-Parmer pH controller (Model 5997-20) was used to measure and maintain the pH in conjunction with two Masterflex peristaltic pumps for the addition of sodium hydroxide and phosphoric acid.

Off-gas carbon dioxide and oxygen concentrations were monitored with an Infrared Industries, Inc. (Santa Barbara, CA) Model # 703-075 carbon dioxide gas detector and a Leeds and Northrup 7863 thermomagnetic oxygen analyzer, respectively.

3.2.3 Fermentation System

Fermentations were conducted in an 18 liter Bioengineering AG Laboratory fermenter. The data acquisition system supplied as part of the FluroMeasure System data logged fluorescence, optical density, off-gas oxygen, off-gas carbon dioxide, pH, dissolved oxygen, and dissolved carbon dioxide. Fructose and ammonium chloride concentrations were maintained via pH-controlled additions when constant concentrations were desired. The dissolved oxygen concentration was regulated by a home-made controller, which manipulated the fermenter agitation rate.

3.2.4 Computation of Pathway Fluxes

Preliminary data manipulations were performed on an IBM PC. A VAX 11/780 and a MicroVAX 3500 were used to perform all smoothing, interpolations and model pathway calculations. The off-line data were smoothed and interpolated with cubic splines. On-line data were collected at rates of two to eight samples per minute over the course of each fermentation. Other on-line data were smoothed and derivatives calculated according to the method developed by Savitzky and Golay[7] and corrected by Steiner *et al.*[8]

3.3 APPLICATION OF THE METABOLIC MODEL

In the previous chapter *A. eutrophus*'s major metabolic pathways and associated stoichiometry were described in detail. Based upon these five metabolic pathways, a reaction network incorporating transient macroscopic balances over the entire reactor system was developed for the fed-batch system used in these experiments. The metabolic pathways and their relationship within the model framework have been summarized in Figures 2.1 and 2.2. The assumptions made in the development of model equations have already been discussed. From Chapter 2's development, the following relationships, relating intracellular pathway rates to extracellular, bulk-phase quantities, were derived:

$$\mathbf{v}_B = \frac{1}{\mathbf{X}}\left[\frac{d\mathbf{C}^l_{Bio}}{dt} + \frac{\mathbf{C}^l_{Bio}}{\mathbf{V}^l}\frac{d\mathbf{V}^l}{dt}\right] \tag{2.41}$$

$$= -\frac{4}{\mathbf{X}}\left[\frac{d\mathbf{C}^l_{NH_3}}{dt} + \frac{\mathbf{C}^l_{NH_3}}{\mathbf{V}^l}\frac{d\mathbf{V}^l}{dt} + \frac{\mathbf{f}_{NH_3}}{\mathbf{V}^l}\mathbf{C}^l_{f,NH_3}\right] \tag{2.42}$$

$$\mathbf{v}_R = \frac{2}{\mathbf{X}}\left[\frac{\mathbf{F}}{\mathbf{V}^l}\left(\mathbf{C}^g_{O_2,in} - \mathbf{C}^g_{O_2,out}\right) - \frac{d\mathbf{C}^l_{O_2}}{dt} - \frac{\mathbf{C}^l_{O_2}}{\mathbf{V}^l}\frac{d\mathbf{V}^l}{dt} - \left(\frac{\mathbf{V}^g}{\mathbf{V}^l}\frac{d\mathbf{C}^g_{O_2}}{dt} + \frac{\mathbf{C}^g_{O_2}}{\mathbf{V}^l}\frac{d\mathbf{V}^g}{dt}\right)\right] \tag{2.43}$$

$$\mathbf{v}_1 = -\frac{2}{3\mathbf{X}}\left[\frac{d\mathbf{C}^l_{Fruc}}{dt} + \frac{\mathbf{C}^l_{Fruc}}{\mathbf{V}^l}\frac{d\mathbf{V}^l}{dt} - \frac{\mathbf{f}^l_{Fruc}}{\mathbf{V}^l}\mathbf{C}^l_{f,Fruc}\right] - \frac{2}{3}\mathbf{v}_B \tag{2.44}$$

$$\mathbf{v_2} = \frac{1}{\mathbf{X}}\left[\frac{1}{3}\left(\frac{d\mathbf{C}^l_{Fruc}}{dt} + \frac{\mathbf{C}^l_{Fruc}}{\mathbf{V}^l}\frac{d\mathbf{V}^l}{dt} - \frac{\mathbf{f}_{Fruc}}{\mathbf{V}^l}\mathbf{C}^l_{f,Fruc}\right)\right. \tag{2.45}$$
$$+ \frac{\mathbf{F}}{\mathbf{V}^l}\left(\mathbf{C}^g_{CO_2,out} - \mathbf{C}^g_{CO_2,in}\right) - \left(\frac{\mathbf{V}^g}{\mathbf{V}^l}\frac{d\mathbf{C}^g_{CO_2}}{dt} + \frac{\mathbf{C}^g_{CO_2}}{\mathbf{V}^l}\frac{d\mathbf{V}^g}{dt}\right)$$
$$\left. + \frac{d\mathbf{C}^l_{CO_2}}{dt} + \frac{\mathbf{C}^l_{CO_2}}{\mathbf{V}^l}\frac{d\mathbf{V}^l}{dt}\right] + \frac{1}{3}\mathbf{v}_B$$

$$\mathbf{v_3} = \frac{1}{\mathbf{X}}\left[\frac{d\mathbf{C}^l_{PHB}}{dt} + \frac{\mathbf{C}^l_{PHB}}{\mathbf{V}^l}\frac{d\mathbf{V}^l}{dt}\right]. \tag{2.46}$$

By following the time course of the appropriate extracellular experimental observables, we can infer the fluxes through each metabolic pathway.

One comment needs to be made with regard to the experimental application of Eqs. (2.41)–(2.46). Through nearly all fermentations performed, it was discovered that on average, approximately 10% of the fructose consumed could not be accounted for in an overall carbon balance. Analysis of the carbon balance suggested that fructose participation in the model calculations should be obtained through the closure of the acetyl-CoA balance (Eq. 2.36). Experience with the fermentation system, particularly with the pH-controlled addition system, the mechanical stability of the foam head, and the participation and placement of a mechanical foam breaker, suggested strongly that the added fructose (and ammonium chloride and sodium hydroxide) was partially suspended and retained in the foam phase. The details and analysis that led to these conclusions are discussed in Appendix 2.

3.4 RESULTS

An initial series of fermentations were run first to investigate the effects of different concentrations of fructose, ammonium and dissolved oxygen on *Alcaligenes eutrophus* H16's metabolism, followed by an investigation of the effects of ammonium limitation, ammonium exhaustion, and the release from ammonium exhaustion.

3.4.1 Nutrient Concentration Effects

Normal, balanced growth was shown to occur under conditions in which the fructose concentration ranged between 2 and 10 g/l, the ammonium chloride concentration ranged between 0.3 and 1.3 g/l, and the dissolved oxygen partial pressure was above 50 mm Hg. These conclusions were reached, based upon the results of several fermentations with nutrient concentrations falling within these ranges as well as on the results of a previous study.[9] Because of experimental limitations, the lowest controllable ammonium chloride and fructose concentrations were 0.1 to 0.2 g/l and 0.2 to 0.8 g/l, respectively. With the dissolved oxygen controller, the dissolved oxygen partial pressure could be easily regulated down to *ca* 5 mm Hg.

Tables 3.1 and 3.2 summarize the arithmetic averages of measurements taken during six runs under balanced growth, of four runs under low ammonium chloride concentrations ($C^l_{NH_4^+} \leq 0.2$ g/l NH_4Cl), and of two runs under low fructose concentration ($C^l_{Fruc} \leq 0.8$ g/l fructose). In computing the values

used in these compilations, each metabolic parmeter of interest was determined graphically from its respective time evolution plot. Values from two to five hours after inoculation were disregarded to avoid inclusion of lag-phase influences and of values based on small differences between large numbers, *e.g.*, the difference between the inlet and outlet oxygen concentrations. Also, regions in which the controlled nutrient concentration varied excessively on the order of the cell doubling time (*ca* three hours) were equally disregarded.

The balanced growth results including the standard deviations for the six runs serve as a point of reference for all unbalanced fermentations considered. Table 3.1 describes a number of relevant biological parameters, including the carbon dioxide production rate normalized by the biomass concentration (CDPR) and the relative ratio of PHB to biomass, or specific PHB concentration. Biomass is considered to comprise the total dry cell weight minus the portion of the cell dry weight that is due to intracellular PHB. This is equivalent to what other researchers have called residual biomass. Also the fructose consumption rate normalized by the biomass concentration (FCR) is included as well as an indication of the partitioning of the input fructose among the various terminal carbon pathways within the cell. For example, FCR_2 represents the specific rate at which fructose is consumed to support citric acid cycle activity, including fructose carbon evolved as carbon dioxide in the glycolysis pathway. The data in Table 3.2 describe the average pathway fluxes for each of the model's five pathways.

There are some indications of differences between the balanced growth results and the low ammonium chloride and low fructose concentration results,

suggesting that these concentrations begin to influence the cell's metabolism. It should be noted, however, that except for a few instances, all of the low ammonium and low fructose pathways and associated ratios fall within one standard deviation of the balanced growth values.

TABLE 3.1: Average metabolic ratios for balanced growth and low nutrient concentration fermentations

	RATIO VALUES		
Metabolic Ratios*	**Balanced Growth†**	**Low NH_4^+ Concentration**	**Low Fructose Concentration**
PHB/Biomass	0.15(0.06)	0.15	0.16
FCR	27.4(1.2)	27.8	29.5
FCR_B/FCR	0.50(0.04)	0.49	0.49
FCR_2/FCR	0.38(0.02)	0.38	0.38
FCR_3/FCR	0.12(0.03)	0.14	0.13
CDPR	11.4(0.9)	11.6	12.5

*Abbreviations: FCR, specific fructose consumption rate [(C-mmol fructose)/((g biomass)(hr))]; FCR_i, specific fructose consumption rate that is due to the i^{th} pathway [(C-mmol fructose)/((g biomass)(hr))]; CDPR, specific carbon dioxide production rate [(mmol CO_2)/((g biomass)(hr))].

†Values in parenthesis indicate the standard deviation of six experiments.

Following this line of reasoning and proposing a general Monod relationship for cell growth,

$$\mathbf{v}_B = \frac{\mathbf{v}_{B,max}\ \mathbf{C}_i}{\mathbf{K}_{m,i} + \mathbf{C}_i}, \tag{3.1}$$

the results from Table 3.2 suggest that $\mathbf{K}_{m,i} \ll \mathbf{C}_i$, where $\mathbf{C}_i$ represents the lowest level at which we are able to control the ammonium chloride or fructose concentration.

TABLE 3.2: Average pathway fluxes for balanced growth and low nutrient concentration fermentations

	PATHWAY FLUXES*		
Pathways	Balanced Growth†	Low NH_4^+ Concentration	Low Fructose Concentration
v_B	14.0(0.7)	13.6	14.4
v_R	18.7(1.7)	17.7	19.1
v_1	9.1(0.7)	9.4	10.1
v_2	6.8(0.6)	7.0	7.5
v_3	2.3(0.3)	2.5	2.6

*Pathway fluxes, v_i, expressed as (C-)mmol product/((g biomass)(hr)).
†Values in parentheses indicate the standard deviation of six experiments.

Dissolved oxygen, on the other hand, proved to be considerably easier to regulate, predominantly because of its low solubility in aqueous solution and high rate of utilization by the cells. For fermentations run below *ca* 50 mm Hg or about 30% of saturation, the effect of dissolved oxygen partial pressure began to become apparent. To illustrate this point, the dissolved oxygen concentration was dropped in a stepwise manner every three hours through the course of a fermentation. The results presented in Tables 3.3 and 3.4 demonstrate that as the dissolved oxygen partial pressure drops, pathway fluxes and utilization of extracellular carbon shift. In light of the transient nature of this experiment, it is important to remember that these values are approximate in the sense that the cells may not be at a metabolic steady state. The values reported are an average over each dissolved oxygen concentration region.

Using a Lineweaver-Burk type of analysis for the effect of dissolved oxygen

TABLE 3.3: Transient metabolic ratios for growth under decreasing dissolved oxygen concentration

Metabolic Ratios*	RATIO VALUES† 40 mm Hg	20 mm Hg	5 mm Hg
PHB/Biomass	0.075 (0.06–0.09)	0.085 (0.06–0.11)	+ (0.09–0.17)
FCR	23.5 (23–24)	22.0 (21–23)	19.0 (18.5–19.5)
FCR_B/FCR	0.52 (0.52–0.53)	0.48 (0.46–0.50)	0.35 (0.33–0.37)
FCR_2/FCR	0.41 (0.40–0.43)	0.40 (0.38–0.43)	0.43 (0.40–0.45)
FCR_3/FCR	0.075 (0.045–0.090)	0.112 (0.075–0.15)	0.225 (0.18–0.255)
CDPR	10.2 (9.8–10.5)	9.9 (9.6–10.2)	9.4 (9.2–9.7)

*Abbreviations: FCR, specific fructose consumption rate [(C-mmol fructose)/((g biomass)(hr))]; FCR_i, specific fructose consumption rate that is due to the i^{th} pathway [(C-mmol fructose)/((g biomass)(hr))]; CDPR, specific carbon dioxide production rate [(mmol CO_2)/((g biomass)(hr))]; +, increasing concentration (no average value).

†Data in parenthesis represent the range of values observed over each dissolved oxygen concentration.

concentration on the respiratory pathway, *i.e.*

$$\frac{1}{\mathbf{v}_R} = \frac{\mathbf{K}_{m,O_2}}{\mathbf{v}_{R,max}} \left(\frac{1}{\mathbf{C}^l_{O_2}} \right)^n + \frac{1}{\mathbf{v}_{R,max}}, \tag{3.2}$$

we can estimate $\mathbf{K}_{m,O_2}$. Typically, when normal Michaelis-Menten kinetics as in Eq. (3.1) is assumed, n is set to one. In this case, a double reciprocal plot using the data in Table 3.2 and the balanced growth point of $\mathbf{v}_R = 18.7$ mmol H_2O/((g biomass)(hr)) at 150 mm Hg did not give a linear result, suggesting the presence of some form of cooperativity. From a Hill plot, *i.e.*, plotting $\ln \left(\frac{\mathbf{v}_R}{\mathbf{v}_{R,max} - \mathbf{v}_R} \right)$

TABLE 3.4: Average transient pathway fluxes for growth under decreasing dissolved oxygen concentration

	PATHWAY FLUXES†		
Pathways*	**40 mm Hg**	**20 mm Hg**	**5 mm Hg**
$\mathbf{v}_B$	12.2 (11.0–12.5)	10.8 (10.3–12.2)	6.6 (5.5–10.5)
$\mathbf{v}_R$	16.4 (14.0–16.4)	15.8 (15.6–16.2)	15.1 (14.6–15.3)
$\mathbf{v}_1$	7.4 (7.1–7.7)	7.6 (7.2–8.2)	8.2 (7.1–8.3)
$\mathbf{v}_2$	6.3 (6.0–6.4)	6.1 (5.8–6.2)	5.4 (5.1–5.6)
$\mathbf{v}_3$	0.9 (0.7–1.2)	1.6 (0.8–2.3)	2.8 (2.3–3.1)

*Pathway fluxes, $\mathbf{v}_i$, expressed as (C-)mmol product/((g biomass)(hr)).
†Data in parenthesis represent the range of values observed over each dissolved oxygen concentration.

versus $\ln\left(\mathbf{C}^l_{O_2}\right)$ and assuming $\mathbf{v}_{R,max} = 18.7$ mmol H_2O/((g biomass)(hr)), a value of $n = 0.25$ (r=0.98) was determined. Returning to Eq. (3.2) and using the data from Table 3.2 and $n = 0.25$, linear regression leads to $\mathbf{v}_{R,max} = 18.5$ mmol H_2O/((g biomass)(hr)) and $\mathbf{K}_{m,O_2} = 0.34$ (mm Hg)$^{0.25}$ (r=0.98). This suggests that $\ln\left(\mathbf{C}^l_{O_2}\right)$ must be approximately 0.8 mm Hg for $\mathbf{v}_R = \frac{1}{2}\mathbf{v}_{R,max}$. Unfortunately, this concentration is beyond the limits of the dissolved oxygen controller. Experimentally speaking, determination of $\mathbf{K}_{m,O_2}$, and for that matter the other $\mathbf{K}_{m,i}$, is better suited for steady-state, chemostat-type studies. The important point, however, is that the effective $\mathbf{K}_{m,O_2}$ is very low relative to the experimental abilities to control it.

From the results of these constant concentration studies, it became clear

that because of the low $K_{m,i}$ values for fructose, ammonium and oxygen, experimental limitations restricted the usefulness of this approach in ascertaining information useful to enlightening the regulatory schemes used by *A. eutrophus*. Therefore, focus switched toward the use of nutrient limitation and exhaustion techniques.

3.4.2 Ammonium Limitation

To investigate *Alcaligenes eutrophus* H16's response to nitrogen limitation, an *Alcaligenes eutrophus* H16 fed-batch fermentation was subjected to the following growth conditions: Medium containing *ca* 0.3 g/l ammonium chloride was inoculated with cells. As the cells multiplied, the ammonium level was permitted to decline for six hours. At six hours a peristaltic pump began constant rate feeding of a concentrated ammonium chloride solution (*ca* 134 g/l) at a rate of *ca* 0.17 g NH_4Cl/(l culture)/hr. At seven hours the cells' ammonium consumption rate exceeded the ammonium chloride feed rate. Subsequently, the ammonium concentration dropped below detectable levels around eight hours, and the cells became ammonium-limited. The dissolved oxygen concentration was maintained at *ca* 130 mm Hg, and the fructose concentration was maintained at *ca* 5 g/l.

The smoothed raw data for this experiment are presented in Figure 3.2. The pseudoammonium chloride concentration, Φ_{NH_4Cl} (integral of the ammonium chloride production rate per liter, Eq. 2.50), in Figure 3.2a diverges exponentially towards zero from its initial value up to 8.5 hours. Consequently, the

overall ammonium chloride consumption increases exponentially, as indicated by the derivative of the pseudoammonium chloride concentration curve, *i.e.*, the negative of the ammonium production rate. Since both biomass and the ammonium consumption rate increase exponentially, this implies that ammonium chloride consumption is directly related to biomass synthesis, leading to a constant specific ammonium consumption rate. At *ca* 8.5 hours, the ammonium consumption rate becomes restricted, and the pseudoammonium chloride curve becomes linear, signifying a constant consumption rate. As would be expected for constant consumption of a key biosynthetic nutrient, the biomass concentration increases linearly. Simultaneously, the PHB concentration begins to increase noticeably. The ammonium-limited growth rate also manifests itself in changes in the off-gas carbon dioxide and off-gas oxygen exit gas concentration trajectories (Figure 3.2b).

Figure 3.3 depicts the time evolution of the fluxes of the five metabolic pathways. The biosynthesis pathway, Figure 3.3a, initially averages between 13 and 14 C-mmol biomass/((g biomass)(hr)) for the first eight hours. At six hours, a noticeable decline in the biosynthesis pathway rate becomes apparent. From eight hours to the end of the fermentation, the decline in the biosynthesis pathway rate asymptotically approaches zero, dropping by 70% relative to its earlier maximum value. Performing a mass balance on ammonium chloride in the fermenter under these conditions and assuming negligible volume changes, the rate of ammonium production equals the negative of the addition rate:

$$\frac{dC_{NH_4^+}}{dt} = \left[\begin{matrix}Rate\ of\\ addition\end{matrix}\right]_{NH_4^+} + \left[\begin{matrix}Rate\ of\\ production\end{matrix}\right]_{NH_4^+} = 0\ . \qquad (3.3)$$

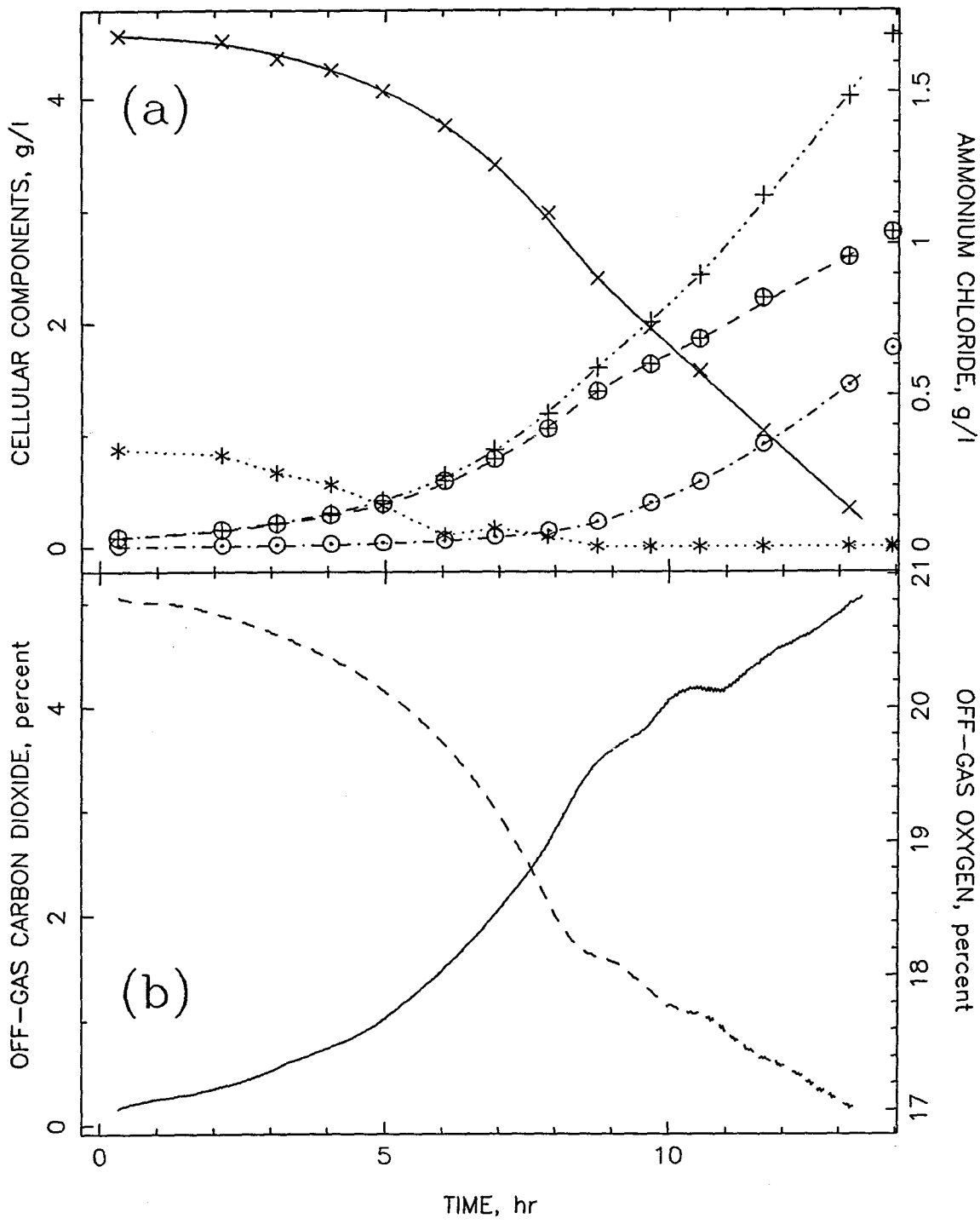

Figure 3.1: Ammonium limitation experiment: raw data. **(a)** Cell dry weight, $+$; biomass, $\oplus$; PHB, $\odot$; bulk ammonium chloride, $*$; pseudoammonium chloride, Φ_{NH_4Cl} (time integral of ammonium chloride production rate per liter, Eq. 2.50), $\times$. **(b)** Off-gas carbon dioxide, —— ; off-gas oxygen, – – – .

Similarly, the change in biomass concentration is related the ammonium addition rate:

$$\frac{d\mathbf{C}_{Bio}}{dt} = \begin{bmatrix} Rate\ of \\ production \end{bmatrix}_{Bio} = -\mathbf{Y}_{NH_4^+} \cdot \begin{bmatrix} Rate\ of \\ production \end{bmatrix}_{NH_4^+} = constant\ , \tag{3.4}$$

where $\mathbf{Y}_{NH_4^+}$ is the (presumed constant) ammonium yield coefficient (g biomass/g NH_4Cl). Therefore, the biomass concentration is related to the specific growth rate, μ, in the following manner:

$$\frac{d\mathbf{C}_{Bio}}{dt} = \mu \cdot \mathbf{C}_{Bio} = constant\ . \tag{3.5}$$

According to the model, the specific growth rate is related to the biosynthesis pathway flux by the factor of the molecular weight of biomass, MW_{Bio}:

$$\mu = \mathbf{v}_B \cdot \mathrm{MW}_{Bio}\ . \tag{3.6}$$

Under conditions of a constant supply of ammonium chloride, as the concentration of cells increases, μ, and therefore $\mathbf{v}_B$, must inversely decrease, which is the pattern observed in this experiment. This justifies the use of a constant yield coefficient, $\mathbf{Y}_{NH_4^+}$, in design and analysis of this fermentation under these or similar conditions.

Following the three-hour post-inoculation period, the respiratory pathway flux (Figure 3.3a) increases gradually from 16 to 18 mmol H_2O/((g biomass)(hr)) from three to eight hours. After eight hours and the onset of ammonium limitation, $\mathbf{v}_R$ drops asymptotically to the end of the run, declining 35%.

Focusing on Figure 3.3b and the interplay between $\mathbf{v}_1$, $\mathbf{v}_2$, and $\mathbf{v}_3$, $\mathbf{v}_1$ and $\mathbf{v}_3$ increase gradually as the bulk ammonium concentration decreases until the

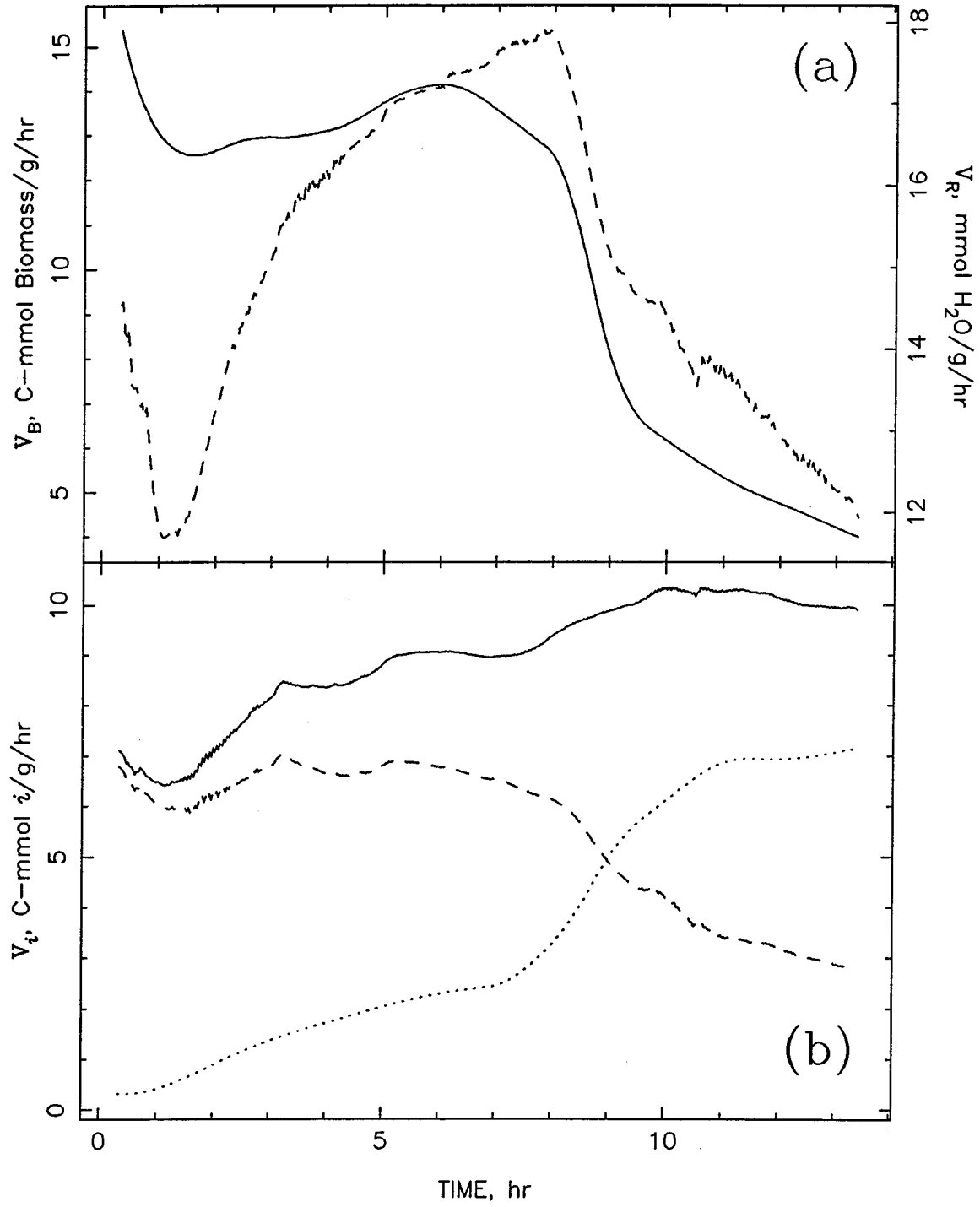

Figure 3.2: Ammonium limitation experiment: pathway fluxes. **(a)** Biosynthesis activity ($\mathbf{v}_B$), ——— ; respiration activity ($\mathbf{v}_R$), − − − . **(b)** Glycolysis activity ($\mathbf{v}_1$), ——— ; citric acid cycle activity ($\mathbf{v}_2$), − − − ; PHB polymerization activity ($\mathbf{v}_3$), ····· .

onset of ammonium limitation. At this point, $\mathbf{v_2}$, which had previously remained constant at about 6.5 C-mmol CO_2/((g biomass)(hr)), declines in asymptotic fashion some 60% while $\mathbf{v_1}$ and $\mathbf{v_3}$ continue to increase 10% and 280%, respectively. While $\mathbf{v_3}$ initially increases strongly during early limited growth, $\mathbf{v_3}$ clearly reaches a maximum of 7 C-mmol PHB/((g biomass)(hr)) before the end of the experiment. The increase in $\mathbf{v_1}$ is predominantly due to the increase in $\mathbf{v_3}$, strongly offsetting the decrease in $\mathbf{v_2}$. The onset of ammonium limitation, therefore, begins shifting the ultimate destination of glycolytic carbon from the citric acid cycle to PHB polymerization. Initially, acetyl-CoA utilization by the citric acid cycle dominates, accounting for 80% or more of the acetyl-CoA consumption. However, as ammonium limitation is approached, there is a noticeable decline in the $\mathbf{v_2}$ to $\mathbf{v_1}$ ratio; beginning at nine hours, glycolytically produced acetyl-CoA is channeled increasingly into PHB synthesis.

Table 3.5 indicates how the stoichiometric relationships among nutrient utilization and growth, as indicated by the appropriate yield coefficients, shift through the course of the run. It is interesting that the overall stoichiometry of fructose and oxygen utilization for biomass synthesis change substantially while that for ammonium utilization does not. The former metabolites are involved in PHB synthesis, whereas ammonium is not.

Figure 3.4 provides a feel of how the relationship between PHB and biomass is influenced by the effects of low ammonium concentration and ammonium limitation. The ratio of PHB to biomass remains relatively constant through unrestrained growth, although there is evidence of an increase in intracellular

TABLE 3.5: Yield coefficients for the ammonium limitation fermentation

Yield Coefficient	Unrestrained Growth	End of Fermentation
Y_{O_2} $[\frac{\text{g bio}}{\text{mol } O_2}]$	37	17
Y_{Fruc} $[\frac{\text{g bio}}{\text{g Fruc}}]$	0.43	0.18
$Y_{NH_4^+}$ $[\frac{\text{g bio}}{\text{g } NH_4Cl}]$	1.6	1.6

PHB content. After eight hours this ratio increases strongly in a linear fashion with time until the end of the experiment.

Comparing the relative ratio of $\mathbf{v}_B$ to $\mathbf{v}_1$ gives an indication of how the cells are allocating the fructose consumed between catabolic/PHB polymerization pathways and anabolic pathways. Up until six hours the ratio of $\mathbf{v}_B$ to $\mathbf{v}_1$ averages 1.55 C-mmol biomass/C-mmol AcCoA. After six hours the ratio shifts to much lower values, ending at 0.4 C-mmol biomass/C-mmol AcCoA as $\mathbf{v}_B$ decreases and $\mathbf{v}_1$ increases because of ammonium limitation.

Figure 3.5 highlights the specific fructose consumption rate as well as the partitioning of fructose consumption among the three terminal carbon pathways. Figure 3.5a describes the time evolution of the fructose consumption rate-per-gram biomass (FCR). The FCR ranges between 26 and 28 C-mmol Fructose/((g biomass)(hr)) during exponential growth. Following the onset of ammonium limitation, fructose utilization declines sharply with a total reduction of 30% by the end of the experiment.

Figure 3.5b gives an indication of the distribution or partitioning of fructose utilization among the biosynthesis, citric acid cycle and PHB polymerization

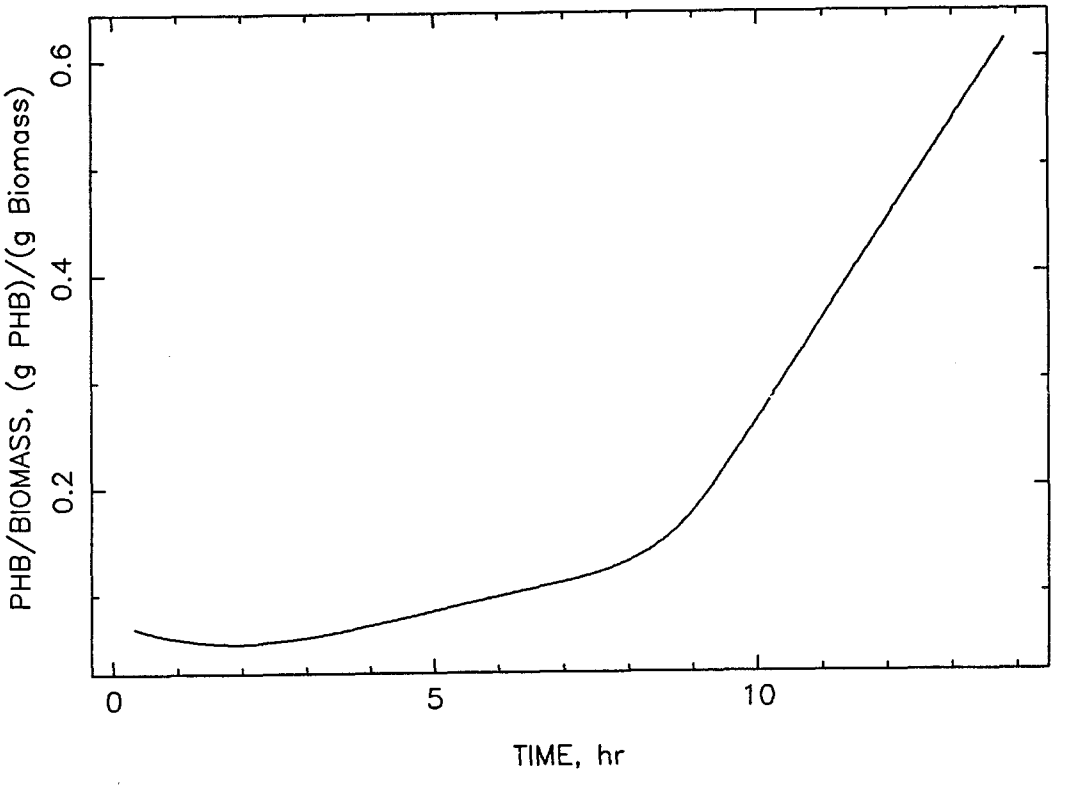

Figure 3.3: Ammonium limitation experiment: ratio of PHB to biomass.

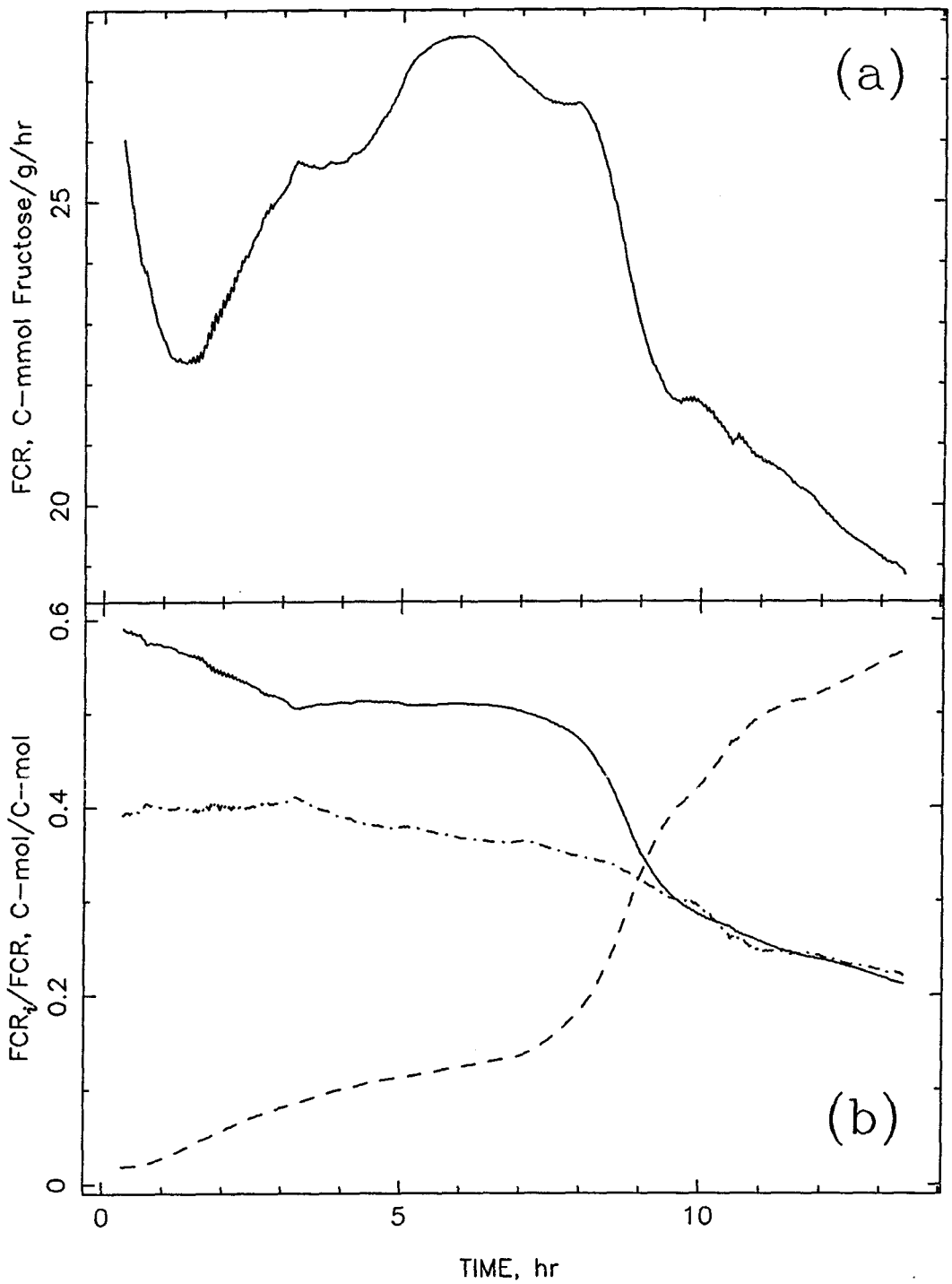

Figure 3.4: Ammonium limitation experiment: specific fructose consumption rate (FCR) and partitioning of fructose between the terminal carbon pathways. **(a)** Specific fructose consumption rate (FCR). **(b)** Fraction of fructose directed to biosynthesis (FCR_B/FCR), ——— ; fraction of fructose directed to the citric acid cycle (FCR_2/FCR), $- \cdot - \cdot$; fraction of fructose directed to PHB polymerization (FCR_3/FCR), $- - -$.

pathways. With regard to the citric acid cycle, initially 40% of the fructose is converted to carbon dioxide in this pathway early in the fermentation, including carbon dioxide evolved via the preceding Entner-Doudoroff pathway. From four to eight hours this gradually drops to 35% and continues to drop to an end value of 22%. The PHB polymerization pathway fructose consumption displays an increase from 3 to 12% during most of unrestrained growth, including carbon dioxide evolved from glycolysis. After the onset of limitation, the percentage of fructose consumed in the PHB polymerization pathway increases dramatically ending, at a value of 57%. The amount of fructose dedicated to biosynthetic activities averages just over 50%, beginning after three hours. Beginning at seven hours, this value begins to decrease, dropping asymptotically after eight hours to a final value of 22%.

It is particularly interesting to note that the percentage of fructose dedicated to citric acid cycle activity and biosynthesis coincides during most of ammonium limitation. From the model's viewpoint, this is implied by the decrease in biosynthesis ATP demand. Applying a quasi-steady-state approximation to the intracellular ATP balance in Eq. 2.37 and assuming values of $Y_{ATP}^{max} \approx 0.47$ C-mmol biomass/mmol ATP and P/O ≈ 3.85 mmol ATP/mmol-atom oxygen,[10] the drop in biosynthesis, *i.e.*, drop in biosynthetic ATP demand, is of the same order as the decrease in respiratory ATP production; the combined glycolytic and citric acid cycle contributions to ATP production are of little consequence, particularly since the decrease in $\mathbf{v}_2$ is partially offset by the increase in $\mathbf{v}_1$. Moving to the NADH intracellular balance in Eq. 2.38 and again applying the

quasi-steady-state approximation, the increases in glycolysis and PHB synthesis nearly cancel each other. From Chapter 2, $(Y_{NADH}^{max})_{th}$ was estimated at 40 C-mmol biomass/mmol NADH; therefore, estimated changes in biosynthesis have little effect on the intracellular NADH balance. Consequently, the citric acid cycle activity must decline because of the drop in respiratory activity and, ultimately, because of the decline in ATP demand, if the NADH balance is valid.

Through the end of unrestrained growth, the carbon dioxide production rate normalized by biomass (CDPR) remains constant at 11 mmol CO_2/((g biomass)(hr)) (Figure 3.6). At the onset of limitation, the CDPR declines rapidly, predominantly because of the decrease in citric acid cycle activity.

The ammonium consumption rate normalized by the biomass (ACR), starting about four hours after inoculation, is shown in Figure 3.7a. Until between eight and 8.5 hours, the bulk concentration of ammonium chloride in the fermenter is nonzero (Figure 3.2a). In fact, beginning at five hours, the ammonium chloride concentration dips below 0.1 g/l and remains at this level by virtue of ammonium chloride feeding. From 4.5 to eight hours there is a distinct, gradual decline in the ACR prior to the onset of ammonium limitation. In their model for autotrophic batch growth, Heinzle and Lafferty[11] suggested that the growth rate is influenced by the existence of passive and active ammonium transport mechanisms. Examining Figure 3.7b, $\mathbf{v}_B$ does appear to increase slightly as the ACR declines initially. However, beginning at an ACR of 0.225 g NH_4Cl/((g biomass)(hr)) corresponding to approximately 5.5 hours, $\mathbf{v}_B$ and the ACR are extremely linear, suggesting that $\mathbf{v}_B$ is indeed influenced by a lower ACR in the presence of a nonzero ammonium concentration. In the case of the other pathway

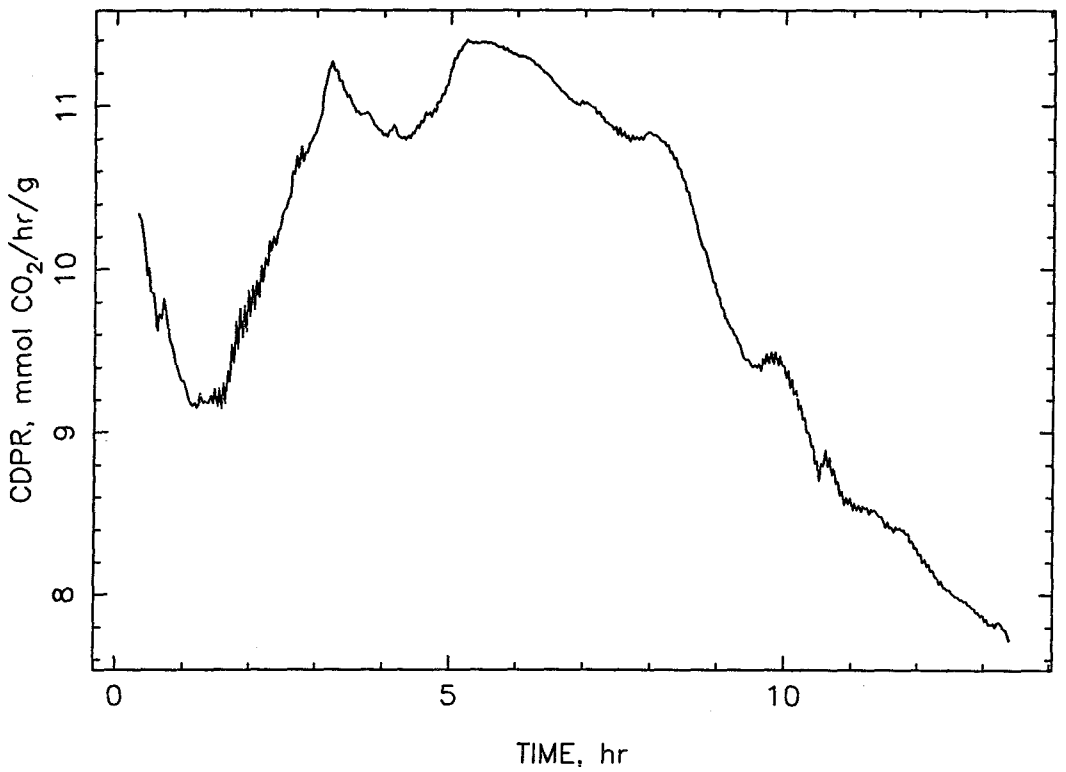

Figure 3.5: Ammonium limitation experiment: specific carbon dioxide production rate (CDPR).

fluxes, it is quite clear that each flux increases slightly as the ACR drops from its maximal value of almost 0.235 g NH_4Cl/((g biomass)(hr)) to 0.225 g NH_4Cl/((g biomass)(hr)). However, only $\mathbf{v}_1$ and $\mathbf{v}_3$ continue to increase throughout the remainder of the experiment as the ACR drops further. Interestingly, $\mathbf{v}_R$ begins to decline only at the point where the ammonium concentration becomes detectable at approximately 0.2 g NH_4Cl/((g biomass)(hr)), but $\mathbf{v}_2$ begins its descent at a higher ACR.

3.4.3 Ammonium Exhaustion

As has been noted on numerous occasions, *Alcaligenes eutrophus* H16 can accumulate large quantities of PHB, up to 80% of total cell dry weight, under conditions of ammonium exhaustion and in the presence of excess carbon source. In Table 3.6, early and late storage PHB phase data are presented. Early storage phase is defined as beginning approximately three hours after the occurrence of ammonium exhaustion, when all pathway fluxes have reached new quasi-steady-state values. Late storage phase occurs approximately 20 hours after early storage phase or approximately 23 hours after ammonium exhaustion. The tabulated values are an average of five different PHB storage experiments.

Relative to balanced growth conditions, all metabolic parameters are dramatically reduced, except for those associated with PHB synthesis. In particular, citric acid cycle activity is reduced by an order of magnitude. From early storage to late storage, metabolic activity decreases *ca* 50% across the board. As the intrinsic PHB content increases, PHB synthesis decreases. Heinzle and Lafferty[11] characterized this phenomenon as PHB self-inhibition.

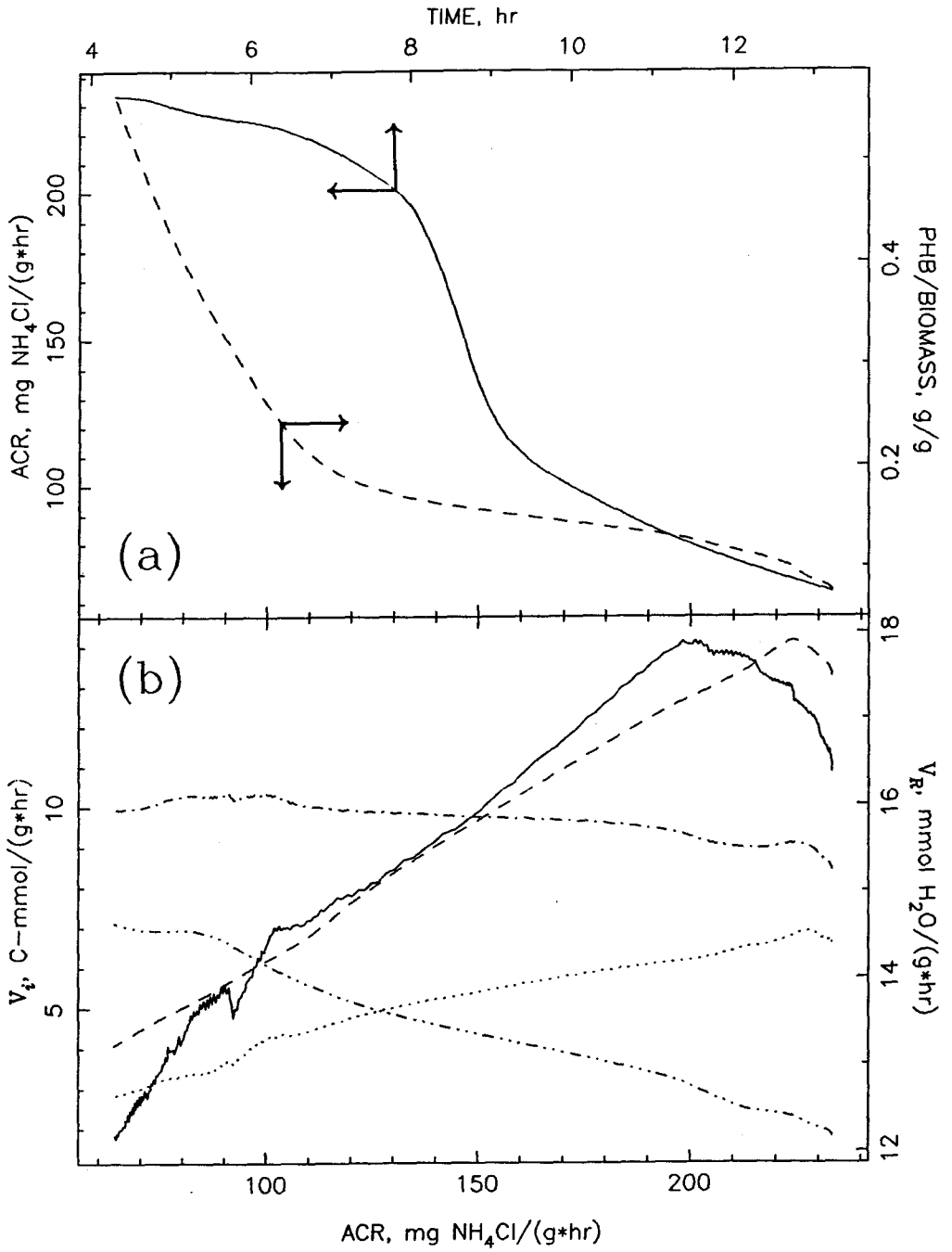

Figure 3.6: Ammonium limitation experiment: specific ammonium consumption rate (ACR) and its relationship to pathway fluxes. **(a)** Specific ammonium consumption rate (ACR), —— ; relationship between PHB/Biomass and the ACR, – – – . **(b)** Relationship between respiration activity and the ACR, —— ; relationship between biosynthesis activity and the ACR, – – – ; relationship between glycolysis activity and the ACR, –·–·; relationship between citric acid cycle activity and the ACR, –···– ; relationship between PHB polymerization activity and the ACR, ····· .

TABLE 3.6: Early and late storage-phase metabolic parameters

Metabolic Parameter	Early Storage Phase	Late Storage Phase
$\mathbf{v}_R$	5.8	3.0
$\mathbf{v}_1$	5.6	3.0
$\mathbf{v}_2$	0.6	0.2
$\mathbf{v}_3$	5.5	2.9
PHB/Biomass	0.56	2.8
FCR	8.2	4.3
FCR_2/FCR	0.11	0.06
FCR_3/FCR	0.89	0.94
CDPR	3.4	1.5

3.4.4 Release from Ammonium Exhaustion

Interest in *A. eutrophus*'s metabolic response to the release from ammonium exhaustion was investigated after an extended period of PHB storage. After exhausting ammonium, *A. eutrophus* cells were allowed to store PHB in the presence of sufficient fructose (3.5 g/l $< \mathbf{C}^l_{Fruc} <$ 5 g/l) for about 14 hours. Following the PHB storage period, a concentrated ammonium chloride solution (40 ml of a 290 g/l ammonium chloride solution) was injected into the fermenter.

Table 3.7 tabulates the shifts in the metabolic parameters between ammonium exhaustion and 2.5 hours after injection of the ammonium chloride solution. Of particular note is that the PHB polymerization pathway runs in reverse, suggesting that PHB is depolymerized to partially meet the cell's biosynthetic energy needs by providing acetyl-CoA to the citric acid cycle pathway and/or providing precursors for biosynthesis.

If PHB depolymerization is indeed providing biosynthetic precursors to biomass synthesis, the model is invalid since it assumes explicitly that only fructose is converted to biosynthetic precursors. For PHB to serve in this capacity, the model would require acetyl-CoA carbon provided from PHB depolymerization to travel "up" the glycolytic pathway, thereby forming fructose, which in turn provides the necessary precursors. This is approximately equivalent to gluconeogenesis, although gluconeogenesis uses different enzymes at key steps. However, running glycolysis in reverse as it pertains specifically to the model formulation (see Eq. 2.9) requires fixation of carbon dioxide. Although *A. eutrophus* is capable of fixing carbon dioxide through the Calvin cycle under autotrophic conditions,[12] carbon dioxide fixation is an inherently energy-intensive process, requiring two NADH and three ATP molecules per carbon dioxide molecule fixed.[13] Reversing the glycolytic pathway does not account for the energy consumption associated with this mechanism. Also, phosphoribulokinase and ribulose-1,5-diphosphate carboxylase, two important Calvin cycle enzymes, are present but inhibited in fructose-grown cells.[14,15] Since physiologically, carbon dioxide fixation is atypical under heterotrophic conditions, a negative glycolysis pathway flux would indicate one shortcoming of this model. The applicability of lumping in this model relative to PHB depolymerization is addressed in more detail in Chapter 5.

The observation that $\mathbf{v}_B$ does not rise from zero C-mmol biomass/((g biomass)(hr)) to near its previously observed balanced growth activity of 14 C-mmol biomass/((g biomass)(hr)) but rather only to 6 C-mmol biomass/((g biomass)(hr)) implies that the cells are either experiencing a lag because of

the previous growth history or inhibition because of the high intracellular PHB content. It should be noted that v_1 is not negative, suggesting that the cell under these circumstances prefers to partition PHB depolymerization products to the citric acid cycle pathway and fructose to both biosynthesis and glycolysis. In examining Table 3.7, it is clear that none of the metabolic parameters rise to balanced growth levels (see Tables 3.1 and 3.2), tending to support the existence of a metabolic lag or inhibition.

TABLE 3.7: Shifts in metabolic parameters that are due to a shift from ammonium exhaustion conditions to a release from exhaustion

Metabolic Parameter	Ammonium Exhaustion	Release from Ammonium Exhaustion
v_B	0	6
v_R	3	11
v_1	4	2.5
v_2	0.2	4.5
v_3	4.0	-2.3
PHB/Biomass	1.5	1.0
FCR	5.0	9.0
FCR_B/FCR	0	0.63
FCR_2/FCR	0.04	0.74
FCR_3/FCR	0.96	-0.38
CDPR	2.0	5.5

3.4.5 Approximating K_{m,NH_4^+}

Using Eq. (3.1), an estimate of the upper bound on the effective Michaelis-

Menten constant for ammonium, $\mathbf{K}_{m,NH_4^+}$, for $\mathbf{v}_B$ can be made. Rearranging Eq. (3.1) and making the appropriate substitutions yield

$$\mathbf{K}_{m,NH_4^+} = \left(\frac{\mathbf{v}_{B,max}\ \mathbf{C}_{NH_4^+}}{\mathbf{v}_B} \right) - \mathbf{C}_{NH_4^+}. \tag{3.18}$$

In analyzing these experiments, the lowest detectable ammonium chloride concentration was *ca* 3 mg NH_4Cl/l; the lowest biosythesis rate we observed (Figure 3.3a) under ammonium limitation was 4 C-mmol biomass/((g biomass)(hr)). Assuming that the balanced growth biosynthesis activity of a $\mathbf{v}_{B,max}$ of 14 C-mmol biomass/((g biomass)(hr)) is the highest achievable growth rate, *i.e.*, $\mathbf{v}_{B,max} = 14$ C-mmol biomass/((g biomass)(hr)) and substituting into Eq. (3.7), suggests that the upper bound on $\mathbf{K}_{m,NH_4^+}$ is 8 mg NH_4Cl/l, or that $\mathbf{v}_B = \frac{1}{2}\mathbf{v}_{B,max}$ at an ammonium chloride concentration of 8 mg/l. As indicated earlier by the concentration effect experiments, this confirms that it would be experimentally difficult to determine the effect of ammonium concentration on the growth rate through regulation of the ammonium concentration in the fermenter.

3.5 DISCUSSION

3.5.1 Nutrient Concentration Effects

Little difference is observed between the averaged balanced growth metabolic parameters and pathway fluxes reported in Tables 3.1 and 3.2 and their counterparts reported for the low ammonium concentration experiments.

With a subtle increase in PHB polymerization acetyl-CoA consumption and with NADH levels rising from slightly depressed respiratory activity and increased citric acid cycle activity, assuming similar oxidative phosphorylation efficiencies relative to balanced growth, it is clear that the cells are beginning to shift fructose resources away from biosynthesis to PHB polymerization.

For the low fructose concentration experiments, a shift in the balance of acetyl-CoA utilization is again observed, with slightly higher consumption by PHB polymerization. As with the low ammonium concentration experiments, the relative ratio of citric acid cycle activity to respiratory activity suggests an increase in NADH levels. Although not observed in the low ammonium case, the increase in respiration activity suggests an increased supply and demand for ATP for unknown reasons.

Much more dramatic effects are observed with the low dissolved oxygen concentration experiment by virtue of the ability to better control dissolved oxygen at low levels relative to the ability to control ammonium and fructose concentrations. As with the previous cases, acetyl-CoA consumption shifts away from biosynthesis and the citric acid cycle to PHB polymerization. Respiration activity does not decrease the same relative amount as biosynthesis, strongly implying respiration's dual role as ATP provider for biosynthesis as well as for maintenance activities.

3.5.2 Ammonium Limitation

Ammonium transport has been intensely researched; a number of organisms have been identified that possess active, ATP-dependent and passive ammo-

nium transport mechanisms.[1] Jahns *et al.* have investigated ammonium transport in *Alcaligenes eutrophus* H16 using methlyammonium.[16] Their findings support the presence of an active, ATP-dependent ammonium transport mechanism that is derepressed at ammonium levels below about 2 mM ammonium (0.1 g/l NH_4Cl). The increase in the respiratory rate with a corresponding decrease in biosynthesis prior to the onset of ammonium limitation seems to agree with Jahns *et al.*'s findings, suggesting that increased respiratory activitiy is linked to the increased ATP demand required for active ammonium transport.

The response to ammonium limitation is clearly highlighted in the increase in the PHB/biomass ratio as indicated by PHB polymerization's consumption of approximately 70% of glycolytically produced acetyl-CoA by the end of the experiment. It is worth noting that while biosynthesis and PHB polymerization are both active, *A. eutrophus*' specific fructose consumption rate is less than that observed under balanced growth, suggesting inhibition of fructose uptake.

The known regulatory scheme depicting the influence of intracellular species on specific regulatory enzymes for *Alcaligenes eutrophus* H16's carbon pathways is presented in Figure 2.1. As ammonium becomes limiting, biosynthesis activity is reduced. As the biosynthesis rate decreases, demand for NADH and ATP drops, suggesting that intracellular levels of these two cofactors increases. The initial level of regulation should most likely be either at the respiratory level and/or at the citric acid cycle level. Given the yield coefficients for ATP and NADH, $Y_{ATP}^{max} \approx 0.47$ C-mol biomass/mol ATP and $(Y_{NADH}^{max})_{th} \approx 40$ C-mol biomass/mol NADH, and the P/O ratio, 3.85 mol ATP/mol-atom oxygen, biosynthesis directly consumes ATP at a substantially higher rate than NADH.

One could then argue, on this basis, that reduced biosynthesis initially raises the intracellular ATP level. Although ATP can inhibit citric acid cycle activity at isocitrate dehydrogenase (IDH),[15] culture fluorescence measurements suggest that NADH levels increase at the onset of ammonium limitation (Chapter 7). Therefore, ATP appears first to inhibit respiratory activity, resulting in reduced oxidation and subsequent accumulation of NADH, leading to inhibition of IDH and attenuation of citric acid cycle activity. Acetyl-CoA normally consumed by the citric acid cycle accumulates, increasing the AcCoA/CoASH ratio. As CoASH levels begin to drop, β-ketothiolase inhibition is partially relieved, and PHB polymerization pathway activity increases.[17,26]

One aspect of this scenario, however, appears initially not to fit with the regulatory scheme presented in Figure 2.1. With increased intracellular concentrations of NADH and ATP, inhibition of glucose-6-phosphate dehydrogenase (G6PDH) in the Entner-Doudoroff pathway might be expected.[15,18] However, *in vitro* studies of G6PDH and IDH indicate that the competitive inhibition of G6PDH occurs at higher NADH levels than the noncompetitive inhibition of IDH; this same comparison with respect to ATP is complicated by ATP's allosteric inhibition of G6PDH and competitive inhibition of IDH[15,18] The model results suggest that activation of G6PDH occurs as evidenced by the small increase in the glycolytic pathway rate upon imposition of ammonium limitation. One possible explanation may be that intracellular ATP levels are not significantly increased and perhaps they even decrease. If this is true, pyruvate kinase (PK) may not be inhibited by ATP,[19] reducing levels of phosphoenolpyruvate (PEP), a strong regulator of G6PDH, and thereby relieving this inhibition of

G6PDH that is due to the combined citric acid cycle and PHB polymerization pathway activities.[20] This is plausible if there is some other rate-limiting reaction step between G6PDH and IDH, which prevents elevation of PEP levels as the glycolysis pathway flux is elevated. The implication is that the increase in the NADH level alone is not sufficient to reduce G6PDH activity, particularly if PEP inhibition is partially relieved. The fact that the glycolytic pathway flux remains at an elevated level while citric acid cycle activity declines is clear evidence of an increase in the AcCoA/CoASH ratio.

Focusing upon the relative decreases in biosynthesis, citric acid cycle, and respiratory activity, it appears that the citric acid cycle is more tightly regulated relative to respiration's apparent regulation based upon the citric acid cycle's intermediate pathway flux decrease relative to the large reduction in the biosynthesis rate and the smaller reduction in respiratory activity. The implication is that glycolytic NAD reduction satisfies an increasing fraction of respiration's required NADH demand to meet biosynthesis' decreasing ATP consumption as well as (presumed constant) cell maintenance ATP requirements.

3.5.3 Ammonium Exhaustion

As *A. eutrophus*' metabolic stoichiometry indicates (Eqs. 2.10 and 2.16), there is a net production of three NADH per PHB monomeric unit polymerized, suggesting, in essence, that citric acid cycle-produced NADH is virtually unneeded to meet respiration demand; this is confirmed by the nearly negligible citric acid cycle activity. As with ammonium limitation, citric acid cycle activity

is the most reduced pathway flux other than biosynthesis. Unlike the response to ammonium limitation, glycolysis is inhibited, although less so than respiration. This observation suggests that regulation of G6PDH by NADH and ATP does occur, but that the sensitivity of G6PDH to these species is indeed less than that observed for isocitrate dehydrogenase. Culture fluorescence measurements indicate that NADH levels are significantly higher under ammonium exhaustion (see Chapter 7). Further, if pyruvate kinase is inhibited by ATP, intracellular levels of PEP are probably higher, contributing further to inhibition of G6PDH and to reduced glycolysis activity.

With a net production and subsequent accumulation of NADH because of PHB polymerization and low respiratory activity, it is apparent that these circumstances must contribute to the reduced activity of glycolysis and the citric acid cycle as PHB storage progresses. As PHB polymerization slows, there is the associated decrease in all other pathway rates. It has been suggested that PHB is capable of inhibiting PHB synthesis.[11] Given the evidence presented, intracellular accumulation of NADH, and possibly PEP and ATP, with subsequent inhibition of G6PDH appears more probable, although acetacetyl-CoA inhibition of acetacetyl-CoA reductase may contribute to this process.[27] If glycolysis becomes inhibited enough by increasing intracellular metabolite levels, PHB polymerization may exceed the rate at which acetyl-CoA is supplied. Subsequently, a drop in the AcCoA/CoASH ratio could occur, with β-ketothiolase polymerization activity becoming more restricted with increasing CoASH concentration.

Other reasons, however, may exist. One possibility is that cell size restricts PHB accumulation, although it has been shown that the cell is capable of expanding dramatically without sacrificing cell water.[21,22] Another explanation may be related to enzyme turnover and enzyme pool maintenance. As time progresses, the enzymes responsible for PHB polymerization may undergo loss of activity. Results of experiments conducted under nitrogen-exhausted conditions in the presence of excess carbon for very long times ($t \gg 96$ hours) have not been reported in the literature.

3.5.4 Release from Ammonium Exhaustion

The discovery that ammonium-exhausted cells did not immediately return to balanced growth pathway flux levels when an exogeneous ammonium source was introduced proved somewhat surprising. The observation that the ratios of $\mathbf{v}_B$ to $\mathbf{v}_R$ and $\mathbf{v}_2$ to $\mathbf{v}_R$ are 75% and 125%, respectively, of the balanced growth values suggests that the cells are working much harder to form biomass than under previously observed circumstances. This relative increase in energy production may be needed to overcome the lag imposed on the cell's biosynthetic mechanisms because of the previous nongrowth period. Stouthamer has demonstrated, using theoretical calculations, that biomass synthesis from simple components requires larger amounts of energy than biosynthesis from complex sources such as fructose.[23] Since the level of citric acid cycle activity is higher than normal balanced growth conditions, thereby producing more reducing equivalents, this might suggest that depolymerized PHB, or more specifically,

acetyl-CoA, is being used to make biomass since it is less complex than fructose. This contradicts the model's results, which indicate that depolymerized PHB is used exclusively in the citric acid cycle.

This may not be a complete explanation, however. One must also consider the physical presence of PHB within the cell. Under these circumstances, PHB constitutes 60% of the cell dry weight. As large granular bodies, the presence of PHB may present a physical impediment to cell growth.

Referring to Figure 2.1, it might be proposed, given regulatory considerations, that the glycolytic pathway must be inhibited, thereby reducing the amount of glycolytically produced acetyl-CoA and allowing the Ac-CoA/CoASH ratio to drop, allowing PHB depolymerization to occur. It is unclear at what level this control might be exerted on the Entner-Doudoroff pathway. Low levels of NADH and high levels of CoASH are conducive to PHB depolymerization.[17,24] Culture fluorescence data, however, indicate that NADH levels are still very high (see Chapter 7).

3.6 CONCLUSIONS

As the previous experiments have demonstrated, *Alcaligenes eutrophus* H16's internal metabolic responses to varying restrictions on ammonium availability differ dramatically. The common thread, however, is an increase in PHB polymerization over and above balanced growth levels under conditions of ammonium restriction on biosynthesis.

3.7 REFERENCES

1. Kleiner, D., *FEMS Microbiol. Rev.*, **32**, 87 (1985).
2. Gottschalk, G., Eberhardt, U., and Schlegel, H.G., *Arch. Mikrobiol.*, **48**, 95 (1964).
3. Schlegel H.G., Gottschalk G., and Bartha R., *Nature*, **191**, 463 (1961).
4. Pfennig, N., and Lippert, K.D., *Arch. Mikrobiol.*, **55**, 245 (1966).
5. Braunegg, G., Sonnleitner, B., and Lafferty, R.M., *Appl. Microbiol. Biotech.*, **6**, 29 (1978).
6. Lee, C., and Lim, H., *Biotechnol. Bioeng.*, **22**, 637 (1980).
7. Savitzky, A., and Golay, M.J.E., *Anal. Chem.*, **36**, 1627 (1964).
8. Steiner, J., Termonia, Y., and Deltour, J., *Anal. Chem.*, **44**, 1906 (1972).
9. Bogensberger, B., Dissertation, Universität Graz (1982).
10. Drozd, J.W., and Jones, C.W., *Biochem. Soc. Trans.*, **2**, 529 (1974).
11. Heinzle, E. and Lafferty, R.M., *Eur. J. Appl. Microbiol.*, **11**, 8 (1980).
12. Bowien, B., and Schlegel, H.G., *Ann. Rev. Microbiol.*, **35**, 405 (1981).
13. Lehninger, A.L., *Principles of Biochemistry*, Worth Publisher, Inc., New York, New York (1982).
14. Abdelal, A.T.H., and Schlegel, H.G., *Biochem. J.*, **139**, 481 (1974).
15. Glaeser, H., and Schlegel, H.G., *Arch. Mikrobiol.*, **86**, 327 (1972).

16. Jahns, T., Kaltwasser, H., and Kleiner, D., *Arch. Microbiol.*, **145**, 306 (1986).

17. Oeding, V., and Schlegel, H.G., *Biochem. J.*, **134**, 239 (1973).

18. Blackkolb, F., and Schlegel, H.G., *Arch. Mikrobiol.*, **63**, 177 (1968).

19. Wilke, D., and Schlegel, H.G., *Arch. Microbiol.*, **105**, 109 (1975).

20. Tunail, N., and Schlegel, H.G., *Biochem. Biophys. Comm.*, **49**, 1554 (1972).

21. Mas, J., Pedrós-Alió, C., and Guerrero, R., *J. Bacteriol.*, **164**, 749 (1985).

22. Pedrós-Alió, C., Mas, J., and Guerrero, R., *Arch. Microbiol.*, **143**, 178 (1985).

23. Stouthamer, A.H., *Microbial Biochemistry*, J.R. Quayle, ed., University Park Press, Baltimore, **21**, 1 (1979).

24. Senior, P.J., and Dawes, E.A., *Biochem. J.*, **134**, 225 (1973).

25. Entner, N., and Doudoroff, M., *J. Biol. Chem.*, **196**, 853, (1952).

26. Haywood, G.W., Anderson, A.J., Chu, J., and Dawes, E.A., *FEMS Microbiol. Lett.*, **52**, 91 (1988).

27. Haywood, G.W., Anderson, A.J., Chu, J., and Dawes, E.A., *FEMS Microbiol. Lett.*, **52**, 259 (1988).

CHAPTER 4

OXYGEN EFFECTS

4.1 INTRODUCTION

Having examined *A. eutrophus*' metabolic response to changes in the biosynthesis rate through direct manipulation of ammonium concentration and ammonium availability, we now examine the effects of oxygen availability on cell growth and PHB synthesis. Using a single fermentation, the effects of two different oxygen limitation periods, *i.e.*, two different oxygen transfer rates, as well as the release from oxygen limitation, are investigated.

As with ammonium limitation, restriction of oxygen availability directly influences only one of *Alcaligenes eutrophus* H16's metabolic pathways — respiration. Restricted respiration activity limits oxidative phosphorylation-linked ATP production within the cell. Consequently, pathways dependent upon consumption of large quantities of respiration-generated ATP are profoundly impacted. Substrate-level phosphorylation, however, is not affected directly. Primarily, reduced ATP production levels would be expected to impact energy-intensive biosynthesis. Also, reduced oxidative phosphorylation activity consumes smaller quantities of predominantly citric acid cycle-produced NADH normally targeted to meet respiratory consumption demand. On a secondary level, NADH normally consumed in the biosynthesis process is unused if reduced ATP availability limits biomass synthesis. From a simple, straightforward analysis, therefore, we can expect that biosynthesis rates would be reduced and NADH levels would become elevated under oxygen-limited growth conditions.

Using the metabolic model framework developed in Chapter 2 (Eqs. (2.41)–(2.46)), *Alcaligenes eutrophus* H16's metabolic response to oxygen limitation and release from oxygen limitation are assessed in terms of changes in the biosynthesis, glycolysis, citric acid cycle, PHB polymerization, and respiratory pathway fluxes. Comparing these results with those of balanced growth and incorporating information gleaned from *in vitro* kinetic studies on key regulatory enzymes will allow us to better understand *A. eutrophus*' oxygen-limited response and release from oxygen limitation regulatory response and associated influence on PHB production.

4.2 MATERIALS AND METHODS

4.2.1 Organism

Alcaligenes eutrophus H16 (ATCC 17699) was stored on nutrient broth slants with 0.5% fructose added to retain induction of the fructose catabolism enzyme system;[1] cells were restreaked every two months. During liquid cultivation, *A. eutrophus* was grown heterotrophically on media described by Schlegel *et al.*[2] and micronutrient supplement described by Pfennig and Lippert.[3] Cells were grown at 31°C and pH 6.8. Oxygen limitation was achieved by setting and holding the air flow rate and adjusting the agitation rate such that the cells' maximum oxygen consumption rate exceeded the oxygen gas to liquid transfer rate.

4.2.2 Analytical Methods

Fructose concentrations were determined spectrophotometrically with the Boehringer Mannheim GMBH Glucose/Fructose assay kit (Cat. No. 139106). PHB was determined after the method of Braunegg *et al.*[4] Ammonium, determined as ammonium chloride, was measured by an ammonium probe (Ingold Electrodes, Inc., Series 7500). Dry weight determinations were made through the membrane filtration technique. Biomass was calculated from the difference between the dry weight and PHB concentrations.

Dissolved oxygen concentrations were determined with an Instrumentation Laboratories (IL) 531 Industrial Dissolved Oxygen monitor and an Ingold Electrodes, Inc. polarographic oxygen-sensing probe. Dissolved carbon dioxide was measured with an Ingold carbon dioxide monitor (Model 1230), using an Ingold dissolved carbon dioxide probe (Model 780). Optical density was determined at 420 nm with a Spectronic 20 (Bausch and Lomb) modified to accept the flow-cell described by Lee and Lim.[5] A Cole-Parmer pH controller (Model 5997-20) was used to measure and maintain the pH in conjunction with two Masterflex peristaltic pumps for the addition of sodium hydroxide and phosphoric acid. Off-gas carbon dioxide and oxygen concentrations were monitored with an Infrared Industries, Inc. (Santa Barbara, CA) Model # 703-075 carbon dioxide gas detector and a Leeds and Northrup 7863 thermomagnetic oxygen analyzer, respectively.

4.2.3 Fermentation System

Fermentations were conducted in an 18 liter Bioengineering AG Laboratory fermenter. The data acquisition system supplied as part of the FluroMeasure System data logged fluorescence, off-gas oxygen, off-gas carbon dioxide, pH, dissolved oxygen, and dissolved carbon dioxide. Fructose and ammonium chloride concentrations were maintained via pH-controlled addition of concentrated fructose (1000 g/l) and ammonium chloride (134 g/l) feed solutions. The dissolved oxygen concentration was regulated by a home-made controller, which manipulated the fermenter agitation rate.

4.2.4 Computation of Pathway Fluxes

Preliminary data manipulations were performed on a IBM PC. A VAX 11/780 and a MicroVAX 3500 were used to perform all smoothing, interpolations and model pathway calculations. The off-line data were smoothed and interpolated with cubic splines. On-line data were collected at rates of eight samples per minute over the course of the fermentation. Other on-line data were smoothed and derivatives calculated according to the method developed by Savitzky and Golay[6] and corrected by Steiner *et al.*[7]

4.3 RESULTS

An experiment was run to examine the pathway flux responses of *A. eu-*

trophus to conditions of dissolved oxygen limitation and release from limitation. Following inoculation of the fermenter, the agitation rate was initially set and held at 200 rpm, and the aeration rate was set at *ca* 0.16 vvm. At 13 hours the agitation rate was raised to 300 rpm. Finally, at 20 hours, the agitation rate was once again raised to 800 rpm. The aeration rate remained constant throughout the experiment. The fructose and ammonium chloride concentrations were regulated between five and six g/l and 0.9 and one g/l, respectively.

4.3.1 Dissolved Oxygen Limitation and Release from Limitation

Figure 4.1 depicts the associated smoothed fermentation observables. Oxygen transfer from the gas to the liquid phase can be modeled by

$$Q_{O_2} = (k_L a)_{O_2} \left(p^*_{O_2} - p^l_{O_2} \right), \tag{4.1}$$

where Q_{O_2} is the rate at which oxygen is transported from the gas phase into the liquid phase (mol O_2/l/hr), $(k_L a)_{O_2}$ is the liquid phase oxygen mass transfer coefficient (mol O_2/(l·hr·mm Hg)), $p^*_{O_2}$ is the partial pressure of oxygen in the gas phase (mm Hg) at the surface of a rising bubble, and $p^l_{O_2}$ is the bulk phase oxygen partial pressure. $(k_L a)_{O_2}$ is nearly constant at constant air flow rate and agitation rate.

As the dissolved oxygen partial pressure tends toward zero, the cells approach the maximum rate at which oxygen can be transferred to the culture. In Figure 4.1a this occurs at *ca* six hours. At 13 hours when the agitation rate is increased from 200 to 300 rpm, the dissolved oxygen concentration increases to

about 40 mm Hg before dropping below detectable levels. Increasing the agitation rate increases $(k_L a)_{O_2}$, allowing a higher maximum rate of oxygen transfer to the culture. Finally, at 20 hours the dissolved oxygen concentration increases to about 150 mm Hg because of the subsequent increase in $(k_L a)_{O_2}$ when the agitation rate is raised from 300 to 800 rpm.

Both the off-gas carbon dioxide and off-gas oxygen concentrations (Figure 4.1b) exhibit very flat profiles during both oxygen limitation regions. The shift from 200 to 300 rpm nearly approximates a step change in both off-gas concentrations. As expected, the carbon dioxide off-gas concentration increases dramatically following the agitation shift from 300 to 800 rpm, while the oxygen off-gas concentration decreases.

From Figure 4.1a it is quite evident that oxygen limitation has a profound effect upon the various cellular components. During both limitation regions the dry weight and biomass concentrations increase in a near linear fashion, although both appear to depart from a linear increase rate at the end of the first limitation period. During the second oxygen limitation period, both dry weight and biomass increase at higher rates than in the previous period, reflecting the higher gas-to-liquid oxygen transfer rate. The PHB concentration begins to increase as a weak exponential early in the first limitation period but increases at a much more linear rate during the second limitation period. Upon release from oxygen limitation, PHB increases initially before leveling off; cell dry weight and biomass increase at their highest rates.

The time evolution of the five pathways of interest are displayed in Figure 4.2. Following what might be construed as a brief lag period, the biosynthesis

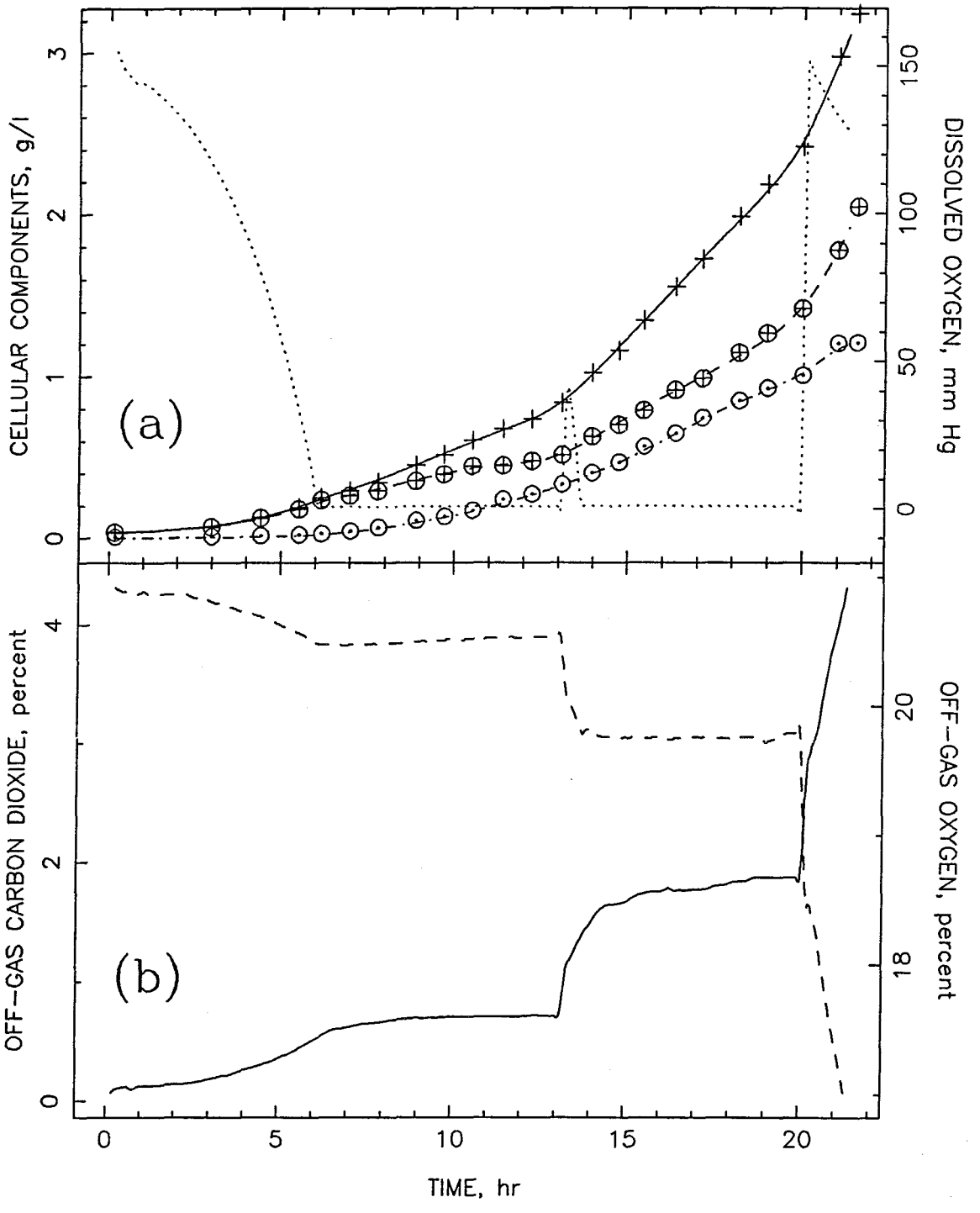

Figure 4.1: Oxygen limitation experiment: raw data. **(a)** Cell dry weight, + ; biomass, ⊕ ; PHB, ⊙ ; dissolved oxygen concentration, ····· . **(b)** Off-gas carbon dioxide, —— ; off-gas oxygen, – – – .

pathway flux, $\mathbf{v}_B$ (Figure 4.2a) increases to and remains at a balanced growth level from three to six hours. At the onset of the first oxygen limitation period, $\mathbf{v}_B$ drops sharply. Between 6.5 and nine hours, $\mathbf{v}_B$ appears to level off in an asymptotic manner before continuing its descent. The sudden drop in $\mathbf{v}_B$ with subsequent recovery may reflect the shock to the cell's metabolism because of the rapid onset of oxygen limitation.

In the case of ammonium limitation, the effect of limitation caused an asymptotic decrease in $\mathbf{v}_B$. In the case of oxygen limitation, the initial decrease is asymptotic in nature but continues dropping rather than leveling off. This highlights the intrinsic differences between the use of ammonium and oxygen with regard to biosynthesis. While ammonium is utilized directly in biomass synthesis, oxygen's role is to facilitate production of ATP. As discussed in Chapter 2, ATP is consumed in biosynthesis reactions, *i.e.*, biomass formation and turnover of proteins, as well as fulfilling so-called cell maintenance requirements.[8] Generally, this maintenance demand for ATP is considered to be at a constant rate of ATP consumption. As the oxygen consumption rate on a per biomass basis shrinks, the amount of ATP generated per unit biomass also becomes more and more restricted. The rate of ATP production on a per biomass basis, $\mathbf{q}_{\mathrm{ATP}}$, can be considered offset by $\mathbf{v}_B$ and $\mathrm{m}_{\mathrm{ATP}}$, the rate of ATP consumption per unit of biomass for maintenance purposes, in the following manner:

$$\mathbf{q}_{\mathrm{ATP}} = \frac{1}{\mathrm{Y}_{\mathrm{ATP}}^{\mathrm{max}}}\mathbf{v}_B + \mathrm{m}_{\mathrm{ATP}}, \tag{4.2}$$

where $\mathrm{Y}_{\mathrm{ATP}}^{\mathrm{max}}$ is the ATP yield coefficient (g biomass/mol ATP).[9] Applying a quasi-steady state approximation to the intracellular ATP balance (Eq. (2.37))

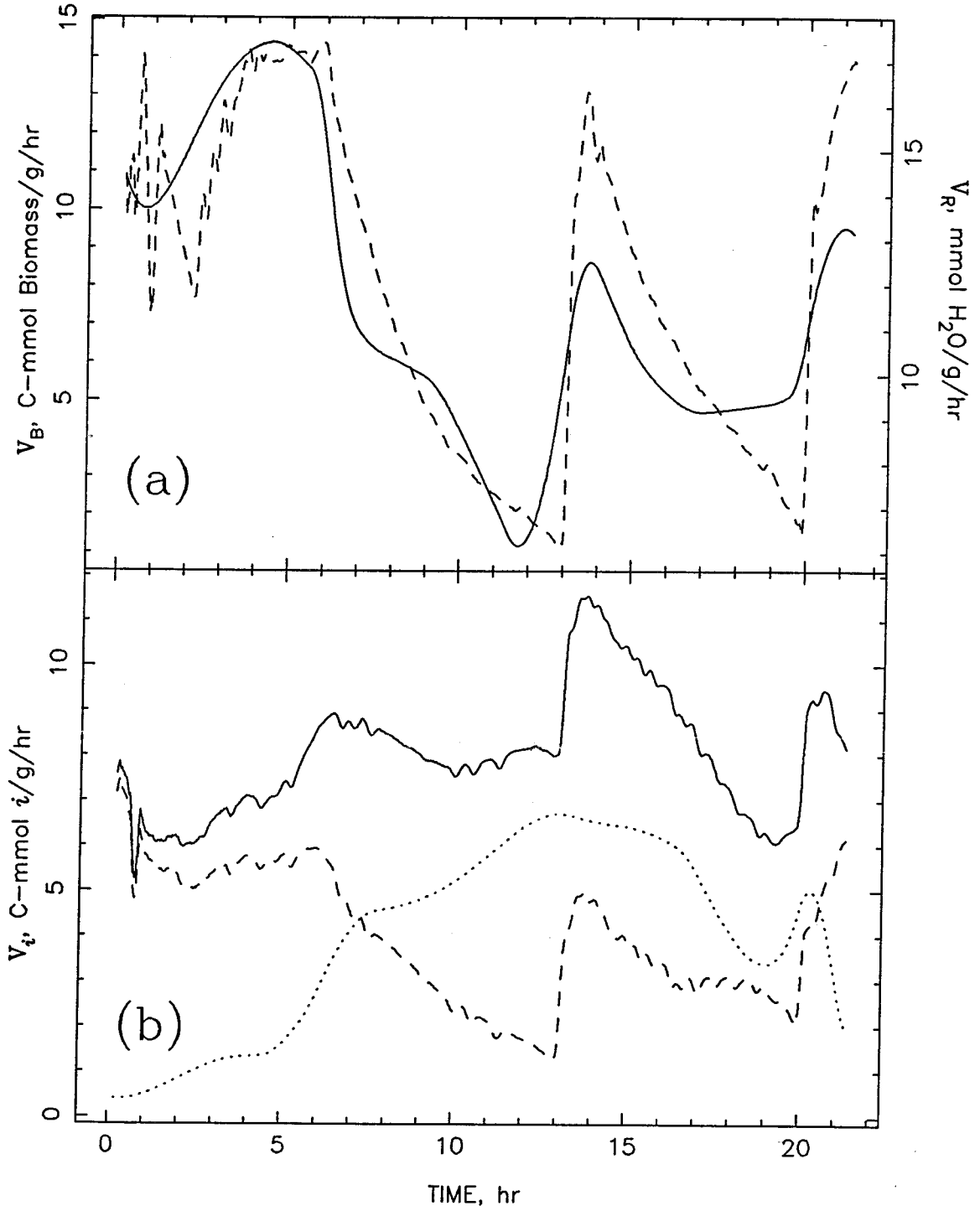

Figure 4.2: Oxygen limitation experiment: pathway fluxes. **(a)** Biosynthesis activity ($\mathbf{v}_B$), ——— ; respiration activity ($\mathbf{v}_R$), – – – . **(b)** Glycolysis activity ($\mathbf{v}_1$), ——— ; citric acid cycle activity ($\mathbf{v}_2$), – – – ; PHB polymerization activity ($\mathbf{v}_3$), – · – · .

allows definition of q_{ATP} relative to the various ATP sources within the cell:

$$q_{ATP} = \frac{1}{4}v_1 + \frac{1}{2}v_2 + (P/O)v_R. \tag{4.3}$$

From Figure (4.2), v_1 is relatively constant. However, v_R and v_2 both decline asymptotically. If

$$\left| m_{ATP} - \left(\frac{1}{4}v_1 + \frac{1}{2}v_2\right)\right| \ll (P/O)v_R, \tag{4.4}$$

(Drozd and Jones estimated $P/O \approx 3.85$[10]), then v_B will decrease asymptotically if v_R decreases asymptotically. However, if

$$\left| m_{ATP} - \left(\frac{1}{4}v_1 + \frac{1}{2}v_2\right)\right| \approx \tilde{0}[(P/O)v_R], \tag{4.5}$$

i.e., q_{ATP} approaches m_{ATP} in magnitude, v_B will decrease at a faster rate than v_R, going to zero when $q_{ATP} = m_{ATP}$.

Upon the upward shift in agitation rate, v_B increases to 60% of its pre-oxygen limitation level before descending as previously observed. However, as v_B reaches 5 C-mmol biomass/((g biomass)(hr)), the biosynthesis rate levels off, unlike the previous limitation period. Previous researchers have shown that under conditions of extended restricted respiration rates ($t \geq 10$ hours), *A. eutrophus* produces small quantities of metabolites characteristic of anaerobic fermentations such as ethanol; the associated dehydrogenases have also been detected.[11,12] The data for v_B here suggest, therefore, that the cells are deriving ATP from a secondary source, thereby allowing the biosynthesis rate to stabilize. Should this indeed be the case, the model may not be suitable under these conditions. As the oxygen transfer rate dramatically increases and the

cells are relieved of oxygen limitation, $\mathbf{v}_B$ increases to a value of about 70% of its prelimitation level before the experiment is terminated. If fermentation products were previously produced, the fact that the biosynthesis rate does not increase to a value near 14 C-mmol biomass/((g biomass)(hr)) may indicate inhibition by these products, lower growth efficiency because of consumption of fermentation products, transient shifts in intracellular enzyme pools, inducing an effective lag, or growth inhibition that is due to high PHB content (to be discussed later).

Shortly after the three-hour post-inoculation period, the respiration rate, $\mathbf{v}_R$ (Figure 4.2a), plateaus at a balanced growth level. Not surprisingly, since the same arguments used to describe the asymptotic decrease in biosynthesis activity under ammonium limitation are equally applicable here (Eqs. (3.3)–(3.4)), $\mathbf{v}_R$ decreases asymptotically during both limitation periods. Between the two oxygen limitation periods, $\mathbf{v}_R$ jumps nearly to its prelimitation rate before descending again. Upon the final release from limitation, $\mathbf{v}_R$'s response is not as sharp nor as high as that observed during the first agitation shift, suggesting that $\mathbf{v}_R$'s relatively sluggish response may be associated with the possible change in cell metabolism.

The time evolutions of glycolysis ($\mathbf{v}_1$), citric acid cycle ($\mathbf{v}_2$), and PHB polymerization ($\mathbf{v}_3$), activities in Figure 4.2b provide an interesting insight to the cell's response to oxygen limitation. Prior to the onset of oxygen limitation, all three pathway rates are relatively constant. $\mathbf{v}_1$, $\mathbf{v}_2$, and $\mathbf{v}_3$ do increase slightly, suggesting that these pathways are manifesting a cellular response to the drop in oxygen concentration below unrestrictive levels.

At the onset of limitation, all three pathways undergo dramatic changes. Within two hours, $\mathbf{v}_3$ increases 300% and ultimately rises to 7 C-mmol PHB/((g biomass)(hr)), a level approximately equivalent to that observed during ammonium exhaustion (Chapter 2). $\mathbf{v}_2$ decreases asymptotically for a 75% decrease. Reflecting the dramatic increase in $\mathbf{v}_3$, $\mathbf{v}_1$ rises 25% during the early portion of this limitation period. $\mathbf{v}_1$ does decrease slightly, reflecting the decrease in citric acid cycle activity, but ultimately plateaus at roughly 15% above its prelimitation value.

After the shift upward in agitation rate, each nonbiosynthetic carbon pathway responds in an unexpected manner. Citric acid cycle activity responds similarly to respiratory activity, although $\mathbf{v}_2$ appears also to plateau as observed with $\mathbf{v}_B$ while still maintaining a general downward trend. Shortly after the shift in agitation rate, $\mathbf{v}_3$ declines slightly but not at the rate expected. The PHB polymerization rate continues to decrease, reaching a level intermediary to its beginning and peak values. Reflecting the large increase in $\mathbf{v}_2$ and the relative constancy of $\mathbf{v}_3$, glycolysis activity jumps nearly 45% before dropping linearly, reflecting reductions in both $\mathbf{v}_2$ and $\mathbf{v}_3$.

Upon release from oxygen limitation, $\mathbf{v}_2$ again mirrors $\mathbf{v}_R$, returning to its prelimitation level. Surprisingly, $\mathbf{v}_3$ increases 40% before reversing this unexpected trend. As a consequence of the increases in $\mathbf{v}_2$ and $\mathbf{v}_3$, $\mathbf{v}_1$ increases 60% before dropping because of the decrease in $\mathbf{v}_3$.

Figure 4.3 depicts the time evolution of the ratio of PHB to biomass. Initially, the PHB/biomass ratio remains constant but increases markedly in near

linear fashion at the onset of oxygen limitation. Following the step increase in agitation rate, the PHB/biomass ratio "stalls" during the second limitation period, drifting only slightly relative to the dramatic changes observed in the first limitation period. Following the release from oxygen limitation, the PHB/biomass ratio turns downward, reflecting the relative changes in biosynthesis and PHB polymerization activities.

From Figure 4.4a it is apparent that the cell's utilization of fructose varies considerably, given the specific fructose consumption rate's (FCR) wide fluctuations with time. Beginning with the first oxygen limitation period, the FCR drops sharply, breaking its steep descent at the point the biosynthesis rate briefly plateaus at about seven hours before continuing to drop with a shallower slope for a total decrease of 50%. During the agitation switch, the FCR increases sharply to its prelimitation level before beginning another sharp decrease. The FCR does not fully recover after the release from oxygen limitation, responding in a manner similar to $\mathbf{v}_3$.

The partitioning of the consumed fructose resources between biosynthesis, citric acid cycle, and PHB polymerization activities is presented in Figure 4.4b. At the onset of the first oxygen limitation period, fructose resources are increasingly shifted to PHB polymerization and away from biosynthesis and citric acid cycle activities. When the agitation rate shifts upward at 13 hours, both FCR_B/FCR and FCR_2/FCR increase with a concommitant decrease in FCR_3/FCR, but never surpass FCR_3/FCR or attain their previous prelimitation values. Through the second limitation period, PHB polymerization fructose consumption still dominates but does not increase, nor does FCR_B/FCR or

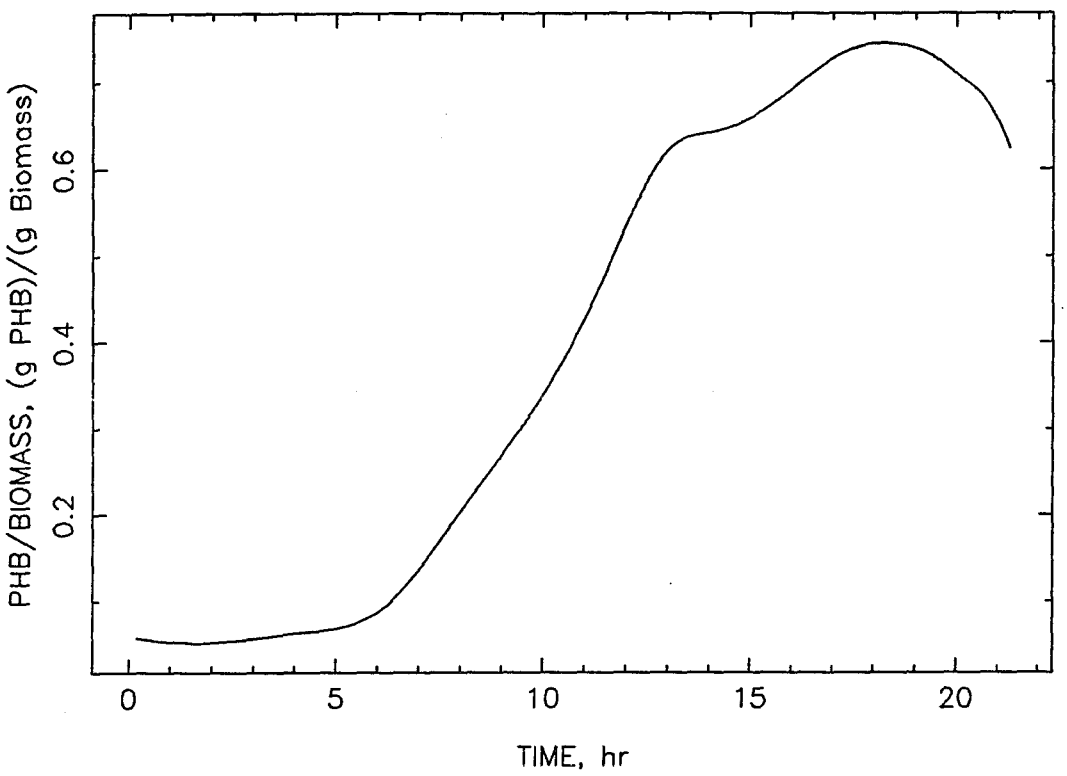

Figure 4.3: Oxygen limitation experiment: ratio of PHB to biomass.

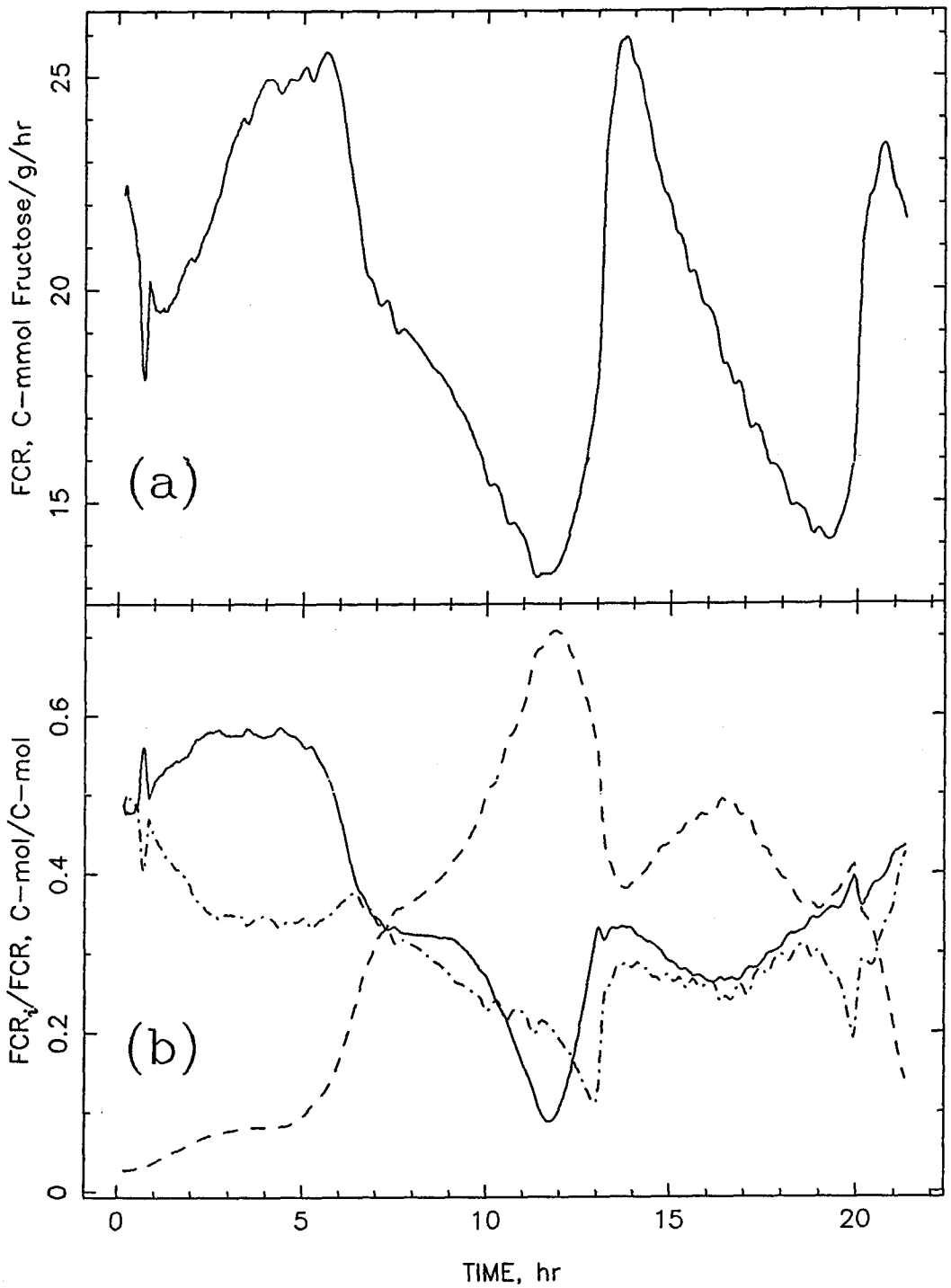

Figure 4.4: Oxygen limitation experiment: specific fructose consumption rate (FCR) and partitioning of fructose between terminal carbon pathways. **(a)** Specific fructose consumption rate (FCR). **(b)** Fraction of fructose directed to biosynthesis (FCR_B/FCR), ——— ; fraction of fructose directed to the citric acid cycle (FCR_2/FCR), $-\cdot-\cdot-$; fraction of fructose directed to PHB polymerization (FCR_3/FCR), $- - -$.

FCR_2/FCR decrease significantly, as in the first oxygen limitation period. Only after the release from oxygen limitation does the partitioning of fructose begin to resemble the prelimitation conditions.

At the onset of the first oxygen limitation period, the specific carbon dioxide production rate (CDPR, Figure 4.5) drops asymptotically, reflecting a general decrease in fructose catabolic activity. Shifting the agitation rate results in the CDPR jumping up to over 5% of its prelimitation value before again dropping; release from oxygen limitation reflects the contribution of increased citric acid cycle activity.

Figure 4.6 describes the relationship between the oxygen consumption rate normalized by biomass (OCR) and the various pathways and the PHB/biomass ratio. The OCR relates linearly with $\mathbf{v}_R$ (not shown) with a slope of 2 mmol H_2O/mmol O_2. In this experiment the OCR was observed over the range from *ca* OCR_{max} to $\frac{1}{3}OCR_{max}$ (Figure 4.6a); OCR_{max} is the maximum prelimitation specific oxygen consumption rate. These figures demonstrate a number of similarities and differences for the pathway fluxes between the two oxygen limitation regions. The pre-oxygen limitation and first oxygen limitation periods are represented by the solid curves; the second oxygen limitation period is represented by the broken curves.

Beginning with the biosynthesis pathway flux (Figure 4.6c), both limitation periods result in relationships with the OCR which are qualitatively similar. Only as the OCR approaches its lowest point does $\mathbf{v}_B$ deviate significantly. It is interesting to note the 15% drop in $\mathbf{v}_B$ at constant OCR prior to the onset of the first limitation period, suggesting that oxygen concentration effects may

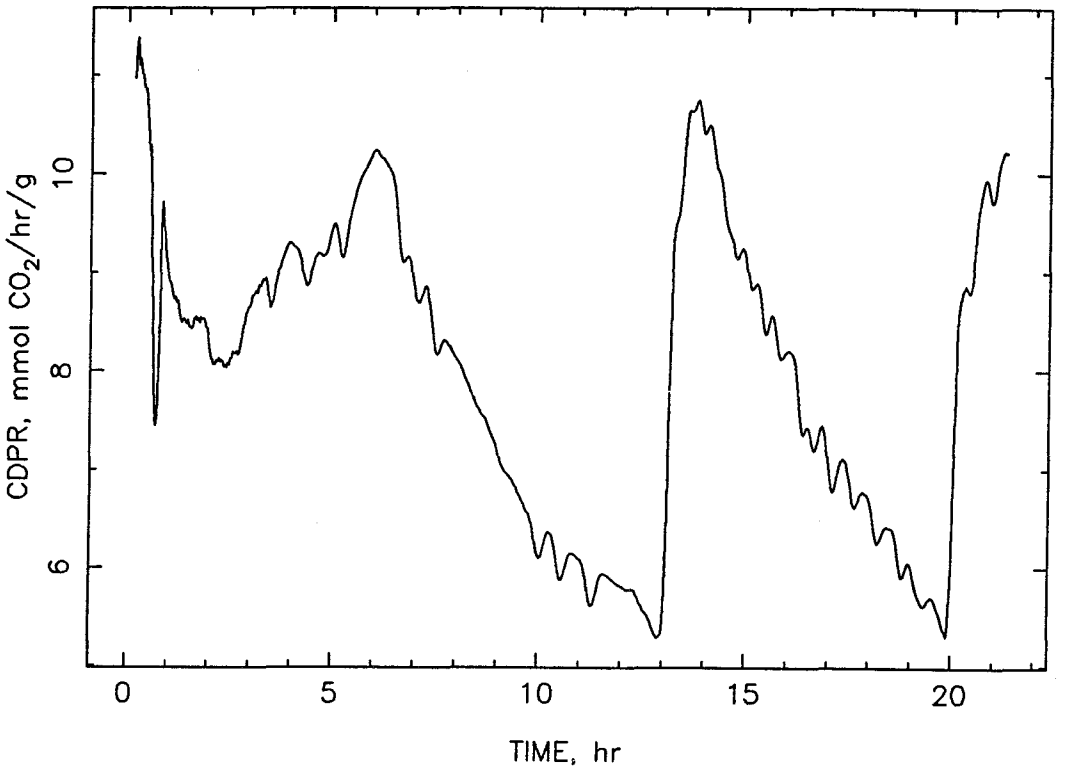

Figure 4.5: Oxygen limitation experiment: specific carbon dioxide production rate (CDPR).

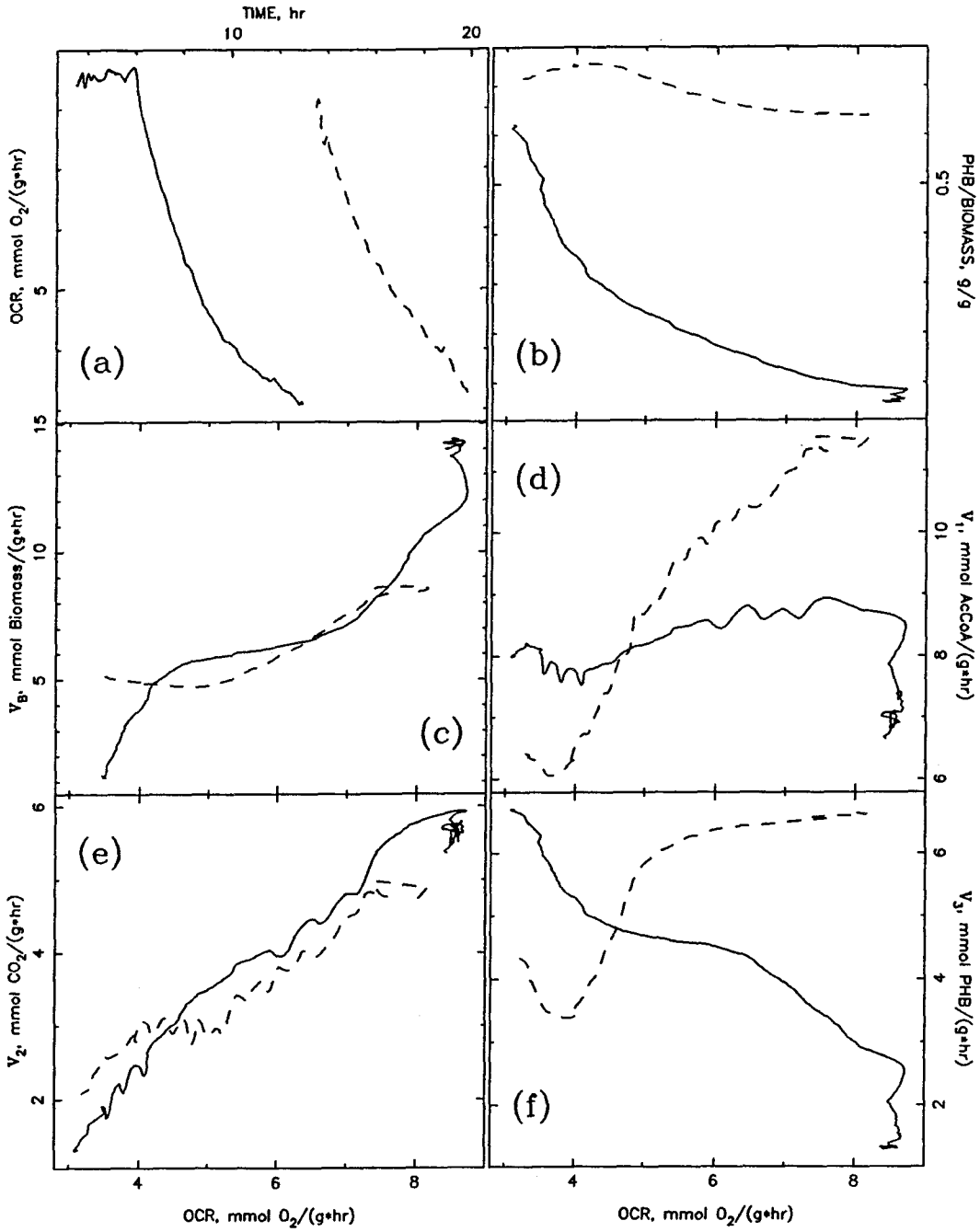

Figure 4.6: Oxygen limitation experiment: specific oxygen consumption rate (OCR) and its relationship to pathway fluxes. **(a)** Specific oxygen consumption rate (OCR). Solid lines represent the beginning of the experiment through the end of the first limitation period. Broken lines represent the second limitation period. **(b)** Relationship between the PHB/biomass ratio and the OCR. **(c)** Relationship between biosynthesis activity and the OCR. **(d)** Relationship between glycolysis activity and the OCR. **(e)** Relationship between citric acid cycle activity and the OCR. **(f)** Relationship between PHB polymerization activity and the OCR.

influence cellular metabolism. The fact that biosynthesis activity during the second oxygen limitation period does not increase upon the sudden change in agitation rate at 13 hours to the same activity as was reached during the first limitation period at the same OCR, highlights the sluggish response of biomass synthesis to sudden increases in its rate.

$\mathbf{v}_1$ and $\mathbf{v}_3$ (Figures 4.6d and 4.6f) increase in the early constant OCR region 20% and 70%, respectively. With both $\mathbf{v}_1$ and $\mathbf{v}_3$, the second oxygen limitation period differs dramatically with the response observed in the first limitation period. While glycolytic activity remains constant and PHB polymerization activity increases fairly linearly with decreasing OCR during the first limitation period, both decrease with decreasing OCR during the second limitation period. The large increase in $\mathbf{v}_1$ with subsequent drop strongly reflects the changes in $\mathbf{v}_2$. The fact that $\mathbf{v}_3$ does not noticeably change with the increase in OCR may imply a hysteresis effect with regard to regulation.

During the second limitation region as the OCR passes through 5 mmol O_2/((g biomass)(hr)), it would appear that the cell's metabolism has been altered. While $\mathbf{v}_2$ is nearly identical during both limitation periods, there is a small, but noticeable change at this point. Similarly $\mathbf{v}_B$ plateaus rather than continues to descend, and $\mathbf{v}_3$ falls off sharply.

While the first limitation period strongly influences the increase in the PHB/biomass ratio (Figure 4.8b), this same ratio is relatively unaffected during the second limitation period, increasing only slightly at the end. The implication is that at some level, the cell determines the appropriate concentration of PHB reserves given the prevailing conditions. During the first limitation period, there

is a large increase in the PHB/biomass ratio as the cell adjusts to a falling specific oxygen consumption rate. Because the PHB/biomass ratio does not change significantly during the second limitation region, this suggests that the cell has metabolically deemed this as an appropriate PHB level. As the OCR falls, particularly at the end of this region, there is an increase in the PHB/biomass ratio as $\mathbf{v}_3$ increases, implying that once again the cells are readjusting the level of intracellular PHB reserves.

4.3.2 Approximating $\mathbf{K}_{m,O_2}$

Following the line of reasoning employed with the ammonium limitation case in Chapter 3, an estimate of the upper bound to $\mathbf{K}_{m,O_2}$ with regard to $\mathbf{v}_R$ can be made using the results of the oxygen limitation experiments. Recalling the form of Eq. (3.18) and making the appropriate modifications lead to

$$\mathbf{K}_{m,O_2} = \left(\frac{\mathbf{v}_{R,max}\ \mathbf{C}^l_{O_2}}{\mathbf{v}_R} \right) - \mathbf{C}^l_{O_2} \ . \tag{4.6}$$

Assuming a $\mathbf{v}_{R,max}$ value of 18.7 mmol H_2O/((g biomass)(hr)) from balanced growth (Table 3.2) and the lowest observed respiration pathway flux for $\mathbf{v}_R$ of 6 mmol H_2O/((g biomass)(hr)), we can estimate an upper bound for $\mathbf{K}_{m,O_2}$ of 2.1 mm Hg, taking the limit of Eq. (4.6) as the oxygen partial pressure, $\mathbf{C}^l_{O_2}$, tends to zero. The lowest possible dissolved oxygen partial pressure reliably detectable with the dissolved oxygen probe used in this work is about 2 mm Hg. Thus, detailed experimental characterization of the oxygen partial pressure dependence of cell kinetics is difficult to achieve.

4.4 DISCUSSION

4.4.1 Dissolved Oxygen Limitation

Clearly, as the specific oxygen consumption rate decreases, the cell's major source of ATP production is attenuated. Dwindling ATP resources must be allocated between biosynthetic and maintenance requirements. As the respiratory activity decreases, a shrinking NADH sink results in a backup of citric acid cycle-supplied NADH within the cell; this is confirmed by culture fluorescence measurements (Chapter 7). As Figure 2.1 indicates, an increased NADH intracellular concentration inhibits isocitrate dehydrogenase in the citric acid cycle, thereby attenuating this pathway's activity.[13] As with ammonium limitation (Chapter 3), a small increase in glycolysis activity is observed, suggesting that NADH regulation of glucose-6-phosphate dehydrogenase (G6PDH) is still negligible under these conditions and may be further annulled by a low intracellular ATP concentration.[14,15] Also, a decreased ATP concentration with subsequent increase in AMP may serve to enhance pyruvate kinase activity.[16] This would result in a reduction of phosphoenolpyruvate (PEP) levels, particularly if there is a kinetically slower step between pyruvate kinase and G6PDH, and would remove further inhibition of G6PDH. In light of the fact that PHB polymerization consumes one NADH per PHB monomer unit polymerized, other researchers have ascribed to PHB polymerization the function of an electron sink under these conditions, thereby helping to relieve the cell of the burden of an increasingly reduced intracellular nicotinamide adenine dinucleotide pool.[17] As with ammonium limitation (Chapter 3), reduced citric acid cycle activity and increased

glycolytic activity shift the AcCoA/CoASH ratio to higher values, thereby reducing the intracellular CoASH concentration and its associated inhibition of β-ketothiolase and encouraging PHB polymerization.[18,19,26]

Comparing the results from the first oxygen limitation period to those of the second, it is quite clear that the cell's response to the second limitation period is fundamentally different. Unlike the asymptoticlike decreases in pathway fluxes observed in the first limitation period, the leveling of biosynthesis and citric acid cycle activity relative to the decline in glycolysis and repiratory rates indicates that a new source of ATP capable of partially supporting biosynthesis has been tapped. Identification of anaerobic fermentation products as well as the associated dehydrogenases has been made in other reported *A. eutrophus* fermentations where oxygen supplies were restricted for extended periods of time.[20–25] These two observations suggest strongly that the intrinsic nature of *A. eutrophus*'s metabolism has shifted between the two limitation periods. This is confirmed in the relationships between the specific oxygen consumption rate and the pathway fluxes. In both instances, only citric acid cycle activity is consistently linear with the OCR. While glycolysis and PHB polymerization activities appear to be related to the OCR during the first limitation period, it is clear that this relationship changes dramatically during the second limitation period. It is interesting to note that the glycolysis pathway flux is also linear with the OCR during the second limitation period.

Because PHB polymerization does not drop substantially between the two limitation periods, the question arises as to whether other control elements are

acting upon the cell. On the basis of previous experience, PHB polymerization would have been expected to decrease as biosynthesis and citric acid cycle activities increase, thereby signaling consumption of inhibitory NADH and a reduction of the AcCoA/CoASH ratio. However, according to the model, glycolysis activity also increases to compensate for the increase in citric acid cycle activity while maintaining the level of PHB polymerization.

In other experiments, particularly in the case of balanced growth, it has been observed that if the inoculum contains a high PHB/biomass ratio, this ratio drops during the course of the fermentation until a typical balanced growth level is achieved, plateauing at that level through the end of the experiment or until some form of limitation is encountered. In the case of the second oxygen limitation period, the PHB/biomass ratio is high initially and does not change substantially later. Perhaps at the beginning of the second oxygen limitation period, the PHB/biomass ratio is at or near an appropriate level, as determined by cell regulation, for the prevailing oxygen-limited conditions. To maintain this level, PHB polymerization does not drop as the agitation speed shifts from 200 to 300 rpm and the second oxygen limitation period is initiated. The implication is that if the high PHB polymerization pathway flux during the second limitation period is appropriate for the particular oxygen limitation conditions encountered and the changes in respiratory activity are nearly identical in both limitation periods, PHB polymerization is slow to respond to this same level as in the first limitation period, resulting in a hysteresis effect or lag in the regulation or the response of PHB polymerization.

4.4.2 Release from Dissolved Oxygen Limitation

Upon release from oxygen limitation, all pathway fluxes with the exception of biosynthesis activity increase to values within 85 to 100% of normal balanced growth levels within one hour; biosynthesis activity recovers by only 70%. Unlike the behavior following the increase in agitation rates between the two oxygen limitation periods, PHB polymerization does eventually drop following a brief increase, suggesting again a lag in PHB polymerization control. It is conceivable, had the experiment been allowed to continue further, that PHB depolymerization would have occurred, judging from the trend in v_3 (Figure 4.2b).

Inhibition of biosynthesis may result from a number of sources. The simplest explanation revolves around the concept of a lag period as the cells readjust enzyme pools to take advantage of favorable growth conditions. Had the cells been utilizing fermentation-type enzymes, reutilization of fermentation products requiring larger energy input for formation of biosythetic precursors might also hinder biosynthesis. And finally, the presence of large PHB granules may have physically hindered cell growth and division (See Chapter 6).

4.5 CONCLUSIONS

As observed in the ammonium limitation (Chapter 3) and the ammonium exhaustion (Chapter 2) cases, restriction of biosynthesis results in elevated NADH levels with subsequent increases in PHB polymerization activity

as increased NADH levels begin to exert regulatory control over key pathway enzymes. Subsequently, citric acid cycle consumption of glycolytically produced acetyl-CoA dwindles, allowing PHB polymerization inhibition to be relieved with the resulting dramatic increase in PHB polymerization pathway activity. The PHB polymerization pathway flux is comparable to that observed under ammonium exhaustion conditions.

4.6 REFERENCES

1. Gottschalk, G., Eberhardt, U., and Schlegel, H.G., *Arch. Mikrobiol.*, **48**, 95 (1964).
2. Schlegel H.G., Gottschalk G., and Bartha R., *Nature*, **191**, 463 (1961).
3. Pfennig, N., and Lippert, K.D., *Arch. Mikrobiol.*, **55**, 245 (1966).
4. Braunegg, G., Sonnleitner, B., and Lafferty, R.M., *Appl. Microbiol. Biotech.*, **6**, 29 (1978).
5. Lee, C., and Lim, H., *Biotechnol. Bioeng.*, **22**, 637 (1980).
6. Savitzky, A., and Golay, M.J.E., *Anal. Chem.*, **36**, 1627 (1964).
7. Steiner, J., Termonia, Y., and Deltour, J., *Anal. Chem.*, **44**, 1906 (1972).
8. Tempest, D.W. and Neijssel, O.M., *Ann. Rev. Microbiol.*, **38**, 459 (1984).
9. Stouthamer, A.H., and Bettenhaussen, C.W., *Arch. Microbiol.*, **111**, 21 (1976).
10. Drozd, J.W., and Jones, C.W., *Biochem. Soc. Trans.*, **2**, 529 (1974).
11. Vollbrecht, D., Schlegel, H.G, Stoschek, G., and Stoschek, G., *Eur. J. Appl. Microbiol.*, **7**, 267 (1979).
12. Schlegel, H.G. and Vollbrecht, D., *J. Gen. Microbiol.*, **117**, 475 (1980).
13. Glaeser, H. and Schlegel, H.G., *Arch. Mikrobiol.*, **86**, 327 (1972).
14. Blackkolb, F. and Schlegel, H.G., *Arch. Mikrobiol.*, **63**, 177 (1968).

15. Tunail, N. and Schlegel, H.G., *Biochem. Biophys. Comm.*, **49**, 1554 (1972).

16. Wilke, D. and Schlegel, H.G., *Arch. Microbiol.*, **105**, 109 (1975).

17. Dawes, E.A. and Senior, P.J., *Adv. Microb. Physiolog.*, **10**, 135 (1973).

18. Oeding, V. and Schlegel, H.G., *Biochem. J.*, **134**, 239 (1973).

19. Senior, P.J. and Dawes, E.A., *Biochem. J.*, **134**, 225 (1973).

20. Vollbrecht, D., Schlegel, H.G., Stoschek, G., and Janczikowski, A., *Eur. J. Appl. Microbiol. Biotechnol.*, **7**, 267 (1979).

21. Schlegel, H.G. and Vollbrecht, D., *J. Gen. Microbiol.*, **117**, 475 (1980).

22. Steinbüchel, A.E. and Schlegel, H.G., *Eur. J. Biochem.*, **130**, 321 (1983).

23. Steinbüchel, A.E. and Schlegel, H.G., *Eur. J. Biochem.*, **130**, 329 (1983).

24. Steinbüchel, A.E., Kuhn, M., Niedrig, M., and Schlegel, H.G., *J. Gen. Microbiol.*, **129**, 2825 (1983).

25. Steinbüchel, A.E. and Schlegel, H.G., *Eur. J. Biochem.*, **141**, 555 (1984).

26. Haywood, G.W., Anderson, A.J., and Dawes, E.A., *FEMS Microbiol. Lett.*, **52**, 91 (1988).

CHAPTER 5

FRUCTOSE EFFECTS

5.1 INTRODUCTION

In the previous investigations with ammonium and oxygen, it was found that the metabolic impact of these nutrients can be directly related to the biosynthetic and respiratory pathways, respectively, and indirectly to all the other pathways through feedback mechanisms. On the other hand, fructose impacts both biosynthesis and glycolysis directly and the other pathways indirectly. Subsequently, *Alcaligenes eutrophus* H16's response to limited fructose resources is of interest, particularly with respect to how these fructose resources are allocated among the various pathways.

Fructose serves three different functions within *Alcaligenes eutrophus* H16 — as a carbon source for biomass synthesis, as an energy source for biosynthesis and cell maintenance, and as a carbon source for PHB polymerization. When fructose availability is restricted, the cell must impose regulatory methodology, which dictates selective parceling of fructose among the three areas of demand, given the prevailing exogenous and endogenous environments. In the case of fructose exhaustion, the cell may choose to metabolize intracellular PHB reserves for purposes of biosynthesis and/or energy production. Although the case of fructose exhaustion may not be encompassed fully within the domain of the metabolic model proposed in Chapter 2, it does provide an insight into yet another facet of *A. eutrophus*' metabolic regulatory scheme.

Using the metabolic model framework developed in Chapter 2 (Eqs. (2.41)–(2.46)), *Alcaligenes eutrophus* H16's metabolic responses to fructose limitation and release from fructose limitation and exhaustion are assessed in terms of changes in the biosynthesis, glycolysis, citric acid cycle, PHB polymerization, and respiratory pathway fluxes. Metabolic responses to fructose exhaustion are examined only in terms of biosynthesis, respiration, and PHB polymerization activities, since these pathways are determined directly from fermentation observables and are not influenced by the model stoichiometry (see Eqs. (2.41), (2.43), and (2.46)). Comparing these results with those of balanced growth and incorporating information gleaned from *in vitro* kinetic studies on key regulatory enzymes will allow us to better understand *A. eutrophus*' regulatory responses and associated influence on PHB production that are due to changing exogenous fructose environments.

5.2 MATERIALS AND METHODS

5.2.1 Organism

Alcaligenes eutrophus H16 (ATCC 17699) was stored on nutrient broth slants with 0.5% fructose added to retain induction of the fructose catabolism enzyme system;[1] cells were restreaked every two months. During liquid cultivation, *A. eutrophus* was grown heterotrophically on media described by Schlegel *et al.*[2] and micronutrient supplement described by Pfennig and Lippert.[3]

Cells were grown at 31°C and pH 6.8. In the case of fructose-limited growth, a concentrated fructose solution was pumped into the fermenter at a constant flow rate.

5.2.2 Analytical Methods

Fructose concentrations were determined spectrophotometrically with the Boehringer Mannheim GMBH Glucose/Fructose assay kit (Cat. No. 139106). PHB was determined after the method of Braunegg *et al.*[4] Ammonium, determined as ammonium chloride, was measured by an ammonium probe (Ingold Electrodes, Inc., Series 7500). Dry weight determinations were made through the membrane filtration technique. Biomass was calculated from the difference between the dry weight and PHB concentrations.

Dissolved oxygen concentrations were determined with an Instrumentation Laboratories (IL) 531 Industrial Dissolved Oxygen monitor and an Ingold Electrodes, Inc. polarographic oxygen-sensing probe. Dissolved carbon dioxide was measured with an Ingold carbon dioxide monitor (Model 1230) using an Ingold dissolved carbon dioxide probe (Model 780). Optical density was determined at 420 nm with a Spectronic 20 (Bausch and Lomb) modified to accept the flow-cell described by Lee and Lim.[5] A Cole-Parmer pH controller (Model 5997-20) was used to measure and maintain the pH in conjunction with two Masterflex peristaltic pumps for the addition of sodium hydroxide and phosphoric acid. Off-gas carbon dioxide and oxygen concentrations were monitored with an Infrared Industries, Inc. (Santa Barbara, CA) Model # 703-075 carbon dioxide

gas detector and a Leeds and Northrup 7863 thermomagnetic oxygen analyzer, respectively.

5.2.3 Fermentation System

Fermentations were conducted in an 18 liter Bioengineering AG Laboratory fermenter. The data acquisition system supplied as part of the FluroMeasure System data logged fluorescence, off-gas oxygen, off-gas carbon dioxide, pH, dissolved oxygen, and dissolved carbon dioxide. The ammonium chloride concentration was maintained via pH-controlled additions of a concentrated ammonium chloride (134 g/l) feed solution. The dissolved oxygen concentration was regulated by a homemade controller that manipulated the fermenter agitation rate.

5.2.4 Computation of Pathway Fluxes

Preliminary data manipulations were performed on an IBM PC. A VAX 11/780 and a MicroVAX 3500 were used to perform all smoothing, interpolations and model pathway calculations. The off-line data were smoothed and interpolated with cubic splines. On-line data were collected at eight samples per minute over the course of each fermentation. Other on-line data were smoothed and derivatives calculated according to the method developed by Savitzky and Golay[6] and corrected by Steiner *et al.*[7]

5.3 RESULTS

Initially the fermenter was inoculated with a fructose concentration of *ca* 1.2 g/l (Figure 5.1a). The dissolved oxygen and ammonium chloride concentrations were maintained between 120 to 140 mm Hg and 0.7 to 1.0 g/l, respectively. At approximately 5.4 hours, the fructose concentration was allowed to fall to undetectable levels and to remain at this level for 1.1 hours. At 6.5 hours the fructose feed pump was started; a 1000 g/l fructose solution was fed to the fermenter at a rate of 0.34 ml/hr/l culture. During this period, the cells' fructose consumption rate was limited by the fructose feed rate; therefore, the bulk fructose concentration did not rise to detectable levels. Two hours later, the fructose feed pump rate was increased to exceed cellular consumption and to allow the fructose concentration to rise to *ca* 0.4 g/l. At 10.5 hours the fructose feed pump again was turned off, followed by fructose exhaustion at 10.8 hours. At 11.25 hours the fructose pump was turned on at a rate of *ca* 0.83 ml/hr/l culture. This feed rate was further elevated to *ca* 1.04 ml/hr/l culture at 13.5 hours and maintained at this rate through the end of the experiment. From 11.25 hours until the end of the experiment, cellular fructose consumption was limited by the fructose feed rates.

5.3.1 Fructose Limitation, Exhaustion, Release from Limitation, and Release from Exhaustion

The time evolution of the cellular components is described by Figure 5.1a, and the time evolution of the off-gas carbon dioxide and off-gas oxygen con-

centrations are described in Figure 5.1b. Included in Figure 5.1a along with the bulk fructose concentration is the integral of the fructose consumption rate per liter, or pseudofructose concentration, Φ_{Fruc} (Eqs. (2.49) and (2.50)). The derivative of this curve is an indication of the fructose consumption rate per liter culture. Note that during the fructose feeding segments of this experiment, the derivative of the pseudofructose concentration curve is constant. Also notice how the cellular components and off-gas concentrations respond to the periods of unrestrained growth (0–5.4, 8.5–10.8 hours), releases from fructose exhaustion (6.5 and 11.25 hours), release from fructose limitation (8.5 hours) and growth under limited conditions (6.5–8.5, 11.25–16^+ hours).

The oscillatory behavior observed in the off-gas concentrations during the periods of limited growth requires special attention. Initially it was thought that these oscillations were manifestations of shifts between growth and PHB storage metabolic regimes. Closer examination revealed, however, that these oscillations were actually caused by pH-induced fluctuations in the fructose feeding rate.

In Figure 5.2 plots of the unsmoothed, raw data of the off-gas oxygen concentration and fermenter pH from the last fructose limitation region are presented. As the pH slowly drops, indicating consumption of ammonium and the associated expulsion of a proton, the low controller set point is reached and the ammonium chloride and sodium hydroxide addition pumps are activated. The exact point at which the controller is turned on can be seen in the sudden, disjointed drop in the recorded pH — this is an electrical artifact in the analog output triggered by the activation of the pump relay. After a brief delay attributible to the time necessary for the fermenter off-gas to leave the fermenter

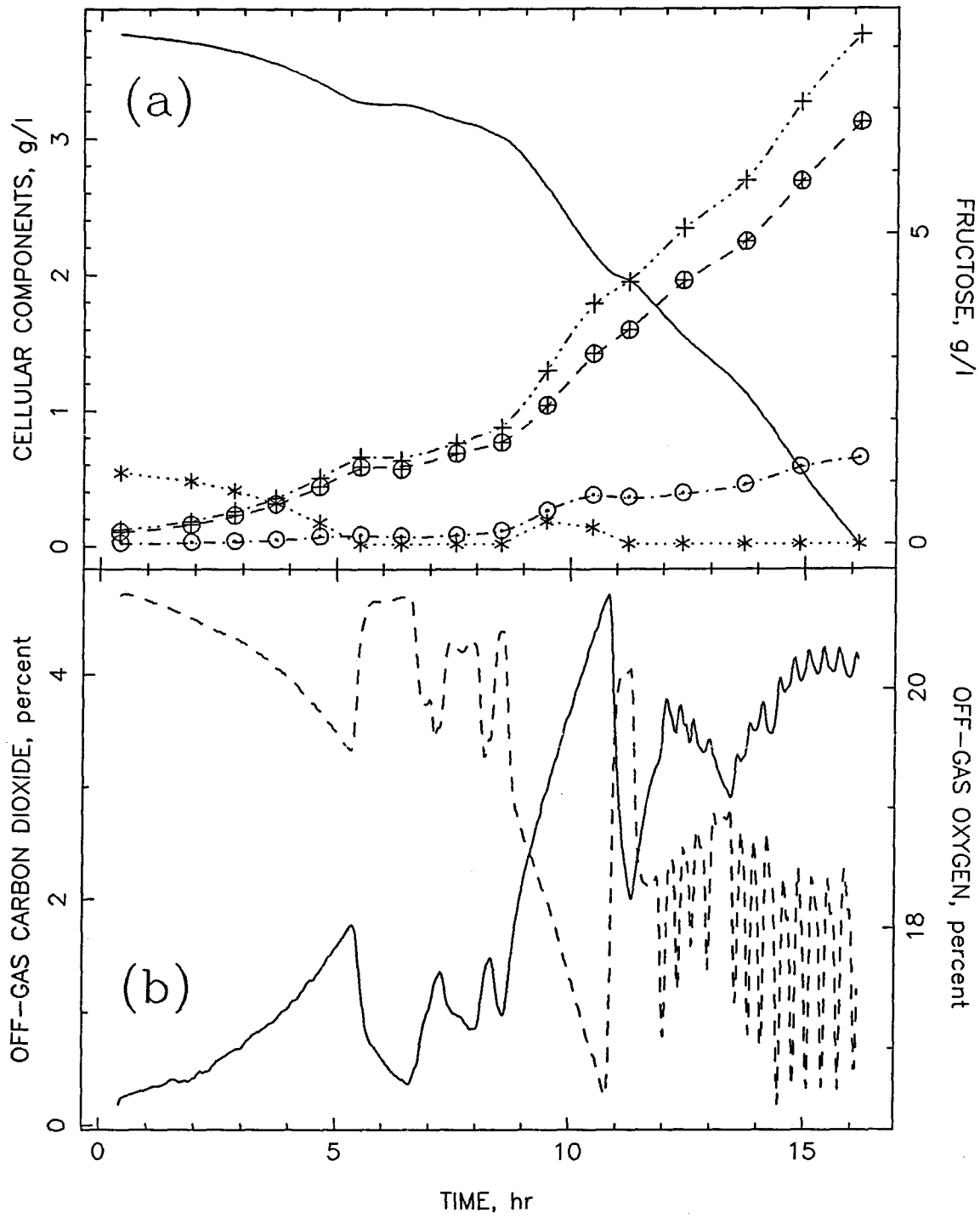

Figure 5.1: Fructose limitation and exhaustion experiment: raw data. **(a)** Cell dry weight, $+$; biomass, $\oplus$; PHB, $\odot$; bulk fructose, $*$; pseudofructose, Φ_{Fruc} (time integral of fructose consumption rate per liter, Eq. (2.50)), ——— . **(b)** Off-gas carbon dioxide, ——— ; off-gas oxygen, – – – .

and reach the off-gas oxygen analyzer, the off-gas oxygen concentration drops sharply, indicating an increase in oxygen consumption.

The pH-controller's influence on the fructose feed rate proved to be an accident in design. Both the fructose and ammonium chloride feed lines were connected via a "y"-connector on the inlet of a flow break which in turn was connected to a culture broth recirculation loop. A flow visualization technique employing the addition of bromphenol blue to the fructose feed solution facilitated elucidation of this pH-influenced phenomenon. When dissolved in the concentrated fructose solution, the bromphenol blue lacked sufficient hydration to color the solution noticeably. Therefore, the fructose solution remained clear. This effect allowed observation of two things: mixing between the fructose and ammonium chloride streams and partitioning of the flows. In other words, if mixing occurred between the fructose and ammonium chloride solutions, the ammonium chloride solution turned blue. If both fructose and ammonium chloride solutions were flowing simultaneously, differentiation between the two flows was possible since the denser, more viscous fructose solution would remain colorless and the ammonium chloride solution would turn blue.

Use of the bromphenol dyeing technique provided the following information: Because of the geometry of the previously mentioned arrangement, the fructose solution would slowly displace the quiescent ammonium chloride solution in the ammonium chloride inlet feed line because of the fructose solution's higher density and the effects of gravity. By best estimate, 20% or less of the fructose feed solution was diverted to displace or mix with the ammonium chloride solution during the period of inactive pH control. The rest of the fructose

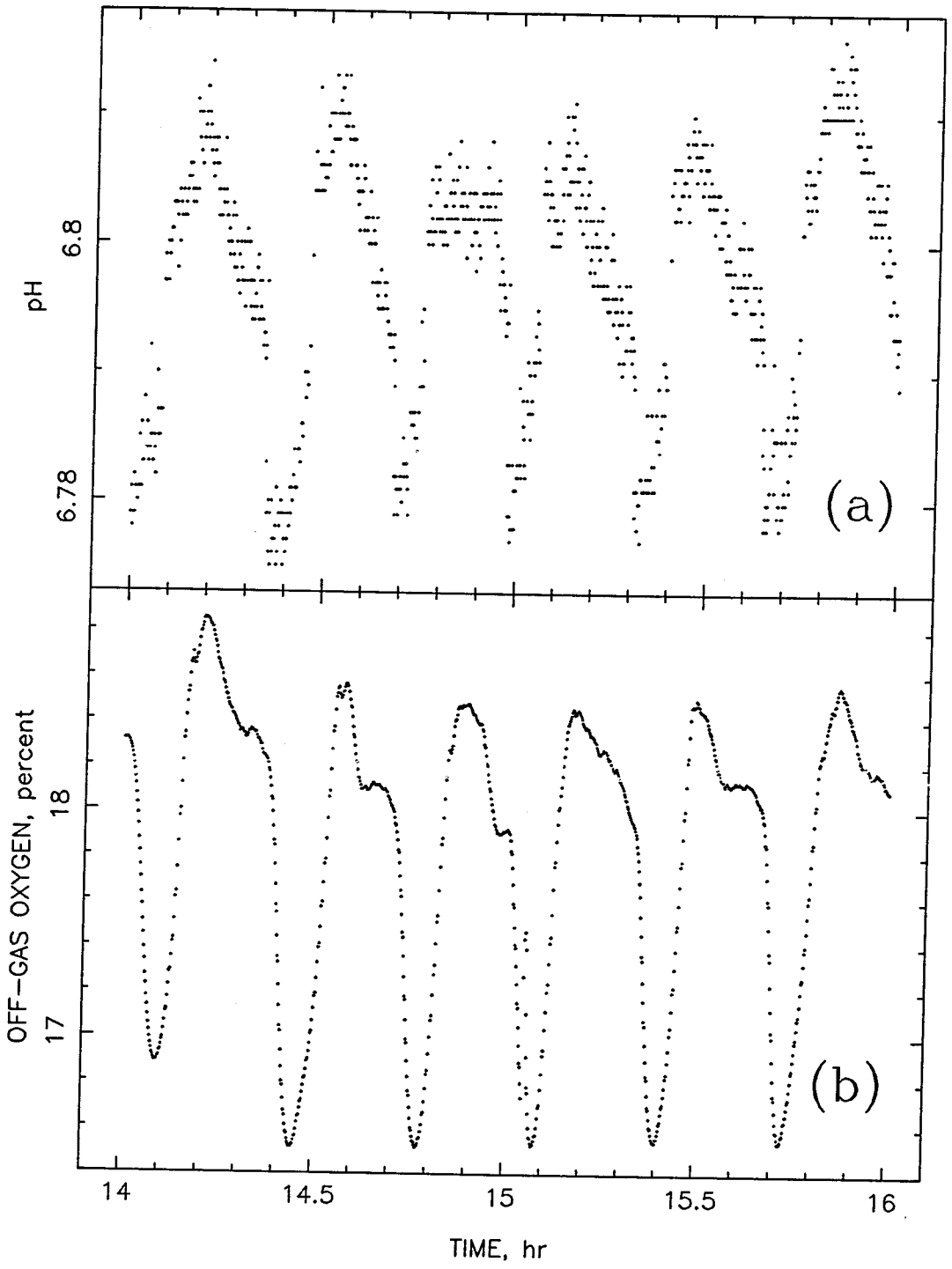

Figure 5.2: Fructose limitation and exhaustion experiment: influence of pH control. **(a)** Fermenter pH. **(b)** Off-gas oxygen concentration.

solution flowed into the fermenter. Once pH control was activated, the dissolved portion of the fructose solution in the ammonium chloride line was slowly added to the fermenter, effectively increasing the short-term rate of fructose addition, until the pH control pulse stopped. It is unclear whether all of the fructose in the ammonium chloride was immediately flushed out upon activation of pH control. Given the flow visualization, it was apparent that the fructose solution did not readily mix with the ammonium chloride solution. If this is true it would suggest that as the ammonium chloride solution was pumped, only the dissolved portion of the fructose in the line would be effectively pumped out, leaving the remaining viscous fructose solution clinging to the walls of the tubing and slowly dissolving into the passing ammonium chloride stream. This would result in a more distributed increase in the short-term fructose feeding rate as opposed to a pulse input.

Returning to Figure 5.2, the fact that the drop in the off-gas oxygen concentration ceased shortly after pH control ceased (the large disjointed increase in the pH) should be noted. Off-line samples were taken in between spikes; the fructose concentration was always below detectable levels. In light of these two observations, it seems reasonable to assume that the culture was fructose-limited throughout these oscillations, except, possibly, at the very beginning of pH control action, since the off-gas peaks occurred only while pH control was activated. As a final piece of supporting data, the culture fluorescence peaks were "flat-topped" except for an initial spike (not shown). Consequently, although the fructose feed rate was oscillatory, this region may be approximated as fructose-limited at the prevailing time-averaged fructose feed rate.

Because the time scale of these oscillations are short relative to the sampling frequency (approximately three oscillations per off-line sample), pathway flux calculations based upon changes in biomass and PHB concentrations can be considered to be only time-averaged rates, much like the fructose feed rate. However, on the basis of the observations of other fermentation parameters and previous experimental results, it should be possible to conjecture what the biomass and PHB responses were during these oscillations.

Figure 5.3 presents the pathway flux results for this experiment; deletion of the glycolysis and citric acid cycle activities during the fructose exhaustion periods will be discussed shortly. Following a balanced growth start, the biosynthesis pathway rate, $\mathbf{v}_B$, drops dramatically as fructose is exhausted. It has been shown previously that *A. eutrophus* is capable of continuing biosynthesis in the absense of an extracellular carbon source and in the presence of all other required nutrients through the consumption of PHB.[1] This will become more apparent shortly. Following fructose exhaustion, biosynthesis activity increases but is restricted by fructose availability. Once the fructose concentration rises to detectable levels, $\mathbf{v}_B$ increases accordingly. As the second fructose exhaustion period sets in, $\mathbf{v}_B$ drops *ca* only 50%, as compared to the previous exhaustion period. It is likely that $\mathbf{v}_B$ actually drops lower than this value; the brevity of this fructose exhaustion period and the small number of off-line data points do not allow adequate examination of this period. Clearly, though, biosynthesis is supported by depolymerization of PHB in the presence of ammonium chloride. As fructose feeding is reinitiated, a small increase in $\mathbf{v}_B$ is reflected, followed by a decline in activity. With a 25% shift upward in the fructose feed rate,

biosynthesis responds with *ca* a 30% increase in activity before again falling off. As we saw with the ammonium limitation case, we would expect to see biosynthesis activity decline as time progresses because of the reduction in the specific fructose consumption rate (see Eqs. (3.3)–(3.6) and Figure 5.3a).

After the two-hour post-inoculation period, the respiration pathway flux, $\mathbf{v}_R$, increases to balanced growth levels. During the first fructose exhaustion period, $\mathbf{v}_R$ drops over 85%, indicating a dramatic reduction in NADH availability. Clearly, endogenous respiration occurs at the expense of PHB. As fructose exhaustion shifts to fructose limitation, $\mathbf{v}_R$ increases, experiencing two oscillations that are due to two pH-control additions (pH not shown), and responds very strongly to the rise in fructose concentration. The increase in $\mathbf{v}_R$ to levels above the balanced growth average may be in response to the dwindling, low fructose concentration or else in response to the previous fructose exhaustion/limitation growth history. Fructose exhaustion again reduces respiratory activity but only to 4 mmol H_2O/((g biomass)(hr)). This higher endogenous respiration activity appears to correlate with the perceived higher biomass synthesis rate relative to the previous fructose exhaustion period at 5.4 hours. In the final fructose limitation period, $\mathbf{v}_R$'s response follows the trend set by $\mathbf{v}_B$, on average. Relative to all other pathways, respiration responds the most to fluctuations in the effective, short-term fructose feed rate.

Glycolytic pathway activity, $\mathbf{v}_1$, in Figure 5.3b qualitatively resembles $\mathbf{v}_R$. Beginning at 8 C-mmol AcCoA/((g biomass)(hr)), $\mathbf{v}_1$ rises to 10 C-mmol AcCoA/((g biomass)(hr)), just above balanced growth levels, before the onset of fructose exhaustion.

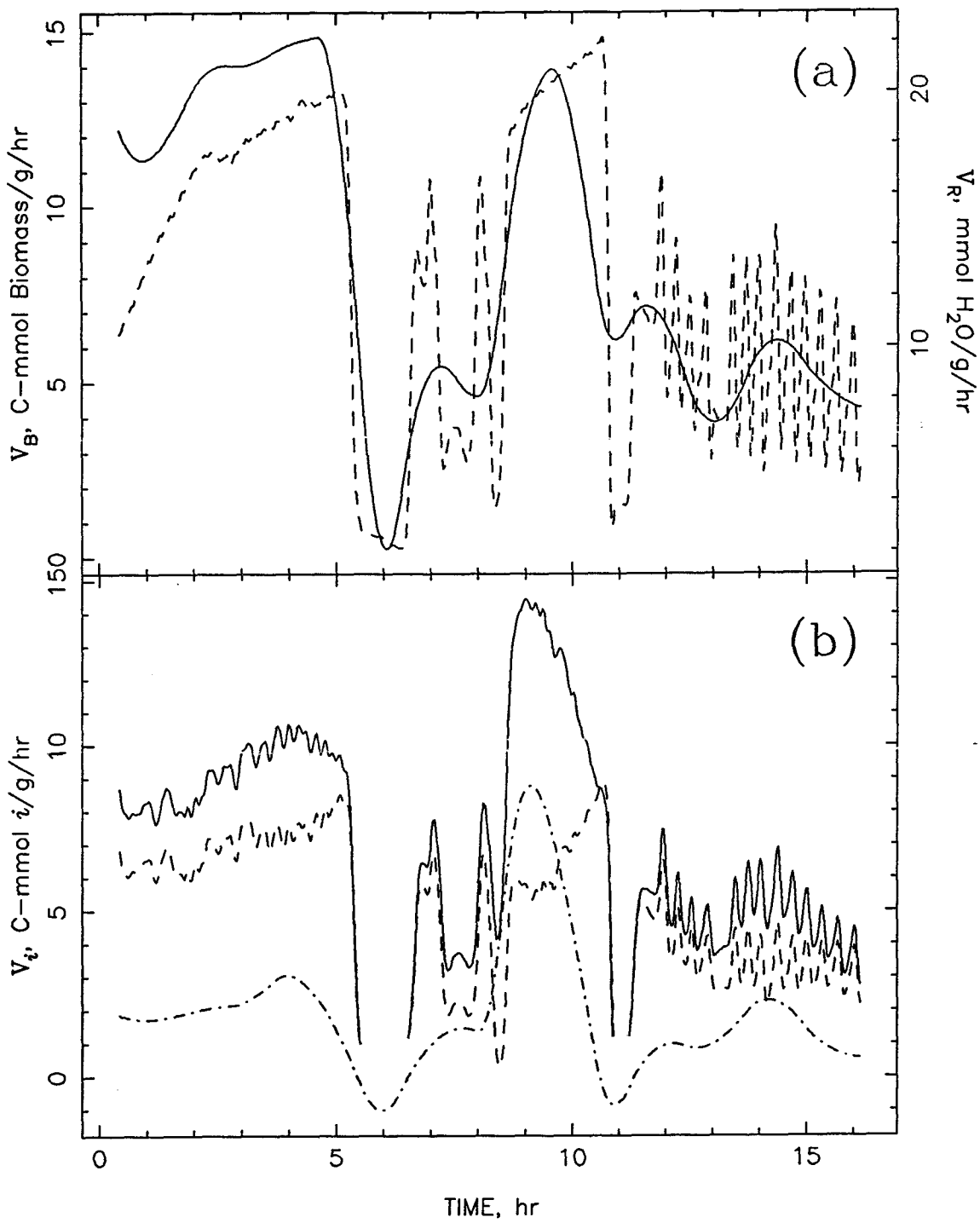

Figure 5.3: Fructose limitation and exhaustion experiment: pathway fluxes. **(a)** Biosynthesis activity ($\mathbf{v}_B$), ——; respiration activity ($\mathbf{v}_R$), – – –. **(b)** Glycolysis activity ($\mathbf{v}_1$), ——; citric acid cycle activity ($\mathbf{v}_2$), – – –; PHB polymerization activity ($\mathbf{v}_3$), – · – · –. *Note:* $\mathbf{v}_1$ and $\mathbf{v}_2$ fructose exhaustion regions have been removed.

With the onset of fructose exhaustion, a question with regard to the applicability of the present model formulation arises. In constructing the associated pathway network, a lumping of all biosynthetic pathways, incorporating fructose as the sole carbon and energy source, was made. From the standpoint of the model, therefore, it is explicitly assumed, structurally and stoichiometrically, that biomass synthesis proceeds directly from fructose. In the case of fructose exhaustion, biosynthesis may proceed at the expense of intracellular PHB. The biosynthetic pathways used for PHB-supported biosynthesis relative to fructose-supported biosynthesis are, in part, different, both in terms of pathways used as well as in energy required. With regard to biosynthetic precursors "siphoned off" the citric acid cycle, PHB- and fructose-supported biosynthesis would be identical. However, glycolytic intermediates used as biosynthetic precursors normally derived from degradation of fructose would have to be "built up" from PHB-derived acetyl-CoA, *e.g.*, phosphoenolpyruvate, requiring different enzymes and energy input not needed for derivation from fructose degradation. Therefore, the model is structurally inconsistent and stoichiometrically invalid when trying to accommodate PHB depolymerization.

For biosynthesis to occur within the explicit mathematical framework of the model under fructose exhaustion conditions, PHB must be first depolymerized to acetyl-CoA and must travel up the glycolytic pathway to reach fructose and then on to biomass. As Eqs. (2.9) and (2.10) imply, reversing glycolysis requires incorporation of carbon dioxide. Although *A. eutrophus* is capable of fixing carbon dioxide via the Calvin cycle,[8] reversing glycolysis in no way accounts for the energy required to accomplish carbon dioxide fixation.[9]

As described in Chapter 2, fructose consumption is back-calculated through closure of the acetyl-CoA balance (Eq. (2.36)). During both fructose exhaustion periods, the specific fructose consumption rate (FCR) is positive instead of zero, confirming that the model structure and stoichiometry during PHB depolymerization are not correct. Since calculation of glycolysis and citric acid cycle activities are not independent of the calculated fructose consumption rate (Eqs. (2.44) and (2.45)), their values cannot be considered valid. Consequently, all calculations dependent upon the fructose consumption rate during both fructose exhaustion periods are ignored.

Upon release from fructose exhaustion, $\mathbf{v}_1$ responds to the fluctuations in the short-term fructose feed rate. As the fructose concentration becomes nonzero, $\mathbf{v}_1$ reaches a previously unobserved activity: 14 C-mmol AcCoA/((g biomass)(hr)), 50% above balanced growth levels. As with the respiration pathway, this may be a response to the previous growth history. However, as the bulk fructose concentration drops, glycolysis activity shifts to a more normal level, unlike $\mathbf{v}_R$'s response. This would suggest that $\mathbf{v}_1$'s initial response may have been due to insufficient regulation; $\mathbf{v}_1$ drops later as regulation is normalized. Prior to the onset of fructose exhaustion, $\mathbf{v}_1$ drops abruptly. In the final fructose limitation period, $\mathbf{v}_1$ is nearly identical to $\mathbf{v}_R$, although the magnitude of the fluctuations are significantly smaller, suggesting that the metabolic dynamics of glycolysis are slower than respiration.

Citric acid pathway activity, $\mathbf{v}_2$, in Figure 5.3b is also qualitatively similar to $\mathbf{v}_R$ and $\mathbf{v}_1$. Beginning at a typical balanced growth level, $\mathbf{v}_2$ noticeably

increases prior to fructose exhaustion. Following the release from fructose exhaustion, $\mathbf{v}_2$ closely mimics the fructose feed rate oscillations observed in $\mathbf{v}_R$ and $\mathbf{v}_1$. As the fructose concentration rises to detectable levels, the citric acid cycle responds with an increase in activity to nearly balanced growth levels. However, unlike $\mathbf{v}_1$, $\mathbf{v}_2$ continues to increase sharply, much in the same manner as $\mathbf{v}_R$, before an abrupt drop as fructose exhaustion is encountered again. After fructose exhaustion, $\mathbf{v}_2$ follows the same fructose limitation pattern observed with $\mathbf{v}_R$ and $\mathbf{v}_1$. However, $\mathbf{v}_2$ appears to remain constant, on average, during the second fructose feed rate section rather than rising and falling as glycolysis activity does. Not surprisingly, the oscillations in $\mathbf{v}_2$ are of the same order of magnitude as those observed in $\mathbf{v}_1$.

The last pathway of interest, the PHB polymerization pathway flux, $\mathbf{v}_3$, is shown in Figure 5.3b. $\mathbf{v}_3$ increases as fructose exhaustion is approached, suggesting that the drop in the bulk fructose concentration does influence the cell. As mentioned previously, $\mathbf{v}_3$ is negative during fructose exhaustion to support endogenous respiration. Following the release from fructose exhaustion and the initiation of the first fructose limitation period, PHB depolymerization ceases, with $\mathbf{v}_3$ rising to 65% of balanced growth levels. As the fructose concentration becomes nonzero, $\mathbf{v}_3$ responds with a dramatic increase. This level of activity is as high or higher than the surge in PHB polymerization activity at the onset of ammonium exhaustion (Chapter 2) and parallels the large increase observed in glycolysis activity. Again, as fructose is exhausted, PHB depolymerization resumes. It is interesting to note that in both PHB depolymerization cases, the absolute rate of depolymerization is over 50% less than balanced growth poly-

merization rates. Following the last release from fructose exhaustion, v_3 rises to a plateau, increases 100% as the fructose feeding rate increases, and tails off in concert with the biosynthesis activity.

Figure 5.4 describes the time evolution of the PHB/biomass ratio. Initially, the PHB/biomass ratio levels off prior to the onset of fructose exhaustion. Following the decline in the PHB/biomass ratio during fructose exhaustion that is due to PHB degradation, PHB clearly increases faster than biomass during the first fructose limitation period until the fructose concentration rises to detectable levels and there is a dramatic rise in the intracellular PHB content — nearly a 200% increase. While the second fructose exhaustion period is considerably shorter, the net decrease in the PHB/biomass ratio is much larger. Whereas in the first fructose exhaustion period biosynthesis activity is low and only PHB depolymerization is highly active, relatively speaking, both biosynthesis and PHB depolymerization are very active during the brief, second fructose exhaustion period, giving rise to the dramatic change in the PHB/biomass ratio. This strongly suggests that the cell metabolically determines the level of PHB adequate for survival before risking depolymerization for purposes of biomass synthesis. There is a slight increase in PHB/biomass shortly after the shift in feed rate, but the PHB/biomass ratio remains fairly constant at an elevated level relative to balanced growth conditions.

Figure 5.5 describes the fructose consumption rate normalized by biomass (FCR) and fructose partitioning between the three terminal carbon pathways. After the two-hour post-inoculation period, the FCR averages at or above balanced growth levels. Both fructose limitation regions follow the same trends

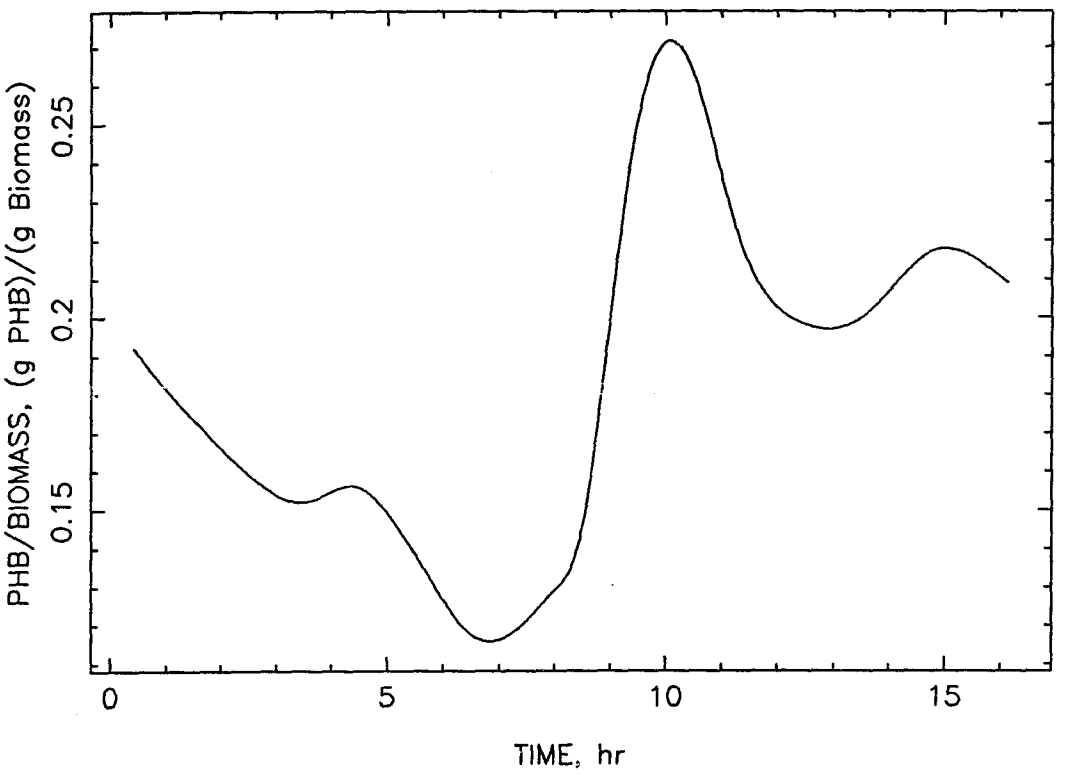

Figure 5.4: Fructose limitation and exhaustion experiment: ratio of PHB to biomass.

observed in $\mathbf{v}_R$, $\mathbf{v}_1$, and $\mathbf{v}_2$. Of particular interest is the portion of the fermentation where the fructose concentration becomes detectable at 8.5 hours; the FCR rises to one of the highest levels ever observed. Again, this may be due to relaxation of regulation or the contribution of an efficient fructose scavenging mechanism.

The most prominent feature about Figure 5.5b is the insignificant changes in the relative fructose consumption by the biosynthesis (FCR_B/FCR), citric acid cycle (FCR_2/FCR), and PHB polymerization (FCR_3/FCR) pathways. throughout the course of the experiment. Only during the approach to and release from fructose exhaustion and during the increase in fructose concentration do these values deviate significantly. It should be noted that FCR_B/FCR and FCR_2/FCR act antagonistically during the fructose limitation oscillations.

The carbon dioxide production rate normalized by biomass (CDPR) in Figure 5.6 provides a strong general indicator of the changes in metabolic activity for this experiment. Of particular note is the change in the CDPR at the onset of both fructose exhaustion periods. Clearly, from a metabolic standpoint, *A. eutrophus* responds abruptly to fructose exhaustion. Unlike a number of the pathway fluxes, the CDPR is nearly identical during both nonzero fructose concentration regions. Also, the metabolic fluctuations during fructose limitation appear to be considerably larger during the first limitation period than during the second, although the averages are about the same.

Because this experiment evolved through numerous changes, it is difficult to draw any firm, direct relationship between the specific fructose consumption rate and the various pathways, particularly in light of the oscillations observed

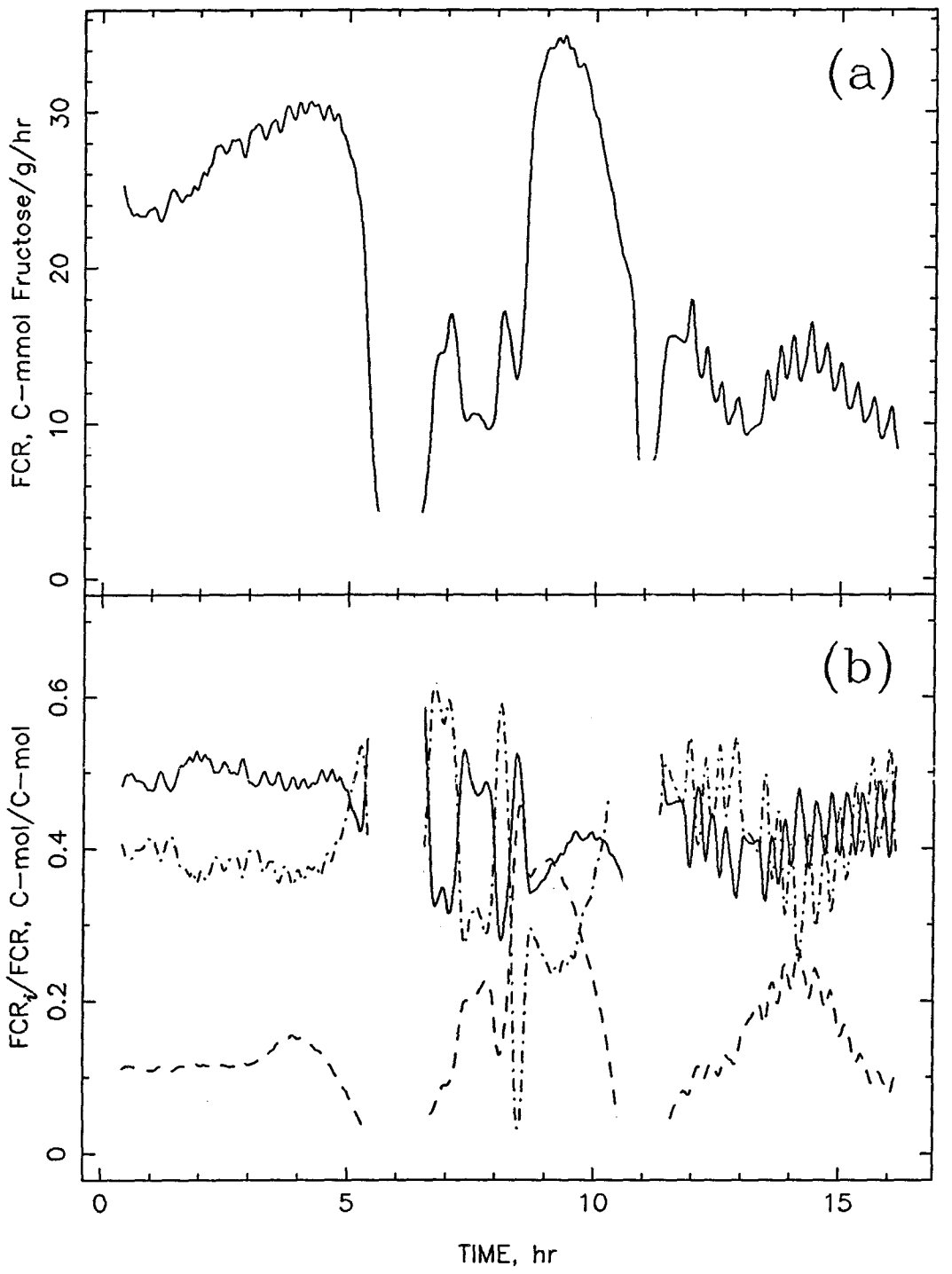

Figure 5.5: Fructose limitation and exhaustion experiment: specific fructose consumption rate (FCR) and partitioning of fructose between terminal carbon pathways. **(a)** Specific fructose consumption rate (FCR). **(b)** Fraction of fructose directed to biosynthesis (FCR_B/FCR), ——— ; fraction of fructose directed to the citric acid cycle (FCR_2/FCR), — · — · ; fraction of fructose directed to PHB polymerization (FCR_3/FCR), — — — . *Note:* Fructose exhaustion regions have been removed.

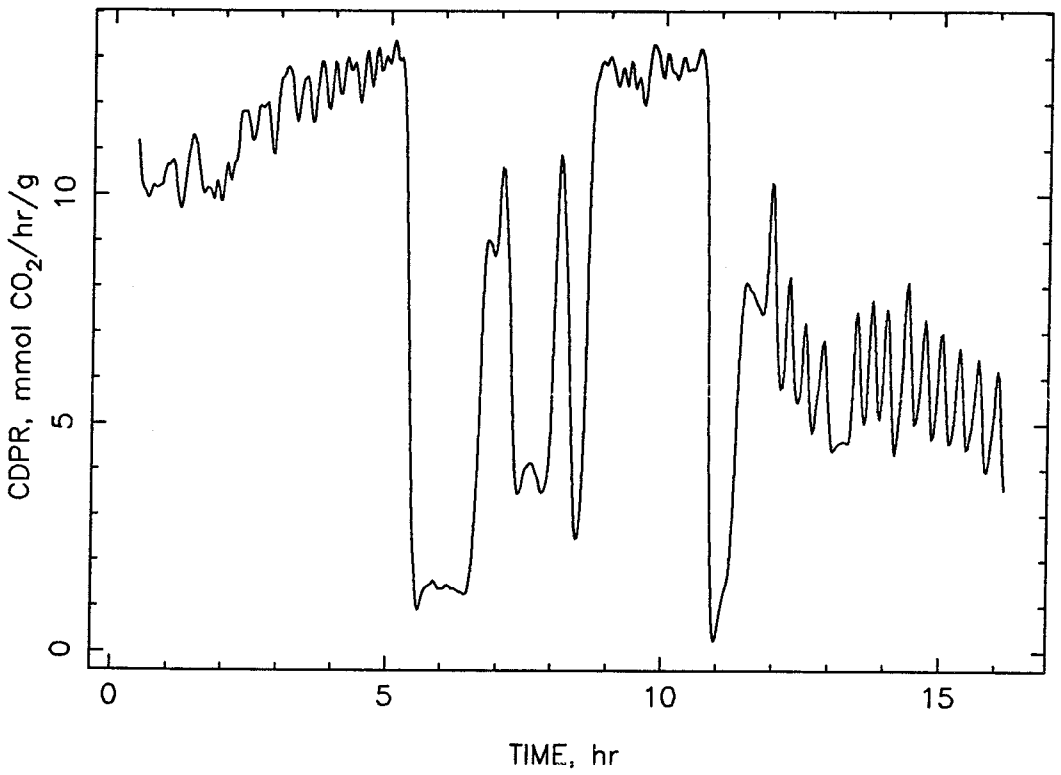

Figure 5.6: Fructose limitation and exhaustion experiment: specific carbon dioxide production rate (CDPR).

and the lack of any long-term constant fructose feed rates. However, because the fructose limitation feed rates at the end of the fermentation were fairly constant for a period of about four hours, an attempt is made to use these data to draw some conclusions. To ease visual comparisons and to compensate for the lack of responsiveness of the biomass and PHB concentrations relative to the two off-gas concentrations, the oscillations are smoothed out, leaving time-averaged values for the pathway fluxes and the FCR.

As seen in Figure 5.7a, the time-averaged FCR ranged from 9.5 to nearly 16 C-mmol fructose/((g biomass)(hr)) from 12 to 16 hours. In virtually all cases, the pathway fluxes (Figure 5.7b) respond linearly to increases and decreases in the FCR. $\mathbf{v}_B$ and $\mathbf{v}_1$ retain very similar relationships with the FCR throughout the limitation period. For $\mathbf{v}_2$ and $\mathbf{v}_3$ there appear to be two distinct regions separated at approximately 13 hours. Prior to 13 hours, $\mathbf{v}_3$ is constant with decreasing FCR, while $\mathbf{v}_2$ decreases almost 35%. From 14.2 to 16.2 hours, $\mathbf{v}_2$ remains relatively constant to the FCR's 35% decrease while $\mathbf{v}_3$ decreases 75%. $\mathbf{v}_R$ also appears to follow the pattern set by $\mathbf{v}_2$; because of the magnitude of the oscillations, it is difficult to smooth $\mathbf{v}_R$'s oscillations completely. It is unclear why $\mathbf{v}_R$, $\mathbf{v}_2$, and $\mathbf{v}_3$ deviate as they do, although the size of this deviation is not overly large.

5.3.2 Approximating $\mathbf{K}_{m,Fruc}$

Since fructose utilization is not associated specifically with one and only one metabolic pathway in our model, we will define an effective Michaelis-Menten

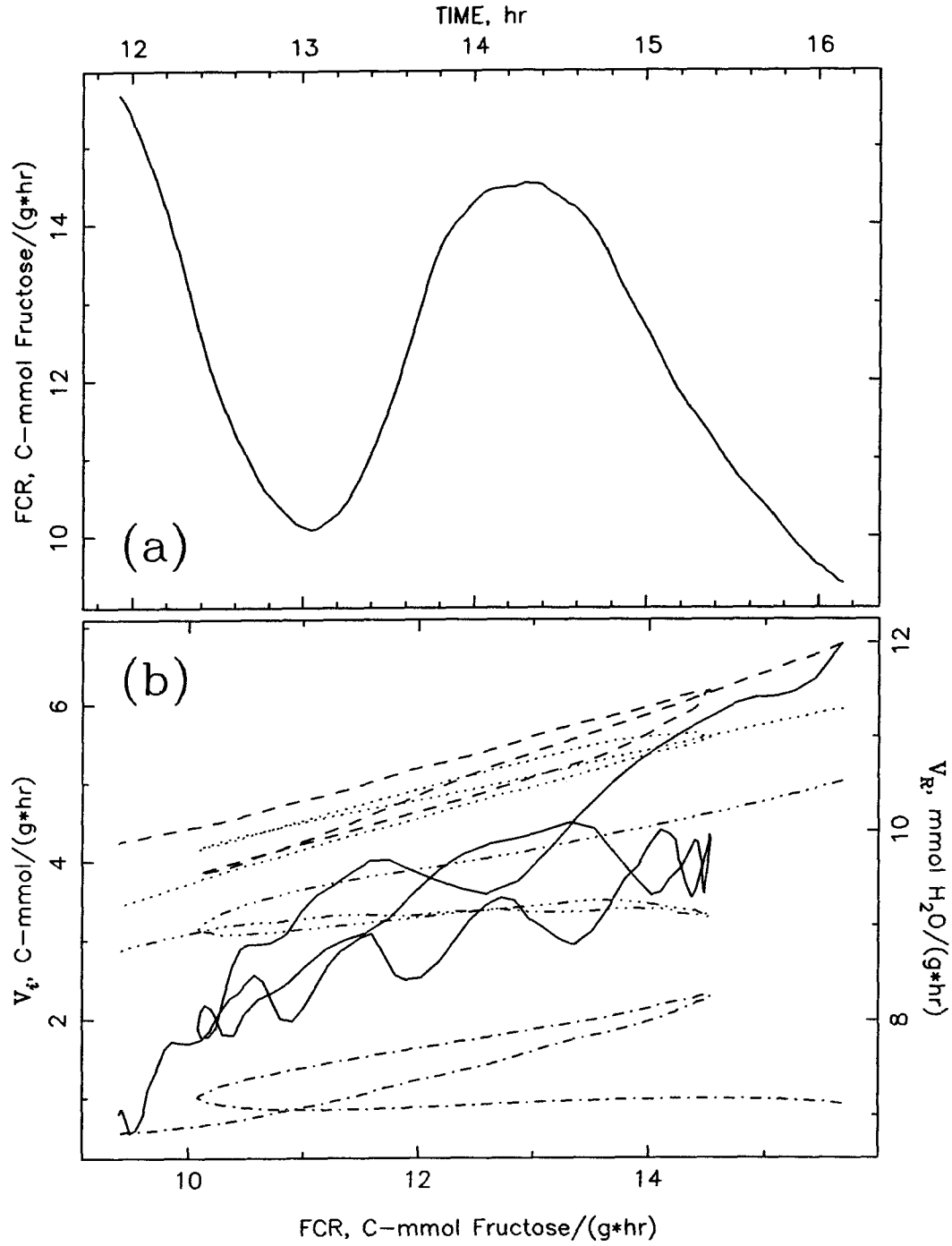

Figure 5.7: Fructose limitation and exhaustion limitation experiment: specific fructose consumption rate (FCR) and its relationship to pathway fluxes. **(a)** Specific fructose consumption rate (FCR). **(b)** Relationship between respiration activity and the FCR, ——— ; relationship between biosynthesis activity and the FCR, – – – ; relationship between glycolysis activity and the FCR, ····· ; relationship between citric acid cycle activity and the FCR, —···— ; relationship between PHB polymerization activity and the FCR, —·—·.

constant, $\mathbf{K}_{m,Fruc}$, appropriate to assessing fructose concentration effects on general fructose consumption. Defining an expression that parallels the formulation of Eq. (3.18), the following expression for fructose consumption results:

$$\mathbf{K}_{m,Fruc} = \left(\frac{\mathbf{FCR}_{max}\, \mathbf{C}^{l}_{Fruc}}{\mathbf{FCR}} \right) - \mathbf{C}^{l}_{Fruc} \,. \tag{5.1}$$

$\mathbf{FCR}_{max}$ is the maximum observed FCR under balanced growth conditions. Using 28 C-mmol fructose/((g biomass)(hr)) for $\mathbf{FCR}_{max}$, the lowest observed FCR in the fructose limitation experiment of *ca* 10 C-mmol fructose/((g biomass)(hr)) for **FCR**, and the lowest detectable fructose concentration of 0.05 g/l for $\mathbf{C}^{l}_{Fruc}$, results in an effective $\mathbf{K}_{m,Fruc}$ of 0.09 g/l fructose. As seen for the same analysis with ammonium and dissolved oxygen, this value is well below the level of control for this experimental system.

5.4 DISCUSSION

5.4.1 Fructose Exhaustion

Not surprisingly, fructose exhaustion significantly reduces metabolic activity in *Alcaligenes eutrophus* H16 as indicated by the drops in the specific carbon dioxide production rate and the specific oxygen consumption rate ($= \frac{1}{2} \times \mathbf{v}_R$). Without a source of fructose, glycolytic and citric acid cycle intermediate levels drop. Consequently, NADH and ATP production also drops. As a result, the AcCoA/CoASH ratio decreases as does the NADH/NAD ratio. As Figure 2.1 indicates, high levels of CoASH inhibit the β-ketothiolase-catalyzed acetyl-CoA

condensation reaction while relieving inhibition of the acetacetyl-CoA cleavage reaction.[10,11,16] Acetacetyl-CoA reductase and PHB synthase polymerization activities are also inhibited.[17,18]. Low NADH levels also relieve inhibition of the β-hydroxybutyrate dehydrogenase-catalyzed β-hydroxybutyrate cleavage reaction.[11] Therefore, PHB depolymerization can proceed, as confirmed by the reversal of PHB polymerization activity. Since PHB depolymerization occurs at less than half the rate at which balanced growth PHB polymerization occurs, this suggests the presence of a metabolically controlled survival mechanism preventing excessive PHB depolymerization.

The second exhaustion period suggests that PHB polymerization can actively support biosynthesis. In this case, only a 50% reduction in biosynthesis activity is observed, relative to the much larger drop in $\mathbf{v}_B$ during the first fructose exhaustion period. As pointed out previously, the model is not designed to analyze PHB depolymerization. Only those pathway flux rates derived from direct observables, *i.e.*, $\mathbf{v}_B$ (Eq. (2.41)), $\mathbf{v}_R$ (Eq. (2.43)), and $\mathbf{v}_3$ (Eq. (2.46)), can be considered valid. With regard to $\mathbf{v}_1$ and $\mathbf{v}_2$, we can only conjecture their activity partially on the basis of the specific carbon dioxide production rate, $\mathbf{v}_B$ and $\mathbf{v}_3$. Intracellular balance calculations, *i.e.*, Eqs. (2.36)–(2.38), are invalid both stoichiometrically and energetically.

5.4.2 Fructose Limitation

During periods of fructose limitation, it is clear that *A. eutrophus* endeavors to increase the relative ratio of PHB to biomass when this ratio is low. This

is particularly obvious in the first fructose limitation period. During the second fructose limitation period, there is a slight increase in the PHB/biomass ratio, but on average, this ratio does not change significantly. As with ammonium and oxygen limitation, *A. eutrophus* appears to increase PHB polymerization and intracellular PHB reserves to meet metabolically determined criteria. Unlike ammonium and oxygen limitation, the increases in PHB polymerization and PHB intracellular levels are not nearly as dramatic nor as high. This may be due, in part, to the fact that biosynthesis is uninhibited, relative to glycolysis, and that PHB polymerization runs at a slightly higher rate because of a slight kinetic advantage. Other than the slight shift to higher PHB synthesis rates, all pathway fluxes, based on relative activities and averaged-out oscillations, do not differ significantly from balanced growth conditions.

Experience has shown that high oxygen consumption rates and high carbon dioxide production rates are strong indicators of biosynthesis activity. It might be proposed, therefore, that the oscillations observed in the respiration, glycolysis, and citric acid cycle activities indicate periods of high and low biosynthetic activity, and conversely, periods of low and high PHB polymerization, or even alternating periods of PHB depolymerization and polymerization. If PHB depolymerization is occurring, this would suggest that the pathway results are of questionable validity. Although past work indicates that these short-term fluctuations may not matter on the time scale of the dynamic response time of biosythesis and PHB polymerization, it is of interest to examine the possible influences of oscillating biosynthesis and PHB polymerization rates on the calculations of $\mathbf{v}_1$ and $\mathbf{v}_2$.

From Eq. (2.44), if the biosynthesis rate were to oscillate, *i.e.*, $\mathbf{v}_B$ increased with increases in fructose consumption, the oscillations observed in the glycolytic pathway flux would be damped since the increase in $\mathbf{v}_B$ would partially cancel out the contribution from increased fructose consumption. Similarly, with Eq. (2.45), an oscillating biosynthesis rate would accentuate the oscillations in citric acid cycle activity. Through closure of the acetyl-CoA balance (Eq. (2.36)),

$$\mathbf{v}_1 = \mathbf{v}_2 + \mathbf{v}_3 \,. \tag{5.2}$$

This indicates, therefore, that $\mathbf{v}_3$ and $\mathbf{v}_2$ would oscillate with periods 180° out of phase with each other, given a nearly constant $\mathbf{v}_1$.

Unfortunately, the estimates for the specific fructose consumption rate and the biosynthesis pathway flux are not independent, since the specific fructose consumption rate is back-calculated through the closure of the acetyl-CoA balance. Replacing the fructose-dependent terms in Eqs. (2.44) and (2.45) with a rearrangement of the closed acetyl-CoA balance expresses $\mathbf{v}_1$ and $\mathbf{v}_2$ in terms of carbon dioxide and PHB with the dependency of $\mathbf{v}_B$ eliminated as shown below (see Chapter 2 for nomenclature):

$$\mathbf{v}_1 = \frac{2}{3\mathbf{X}}\left[\frac{\mathbf{F}}{\mathbf{V}_1}\left(\mathbf{C}^g_{CO_2,out} - \mathbf{C}^g_{CO_2,in}\right) - \left(\frac{\mathbf{V}_2}{\mathbf{V}_1}\frac{d\mathbf{C}^g_{CO_2}}{dt} + \frac{\mathbf{C}^g_{CO_2}}{\mathbf{V}_1}\frac{d\mathbf{V}_2}{dt}\right)\right. \tag{5.3}$$
$$\left. + \frac{d\mathbf{C}^l_{CO_2}}{dt} + \frac{\mathbf{C}^l_{CO_2}}{\mathbf{V}_1}\frac{d\mathbf{V}_1}{dt} + \left(\frac{d\mathbf{C}_{PHB}}{dt} + \frac{\mathbf{C}_{PHB}}{\mathbf{V}_1}\frac{d\mathbf{V}_1}{dt}\right)\right]$$

$$\mathbf{v}_2 = \frac{2}{3\mathbf{X}}\left[\frac{\mathbf{F}}{\mathbf{V}_1}\left(\mathbf{C}^g_{CO_2,out} - \mathbf{C}^g_{CO_2,in}\right) - \left(\frac{\mathbf{V}_2}{\mathbf{V}_1}\frac{d\mathbf{C}^g_{CO_2}}{dt} + \frac{\mathbf{C}^g_{CO_2}}{\mathbf{V}_1}\frac{d\mathbf{V}_2}{dt}\right)\right. \tag{5.4}$$
$$\left. + \frac{d\mathbf{C}^l_{CO_2}}{dt} + \frac{\mathbf{C}^l_{CO_2}}{\mathbf{V}_1}\frac{d\mathbf{V}_1}{dt} - \frac{1}{2}\left(\frac{d\mathbf{C}_{PHB}}{dt} + \frac{\mathbf{C}_{PHB}}{\mathbf{V}_1}\frac{d\mathbf{V}_1}{dt}\right)\right] .$$

These equations can be simplified using familiar nomenclature in the following manner:

$$\mathbf{v}_1 = \frac{2}{3}(\mathrm{CDPR} + \mathbf{v}_3) \tag{5.5}$$

$$\mathbf{v}_2 = \frac{2}{3}\left(\mathrm{CDPR} - \frac{\mathbf{v}_3}{2}\right) . \tag{5.6}$$

Assuming that biosynthesis and PHB polymerization are 180° out of phase, conclusions similar to those reached previously are obtained. During periods of high biosynthesis activity, the specific carbon dioxide production rate will be high and $\mathbf{v}_3$ will be low. When biosynthesis activity is low, the specific carbon dioxide production rate will be low and $\mathbf{v}_3$ will be high. Translating this in terms of Eqs. (5.5) and (5.6) suggests that the oscillations in $\mathbf{v}_1$ will be damped and the oscillations in $\mathbf{v}_2$ will be enhanced because of the contribution of an oscillating PHB polymerization rate.

In Figure 5.6 the specific carbon dioxide production rate for this experiment is shown. Focusing on the second limitation period at about 14 hours, the CDPR averages 6 mmol CO_2/((g biomass)(hr)) with oscillations of approximately ±20%. In this same region in Figure 5.3b, $\mathbf{v}_3$ averages about 2 C-mmol PHB/((g biomass)(hr)). Assuming that ±20% variations can also occur in $\mathbf{v}_3$, we can calculate the peak-to-peak changes in $\mathbf{v}_1$ based on Eq. (5.5). Therefore, when the CDPR equals [6 + 0.2(6)] mmol CO_2/((g biomass)(hr)), $\mathbf{v}_3$ equals [2 − 0.2(2)] C-mmol PHB/((g biomass)(hr)). From Eq. (5.5) this gives a range of 4.8 to 5.9 C-mmol CO_2/((g biomass)(hr)) for $\mathbf{v}_1$ — almost exactly what is shown for $\mathbf{v}_1$ in Figure 5.3b. Because the CDPR is roughly three times larger

than $\mathbf{v_3}$, changes in the magnitude of the PHB polymerization/depolymerization oscillations do not dramatically influence the calculation of $\mathbf{v_1}$.

Making the same calculations and assumptions for $\mathbf{v_2}$ from Eq. (5.6), a peak-to-peak range of 2.4 to 4.3 mmol CO_2/((g biomass)(hr)) is computed. Comparing these values with $\mathbf{v_2}$ in Figure 5.3b shows virtually no differences with $\mathbf{v_2}$ calculated from Eq. (5.6).

Considering these observations, its seems reasonable to assume that the oscillations seen in $\mathbf{v_1}$ and $\mathbf{v_2}$ are fairly accurate representations of the cell's metabolic response. As a side note, these increases in the respiration, glycolysis, and citric acid cycle activities correlate with increases in culture fluorescence (Chapter 7). Therefore, as the specific fructose consumption rate increases, there is a detectable increase in intracellular NAD(P)H levels.

Unlike previous cases of nutrient limitation in which regulation of the various pathways was influenced by ATP and/or NADH levels, fructose limitation effectively regulates the cell's metabolism through availability of carbon. Under conditions of limited carbon and energy, intracellular levels of NADH, ATP, and carbon intermediates would drop as these species were consumed and only slowly replaced. Therefore, AMP, ADP, and NAD concentrations would be relatively high and phosphoenolpyruvate (PEP) levels would be low, thereby activating pyruvate kinase (PK), isocitrate dehydrogenase, and glucose-6-phosphate dehydrogenase (G6PDH) with inhibition by ATP, NADH, and PEP being relaxed.[12–15] What is rather surprising under these circumstances is that the cell slowly accumulates PHB rather than consumes it internally, particularly

since intracellular CoASH levels would be expected to be high. One possible reason may be that PHB polymerization is a relatively simple chemical synthesis, with simpler requirements in terms of precursors and needed enzymes, compared to the myriad of coordinated reactions involved with biosynthesis. A second possible reason may be based on the premise that the oscillations in v_3 could be far more dramatic than previously assumed. Under the previously discussed fructose exhaustion periods, PHB depolymerization is relatively slow compared to polymerization rates already observed. Should the PHB polymerization pathway oscillate between depolymerization and polymerization, it is conceivable that there is a net polymerization rate that is due to the relatively slow rate of depolymerization. Since PHB polymerization does continue in the presence of presumably high levels of CoASH, this suggests that another, as yet unidentified, regulatory element must influence PHB polymerization.

5.4.3 Release from Fructose Limitation and Exhaustion

As intimated earlier, the rapid increase and subsequent decrease in PHB polymerization activity suggest sluggish regulation of glycolysis and PHB polymerization. While under fructose limitation conditions, regulation of PHB polymerization is apparently relaxed to the extent that polymerization can compete successfully with biosynthesis and the citric acid cycle. With the sudden influx of carbon, biosynthesis and the citric acid cycle respond immediately, reaching maximum levels, while PHB polymerization activity apparently overshoots before being brought back in line through tighter regulation. This phenomenon

also applies to glycolysis, suggesting that the sluggish regulation is associated with glycolysis. As fructose exhaustion is approached, both $\mathbf{v}_R$ and $\mathbf{v}_2$ increase, suggesting increased demand for NADH and ATP, presumably related to fructose transport processes.

Prior to the release from limitation under restricted carbon supply conditions, inhibition of G6PDH, isocitrate dehydrogenase, and PK would be minimal because of low ATP and NADH levels, with some activation being supplied by high levels of AMP and ADP. Also carbon metabolic intermediates such as PEP would be low. With the sudden influx of fructose, all pathway fluxes return to maximal values. With G6PDH and PK activities maximized, carbon can initially travel down the glycolytic pathway at maximal rates, causing an increase in the AcCoA/CoASH ratio, ultimately leading to dramatically increased PHB polymerization. With biosynthesis, respiration, citric acid cycle, and PHB polymerization at high activity levels, it is conceivable that accumulation of NADH, ATP, and PEP does not instantaneously occur because of high rates of consumption, thereby giving the sluggish response. Glycolysis and PHB polymerization activities are finally brought in line as NADH, ATP, and PEP levels are raised to balanced growth levels and are capable of exerting adequate regulatory control. As ATP levels increase and AMP levels decrease, activation changes into inhibition with the subsequent increase in PEP levels. Simultaneously, G6PDH becomes inhibited by ATP, NADH, and PEP. Glycolysis activity decreases, allowing the AcCoA/CoASH ratio to drop, thereby reducing PHB polymerization.

5.5 CONCLUSIONS

Unlike the effects observed that are due to restriction of available ammonium or oxygen, restricting fructose does not induce a large increase in PHB polymerization, except when fructose consumption becomes unrestrained following a period of fructose limitation. Although some enhancement of PHB synthesis is observed, fructose limitation serves mainly to "scale down" *A. eutrophus*' metabolic activity. Therefore, *A. eutrophus*' response to fructose limitation is viewed as stemming more from chemical kinetic limitations rather than from the effects of intracellular regulation.

5.6 REFERENCES

1. Gottschalk, G., Eberhardt, U., and Schlegel, H.G., *Arch. Mikrobiol.*, **48**, 95 (1964).
2. Schlegel H.G., Gottschalk G., and Bartha R., *Nature*, **191**, 463 (1961).
3. Pfennig, N., and Lippert, K.D., *Arch. Mikrobiol.*, **55**, 245 (1966).
4. Braunegg, G., Sonnleitner, B., and Lafferty, R.M., *Appl. Microbiol. Biotech.*, **6**, 29 (1978).
5. Lee, C., and Lim, H., *Biotechnol. Bioeng.*, **22**, 637 (1980).
6. Savitzky, A., and Golay, M.J.E., *Anal. Chem.*, **36**, 1627 (1964).
7. Steiner, J., Termonia, Y., and Deltour, J., *Anal. Chem.*, **44**, 1906 (1972).
8. Bowien, B., and Schlegel, H.G., *Ann. Rev. Microbiol.*, **35**, 405 (1981).
9. Lehninger, A.L., *Principles of Biochemistry*, Worth Publisher, Inc., New York, New York (1982).
10. Oeding, V. and Schlegel, H.G., *Biochem. J.*, **134**, 239 (1973).
11. Senior, P.J. and Dawes, E.A., *Biochem. J.*, **134**, 225 (1973).
12. Glaeser, H. and Schlegel, H.G., *Arch. Mikrobiol.*, **86**, 327 (1972).
13. Blackkolb, F. and Schlegel, H.G., *Arch. Mikrobiol.*, **63**, 177 (1968).
14. Wilke, D. and Schlegel, H.G., *Arch. Microbiol.*, **105**, 109 (1975).

15. Tunail, N. and Schlegel, H.G., *Biochem. Biophys. Comm.*, **49**, 1554 (1972).

16. Haywood, G.W., Anderson, A.J., Chu, J., and Dawes, E.A., *FEMS Microbiol. Lett.*, **52**, 91 (1988).

17. Haywood, G.W., Anderson, A.J., Chu, J., and Dawes, E.A., *FEMS Microbiol. Lett.*, **52**, 259 (1988).

18. Haywood, G.W., Anderson, A.J., and Dawes, E.A., *FEMS Microbiol. Lett.*, **57**, 1 (1989).

CHAPTER 6

PHOSPHATE AND PHB EFFECTS

6.1 INTRODUCTION

As with the investigation of ammonium effects, reduced phosphorous availability, provided here in the form of inorganic phosphate, directly impacts the biosynthesis process with subsequent indirect effects on all other pathways. Although a rather small elemental component by weight of biomass in most bacterial systems, phosphorous is critical to the synthesis of such essential biomolecules as ATP, DNA and phospholipids. Whereas nitrogen is also included in these same molecules, phosphorous, unlike nitrogen, is not found in the primary structure of proteins, which comprise *ca* 50% of the biomass in *Alcaligenes eutrophus* H16 (unpublished result). Therefore, the availability of phophorous influences biosynthesis differently than the availability of nitrogen.

With regard to the influence on PHB polymerization, phosphorous can be expected to have a similar effect as observed with ammonium; *i.e.*, as phophorous availability limits biosynthesis, PHB polymerization rates increase. However, as the following sections will show, the effect of phosphorous availability is characteristically different, with the cells being more sensitive to apparent concentration effects than in the case of ammonium limitation.

From a biochemical engineering application standpoint, increasing growth and PHB production is a critical objective in optimizing *Alcaligenes eutrophus* H16 fermentations, particularly if these two objectives can be accomplished simultaneously. However, since PHB is stored as an intracellular polymer in the

form of distinctly visible, granular bodies, the question arises as to what impact the presence of these bodies must have on the cell's metabolism in relation to biomass synthesis, cell division, energy demand, and other characteristics, particularly as the PHB contribution to the cell dry weight increases. Although the effects of this phenomenon have been hinted at in previous chapters, we consider PHB effects here in more detail.

Using the metabolic model framework developed in Chapter 2 (Eqs. (2.41)–(2.46)), *Alcaligenes eutrophus* H16's metabolic responses to phosphate limitation, phosphate exhaustion, and high intracellular PHB concentrations are assessed in terms of changes in the biosynthesis, glycolysis, citric acid cycle, PHB polymerization, and respiratory pathway fluxes. Comparing these results with those of balanced growth and incorporating information gleaned from *in vitro* kinetic studies on key regulatory enzymes will allow us to better understand *A. eutrophus*' regulatory responses and associated influence on PHB production that are due to these three effects.

6.2 MATERIALS AND METHODS

6.2.1 Organism

Alcaligenes eutrophus H16 (ATCC 17699) was stored on nutrient broth slants with 0.5% fructose added to retain induction of the fructose catabolism enzyme system;[1] cells were restreaked every two months. During liquid cultivation, *A. eutrophus* was grown heterotrophically on media described by Schlegel

et al.[2] and micronutrient supplement described by Pfennig and Lippert.[3] Cells were grown at 31°C and pH 6.8.

6.2.2 Analytical Methods

Fructose concentrations were determined spectrophotometrically with the Boehringer Mannheim GMBH Glucose/Fructose assay kit (Cat. No. 139106). PHB was determined after the method of Braunegg *et al.*[4] Ammonium, determined as ammonium chloride, was measured by an ammonium probe (Ingold Electrodes, Inc., Series 7500). Dry weight determinations were made through the membrane filtration technique. Biomass was calculated from the difference between the dry weight and PHB concentrations.

Dissolved oxygen concentrations were determined with an Instrumentation Laboratories (IL) 531 Industrial Dissolved Oxygen monitor and an Ingold Electrodes, Inc. polarographic oxygen-sensing probe. Dissolved carbon dioxide was measured with an Ingold carbon dioxide monitor (Model 1230) using an Ingold dissolved carbon dioxide probe (Model 780). Optical density was determined at 420 nm with a Spectronic 20 (Bausch and Lomb) modified to accept the flow-cell described by Lee and Lim.[5] A Cole-Parmer pH controller (Model 5997-20) was used to measure and maintain the pH in conjunction with two Masterflex peristaltic pumps for the addition of sodium hydroxide and phosphoric acid. Off-gas carbon dioxide and oxygen concentrations were monitored with an Infrared Industries, Inc. (Santa Barbara, CA) Model # 703-075 carbon dioxide gas detector and a Leeds and Northrup 7863 thermomagnetic oxygen analyzer, respectively.

6.2.3 Fermentation System

Fermentations were conducted in an 18 liter Bioengineering AG Laboratory fermenter. The data acquisition system supplied as part of the FluroMeasure System data logged fluorescence, off-gas oxygen, off-gas carbon dioxide, pH, dissolved oxygen, and dissolved carbon dioxide. Fructose and ammonium chloride concentrations were maintained via pH-controlled addition of concentrated fructose (1000 g/l) and ammonium chloride (134 g/l) feed solutions. The dissolved oxygen concentration was regulated by a homemade controller, which manipulated the fermenter agitation rate.

6.2.4 Computation of Pathway Fluxes

Preliminary data manipulations were performed on an IBM PC. A VAX 11/780 and a MicroVAX 3500 were used to perform all smoothing, interpolations and model pathway calculations. The off-line data were smoothed and interpolated with cubic splines. On-line data were collected at rates of eight samples per minute over the course of the fermentation. Other on-line data were smoothed and derivatives calculated according to the method developed by Savitzky and Golay[6] and corrected by Steiner *et al.*[7]

6.3 RESULTS

During an experiment designed to investigate the influence of buffer capac-

ity on carbon dioxide dissolution and desorption, the effects of phosphate limitation and exhaustion were observed. Previous work has shown that *Alcaligenes eutrophus* H16 cells grown autotrophically contain 1.8% (w/w) phosphorous.[8] Assuming that this value was not corrected for PHB content and assuming that the cells contained approximately 20% PHB, the biomass composition would contain 2.3% phosphorous by weight.

In the following experiment only 5% of the normal phosphate buffer (0.34 g/l $Na_2PO_4 \cdot 6H_2O$ and 0.08 g/l KH_2PO_4) was included in the medium. Approximately 600 ml of medium containing the normal concentration of phosphate was used for the inoculum; the inoculum was then added to 12 liters of media containing no phosphate buffer. The fructose and ammonium chloride concentrations were maintained between 0.4 and 1.1 g/l and 0.95 and 1.05 g/l, respectively; dissolved oxygen was maintained at 130 mm Hg.

Assuming a final biomass concentration of 1 g/l (only a concentration of 0.8 g/l biomass was achieved in this experiment) and a negligible starting biomass concentration, approximately 0.75 mM of phosphorous would be consumed. Under normal conditions the medium composition contains 25.1 mM Na_2PO_4 and 11.0 mM KH_2PO_4 or 36.2 mM PO_4^{-3}. At 5% of the normal phosphate medium levels, this would amount to 1.8 mM phosphorous being available in the media, assuming no removal by chelation with metal ionic species. The apparent discrepancy between available phosphorous and estimated biomass-incorporated phosphorous will addressed later.

6.3.1 Phosphate Limitation and Exhaustion

Figure 6.1 relates the time evolution of the cellular components and off-gas carbon dioxide and oxygen. Over the time scales normally observed in these types of experiments (usually 15 hours), the increases in biomass and off-gas carbon dioxide and decrease in off-gas oxygen concentrations are small.

These observations are borne out in Figure 6.2. Following an apparent lag, the biosynthesis pathway ($\mathbf{v}_B$) rises to nearly a balanced growth level. This rapid recovery in the biosynthesis rate is rather surprising since the relative medium ionic strength drops approximately by a factor of 20 following inoculation. From 10 to 17 hours there is an unexpected 25% increase in $\mathbf{v}_B$. Since phosphate is the limiting nutrient, this observation implies that there is an increase in the phosphate concentration or that an improved phosphate scavenging mechanism has been induced. Because the phosphate concentration was not monitored, an increase in phosphate concentration cannot be substantiated. Although *Alcaligenes eutrophus* H16 has been shown to accumulate phosphate intracellularly, there has been no evidence presented thus far to suggest an inducible, low phosphate concentration-scavenging mechanism.[9] As the experiment draws to a close, biosynthesis activity rapidly declines, presumably because of severe phosphate limitation or phosphate exhaustion.

The trajectories of the repiratory pathway flux ($\mathbf{v}_R$), the glycolysis pathway flux ($\mathbf{v}_1$), and the citric acid cycle pathway flux ($\mathbf{v}_2$) suggest that the cells are under stress. Following the three-hour post inoculation period, each pathway flux begins at a very low value and subsequently increases to very high values,

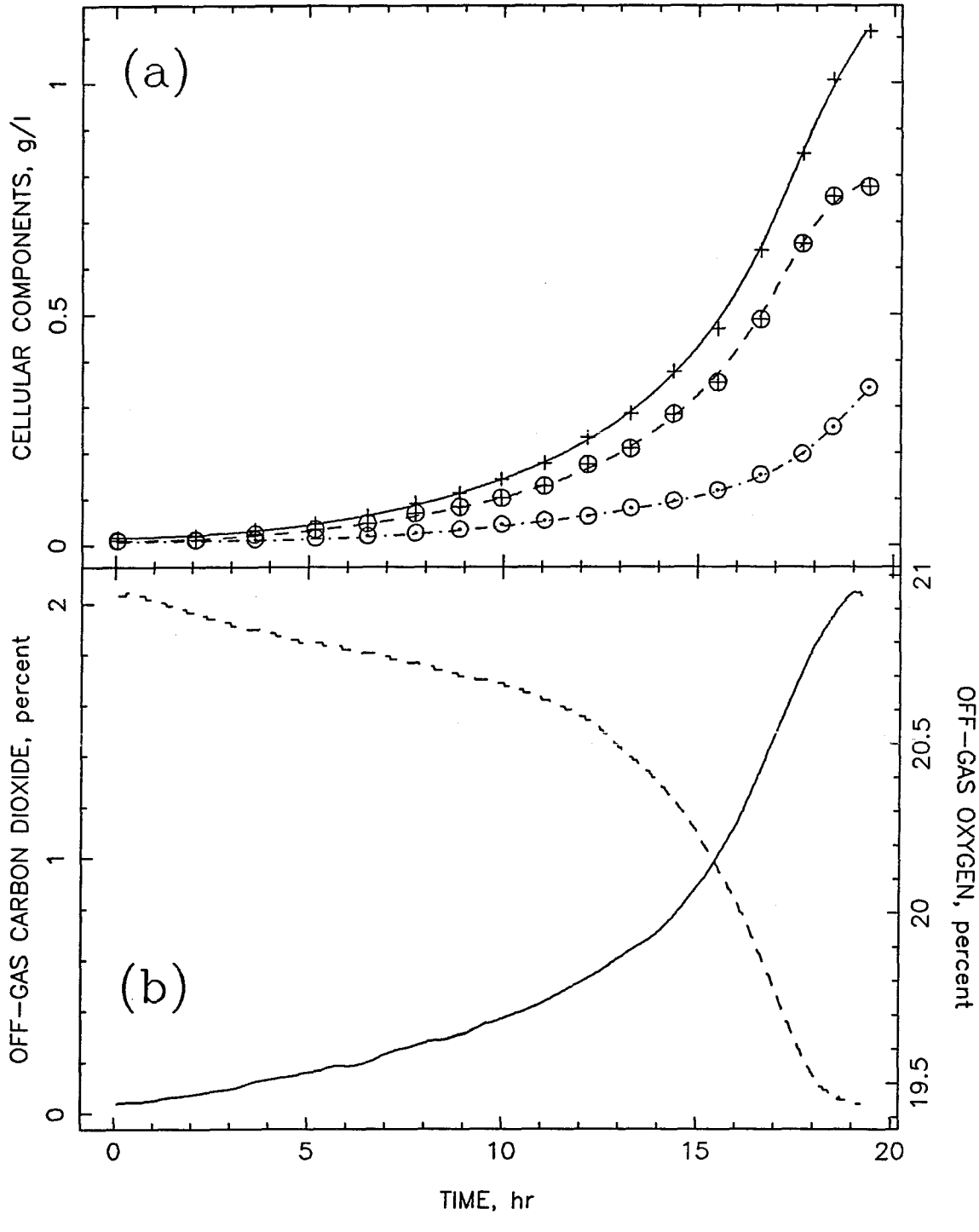

Figure 6.1: Phosphate limitation experiment: raw data. **(a)** Cell dry weight, + ; biomass, $\oplus$; PHB, $\odot$. **(b)** Off-gas carbon dioxide, ——— ; off-gas oxygen, – – – .

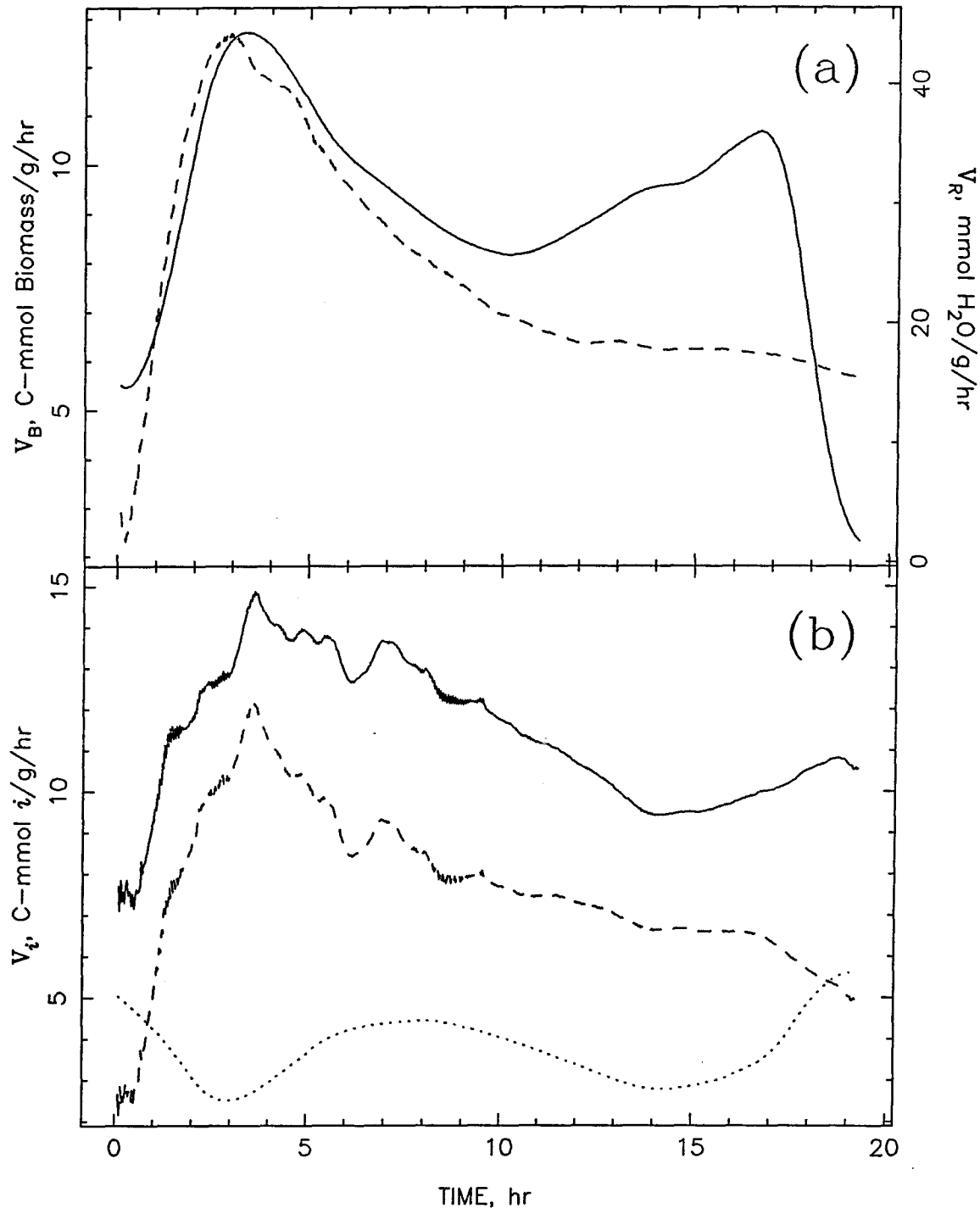

Figure 6.2: Phosphate limitation experiment: pathway fluxes. **(a)** Biosynthesis activity ($\mathbf{v}_B$), —— ; respiration activity ($\mathbf{v}_R$), – – – . **(b)** Glycolysis activity ($\mathbf{v}_1$), —— ; citric acid cycle activity ($\mathbf{v}_2$), – – – ; PHB polymerization activity ($\mathbf{v}_3$), ····· .

particularly in the case of $\mathbf{v}_R$. In light of the way the fermenter medium and inoculum were prepared, these dramatic changes in pathway fluxes may well be a response to osmotic shock. Particularly in the case of $\mathbf{v}_R$, oxygen is consumed at such a high rate as to suggest decoupling of the electron transport chain. As the experiment progresses, all three of these pathways decrease to approximately balanced growth levels values around 14 hours, suggesting that the cells have sufficiently adapted to the low ionic environment to the extent that balanced growth is approached, although biosynthesis activity is still low.

Focusing upon the PHB polymerization pathway flux ($\mathbf{v}_3$) in Figure 6.2b, PHB polymerization activity averages *ca* 50% above balanced growth values through most of the experiment. As other nutrient limitation experiments have shown, high PHB polymerization is a good indicator of unbalanced growth conditions. At about the time $\mathbf{v}_R$, $\mathbf{v}_1$, and $\mathbf{v}_2$ drop to balanced growth levels, $\mathbf{v}_3$ follows suit. As seen in the case of ammonium exhaustion, as biosynthesis activity drops, PHB polymerization increases, implying that phosphate is exhausted.

The initial drop in $\mathbf{v}_3$ is probably due to the high PHB/biomass ratio, and possibly osmotic shock, at the beginning of the experiment (Figure 6.3). As the PHB/biomass ratio reaches about 0.4, $\mathbf{v}_3$ increases, which has the effect of opposing reduction of the PHB/biomass ratio. This supports a previous supposition that the intracellular PHB level is metabolically regulated relative to the existing extracellular growth conditions. As time passes, the PHB/biomass ratio does decrease slightly as balanced growth conditions are approached but increases strongly as biosynthesis declines because of increased PHB polymerization activity and reduced biomass synthesis.

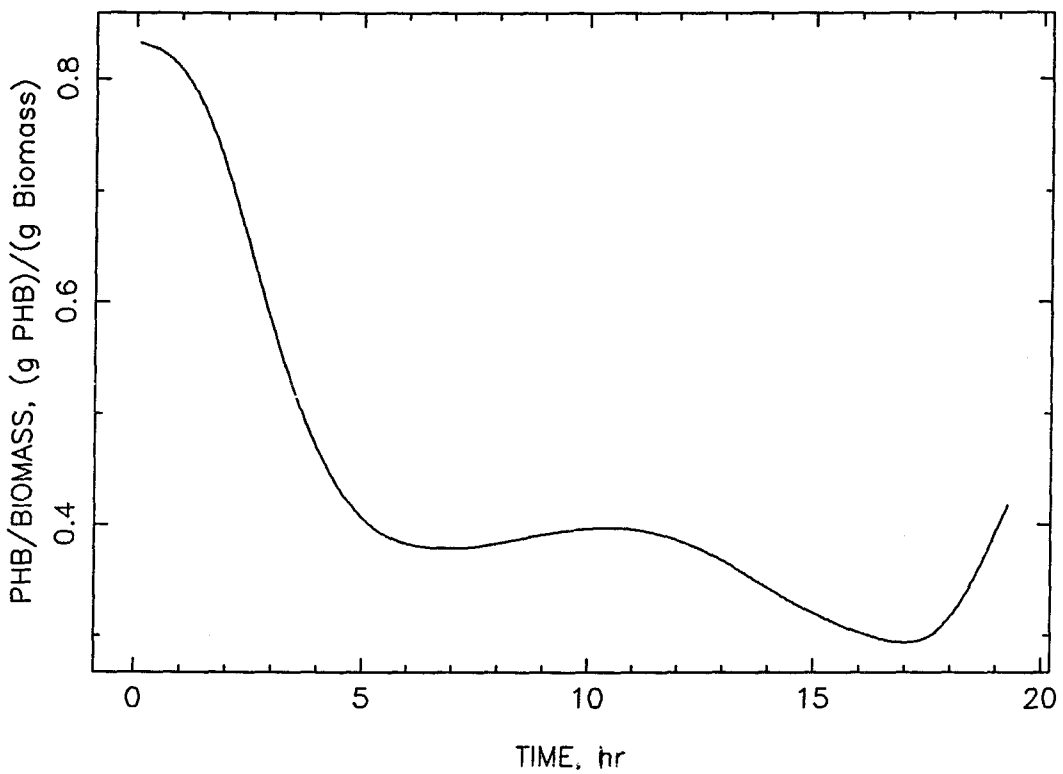

Figure 6.3: Phosphate limitation experiment: ratio of PHB to biomass.

The fructose consumption rate normalized by biomass (FCR) and its distribution among the carbon pathways are depicted in Figure 6.4. During the apparent response to osmotic shock, the cells consume fructose at a relatively high rate, perhaps in an effort to restore disrupted ionic gradients. As most of the pathway fluxes decline to balanced growth levels around 14 hours, the FCR mirrors this change in overall metabolic activity, dropping sharply as biomass synthesis falls off.

As Figure 6.4b demonstrates, fructose demand is largely needed for energy generation in the citric acid cycle; unlike previous nutrient limitation cases, the usual relative fructose consumption by biosynthesis and by the citric acid cycle is inverted. Consequently, fructose consumption in the biosynthesis and PHB polymerization pathways are nearly equal.

6.3.2 Inhibition of Growth by PHB

Besides nutrient limitation, high intracellular PHB concentrations also appear to be inhibitory to cell growth. The previous example may be construed as evidence of this effect, if the apparent phosphate limitation and osmotic shock are ignored, since the biosynthesis rate increases noticeably after the PHB/biomass ratio decreases below 0.4. Evidence for the influence of high intracellular PHB concentration on growth is presented from the following experiment: An ammonium-limited inoculum possessing a high PHB/biomass ratio was used to initiate a fermentation. The fructose and ammonium chloride concentrations were maintained between 4 and 6 g/l fructose and 0.3 and 0.42

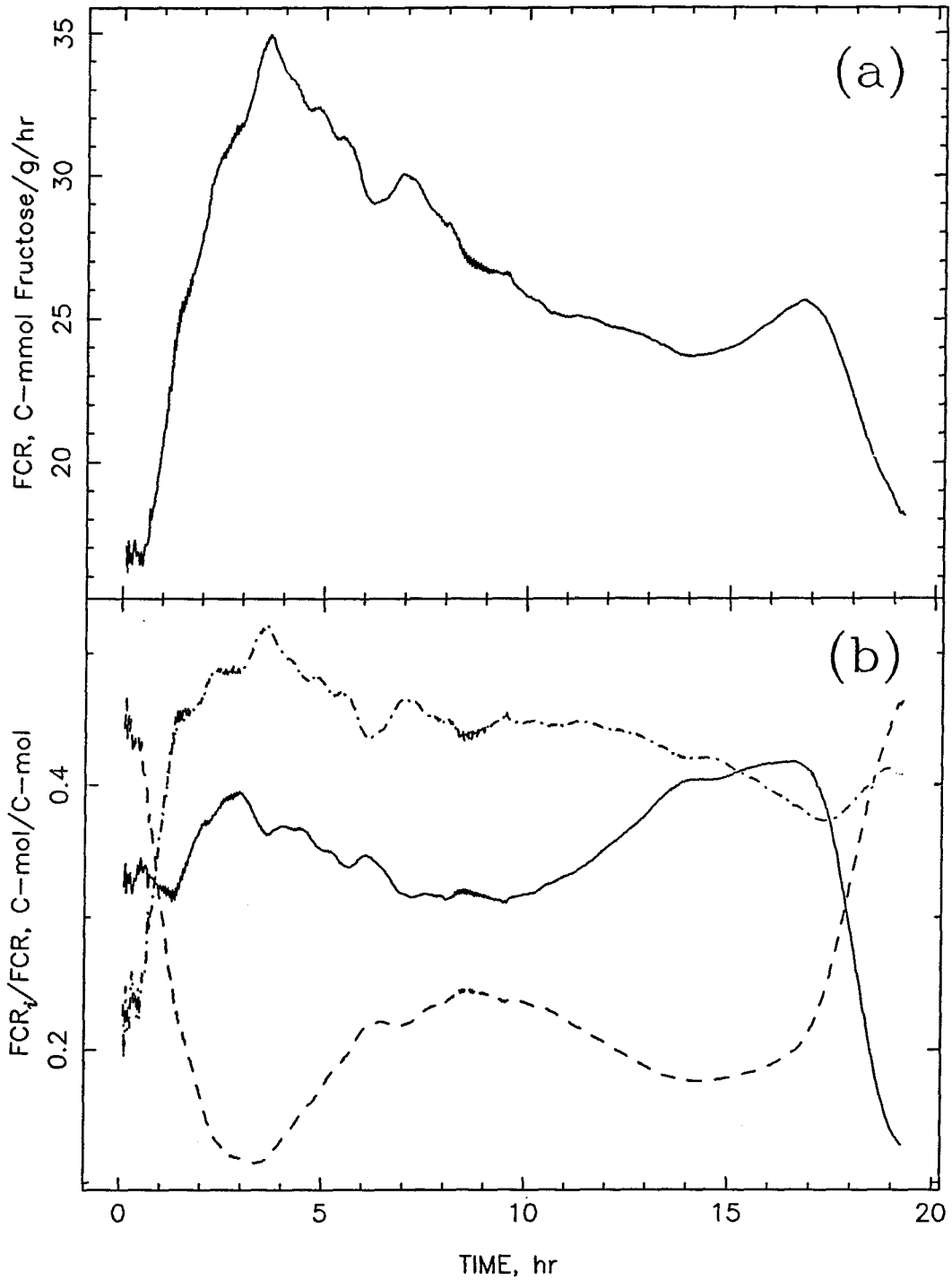

Figure 6.4: Phosphate limitation experiment: specific fructose consumption rate (FCR) and partitioning of fructose between terminal carbon pathways. **(a)** Specific fructose consumption rate (FCR). **(b)** Fraction of fructose directed to biosynthesis (FCR_B/FCR), ——— ; fraction of fructose directed to the citric acid cycle (FCR_2/FCR), — · — · ; fraction of fructose directed to PHB polymerization (FCR_3/FCR), — — — .

TABLE 6.1: Time evolution of pathway fluxes for high PHB/biomass growth

Balanced Pathways* (PHB/biomass)	PATHWAY FLUXES 7 Hours (0.72)	9 Hours (0.54)	11 Hours (0.37)	13 Hours (0.27)
v_B	6.3	7.1	9.1	11.7
v_R	22.0	20.7	19.2	17.9
v_1	5.6	6.6	7.6	7.7
v_2	4.0	5.4	6.1	5.5
v_3	1.6	1.2	1.5	2.2

*Pathway fluxes, v_i, expressed as (C-)mmol product/((g biomass)(hr)).

TABLE 6.2: Time evolution of metabolic parameters for high PHB/biomass ratios

Metabolic Ratios* (PHB/biomass)	RATIO VALUES 7 Hours (0.72)	9 Hours (0.54)	11 Hours (0.37)	13 Hours (0.27)
FCR	15.0	17.0	21.0	23.0
FCR_B/FCR	0.43	0.42	0.46	0.51
FCR_2/FCR	0.40	0.51	0.57	0.35
FCR_3/FCR	0.16	0.10	0.11	0.14
CDPR	6.8	8.8	9.9	9.3

*Abbreviations: FCR, specific fructose consumption rate [(C-mmol fructose)/((g biomass)(hr))]; FCR_i, specific fructose consumption rate due to the i^{th} pathway [(C-mmol fructose)/((g biomass)(hr))]; CDPR, specific carbon dioxide production rate [(mmol CO_2)/((g biomass)(hr))].

g/l NH_4Cl, respectively, and the dissolved oxygen concentration was maintained above 100 mm Hg.

At seven hours after inoculation, it was assumed that the cells were suf-

ficiently acclimated, *i.e.*, beyond lag phase, and were uninhibited by any other factors aside from the effect of a high intracellular PHB concentration. Table 6.2 describes the time evolution of the various metabolic pathway fluxes at two hour time increments. At the same time increments, Table 6.2 presents the FCR, fructose partitioning among the terminal carbon pathways, and the specific carbon dioxide production rate (CDPR).

Unlike previous examples, *i.e.*, release from ammonium exhaustion (Chapter 3), PHB is not depolymerized as the cells grow. Only after the seven-hour PHB/biomass ratio has been reduced by over 60% at 13 hours does the PHB polymerization activity rise to balanced growth levels. Except for $\mathbf{v}_R$, all pathway fluxes are below balanced growth levels but do generally increase with time as intracellular PHB reserves are effectively "diluted" by biomass increases. $\mathbf{v}_R$ decreases with time, suggesting that there exists, initially, a large demand for nonbiosynthetic-associated energy. Even at a PHB/biomass ratio of 0.27 g PHB/g biomass, biosynthesis is still 15% below balanced growth levels. As observed in the previous case of phosphate limitation, a larger fraction of fructose is consumed in the citric acid cycle than the biosynthesis pathway at nine and 11 hours, presumably to meet the high respiratory NADH demand needed for high intracellular PHB growth.

6.4 DISCUSSION

6.4.1 Phosphate Limitation and Exhaustion

The dramatic rise in respiratory activity and associated increases in glycolysis and citric acid cycle activities upon exposure to the lower ionic strength medium indicate the cells' need to generate ATP following the metabolic disruption caused by osmotic shock. It is unclear whether the cells are producing large amounts of ATP for biosynthesis in the presence of low phosphate, attempting to restore and maintain favorable ionic gradients or whether the ionic gradients have been disturbed to the extent that the respiratory efficiency is greatly reduced. Whatever the case may be, there is wholesale consumption of citric acid cycle-produced NADH, necessitating high citric acid cycle activity with associated elevation of glycolysis activity.

Under these conditions it is not surprising that PHB polymerization proceeds at a moderately high level. In a sense, the response of the *A. eutrophus* cells is analogous to that observed during the release from fructose limitation (Chapter 5). The difference here is that ATP levels appear never to increase quite to the extent that inhibition of glycolysis occurs. And with fructose available, glycolysis and the citric acid cycle may function at maximal rates.

There is some question as to the level of NADH within the cell. It is likely that NADH levels are low, given the high respiration rate. If, on the other hand, NADH levels are high, NADH inhibition of isocitrate dehydrogenase must be successfully nullified by the levels of AMP and ADP.[10] Increased activity of

glycolysis has been observed before under high NADH conditions, specifically, for ammonium limitation. If the level of phosphoenolpyruvate (PEP) is low, glucose-6-phosphate dehydrogenase is uninhibited, further indicating that glycolysis is operating at maximal levels.[11,12] Since pyruvate kinase is inhibited by ATP with subsequent elevation of PEP levels, this serves as further evidence of low intracellular ATP levels.[13]

In the release from fructose limitation case, it was conjectured that glycolysis activity was sufficient to meet the demands of the citric acid cycle and maintain a high AcCoA/CoASH ratio adequate to support PHB polymerization at the observed level, thereby relieving CoASH inhibition of β-ketothiolase.[14,23] Apparently, this same phenomenon occurs under phosphate limitation.

With the phosphate buffering capacity reduced by a factor of 20 relative to the normal medium composition, maintenance of a tight pH control range proved difficult because of the medium's increased pH sensitivity to sodium hydroxide additions. However, the pH control fluctuations that are due to overshoot effectively shrank 50% over the course of the experiment (not shown). Previous work with this system indicated that the improved buffering capacity was due to an increase in solvated carbon dioxide species, predominantly carbonate and bicarbonate. In discussions with fellow researchers,[15,16] it was suggested that phosphate is capable of coordinately binding with metal species in solution, especially magnesium. Further investigation revealed that carbonate has approximately the same, although somewhat less, coordination affinity for magnesium as phosphate.[17,18] Using the appropriate equilibrium constants and expressions and noting that incorporation of magnesium into biomass is more than a factor

of three less than phosphorous[8] (and magnesium is not accumulated), it is possible to demonstrate an increase in unchelated, "free" phosphate levels with increasing levels of (bi)carbonate, particularly if the total phosphate concentration is less than the total magnesium concentration. As the concentration of off-gas carbon dioxide increases, so does the carbonate and bicarbonate concentrations. Since (bi)carbonate is capable of partially displacing phosphate in the coordinated magnesium complex, previously unavailable phosphate is released for biosynthesis consumption as the carbon dioxide concentration increases, contributing to the observed increase in biosynthesis activity.

Arguably, there may be other mechanisms that contribute to the increase in biomass synthesis. One possibility is that the cell is slow to overcome the effects of osmotic shock. If this is indeed the case, the proposed phosphate concentration effect may be in error.

Considering a 2.3% (w/w) phosphorous contribution to biomass based on autotrophically grown cells, the initial phosphate concentration, and the final cell concentration, medium phosphate can not be exhausted solely because of its incorporation into biomass. As mentioned previously, *A. eutrophus* can store phosphate intracellularly in the form of polyphosphate.[9] Doi *et al.* investigated *A. eutrophus* storage of polyphosphate using ^{31}P NMR and found that intracellular polyphosphate synthesis was closely related to PHB polymerization.[19] Therefore, since PHB synthesis is, on average, higher than balanced growth levels, intracellular accumulation of polyphosphate may promote the unexpected early phosphate exhaustion. Kaltwasser has shown that *A. eutrophus* is capable of sustaining growth on polyphosphate.[20] Had the experiment been continued

further, this may have been observed. However, the drop in biosynthesis activity may indicate, as observed in the case of fructose exhaustion, that growth sustained by consumption of intracellular reserves is considerably slower compared to utilization of extracellular sources.

6.4.2 PHB Inhibition of Growth

With relatively high respiratory activity and relatively low biosynthesis activity, it is unclear where the ATP produced is being consumed. Certainly this would create a high level of ATP within the cell, unless the respiratory pathway is operating inefficiently, which would imply inhibition of glucose-6-phosphate dehydrogenase, pyruvate kinase and isocitrate dehydrogenase.[10-13] If pyruvate kinase is inhibited, this suggests that PEP also inhibits glucose-6-phosphate dehydrogenase. If glucose-6-phosphate dehydrogenase is inhibited by PEP, according to Figure 2.1, ATP levels must be very high, since NADH levels must be low because of high respiration and low citric acid cycle activities; ATP is the only known effector besides inorganic phosphate capable of regulating pyruvate kinase.[13] PHB depolymerization would be expected, however, since acetoacetyl-CoA reductase is inhibited by NAD[21,22,24], and hydroxybutyrate dehydrogenase inhibition is relieved because of low NADH levels, although pyruvate and, most likely, oxaloacetate levels may be high enough to counter relaxation of NADH inhibition.[22] With glycolysis inhibited and the citric acid cycle dominating fructose catabolism, the citric acid cycle must be consuming most of the acetyl-CoA, thereby keeping the AcCoA/CoASH ratio low and restricting PHB polymerization.

As time progresses, respiration activity decreases and the rates of the other carbon pathways increase, suggesting that indeed the ATP concentration is directing regulation within the cell. As mentioned previously, restriction of biosynthesis is most probably due to the physical presence of large, intracellular PHB granules, although there may be other regulatory elements present that are not known.

6.5 CONCLUSIONS

Given the limited data presented here, it appears that the use of low phosphate concentrations is a possible technique through which growth and relatively high levels of PHB synthesis may be obtained. Unfortunately, the inhibitory effects of high PHB concentrations may limit the usefulness of this approach.

6.6 REFERENCES

1. Gottschalk, G., Eberhardt, U., and Schlegel, H.G., *Arch. Mikrobiol.*, **48**, 95 (1964).
2. Schlegel H.G., Gottschalk G., and Bartha R., *Nature*, **191**, 463 (1961).
3. Pfennig, N., and Lippert, K.D., *Arch. Mikrobiol.*, **55**, 245 (1966).
4. Braunegg, G., Sonnleitner, B., and Lafferty, R.M., *Appl. Microbiol. Biotech.*, **6**, 29 (1978).
5. Lee, C., and Lim, H., *Biotechnol. Bioeng.*, **22**, 637 (1980).
6. Savitzky, A., and Golay, M.J.E., *Anal. Chem.*, **36**, 1627 (1964).
7. Steiner, J., Termonia, Y., and Deltour, J., *Anal. Chem.*, **44**, 1906 (1972).
8. Volova-Kesler, T.G., and Gladchenko, I.A., *Microbiology*, **46**, 212 (1979).
9. Dawes, E.A., and Senior, P.J., *Adv. Microb. Physiolog.*, **10**, 135 (1973).
10. Glaeser, H., and Schlegel, H.G., *Arch. Mikrobiol.*, **86**, 327 (1972).
11. Blackkolb, F., and Schlegel, H.G., *Arch. Mikrobiol.*, **63**, 177 (1968).
12. Tunail, N., and Schlegel, H.G., *Biochem. Biophys. Comm.*, **49**, 1554 (1972).
13. Wilke, D., and Schlegel, H.G., *Arch. Microbiol.*, **105**, 109 (1975).
14. Oeding, V., and Schlegel, H.G., *Biochem. J.*, **134**, 239 (1973).
15. David Malerba, private communication.

16. Gerald Wuenschell, private communication.

17. Havel, J., and Högfeldt, E., *Chemica Scripta.*, **5**, 164 (1974).

18. Riesen, W., Gamsjäger, H., and Schindler, P., *Chimia*, **23**, 186 (1969).

19. Doi, Y., and Kawaguchi, Y., Nakamura, Y., and Kunioka, M., *Appl. Environ. Microbiol.*, **55**, 2932 (1989).

20. Kaltwasser, H., *Arch. Mikrobiol.*, **41**, 282 (1962).

21. Saito, T., Fukui, T., Ikeda, F., Tanaka, Y., and Tomita, K., *Arch. Microbiol.*, **114**, 211 (1977).

22. Senior, P.J., and Dawes, E.A., *Biochem. J.*, **134**, 225 (1973).

23. Haywood, G.W., Anderson, A.J., Chu, J., and Dawes, E.A., *FEMS Microbiol. Lett.*, **52**, 91 (1988).

24. Haywood, G.W., Anderson, A.J., Chu, J., and Dawes, E.A., *FEMS Microbiol. Lett.*, **52**, 259 (1988).

CHAPTER 7

CULTURE FLUORESCENCE IN *Alcaligenes eutrophus* H16 FERMENTATIONS

7.1 INTRODUCTION

Application of culture fluorescence to a wide range prokaryotic[1-4] and eukaryotic[5] fermentations has provided an interesting technique through which an organism's metabolism can be further investigated. Aside from providing a qualitative indication of the cell's internal metabolic state, culture fluorescence adds yet another tool to the biotechnologist's rapidly expanding array of process monitoring and controlling techniques.

In situ culture fluoresence allows for the noninvasive investigation of a microorganism's internal metabolic state. Since most of the culture fluorescence signal is related to the presence and concentration of reduced nicotinamide adenine dinucleotides,[6] NADH and NADPH, the key reducing sources within virtually all living beings, culture fluorescence provides a quick and direct method of assessing the cell's metabolic state under a wide range of fermentation conditions. Although not quantitative such as direct but slow and tedious chemical techniques with questionable reliability, culture fluorescence gives virtually immediate results without disturbing the process or requiring sampling. *In situ* culture fluorescence detects metabolic fluctuations that can transpire on the order of seconds. Such fluctuations are either belatedly or entirely undetected by other more traditional monitoring techniques.

Culture fluorescence has received much attention as an indicator of biomass concentration and cell growth.[3,4,6] On occasion this has been extended to in-

corporate the use of fluorescence as a method of determining nutrient feeding schemes.[7] Culture fluorescence has also been used to examine the metabolic response of organisms to changing growth conditions that impact the organism's metabolic regime.[4,5,8,9] The behavior of synchronized *S. cerevisiae* H1022 cultures has been highly elucidated; culture fluorescence fluctuations have been correlated with metabolic shifts between glucose-repressed and derepressed states as well as with budding behavior.[5] As a way of confirming the sensitive nature of the culture fluorescence signal, respiratory decouplers[10] and iodoacetate[6] have been used to demonstrate the direct relationship between the NAD(P)H pool and observed culture fluorescence. It is this ability to monitor a cell's internal metabolic response to an externally applied environment that gives the study of culture fluorescence its greatest value.

Culture fluorescence has previously been applied to a related *A. eutrophus* strain for a means of confirming the relationship between cellular biomass concentration and culture fluorescence.[11] In this work we extend the application of culture fluorescence to encompass a broad range of *Alcaligenes eutrophus* H16 fermentation conditions, focusing on how changes in nutrient levels influence the observed culture fluorescence and how culture fluorescence is associated with the changes observed in the *A. eutrophus* cell's metabolic activities. Byrom[12] notes, as have numerous other investigators, that an increase in PHB production occurs under unbalanced growth conditions. Typically enhanced PHB synthesis above constituitive levels occurs when intracellular NAD(P)H/NAD(P) and AcCoA/CoASH ratios increase relative to their balanced exponential growth values. Therefore, culture fluorescence is ideally suited for investigating this re-

lationship as well as for understanding other regulatory features of *A. eutrophus*' NAD(P)H pool.

In the course of investigating the intrinsic metabolic characteristics of *A. eutrophus*, the use of culture fluorescence as an indicator of changes in NAD(P)H levels was found to provide new insights relative to observed metabolic fluctuations and fermentation parameter relationships, especially as it related to the regulation of PHB polymerization. In particular, specific fluorescence and a new parameter, μ_{NFU}, were found to correlate strongly with intrinsic PHB levels and increases in PHB production levels, respectively; μ_{NFU} has potential as a useful on-line monitoring parameter.

7.2 APPLICATION TO *A. eutrophus* FERMENTATIONS

In principle, culture fluorescence is the detection of NAD(P)H and all other fluorophores present with fluorescent excitation and emission properties similiar to NAD(P)H. Unfortunately, numerous factors influence the ability to quantify the culture fluorescence signal. Past work has identified that culture fluorescence is influenced by temperature, pH, agitation and aeration.[6] Also, as the cell concentration changes, the effective optical length, the distance the incident light can penetrate the culture broth, changes. The inner filter effect and quenching also influence the perceived fluorescence signal.[13] Nonfluorescent species can attenuate the culture fluorescence signal because of nonproductive absorption of the incident excitation light or absorption of the resultant emitted fluorescent

light. Fluorophores with absorption and emission spectra similiar to NAD(P)H can also contribute to the total culture fluorescence detected. Finally, NAD(P)H can decrease its own fluorescent emissions through self-absorption caused by nonproductive excitation light collisions resulting from energy transfer through other mechanisms such as bimolecular collisions. As other researchers have shown, changes in culture fluorescence correlate with changes in NAD(P)H. Unfortunately, because of the aforementioned reasons, quantification of culture fluorescence as an absolute measure of NAD(P)H is not possible because of culture fluorescence's complex, composite nature.

With regard to *A. eutrophus*, culture fluorescence correlates strongly with the cell's metabolic response to various degrees of metabolic stress, particularly under unbalanced growth circumstances involving nutrient limitation or nutrient exhaustion. These same conditions, in the presence of excess carbon, give rise to increased PHB production.

Metabolically speaking, unbalanced growth occurs under conditions in which a key biosynthetic element or metabolic energy is unavailable or is available only at suboptimal levels. Under these types of circumstances, *A. eutrophus*' metabolism is generally diverted from its balanced, biosynthetic regime to one favoring increased PHB production in the presence of an abundant carbon source. For example, in the case of biosynthetic nutrient limitation, the cell has energy resources available but cannot fully utilize them because biosynthesis is restricted. Carbon flowing through the glycolytic pathway and on to the citric acid cycle creates an abundance of NAD(P)H that cannot be consumed

in biosynthesis or respiration. The NAD(P)H pool increases, leading to feedback regulation of the citric acid cycle at isocitrate dehydrogenase.[14] This, in turn, raises the acetyl-CoA/CoASH ratio, relieving CoASH inhibition of β-ketothiolase[15,16,36], and increases PHB synthesis. Subsequently, an increase in NAD(P)H levels increases the culture fluorescence signal at the same time PHB synthesis increases. Therefore, from an intrinsic metabolic viewpoint, there is a strong correlation between the increase in culture fluorescence, as dictated by the increase in NAD(P)H levels, and the increase in PHB production.

In the following sections, the effects of varying levels of ammonium, fructose, and oxygen are investigated from the perspective of culture fluorescence, which serves as an indicator of changes in NAD(P)H levels reflective of the cellular response to these conditions. Also, a brief aside is made to highlight culture fluorescence's applicability as a process monitor and detector of abnormal fermentation states.

7.3 MATERIALS AND METHODS

7.3.1 Organism

Alcaligenes eutrophus H16 (ATCC 17699) was stored on nutrient broth slants with 0.5% fructose added to retain induction of the fructose catabolism enzyme system;[17] cells were restreaked every two months. During liquid cultivation, *A. eutrophus* was grown heterotrophically on media described by Schlegel

et al.[18] and micronutrient supplement described by Pfennig and Lippert.[19] Cells were grown at 31°C and pH 6.8. Agitation and aeration rates, fructose and ammonium chloride concentrations varied between experiments. In cases of fructose- or ammonium-limited growth, the limiting nutrient was added to the fermenter at a steady rate. In the case of oxygen-limited growth, the agitation and aeration rates were set and held at specified levels.

7.3.2 Analytical Methods

Fructose concentrations were determined spectrophotometrically with the Boehringer Mannheim GMBH Glucose/Fructose assay kit (Cat. No. 139106). PHB was determined after the method of Braunegg *et al.*[20] Ammonium, determined as ammonium chloride, was measured by an ammonium probe (Ingold Electrodes, Inc., Series 7500). Dry weight determinations were made through the membrane filtration technique. Biomass was calculated from the difference between the dry weight and PHB concentrations.

Dissolved oxygen concentrations were determined with an Instrumentation Laboratories (IL) 531 Industrial Dissolved Oxygen monitor and an Ingold Electrodes, Inc. polarographic oxygen-sensing probe. Dissolved carbon dioxide was measured with an Ingold carbon dioxide monitor (Model 1230) using an Ingold dissolved carbon dioxide probe (Model 780). Optical density was determined at 420 nm with a Spectronic 20 (Bausch and Lomb) modified to accept the flowcell described by Lee and Lim.[21] A Cole-Parmer pH controller (Model 5997-20) was used to measure and maintain the pH in conjunction with two Masterflex

peristaltic pumps for the addition of sodium hydroxide and phosphoric acid. Off-gas carbon dioxide and oxygen concentrations were monitored with an Infrared Industries, Inc. (Santa Barbara, CA) Model # 703-075 carbon dioxide gas detector and a Leeds and Northrup 7863 thermomagnetic oxygen analyzer, respectively.

7.3.3 Fluorescence Probe

The culture fluorescence probe was provided by BioChem Technology, Inc. (Malvern, PA) as part of the FluroMeasure^{TM} system. All probe calibrations were performed by BioChem Technology. The nearly linear response of the probe to quinine sulfate additions is shown in Figure 7.1. Fluorescence was reported in normalized fluorescence units (NFU), a convention developed by BioChem Technology. The culture fluorescence data reported are the net difference between the observed total culture fluorescence and the measured, pre-inoculation medium background signal.

7.3.4 Fermentation System

Fermentations were conducted in an 18 liter Bioengineering AG Laboratory fermenter. The data acquisition system supplied as part of the FluroMeasure System data logged fluorescence, optical density, off-gas oxygen, off-gas carbon dioxide, pH, dissolved oxygen, and dissolved carbon dioxide. Fructose and ammonium chloride concentrations were maintained via pH-controlled additions

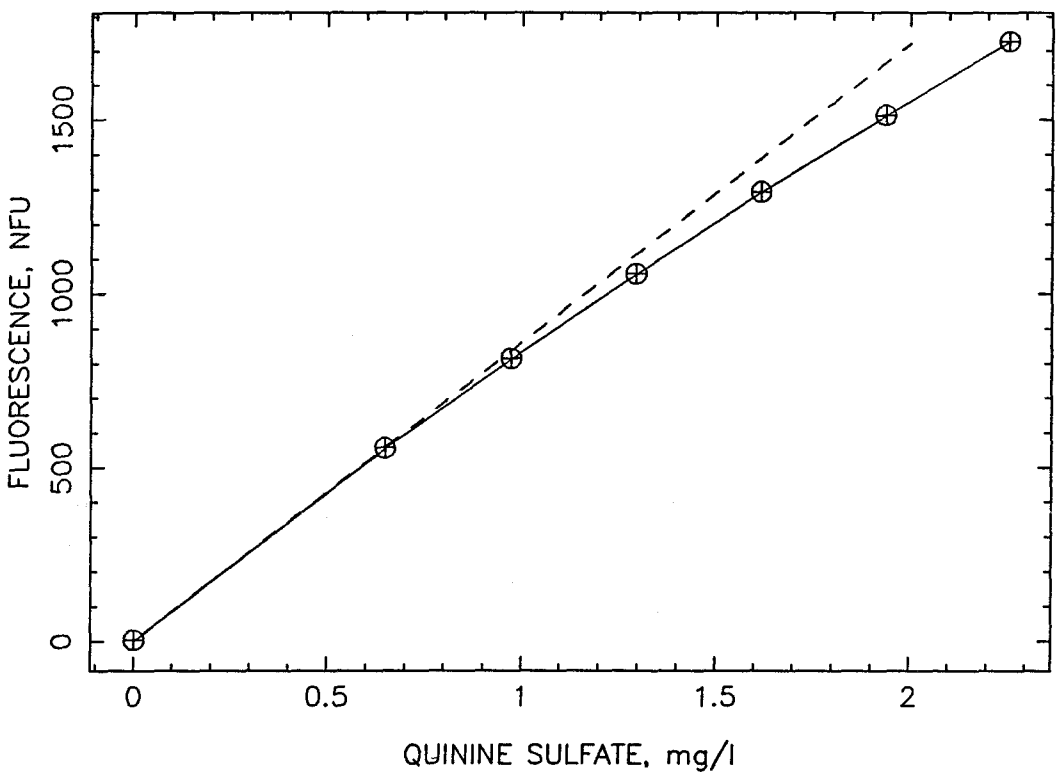

Figure 7.1: FluroMeasure^{TM} System probe's response to increasing concentrations of quinine sulfate. Fluorescence is measured in normalized fluorescence units (NFU). The dashed line provides a reference against which the nonlinear response of the culture fluorescence signal at high concentrations that is due to the inner filter effect may be compared.[13] For the majority of the examples considered, culture fluorescence is below 1000 NFU.

when constant concentrations were desired. The dissolved oxygen concentration was regulated by a homemade controller that manipulated the fermenter agitation rate.

7.3.5 Data Manipulation

The off-line data were smoothed and interpolated with cubic splines. On-line data were collected at rates of two to eight samples per minute over the course of each fermentation. Culture fluorescence data as well as all other on-line data were smoothed and derivatives calculated according to the method developed by Savitzky and Golay[22] and corrected by Steiner *et al.*[23]

7.4 AMMONIUM EFFECTS

7.4.1 Ammonium Exhaustion

Groom *et al.*[11] investigated the culture fluorescence of *A. eutrophus* ATCC 17697 under batch growth conditions. The cells were allowed to grow until biosynthesis was terminated by the exhaustion of the nitrogen source. The cell dry weight continued to increase because of the production of PHB in the presence of abundant fructose. From their work Groom *et al.* concluded that culture fluorescence correlated linearly with cell dry weight or total biomass (Biomass was considered to be comprised of all cellular components and PHB, or residual biomass and PHB). In their discussion they failed to recognize the

change in the slope of the culture fluorescence signal trajectory at the point of nitrogen exhaustion. Also, the residual biomass continued to increase an additional 50% after ammonium exhaustion and cessation of protein production; intracellular PHB content accounted for only 40% of the total dry weight. These results seem to contradict previously published results on the effect of ammonium exhaustion.[24]

In their work, Groom *et al.* made two significant observations. Throughout the duration of their experiments, the cell-free supernatant contributed only 20% to the total observed culture fluorescence. Unfortunately, their medium contained a small amount of yeast extract, thereby opening the possiblity of undefined medium components being metabolized into absorbing or fluorescing entities over and above those produced in our experiments. In analyzing the cell-free extract, they did not chemically detect the presense of NAD(P)H.

An ammonium exhaustion experiment similar in nature to Groom *et al.*'s was conducted. The initial ammonium concentration was 0.2 g/l ammonium chloride. The fructose concentration was maintained between 7 and 3.7 g/l during growth and between 4 and 0.7 g/l during PHB storage; fructose levels were controlled by occasional pulses of an 800 g/l fructose solution. As the fermentation progressed, the ammonium concentration was maintained by pH-controlled additions of ammonium hydroxide. The ammonium concentration rose slightly because of the pH contribution of increasing dissolved carbon dioxide levels. At *ca* 12 hours, the ammonium hydroxide solution was replaced by a sodium hydroxide solution for pH control. The ammonium concentration subsequently fell and was exhausted at *ca* 13 hours.

In order to ascertain if culture fluorescence can be used to detect *A. eutrophus*' metabolic response to the ammonium exhaustion growth/storage transition under different fermentation conditions, a fermentation similar to the first ammonium exhaustion experiment was conducted. Conditions were essentially identical except that the starting ammonium concentration was 0.92 g/l ammonium chloride (no subsequent ammonium hydroxide additions), and the agitation and aeration rates were held at constant values such that growth became limited by the oxygen mass transfer rate. The fructose concentration was maintained between 3 and 7.6 g/l by occasional additions of a 625 g/l fructose solution.

7.4.1.1 Results. Figure 7.2 illustrates temporal changes in fluorescence, ammonium, biomass, cell dry weight, PHB, and off-gas carbon dioxide and oxygen concentrations for the first ammonium exhaustion experiment. Ammonium exhausts at *ca* 13 hours. After 13 hours the increase in cell dry weight is due solely to PHB accumulation. The decrease in the carbon dioxide off-gas concentration and the increase in the oxygen off-gas concentration following ammonium exhaustion confirm cessation of biosynthesis.

Focusing upon culture fluorescence (Figure 7.2a), the signal increases exponentially until ammonium exhaustion. At the transition between growth and the PHB polymerization, the fluorescence trajectory changes abruptly, proceeding for the duration of the experiment at a smaller slope. However, even though ammonium is exhausted at *ca* 13 hours, it is not until nearly 15 hours that this metabolic change manifests itself in the culture fluorescence response.

This shift in the cell's metabolic regime is clearly elucidated in Figure 7.3, which describes the normalized rate of increase in fluorescence, μ_{NFU} (time

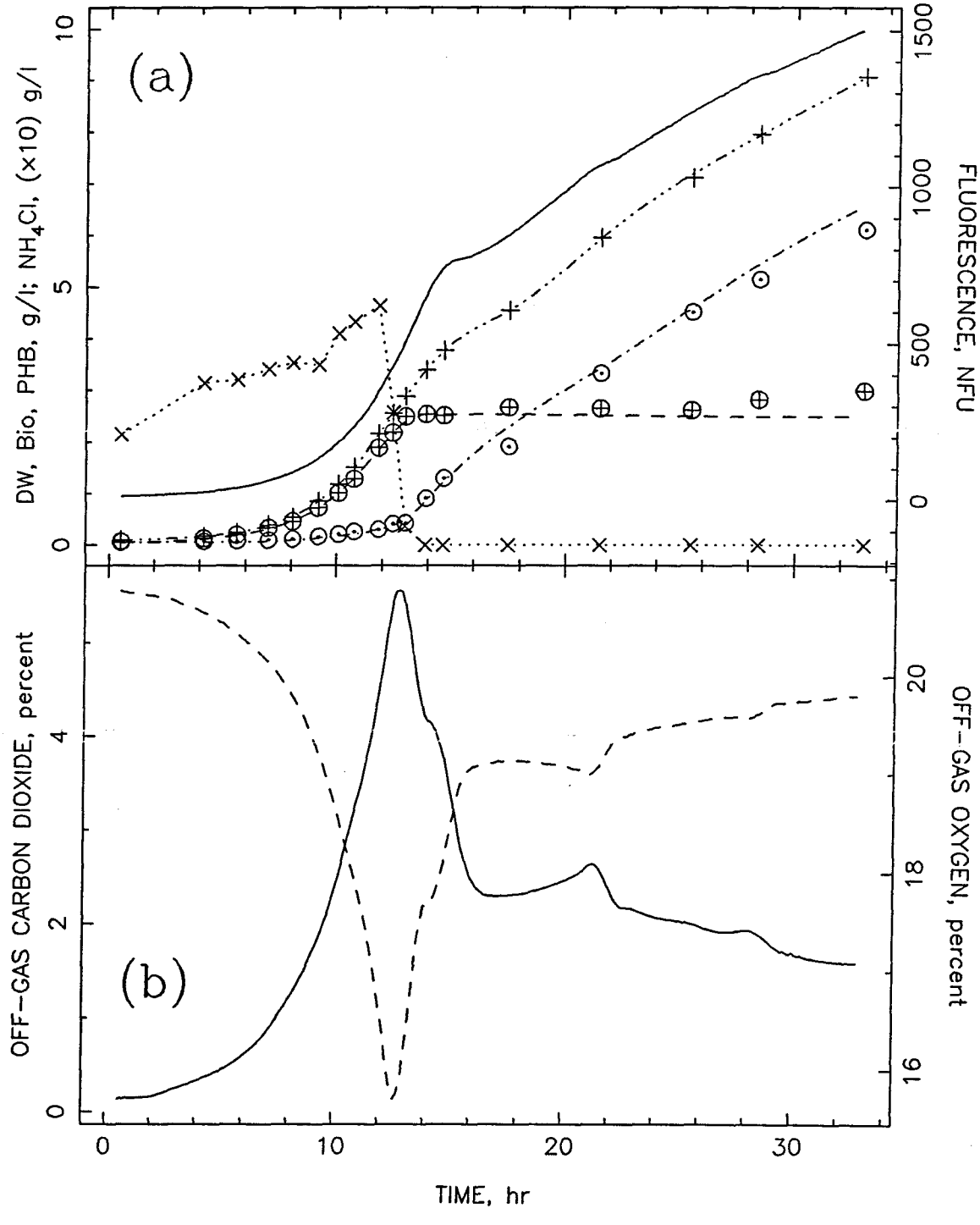

Figure 7.2: Ammonium exhaustion experiment: raw data. **(a)** Culture fluorescence, ——— ; cell dry weight, + ; biomass, ⊕ ; PHB, ⊙ ; ammonium chloride [(×10) g/l], × . **(b)** Off-gas carbon dioxide, ——— ; off-gas oxygen , – – – .

derivative of fluorescence normalized by fluorescence). Prior to ammonium exhaustion μ_{NFU} averages between 0.3 and 0.36 hr^{-1}, approximately equal to *A. eutrophus'* specific growth rate. After ammonium exhaustion, μ_{NFU} drops to 0.06, decreasing thereafter. Unlike the culture fluorescence response, the shift in μ_{NFU} is clearly evident, beginning at 12 hours.

As Groom *et al.*[11] observed, culture fluorescence correlates very closely with cell dry weight (Figure 7.4a). Since the change in dry weight during growth is dominated by increases in biomass and changes in dry weight during PHB storage phase are dominated by PHB increases, this implies that fluorescence correlates well with biomass during growth and with PHB during storage phase. This is borne out in Figure 7.4a.

As an extension of this idea, the specific fluorescence (culture fluorescence normalized by the biomass concentration) during growth would be expected to remain fairly constant during growth but to increase during PHB storage phase (Figure 7.4b). Bowien *et al.*[25] have suggested that the relative ratio of NADH to NAD + NADH hovers around 0.2 under exponential growth conditions. Other researchers have suggested that this ratio increases at the onset of PHB polymerization.[15,16] Assuming that NADH + NAD = constant and that NADH dominates the contribution to the NAD(P)H culture fluorescence signal (NADH + NAD:NADPH + NADP = 10:1[21]), and following this line of reasoning, one would expect to observe a sharp increase in specific fluorescence at the point of ammonium exhaustion. Clearly at the transition between growth and PHB storage, the specific fluorescence increases markedly with a 50% jump. The continued increase in fluorescence during PHB polymerization appears to

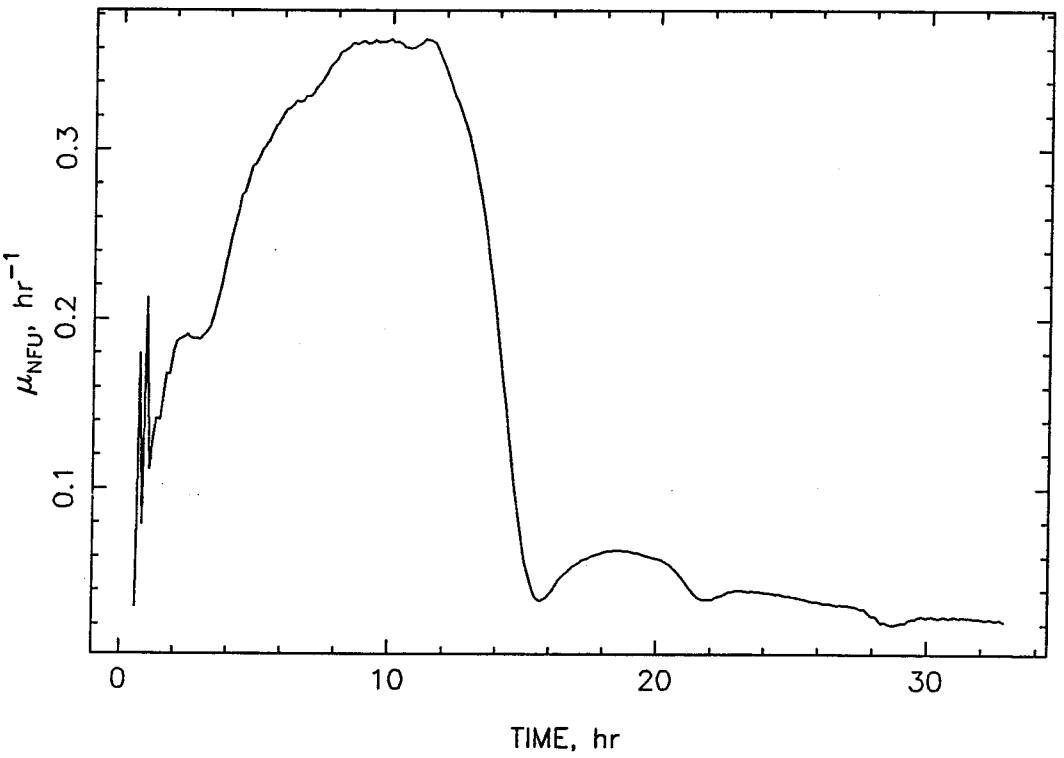

Figure 7.3: Ammonium exhaustion experiment: normalized rate of increase in fluorescence, μ_{NFU}.

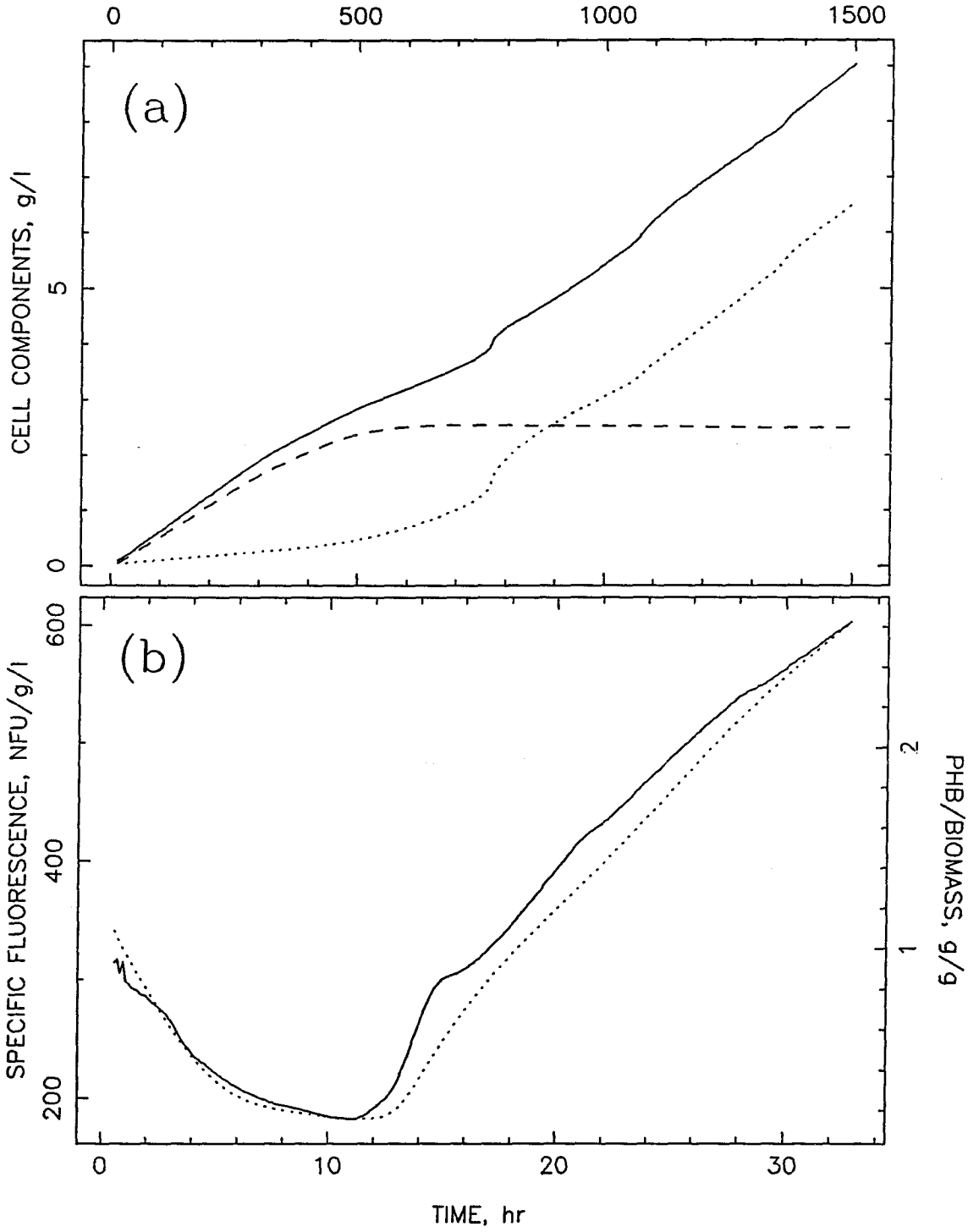

Figure 7.4: Ammonium exhaustion experiment: culture fluorescence relationships. **(a)** Fluorescence relationships: cell dry weight versus culture fluorescence, ——— ; biomass versus culture fluorescence, – – – ; PHB versus culture fluorescence, ····· . **(b)** Time evolution of specific fluorescence, ——— ; time evolution of PHB/biomass ratio, ····· .

be dictated by the direct conversion of fructose to PHB, as suggested by the organism's known metabolism, resulting in the net production of NAD(P)H:

$$\text{Fructose} + \text{PHB}_n + \text{ADP} + 3\text{NAD(P)} \longrightarrow \qquad (7.1)$$
$$2\text{CO}_2 + 3\text{NAD(P)H} + \text{ATP} + \text{PHB}_{n+1}.$$

Returning to Figure 7.4b, the specific fluorescence initially begins at a relatively high level shortly after inoculation and subsequently decreases to a nearly constant value of 200 NFU/g/l prior to ammonium exhaustion. This change in specific fluorescence virtually parallels the PHB/biomass ratio. The initially high PHB/biomass ratio indicates that the inoculum was in PHB storage phase. Simultaneously, as the specific fluorescence drops and levels off, μ_{NFU} (Figure 7.3) rises and levels off. After ammonium exhaustion, μ_{NFU} drops and the specific fluorescence increases. Clearly, μ_{NFU} signals the ammonium-exhaustion meditated increase in the intrinsic PHB concentration.

Figure 7.5 displays temporal changes in fluorescence, ammonium, biomass, cell dry weight, PHB, fluorescence, off-gas carbon dioxide and dissolved oxygen concentrations for the oxygen-limited, ammonium exhaustion experiment. Not surprisingly, when the dissolved oxygen concentration drops to zero (Figure 7.5b), biomass increases only linearly (Figure 7.5a) as does the fluorescence signal. When ammonium is finally exhausted at about 17 hours (Figure 7.4a), oxygen demand drops, resulting in an increase in dissolved oxygen concentration. However, the fluorescence signal's response is of particular note. Unlike the previous example, the fluorescence signal appears to overshoot, followed by a

correction. Again, the response appears delayed relative to ammonium exhaustion. Clearly, the simultaneous release from oxygen deprivation and the onset of ammonium exhaustion has resulted in a characteristically different metabolic response relative to NAD(P)H levels than was seen in the first ammonium exhaustion case.

Unlike the previous ammonium exhaustion experiment, μ_{NFU} (Figure 7.6a) begins to drop before the onset of ammonium exhaustion beginning at the imposition of oxygen limitation; the culture fluorescence's growth/storage transition response is clearly delineated. As with the first ammonium exhaustion experiment, the initial specific fluorescence (Figure 7.6b) begins high but declines thereafter, correlating with the PHB content of the inoculum. At the imposition of oxygen-limitation, the downward trend in specific fluorescence is reversed. Finally, at ammonium exhaustion, the specific fluorescence increases 30%. It is important to note that the specific fluorescence in the growth portion of the oxygen-limited case is higher than the specific fluorescence of the first ammonium exhaustion experiment. This correlates with the higher PHB/biomass ratio found in oxygen-limited, ammonium exhaustion experiment relative to the lower PHB/biomass ratio in the first ammonium exhaustion experiment.

7.4.1.2 Discussion. The apparent delayed response in culture fluorescence observed at ammonium exhaustion in both cases is not caused by *A. eutrophus*' delayed regulatory action. As confirmed by the specific fluorescence, the impression of a delayed response is caused by the culture fluorescence's continued trajectory along the established growth-phase curve while biosynthesis

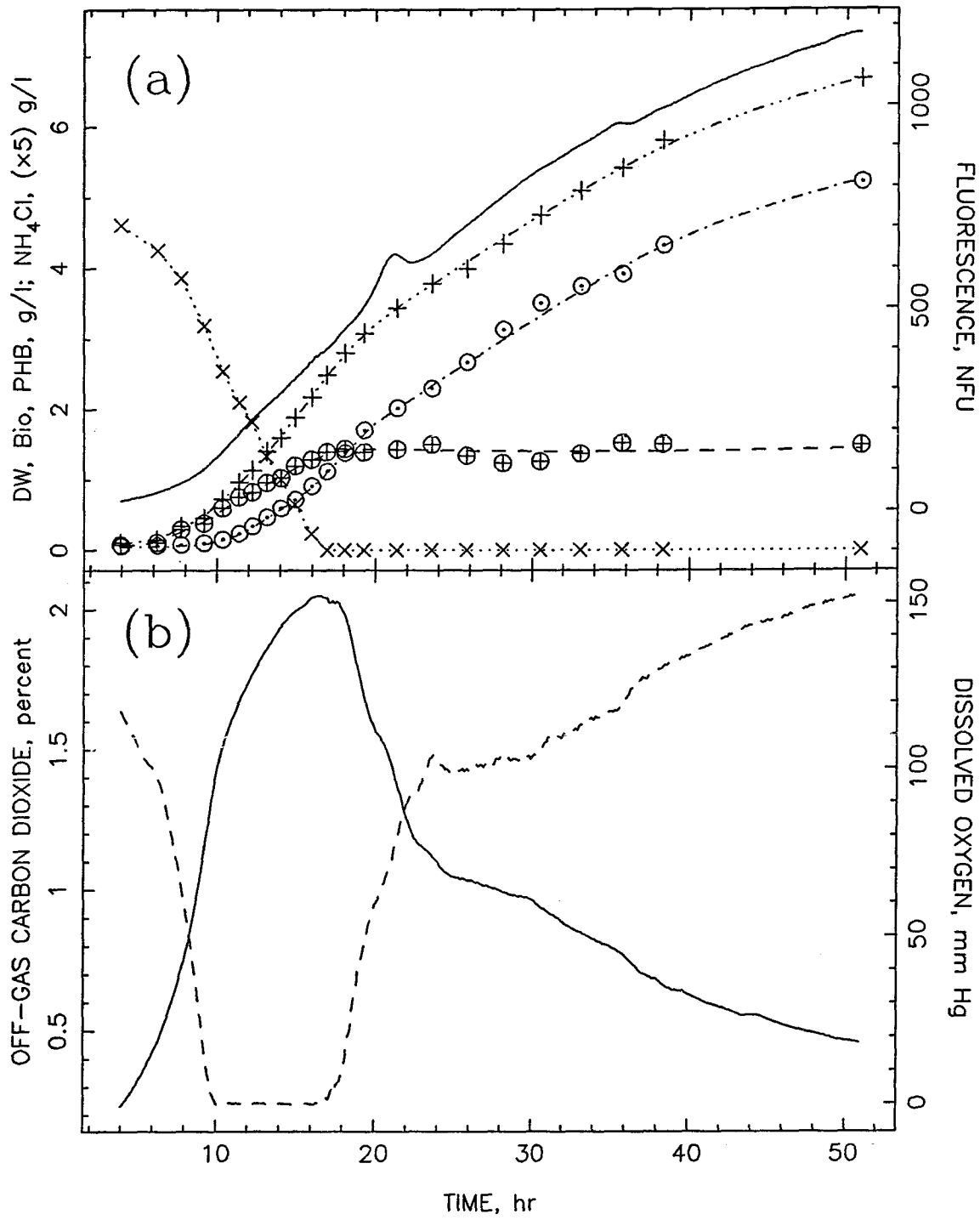

Figure 7.5: Ammonium exhaustion experiment with oxygen limitation: raw data. **(a)** Culture fluorescence, —— ; cell dry weight, + ; biomass, ⊕ ; PHB, ⊙ ; ammonium chloride [(×5) g/l], × . **(b)** Off-gas carbon dioxide, —— ; dissolved oxygen, – – – .

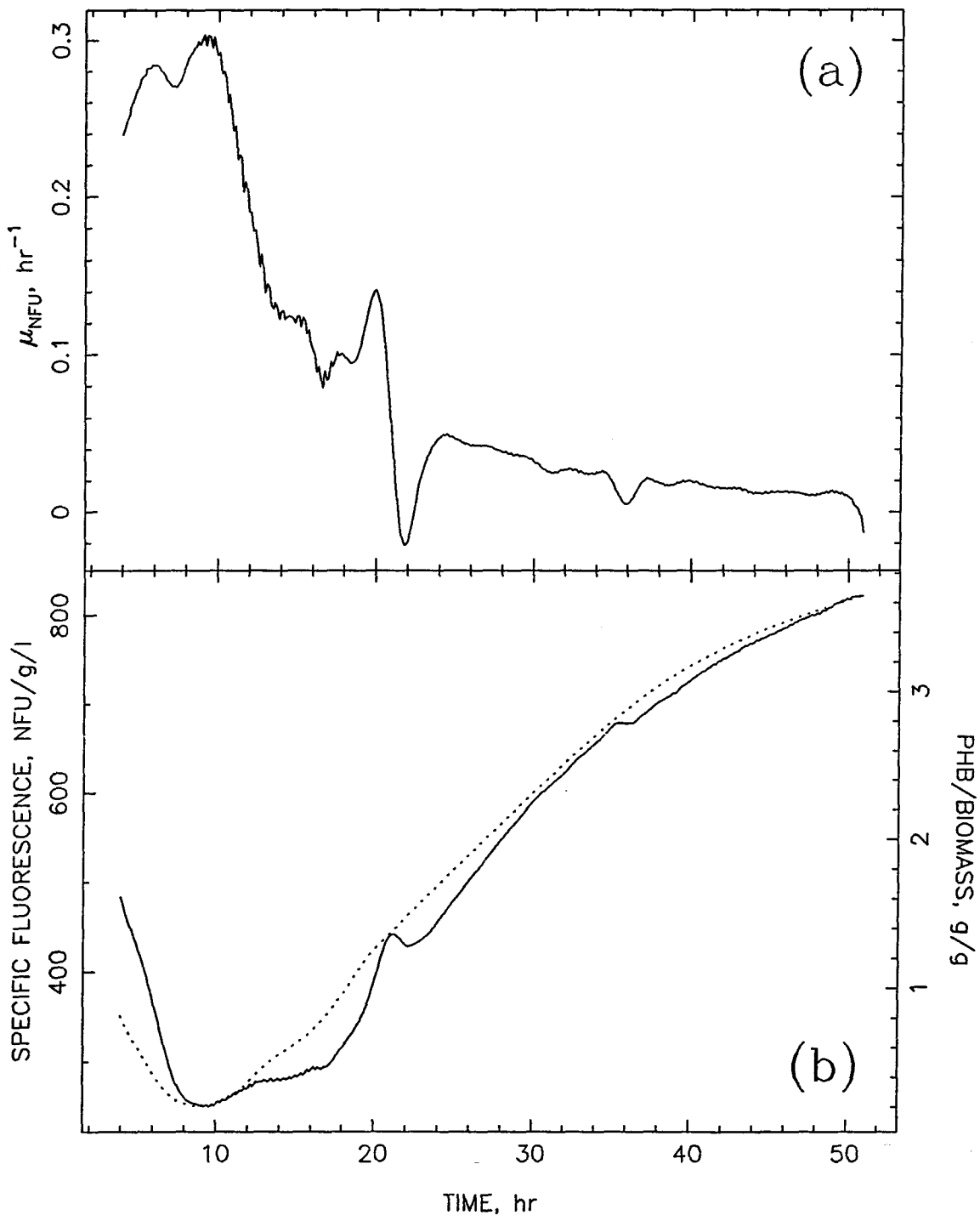

Figure 7.6: Ammonium exhaustion experiment with oxygen limitation: culture fluorescence relationships. **(a)** Normalized rate of increase in fluorescence, μ_{NFU}, ——— . **(b)** Specific fluorescence, ——— ; PHB/biomass ratio, ····· .

activity rapidly diminishes. In this regard, μ_{NFU} proves to be a more reliable and timely indicator of this metabolic switch.

Previously, it was mentioned that Groom *et al.*[11] found 20% of the total culture fluorescence for *A. eutrophus* in a semi-defined media to have arisen from extracellular sources. Following Bowien *et al.*'s suggestion,[25] Groom *et al.*'s suggestion, assuming a constant NAD(P)H/[NAD(P)+NAD(P)H] total intracellular pool, and assuming changes in NAD(P)H constitute the majority of the changes in the corrected culture fluorescence signal (= observed total culture fluorescence – pre-inoculated media background fluorescence – extracellular fluorescence), we can estimate the changes in the NAD(P)H/[NAD(P)+NAD(P)H] ratio. In Figure 7.4b at 11 hours of the first ammonium exhaustion experiment, the culture fluorescence reads 180 NFU/g/l. Using our assumptions, this equates to 144 NFU/g/l because of intracellular NAD(P)H at a NAD(P)H/[NAD(P)+NAD(P)H] ratio of 0.2. At 15 hours, the culture fluorescence reads 300 NFU/g/l or 240 NFU/g/l because of NAD(P)H alone; this computes to a NAD(P)H/[NAD(P)+NAD(P)H] ratio of 0.33. Finally, at the end of the fermenation, Figure 7.5a reads 600 NFU/g/l, or 480 NFU/g/l because of NAD(P)H. This gives a NAD(P)H/[NAD(P)+NAD(P)H] ratio of 0.66.

The validity of this calculation is certainly open to argument. Zabriskie and Humphrey attempted to correlate the intracellular NADH contribution to culture fluorescence by subjecting *S. cerevisiae* to iodoacetate, an inhibitor of the Embden-Meyerhof-Parnas pathway, thereby preventing further production of intracellular energy.[6] Their results suggested that 50% of the culture fluorophore content was intracellular NADH. However, they also noted that the true

NADH contribution may actually exceed 50%, since the effects of iodoacetate is directed only at mitochondrial NADH pools and does not affect cytoplasmic pools. Siano and Mutharasan have also noted that enzymatic binding of NAD(P)H can greatly affect NAD(P)H fluorescence, thereby implying that NAD(P)H molecules distributed throughout the interior of a cell may make differing contributions to the culture fluorescence signal.[26]

Although the previously calculated ratios are gross estimates, it clearly suggests that increasing the NAD(P)H/[NAD(P)+NAD(P)H] ratio is related to increased PHB polymerization. Judging from the change in this ratio at the transition point, 0.2 to 0.33, this would indicate a very dramatic change in metabolic control as evidenced by the shift in the NAD(P)H/NAD(P) pool, which is supported by the observation of increased PHB pathway activity.

7.4.2 Release from Ammonium Exhaustion

Next we examine *A. eutrophus*' response to the addition of ammonium to cells in the PHB polymerization phase. After exhausting ammonium at 12 hours, the *A. eutrophus* cells were allowed to store PHB for about 14 hours. Following the PHB storage period, a concentrated ammonium chloride solution (40 ml of a 290 g/l ammonium chloride solution) was added at 27.8 hours.

7.4.2.1 Results. Figure 7.7 describes the fermentation observables for such a run. It is clear that following this added dose of ammonium chloride, culture fluorescence drops gradually for an initial period (This decrease cannot be attributed to the dilution; the 40 ml were added to 11.6 l.) followed by a sudden

upturn with a slope higher than that of the previous storage phase. As growth continues, μ_{NFU} (Figure 7.8a) averages approximately 0.07 hr^{-1} — considerably less than the 0.3 hr^{-1} observed earlier in the run (Not shown). Clearly, the specific fluorescence and PHB/biomass ratio (Figure 7.8b) begin to drop after addition of ammonium but are still very high relative to previously seen exponential growth values. Again, the high specific fluorescence and PHB/biomass ratio correspond to a low μ_{NFU}.

7.4.2.2 Discussion. Returning to Bowien *et al.*'s suggestion,[25] the ratio of NAD(P)H to NAD(P) + NAD(P)H should have dropped to approximately 0.2 or a specific fluorescence value of 180 NFU/g/l, assuming a 20% extracellular fluorescence contribution. As hinted by the drops in specific fluorescence following inoculation with PHB storage-phase inocula in the two previous ammonium exhaustion examples, the slight drop in specific fluorescence does not approach this value. Clearly there is a strong correlation between the decrease in PHB/biomass ratio and the decrease in specific fluorescence. The later portion of Figure 7.8b clearly demonstrates that the specific fluorescence decreases with time following addition of ammonium, indicating that the cell's metabolism is moving in the direction of restoring the expected NAD(P)H/[NAD(P)+NAD(P)H] ratio.

There may be several reasons to explain why we observe what appears to be a NAD(P)H/NAD(P) hysteresis effect. First, we must note that this late growth metabolism occurs under significantly different physiological conditions than those observed in earlier fermentations. Figure 7.7a indicates that the bulk concentration of PHB decreases after introduction of the ammonium chloride

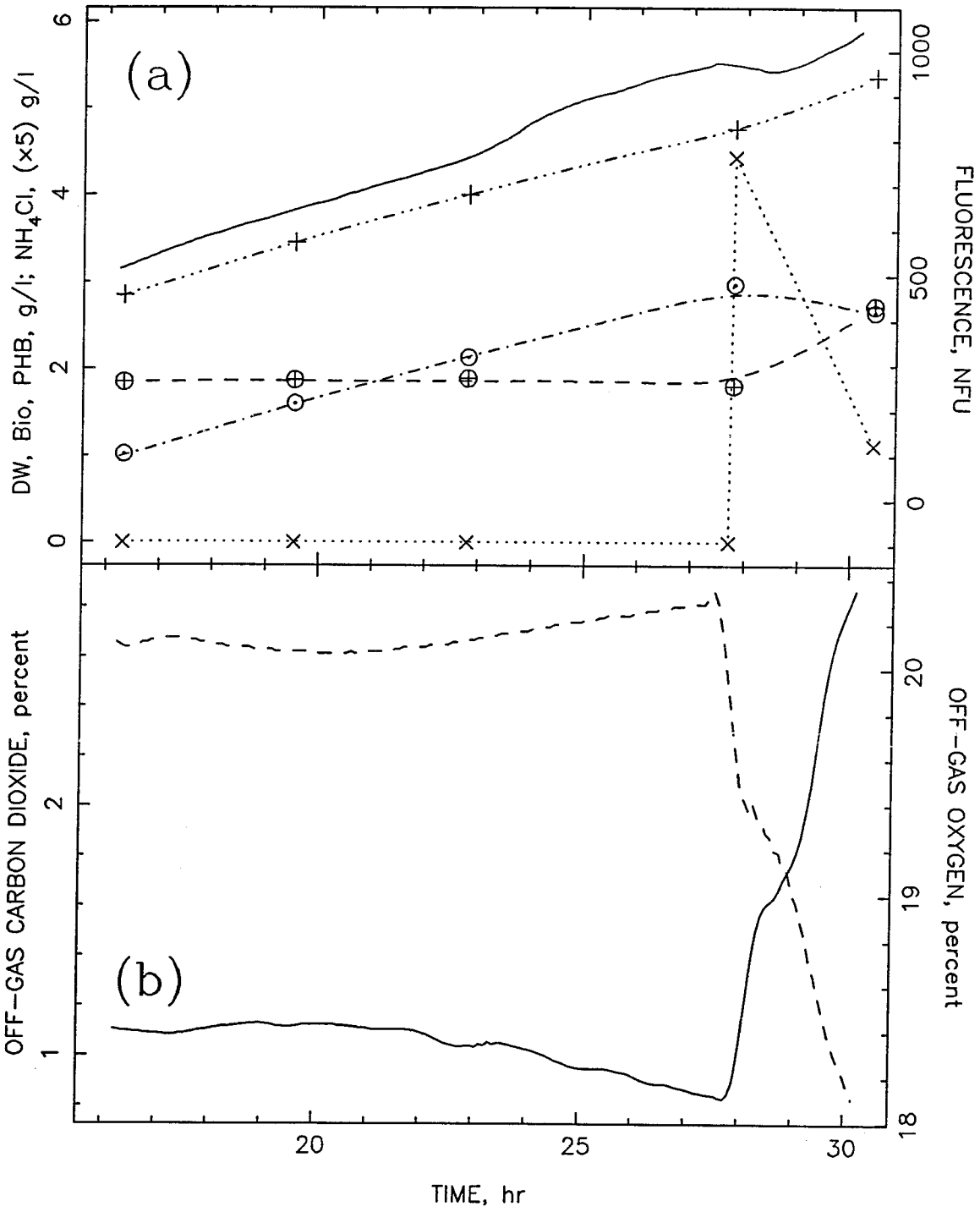

Figure 7.7: Release from ammonium exhaustion experiment: raw data. **(a)** Culture fluorescence, ——— ; cell dry weight, + ; biomass, ⊕ ; PHB, ⊙ ; ammonium chloride [(×5) g/l], × . **(b)** Off-gas carbon dioxide, ——— ; off-gas oxygen, – – – .

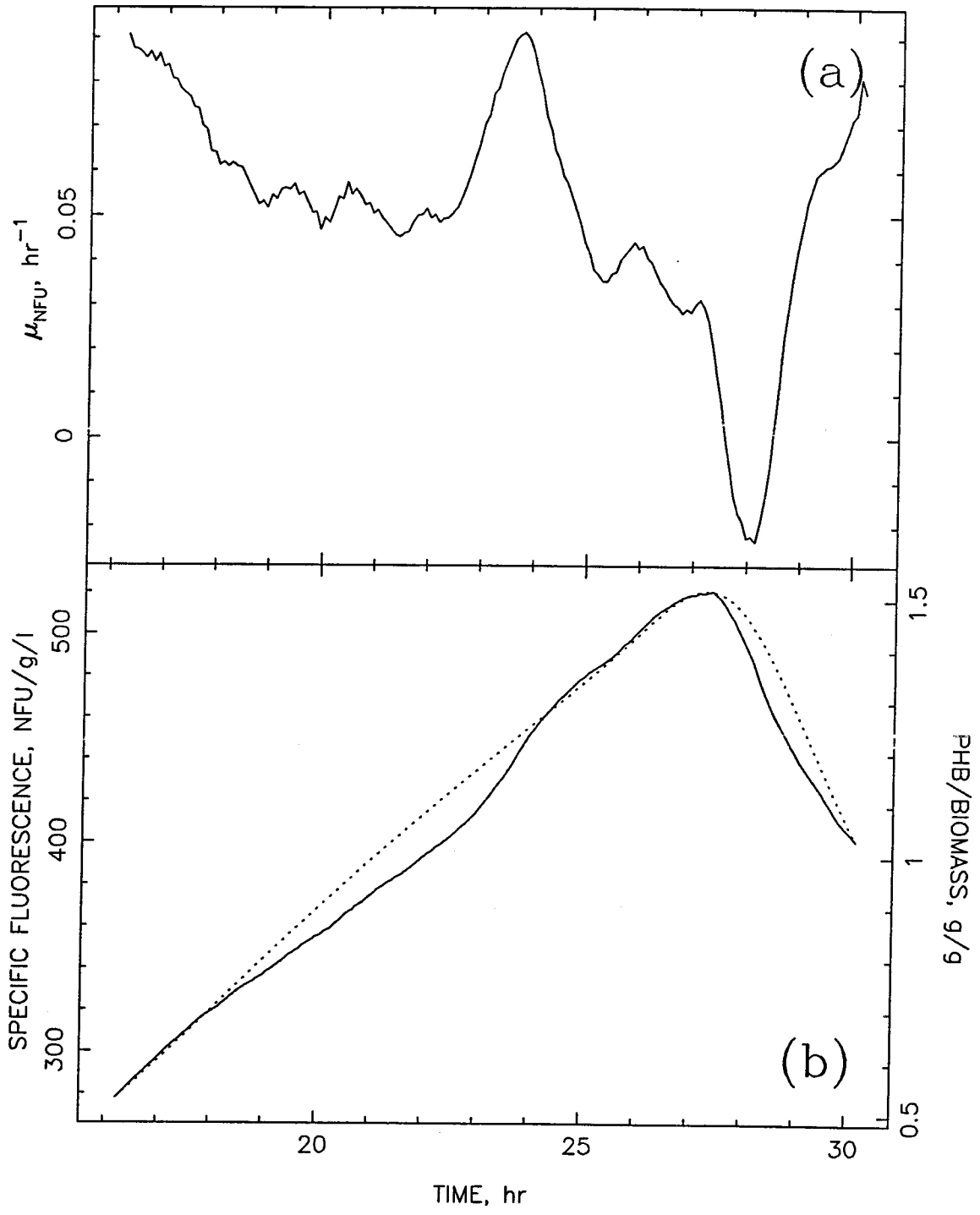

Figure 7.8: Release from ammonium exhaustion experiment: culture fluorescence relationships. **(a)** Normalized rate of increase in fluorescence, μ_{NFU}, ——. **(b)** Specific fluorescence, —— ; PHB/biomass ratio, ·····.

pulse at 27.8 hours. So, rather than relying solely upon fructose for its carbon and energy needs, the cell also metabolizes its PHB reserves. This did not occur in the early, post-inoculation phases of the two previous ammonium exhaustion experiments. However, under those conditions, the PHB/biomass levels were not nearly so high.

Secondly, with large PHB reserves, cell division may be inhibited by the physical presence of the large, granular PHB inclusion bodies. Under normal growth conditions, *Alcaligenes eutrophus* H16's cell shape is elongated. After significant amounts of PHB have been stored, the cell configuration grows much more rounded. Guerrero and co-workers found that the average surface area per *A. eutrophus* N9A cell increases from 7.5 to 12.5 μm^2, with a volume change of 1.208 to 3.808 μm^3 that is due to PHB storage (0 to 96% PHB contribution to dry weight), while retaining the same cell water volume.[27,28] Electron microscopy shows that the interior of the cells are dominated by the large PHB granules.[12]

Groom *et al.*[11] found that PHB absorbs neither at the excitation nor at emission wavelengths used by the FluroMeasure^{TM} probe. This high culture fluorescence may be indicative of the cell self-imposing regulatory constraints upon its metabolism. Presumably, large intracellular PHB granules must be a physical inhibition to growth. A high NAD(P)H/[NAD(P)+NAD(P)H] ratio, therefore, serves the purpose of inhibiting rapid consumption of fructose by inhibiting glucose-6-phosphate dehydrogenase[29,30] and pyruvate kinase[31] in the glycolytic pathway and isocitrate dehydrogenase[14] in the citric acid cycle. Presumably, the acetyl-CoA/CoASH ratio is low enough to prevent PHB

polymerization[15,16]; the high NAD(P)H/[NAD(P)+NAD(P)H] ratio is partially sustained by PHB depolymerization:

$$PHB_n + 2CoASH + NAD \longrightarrow PHB_{n-1} + 2Acetyl\text{-}CoA + NADH. \qquad (7.2)$$

7.4.3 Ammonium Limitation

To investigate the influence on culture fluorescence and on NAD(P)H levels of an ammonium-limited culture, *Alcaligenes eutrophus* H16 cells were subjected to the following growth conditions: Medium containing *ca* 0.3 g/l ammonium chloride was inoculated with cells. As the cells multiplied, the ammonium level was permitted to decline until six hours. At six hours constant rate feeding of a concentrated ammonium chloride solution (*ca* 134 g/l ammonium chloride at 15 ml/hr into *ca* 12 l) commenced. At seven hours the cells' ammonium consumption rate exceeded the ammonium chloride feed rate. Subsequently, the ammonium concentration dropped below detectable levels around eight hours, and the cells became ammonium-limited.

7.4.3.1 Results. Figure 7.9 summarizes the temporal evolution of various observables of the ammonium limitation experiment. From two to eight hours, biomass and culture fluorescence (Figure 7.9a) increase exponentially. (The early portion of culture fluorescence has been removed for later discussion. See 7.7.2.) As the bulk ammonium concentration drops below detectable levels at eight hours, the slope of the fluorescence signal and the slope of the biomass concentration curves initially decrease and continue to increase linearly

throughout the rest of the fermentation. As indicated by the slope of the pseudoammonium concentration curve, Φ_{NH_4Cl}, ammonium consumption is constant (slope = ammonium production rate). Similarly, the off-gas carbon dioxide and oxygen concentrations display parallel trends with exponential increases in carbon dioxide production and oxygen consumption, giving way to linear increases. PHB's initial cell dry weight contribution is minimal but increases exponentially as biosynthesis becomes increasingly more restricted.

The normalized rate of increase in fluorescence, μ_{NFU}, clearly depicts the ammonium limitation shift in the culture fluorescence slope (Figure 7.10a). Since culture fluorescence continues to increase linearly, μ_{NFU} decreases asymptotically. As with previously discussed experiments, the specific fluorescence (Figure 7.10a) decreases early in the experiment. Notice, however, that the starting value is considerably less than those shown in Figures 7.4b and 7.6b, reflecting the greater care used in obtaining an unlimited, exponentially growing inoculum. Clearly, the PHB/biomass ratio confirms this relative to Figures 7.4b and 7.6b. As the ammonium concentration becomes limiting, the specific fluorescence's response is qualitatively similar to that observed at ammonium exhaustion with a small step increase of much smaller magnitude. Specific fluorescence then plateaus momentarily before increasing steadily throughout the rest of the run. This coincides with the increase in the PHB/biomass ratio.

7.4.3.2 Discussion. This fermentation serves as an excellent example of how subtle shifts in the NAD(P)H intracellular concentration relate to levels of PHB polymerization. Following the previously described NAD(P)H/[NAD(P)+NAD(P)H] ratio calculations, the

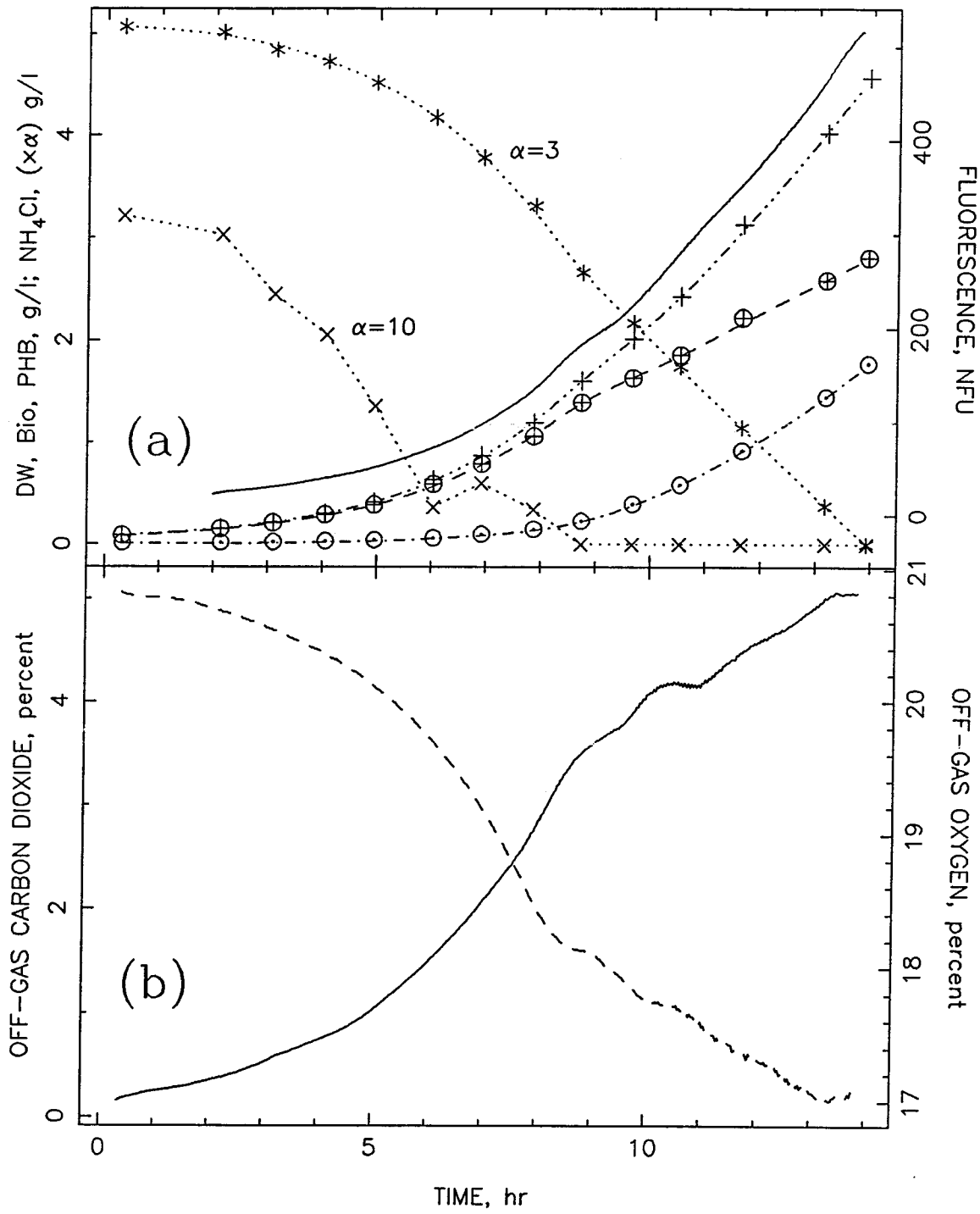

Figure 7.9: Ammonium limitation experiment: raw data. **(a)** Culture fluorescence, ——— ; cell dry weight, + ; biomass, ⊕ ; PHB, ⊙ ; pseudoammonium chloride [(×3) g/l], Φ_{NH_4Cl}, * ; bulk ammonium chloride [(×10) g/l], × . **(b)** Off-gas carbon dioxide, ——— ; off-gas oxygen, – – – .

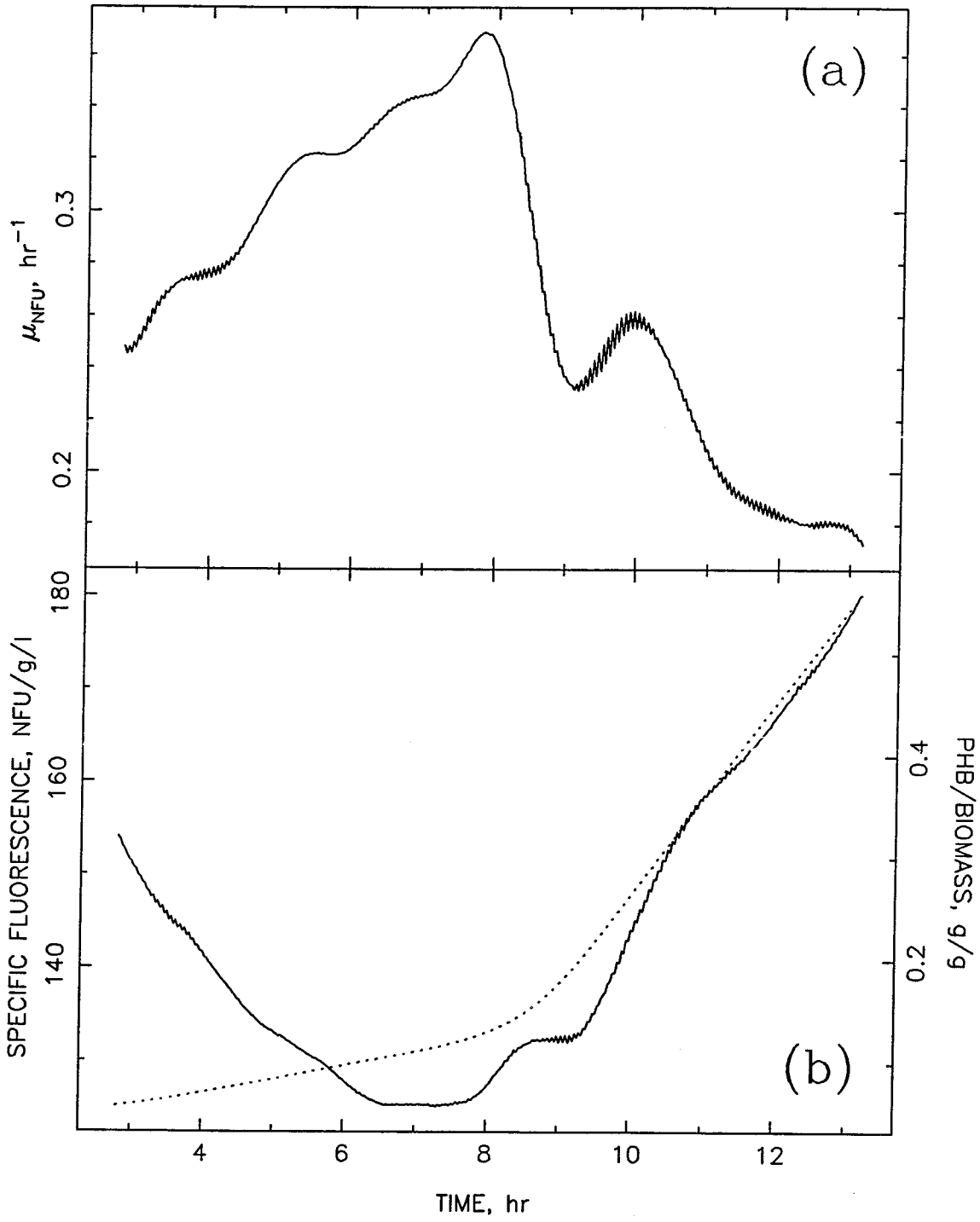

Figure 7.10: Ammonium limitation experiment: culture fluorescence relationships. **(a)** Normalized rate of increase in fluorescence, μ_{NFU}, ——— . **(b)** Specific fluorescence, ——— ; PHB/biomass ratio, ····· .

NAD(P)H/[NAD(P)+NAD(P)H] ratio shifts from 0.20 to 0.21 from 7.9 to 9 hours, respectively, and later to rises to 0.29 at 13 hours. As we saw earlier in the ammonium exhaustion cases, a large increase in the NAD(P)H concentration as indicated by the increase in specific fluorescence signaled the end of biosynthesis and the onset of dramatically increased PHB polymerization. In the case of the linear feeding of ammonium under limited conditions, ammonium is available for biosynthesis but at a steadily decreasing rate on a per unit biomass basis. The emphasis of fructose metabolism, therefore, gradually shifts away from anabolic activities toward increased PHB polymerization as the energy demand for biosynthesis dwindles. The gradual increase in the specific fluorescence and decrease in μ_{NFU} highlight the temporal shift to higher NAD(P)H levels, resulting in relaxation of inhibition of PHB synthesis.

7.5 FRUCTOSE EFFECTS

A single experiment was used to investigate the influence of varying fructose levels on *Alcaligenes eutrophus* H16. Initially the fermenter was inoculated with a fructose concentration of *ca* 1.2 g/l. The dissolved oxygen and ammonium chloride concentrations were maintained between 120 and 140 mm Hg and 0.7 and 1.0 g/l, respectively; the ammonium concentration was maintained via pH-controlled ammonium chloride additions (*ca* 134 g/l ammonium chloride). At approximately 5.4 hours, the fructose concentration was allowed to exhaust and remain exhausted for 1.1 hours. At 6.5 hours the fructose feed pump was

started; a 1000 g/l fructose solution was fed to the fermenter at a rate of 0.34 ml/hr/l culture. The fructose concentration was below detectable levels during this period. Two hours later, the fructose feed pump rate was increased to allow the fructose concentration to rise above zero. At 10.5 hours the fructose feed pump was again turned off, followed by fructose exhaustion at 10.8 hours. At 11.25 hours the fructose pump was turned on at a rate of *ca* 0.83 ml/hr/l culture. This feed rate was further elevated to *ca* 1.04 ml/hr/l culture at 13.5 hours and maintained at this rate through the end of the experiment.

The time evolution of culture fluorescence and the cellular components is described by Figure 7.11a, and the time evolution of the off-gas carbon dioxide and off-gas oxygen concentrations is described in Figure 7.11b. Included in Figure 7.11a along with the actual fructose concentration is the back-calculated pseudofructose concentration, Φ_{Fruc} (See Chapter 2). The fructose production rate per liter culture is directly calculated from the derivative of the pseudofructose concentration curve. Note that during the fructose feeding segments of this experiment, the derivative of the pseudofructose concentration curve is constant. Also notice how the cellular components and off-gas concentrations respond to the periods of unrestrained growth (0–5.4, 8.5–10.8 hours), releases from fructose exhaustion (6.5 and 11.25 hours), release from fructose limitation (8.5 hours) and growth under limited conditions (6.5–8.5, 11.25–16^{+} hours).

The oscillatory behavior observed in the culture fluorescence and the off-gas concentrations during periods of limited growth require special attention. Initially it was thought that these oscillations were manifestations of shifts between growth and PHB storage metabolic regimes. Closer examination revealed,

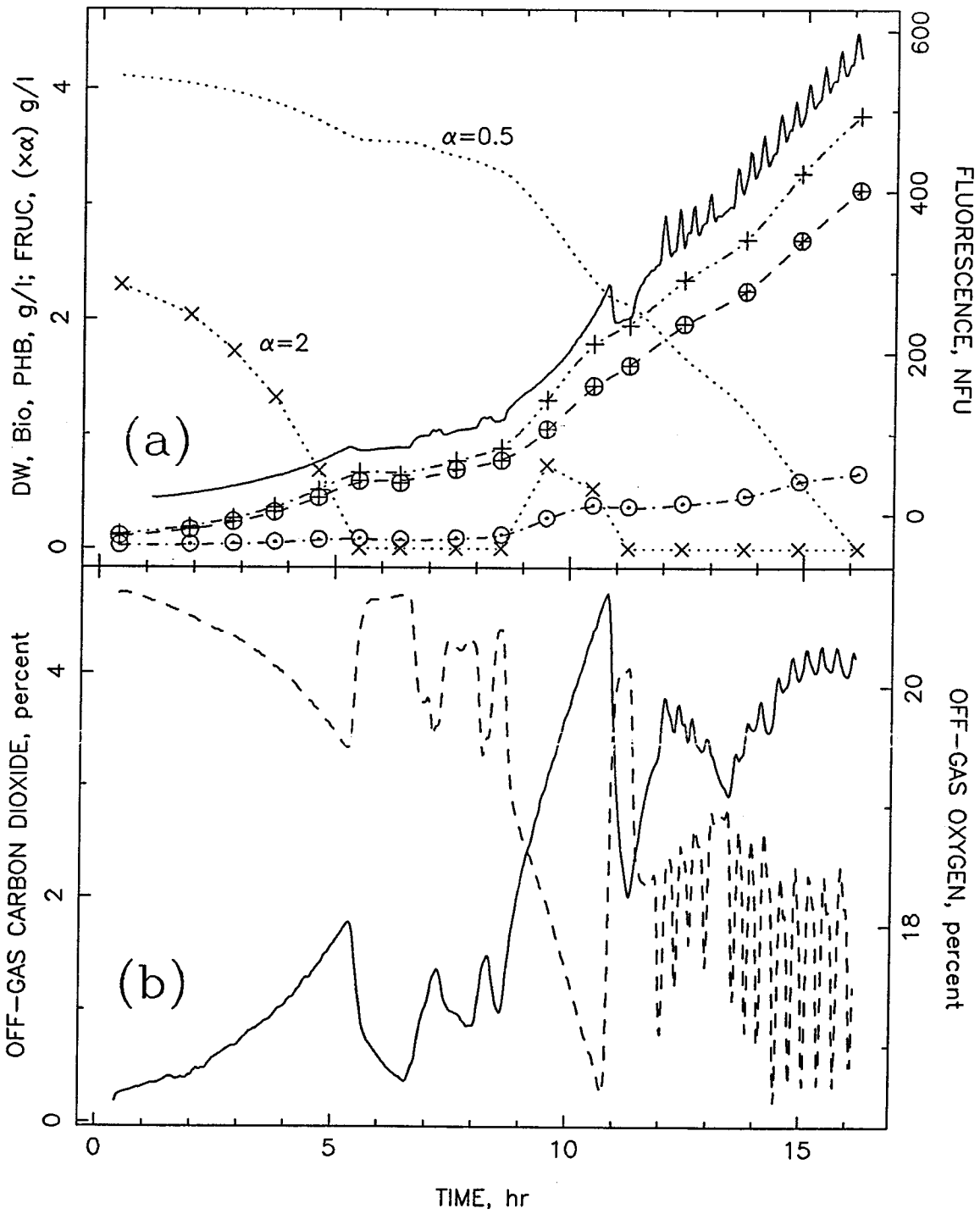

Figure 7.11: Fructose effects experiment: raw data. **(a)** Culture fluorescence, ——— ; cell dry weight, + ; biomass, ⊕ ; PHB, ⊙ ; pseudofructose [(×0.5) g/l], Φ_{Fruc}, ····· ; bulk fructose [(×2) g/l], × . **(b)** Off-gas carbon dioxide, ——— ; off-gas oxygen, – – – .

however, that these oscillations were actually caused by pH-control induced fluctuations in the fructose feeding rate.

Although the time-averaged fructose feed rate was constant, the fructose feed rate over the time scale of 20 minutes fluctuated because of interactions with the pH control system. pH corrective action caused momentary increases in the fructose feed rate, giving rise to the peaks and oscillatory behavior observed in the culture fluorescence and the off-gas concentrations. The cause of this phenomenon has been previously described and analyzed in detail.

7.5.1 Fructose Exhaustion

7.5.1.1 Results. At 5.25 and 10.8 hours the fructose concentration was allowed to become exhausted. On both occasions there was a drop in the culture fluorescence. This coincides with reductions in carbon dioxide production and oxygen consumption. Although difficult to detect, the PHB concentration declines. The drop in fluorescence at 5.25 hours is distinctively less dramatic than that at 10.8 hours. Considering the fructose consumption rate prior to exhaustion (negative value of the pseudofructose concentration slope), the slope prior to 10.8 hours is 2.2 times more negative (2.2 times higher fructose consumption rate) than the slope prior to 5.25 hours. Therefore, the cells "hit the (fructose exhaustion) wall" harder at 10.8 hours.

In both fructose exhaustion cases, μ_{NFU} (Figure 7.12a) drops to *ca* 0.1 hr^{-1}. Unlike previous examples where a μ_{NFU} value of less than 0.3 hr^{-1} indicated PHB synthesis, under these circumstances, PHB is being depolymerized. Apparently,

the point of delineation separating μ_{NFU}'s response to PHB polymerization and depolymerization is that in the latter case, μ_{NFU} drops well below zero initially.

Figure 7.12b clearly indicates a noticeable drop in specific fluorescence. In both exhaustion cases, specific fluorescence increases momentarily prior to exhaustion, with the 10.8 hour more abrupt exhaustion case peaking the highest. Considering the difference between the average specific fluorescence prior to the pre-exhaustion peak and the drop in specific fluorescence, both fructose exhaustion cases drop nearly identical amounts. Relatively speaking, the average specific fluorescence in the the second case is higher than the first as correlated with the differences in the PHB/biomass ratio. Unlike previous examples, the relationship between specific fluorescence and the PHB/biomass ratio is only qualitatively related.

7.5.1.2 Discussion. Clearly, the imposition of fructose exhaustion strongly influences the cell's metabolic response as indicated by the sudden drop in NAD(P)H levels. Because fructose serves as carbon and energy source, its exhaustion immediately suggests depletion of glycolytic and citric acid cycle intermediates. NAD(P)H, of course, is predominantly produced in the citric acid cycle by fructose catabolism. Therefore, we would expect to see a drop in the culture fluorescence level as NAD(P)H is oxidized to meet the cell's requirement for ATP. And indeed this is what is observed. However, the drop in culture fluorescence is not as pronounced as might be expected; this must be attributed directly to the metabolism of the PHB reserves within the cell. Cook and Schlegel have noted that the ATP levels of carbon- and nitrogen-starved autotrophically grown *Alcaligenes eutrophus* H16 cells are as high as in growing

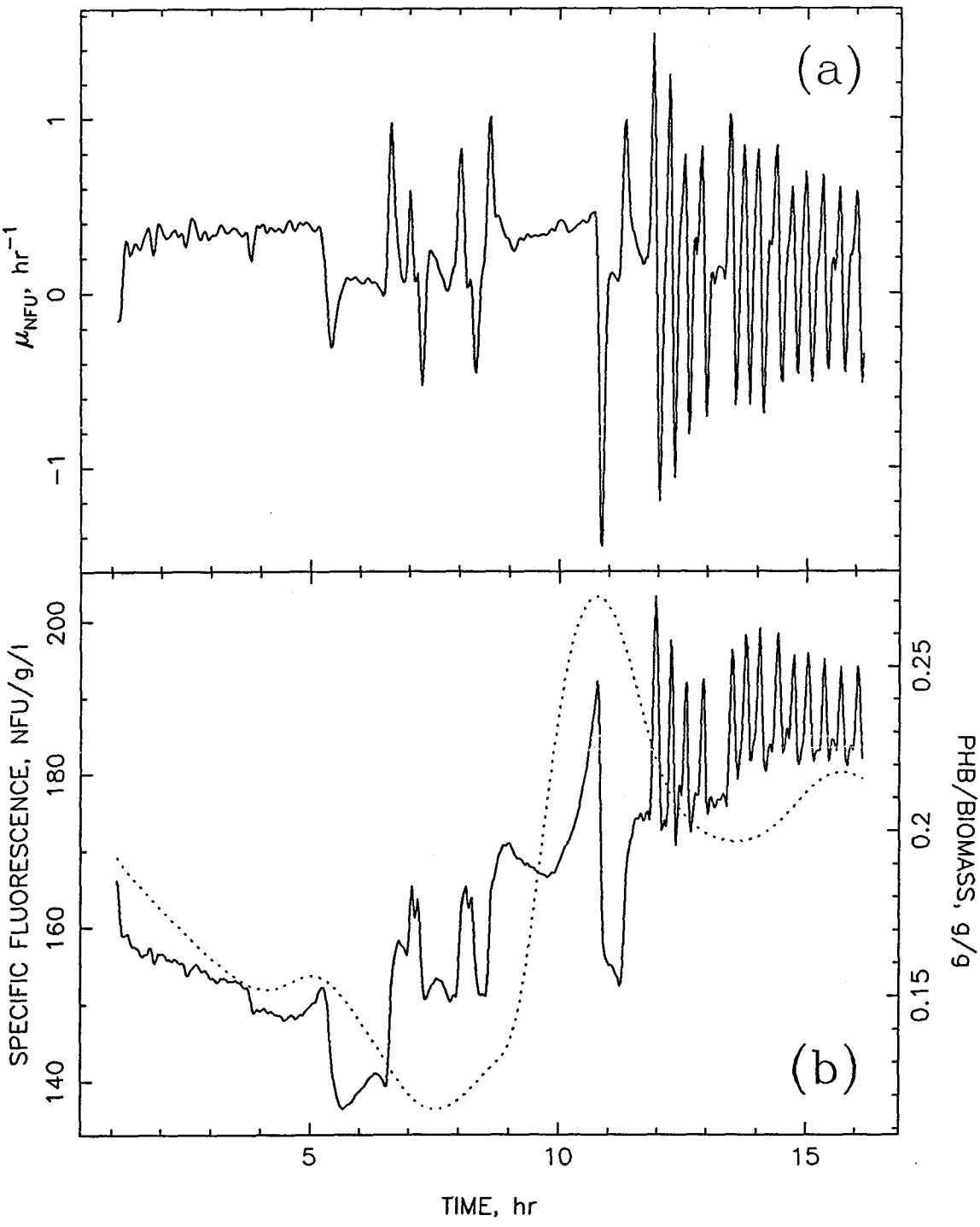

Figure 7.12: Fructose effects experiment: culture fluorescence relationships. **(a)** Normalized rate of increase in fluorescence, μ_{NFU}, ——— . **(b)** Specific fluorescence, ——— ; PHB/biomass ratio, ····· .

cells.[21] Extending this to heterotrophic cultivation, the low NAD(P)H level is apparently in accord with the cell's attempts to maintain a high ATP level.

7.5.2 Release from Fructose Exhaustion

After both fructose exhaustion periods, fructose was supplied to the cells by constant rate feeding beginning at 6.5 and 11.25 hours. Fructose was fed at levels below the cell's optimal requirements.

7.5.2.1 Results. After both the 5.25 and 10.8 hour fructose exhaustion periods, the culture fluorescence signal quickly responded to initiation of fructose feeding by returning to just above pre-exhaustion values (Figure 7.11a); carbon dioxide production and oxygen consumption also increased. Figure 7.12b indicates that the relative increase in specific fluorescence is nearly equal in both cases.

7.5.2.2 Discussion. With the release from fructose exhaustion, glycolytic and citric acid cycle intermediate levels rise. Consequently, NAD(P)H production resumes with the observed increase in culture fluorescence to comparable, but slightly higher, average levels. The slight overall increase suggests a self-imposed cellular response to the previous growth history. In both cases the release from fructose exhaustion is facilitated at fructose feed rates that are proportional to the biomass concentration. This may explain why similar responses in specific fluorescence are observed.

7.5.3 Growth Under Fructose Limitation

Each fructose exhaustion period was followed by a period of linear fructose feeding (6.5 and 11.25 hours). This is evident by the linear slope regions of the pseudofructose concentration, Φ_{Fruc}, in Figure 7.11a.

7.5.3.1 Results. As previously mentioned, fructose-limited growth was influenced by rapid changes in the fructose feed rate. At points at which the fructose feed rate was momentarily increased by pH control action, an upward culture fluorescence spike was observed. When the feed rate dropped at the suspension of pH control action, the culture fluorescence also dropped. Correspondingly, there were sharp increases in carbon dioxide production and oxygen consumption at the onset of each pH-control-induced spike, followed by regions characterized by lower carbon dioxide production and oxygen consumption.

Because of the number of complex processes involved in the creation of biomass and PHB, it is unlikely that short-term changes in cellular components would be detectable, let alone resolved, within the accuracy of the analytical techniques employed. Fructose concentrations were capable of being determined down to 0.05 g/l; in the regions of linear fructose feeding, the fructose concentrations were determined to be well below this level.

In this particular case, μ_{NFU} (Figure 7.12a) provides no useful information aside from the fact that abrupt changes in culture fluorescence and NAD(P)h levels occur. The specific fluorescence (Figure 7.12b), on the other hand, suggests that for each fructose feed rate, there is a minimum NAD(P)H baseline from which momentary increases in the NAD(P)H/[NAD(P)+NADP(P)H] ratio

emanate. This baseline effect is most clearly evident in the upward shift in the fructose feed rate at 13 hours. Correspondingly, there is a small upward shift in the PHB/biomass ratio.

7.5.3.2 Discussion. The fructose limitation oscillations provide an excellent correlation between internal metabolic carbon flux and NAD(P)H levels. As the availability of fructose increases, so do NAD(P)H levels, as evidenced by increases in specific fluorescence. Increased metabolic activity is further confirmed by increased carbon dioxide production and oxygen consumption. Likewise, as fructose availability declines, so do NAD(P)H levels and other measures of cellular activity.

Once again, there is a strong correspondence between specific fluorescence and the PHB/biomass ratio. During the 6.5 to 8.5 hour fructose limitation period, specific fluorescence as well as the PHB/biomass ratio is low. Later, during the second fructose limitation period (11.25 to 16^{+} hours), specific fluorescence is higher, with a correspondingly higher PHB/biomass ratio. As the fructose feed rate increases at 13 hours, specific fluorescence and relative PHB content shift upwards.

7.5.4 Release from Fructose Exhaustion/Limitation

The final region of Figure 7.11 yet to be discussed follows the first linear fructose feeding region and begins at 8.5 hours. In an effort to achieve higher cell concentrations, the first linear fructose feeding region was terminated with a short-term increase in fructose feed rate; this added fructose raised the bulk

fructose concentration above zero and was then allowed to become exhausted, resulting in the second fructose exhaustion region at 10.8 hours.

7.5.4.1 Results. All observables make the largest, continuous increases seen anywhere in the experiment. From Figure 7.12b it is interesting to note that the specific fluorescence increases and initially hovers at a value higher than any attained by previous fructose limitation peaks. This translates into a dramatic rise in the PHB/biomass ratio. Finally, as the fructose concentration drops, the specific fluorescence increases.

7.5.4.2 Discussion. Clearly, having been fructose-exhausted and then fructose-limited, the specific fluorescence indicates a concerted effort on the cell's part to recover from unfavorable growth conditions by increasing NAD(P)H levels and concentrating more heavily upon increasing PHB reserves and less on growth when fructose resources become plentiful. Of particular interest, as the fructose concentration approaches zero prior to the 10.8 hour fructose exhaustion region, the NAD(P)H level spikes upwards, perhaps in a metabolically mediated effort to completely convert the remaining traces of fructose into PHB. Alternatively, perhaps as fructose rapidly dwindles, complex biosynthesis pathways are unable to compete kinetically with relatively simple PHB synthesis; biosynthesis precursors suddenly become unavailable, biosynthetic energy demand drops, and the intracellular levels of NAD(P)H rise.

7.6 OXYGEN EFFECTS

7.6.1 Oxygen Limitation

An experiment designed to test the *Alcaligenes eutrophus* H16's response to oxygen-limited growth and subsequent release from oxygen limitation was conducted. The aeration and agitation rates were set initially at 1.9 l/min and 200 rpm. At 13 hours the agitation rate was increased to 300 rpm; at 20 hours the agitation rate was further increased to 800 rpm. Fructose was maintained between 6 and 4.7 g/l, and ammonium chloride was maintained between 0.8 and 1.0 g/l.

7.6.1.1 Results. Referring to Figure 7.13, oxygen became limiting at 6 hours. From six to 13 hours and 13 to 20 hours, dry weight and biomass concentrations rise linearly with increases in both slopes following the agitation rate transition at 13 hours, reflecting the increase in oxygen transfer rate. Clearly, PHB makes a substantial contribution to the cell dry weight with an exponential increase in concentration beginning at six hours and continuing to 13 hours and a relatively linear rate of increase thereafter.

From six to 13 hours, the increase in culture fluorescence was very linear with time. With the increase in agitation rate from 200 to 300 rpm, there is a small drop in fluorescence, amounting to an approximately 10% reduction in culture fluorescence. Culture fluorescence continues to increase linearly with a larger slope until 20 hours.

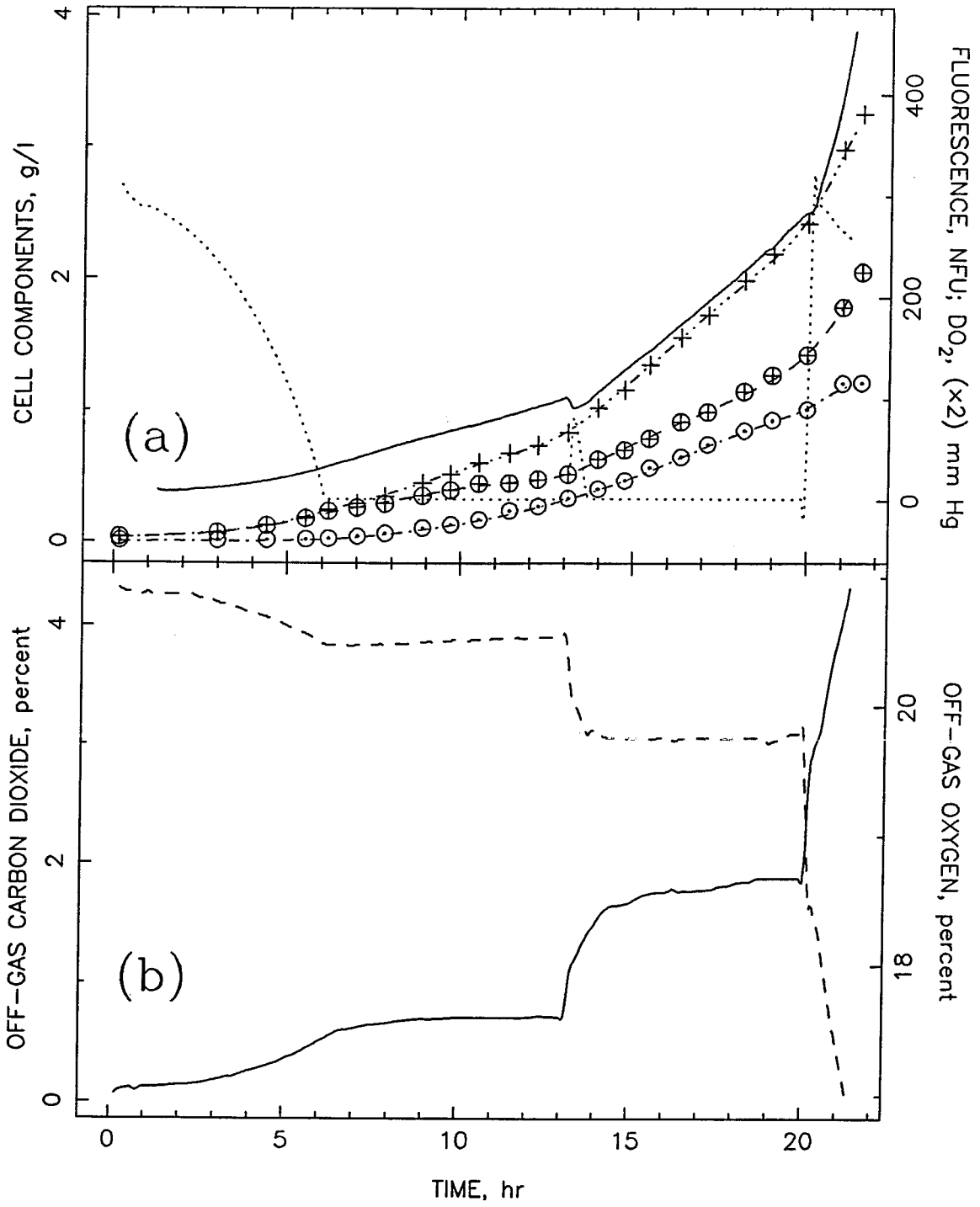

Figure 7.13: Oxygen limitation and release from oxygen limitation experiment: raw data. **(a)** Culture fluorescence, —— ; cell dry weight, + ; biomass, ⊕ ; PHB, ⊙ ; dissolved oxygen, ····· . **(b)** Off-gas carbon dioxide, —— ; off-gas oxygen, – – – .

Prior to six hours, μ_{NFU} averages just above 0.3 hr^{-1} (Figure 7.14a). Beginning with the onset of oxygen limitation, μ_{NFU} drops in an asymptotic manner, serving as an indicator of the level of cellular stress as well as an indicator of increased PHB polymerization. At the 200 to 300 rpm transition, μ_{NFU} drops sharply (off the plot) returning initially to over 0.3 hr^{-1} before again declining asymptotically (*i.e.*, the oxygen consumption rate per unit biomass decreases as cell concentration increases).

Figure 7.14b gives a more elucidating description of the relationship between fluorescence and biomass. As seen before, the specific fluorescence declines following inoculation. As oxygen limitation sets in at six hours, the specific fluorescence begins to increase almost linearly with time. At 13 hours prior to the 200 to 300 rpm transition, the specific fluorescence decreases almost 30%, before continuing to increase.

7.6.1.2 Discussion. As we have seen with ammonium-limited growth, the cells consume oxygen at smaller and smaller rates per unit of biomass. Since oxygen is necessary for NAD(P)H oxidation for production of ATP, reducing the available oxygen supply rate severely restricts ATP availability for biosynthesis. As more fructose is catabolized in the glycolytic pathway, more and more NAD(P)H is produced than can be consumed by oxidative phosphorylation. Consequently, PHB polymerization increases as NAD(P)H levels increase.

After the 200 to 300 rpm transition, the specific fluorescence initially drops before returning to its upward ascent. As can be surmised from Figure 7.14b, the further increase in the PHB/biomass ratio is rather small, leveling off towards the end of this period. This serves as an extremely good example of the relationship

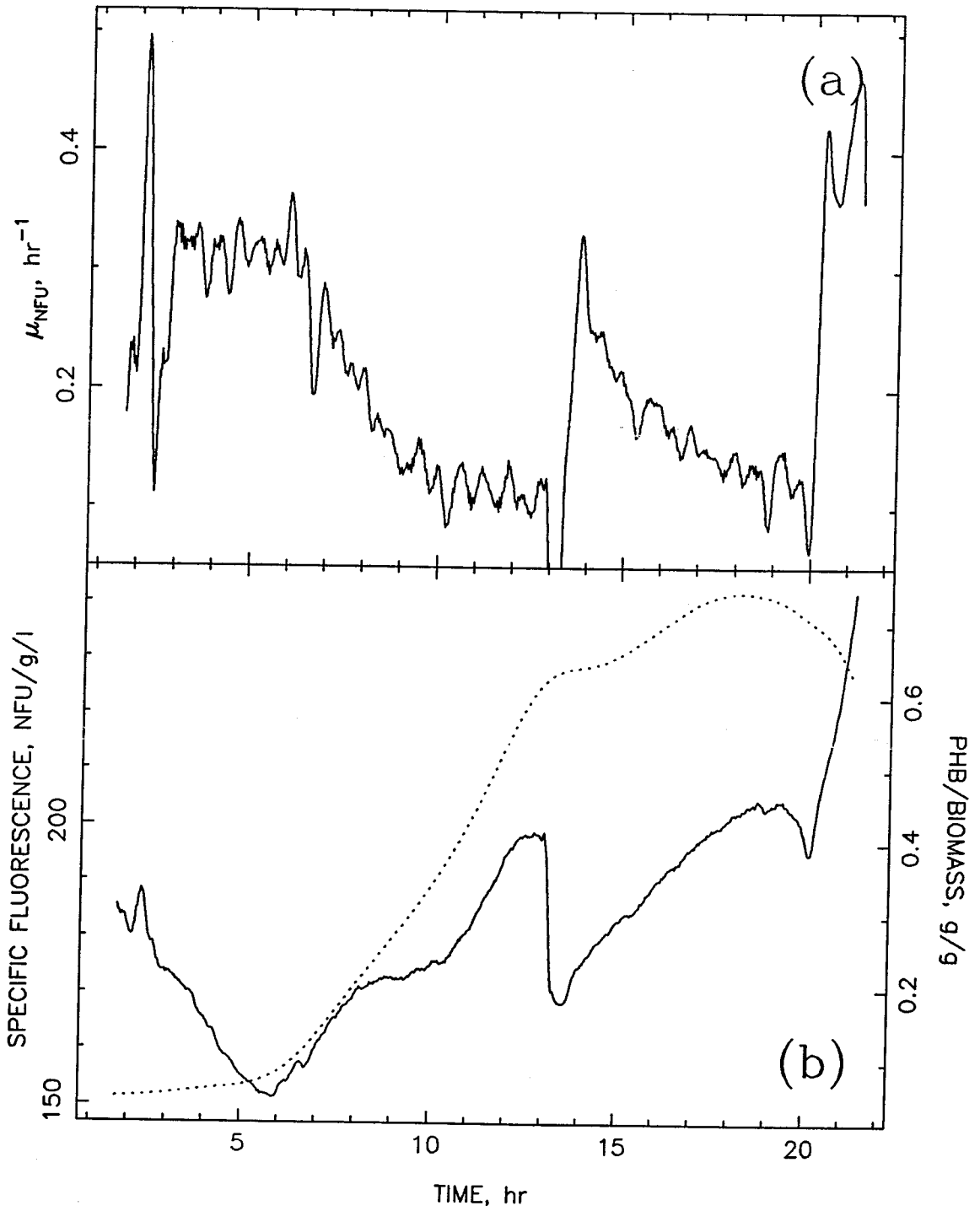

Figure 7.14: Oxygen limitation and release from oxygen limitation experiment: culture fluorescence relationships. **(a)** Normalized rate of increase in fluorescence, μ_{NFU}, ——— . **(b)** Specific fluorescence, ——— ; PHB/biomass ratio, ····· .

between intracellular NAD(P)H levels and intrinsic PHB content. The rapid increase in specific fluorescence from 6 to 13 hours is accompanied by a similar increase in the PHB/biomass ratio. When specific fluorescence drops at the 13 hour agitation rate shift, the PHB/biomass ratio remains constant, only gradually increasing as the specific fluorescence begins to rise. It is important to note that the relative change in the PHB/biomass ratio between 13 and 19 hours compared to 6 hours is proportional to the relative change in specific fluorescence (*i.e.*, intrinsic NAD(P)H levels) at the same points.

Initially, the drop in culture fluorescence at the 13 hour agitation transition (Figure 7.15a) was assumed to be due to a change in the gas holdup, leading to dilution of the number of cells in the fluorescence probe's effective optical window. However, using a correlation for agitated vessels proposed by Richards[32], the void volume at both 200 and 300 rpms is below 2% at the prevailing gas flow rate and power input. Therefore, the change in void volume that is due to the change in agitation rate is unlikely to cause the observed 10% reduction in culture fluorescence. Referring to Figure 7.15a, it is clear that the drop in fluorescence is very sudden. At a sampling rate of eight points per minute, the complete drop in culture fluorescence occurs in about 30 seconds (raw, unsmoothed data shown). Since the increase in agitation rate increases the oxygen mass transfer coefficient, $(k_l a)_{O_2}$, the availability of oxygen to the cells increases. Therefore, the previous NAD(P)H oxidation limitation is relieved, resulting in the observed drop in culture fluorescence.

A second observation made with regard to the change in culture fluorescence was the drop in signal noise after the agitation transition. We would expect

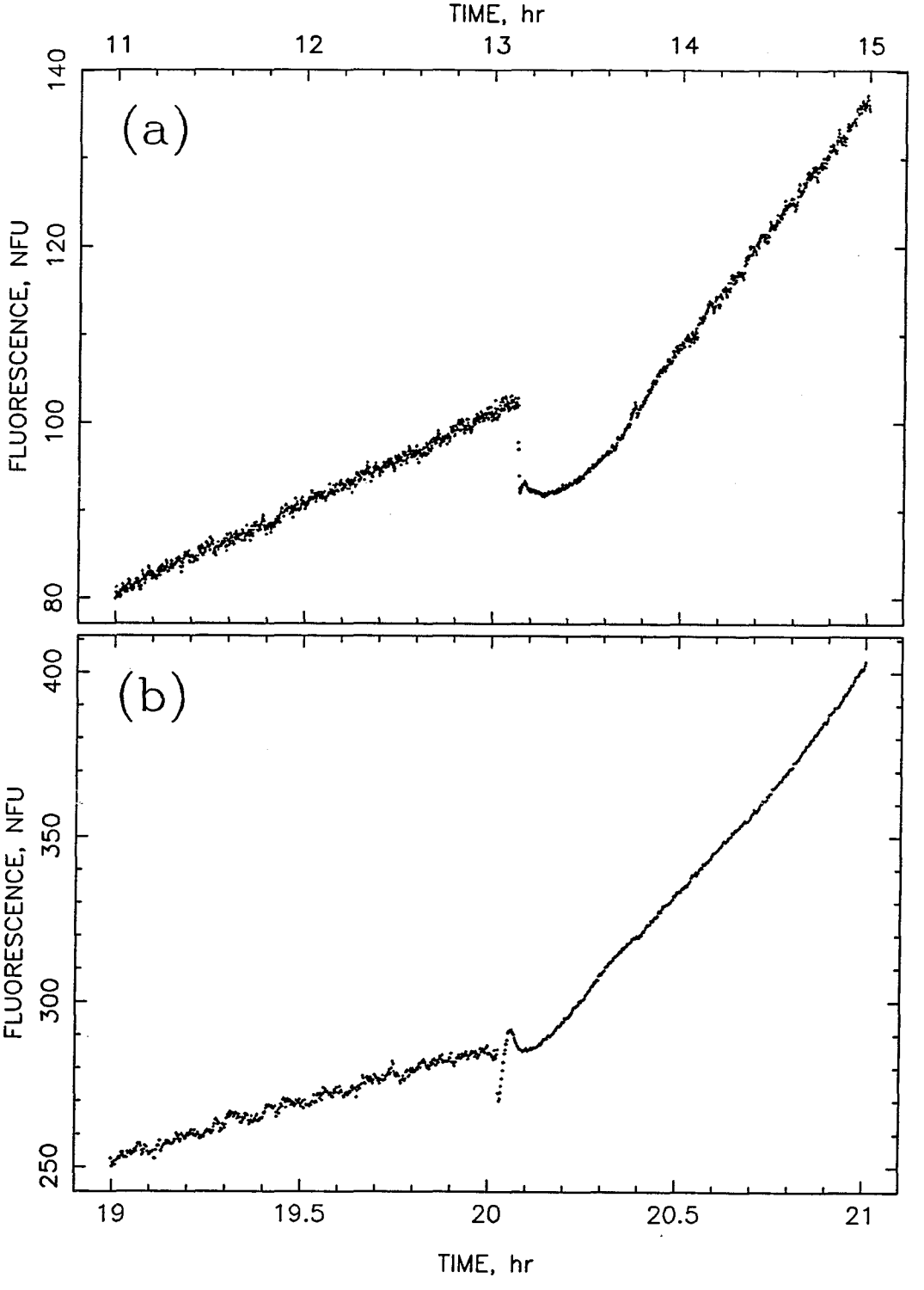

Figure 7.15: Oxygen limitation and release from oxygen limitation experiment: unsmoothed, agitation transition fluorescence raw data. **(a)** 200 to 300 rpm agitation rate transition. **(b)** 300 to 800 rpm agitation rate transition.

the bubble size to be larger in the 200 rpm region than in the 300 rpm region. Using the correlation for the maximum stable, bubble-size diameter suggested by Bailey and Ollis[33], the maximum bubble volume from 200 to 300 rpm would shrink over 40%. Consequently, when larger bubbles pass through the effective optical window, larger discontinuities and disruptions in the culture fluorescence are produced. With smaller, more disperse bubbles, greater continuity in the effective optical window would be observed, leading to a smaller noise component. A similar relative reduction in noise is observed in the 300 to 800 rpm transition region (Figure 7.15b).

A second explanation for the relative changes in the culture fluorescence fluctuations may be due to imperfect mixing. In an experiment conducted in our lab, the bioluminescent bacterium *Photobacterium phosphoreum* was grown in a one liter glass fermenter agitated at 250 rpm with an angled flat-blade impeller. Bioluminescence is highly dependent upon availability of oxygen for the luciferase-mediated light-producing reaction.[34] Variability in light production was detectable not only between the top and bottom phases of the culture broth, but also between dispersed fluid packets within the broth. Since respiration-mediated NAD(P)H oxidation requires oxygen, culture fluorescence fluctuations may propagate from passage of turbulent eddies possessing differing micro-oxygen concentration environments through the optical window. As agitation is increased, mixing improves and localized oxygen concentration variability is reduced.

7.6.2 Release from Oxygen Limitation

7.6.2.1 Results. As Figure 7.13a shows, the release from oxygen limitation at 20 hours because of the 300 to 800 rpm transition caused a large dramatic rate of increase in culture fluorescence. Large rates of increase in dry weight and biomass concentrations are also observed. Surprisingly, PHB also increases initially but appears to plateau, perhaps declining thereafter, had the experiment continued.

Somewhat surprising is the large increase in μ_{NFU} to 0.4 hr^{-1} (Figure 7.14a). It is unclear whether this is a transient or a sustained increase. After 21 hours μ_{NFU} may begin descending, although the specific fluorescence clearly indicates no letting up in the rapid increase in NAD(P)H levels.

As in the 200 to 300 rpm transition, the 300 to 800 rpm transition experiences the same *ca* 10 NFU drop as well as reduction in signal noise (Figure 7.15b). Unlike the 200 to 300 rpm transition, the 300 to 800 rpm transition fluorescence signal recovers to its pretransition level almost immediately. The main difference between the two cases is that under the first agitation transition, oxygen limitation is rapidly reimposed, while in the second case, the cells remain free of oxygen limitation.

7.6.2.2 Discussion. The reason for this sharp increase in fluorescence is somewhat of a mystery. Unfortunately, the run was stopped shortly after the agitation rate was increased, thereby preventing observation of the long-term trend, *i.e.*, whether this increase in culture fluorescence was just a transient or a long-lived change. The increase in fluorescence coupled with dramatically

increased oxygen consumption and carbon dioxide production suggests an increase in metabolic activity, as observed in the fructose limitation oscillations. If a parallel can be drawn with the release from the ammonium exhaustion example, PHB should be metabolized or at least not synthesized at high rates. The immediate increase in PHB following relaxation of oxygen limitation may indicate that some hysterisis occurs in the form of delayed regulatory control. However, the increase in specific fluorescence does correlate with the increase in PHB. The alternate question, then, is why does PHB synthesis appear to stop later if specific fluorescence continues to rise?

Anaerobic fermentation enzymes and their associated products have been found in *A. eutrophus* N9A, but only after incubation for 10 hours or more in oxygen-limited environments.[35] Therefore, the NAD(P)H response to alleviation of oxygen limitation may be related in part to the prescence of these enzymes and the associated anaerobic metabolism.

7.7 PROCESS MONITORING

As an aside to the previous discussions, culture fluorescence was found to vary under conditions not directly related to nutrient levels. In the following sections, these observations are presented from the viewpoint of process monitoring.

7.7.1 Temperature Effects

As other investigators have noted[6], temperature changes can have a profound effect on culture fluorescence. The use of culture fluorescence as a process monitor may be advantageous either as a backup indicator or as a secondary monitor should a primary indicator fail. The previous sections have alluded to the use of culture fluorescence either as an indicator of an undesirable fermentation state or as an indicator of the occurrence of a metabolic shift not readily detected by other more conventional devices: *e.g.*, ammonium or fructose exhaustion. Certainly maintaining the proper temperature within a fermenter is a key factor to any successful fermentation. We now describe a situation in which small changes in temperature influenced the culture fluorescence.

Because of a bad connection between the headplate inlet gas line and the sparger apparatus, some of the inlet air circumvented the sparger, passing through the fermenter headspace straight to the exhaust outlet. Consequently, extremely high agitation speeds were required to maintain the desired dissolved oxygen concentration at the set gas flow rate. As the agitation rate surpassed 1500 rpm, the mechanical heating rate of the culture broth exceeded the cooling system's ability to maintain the desired temperature. As a result, a temperature fail condition resulted at 8 hours with the fermenter temperature rising to 32 or 33°C. The dissolved oxygen controller setpoint was adjusted down 10 mm Hg when this condition was discovered; the resulting drop in agitation speed allowed the fermenter cooling system to bring the temperature back to the setpoint. At 11 hours, the temperature fail condition occurred again, and the same corrective

action was taken. Finally, this complete cycle reoccurred at 12.5 hours before the fermentation was discontinued.

Figure 7.16 describes the time evolution of culture fluorescence, μ_{NFU}, and carbon dioxide and oxygen off-gas concentrations of this particular fermentation. Clearly, there are increases in slope in the normally exponential culture fluorescence curve at 7.8, 11.2 and 12.7 hours. Under balanced growth conditions, μ_{NFU} typically averages about 0.32 hr^{-1}. This figure demonstrates dramatically the increases caused to normally constant μ_{NFU} (under balanced growth) by the slight increases in temperature. In particular, μ_{NFU} detects the increase evident in the culture fluorescence trajectory at 7.8 hours as early as 6.8 hours. Also, between 8.5 and 11.2 hours, μ_{NFU} is abnormally high, suggesting again an unfavorable temperature level. (Unfortunately, temperature levels were not recorded throughout the experiment except at temperature-control fail conditions.) Observation of these conditions directly from the culture fluorescence curve would be extremely difficult and, at the very least, probably belated.

Clearly, as the temperature rises, NAD(P)H levels increase. All enzymes have temperature optima; if moved outside this optimum, specific activity drops. Therefore, temperature maintenance is critical to the fermentation process. As the off-gas concentration curves indicate, carbon dioxide production and oxygen consumption levels increase because of these changes in temperature, dropping after the temperature setpoint is restored. As seen with the previous nutrient limitation cases, increasing NAD(P)H levels signals cellular stress.

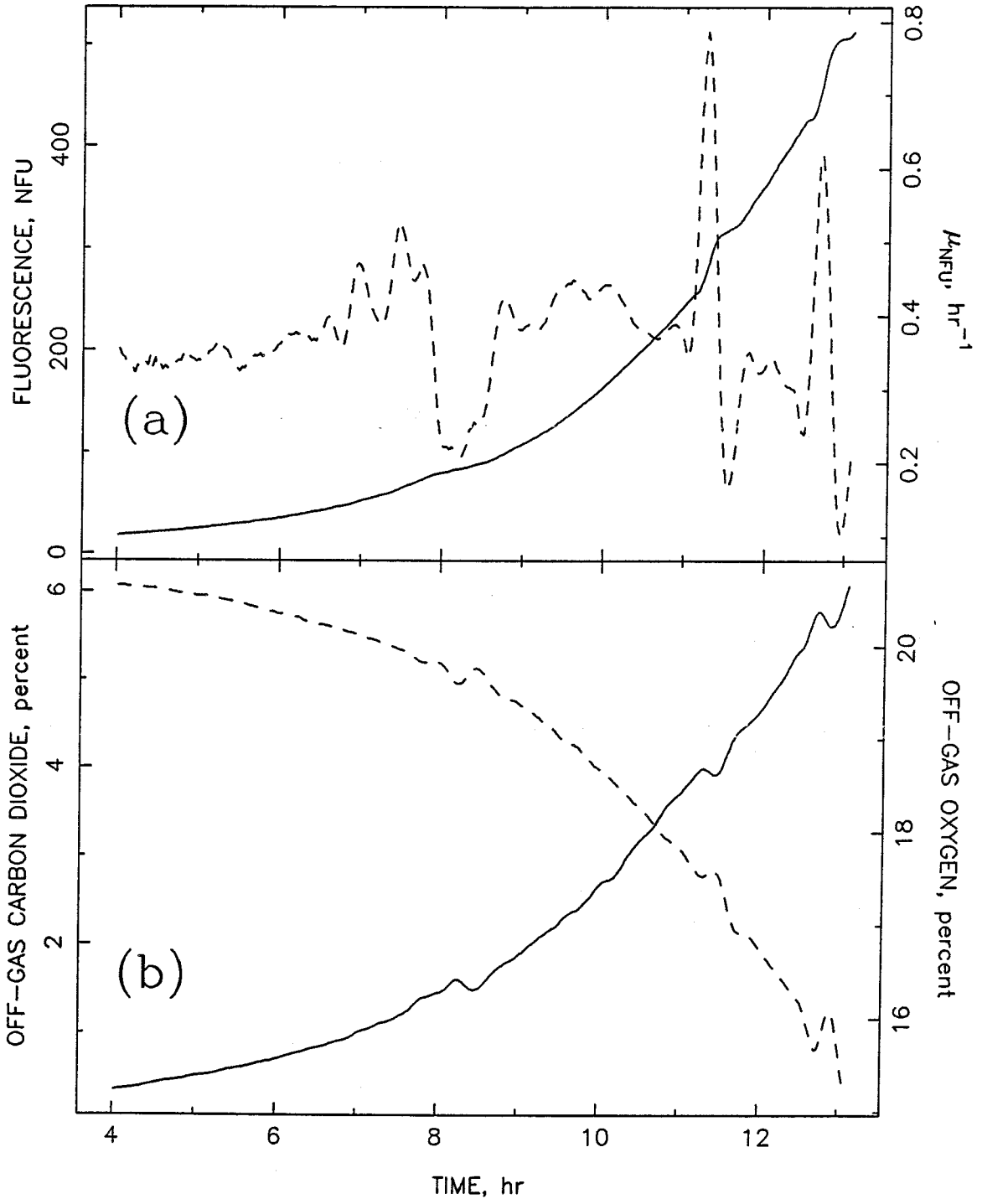

Figure 7.16: Temperature fluctuation experiment. **(a)** Culture fluorescence, ——— ; normalized rate of increase in fluorescence, μ_{NFU}; ····· . **(b)** Off-gas carbon dioxide, ——— ; off-gas oxygen, – – – .

7.7.2 Foreign Substances

Culture fluorescence can also be used for the detection of foreign substances in the growth media, should they have adverse or even beneficial effects. Figure 7.17 describes an unusually large transient in the culture fluorescence shortly after inoculation. Prior to this fermentation, the fermenter had been used for a high density *E. coli* fermentation, using highly enriched media. Apparently, although the fermenter had been thoroughly cleaned before this reported fermentation, some residual material must have been retained. In the course of 1.5 hours, the culture fluorescence increased nearly 500% (assuming an average baseline value of 20 NFU) before returning to its baseline value. No deleterious effects were observed throughout the rest of the fermentation. If this change is entirely due to the increase in NAD(P)H, this suggests that virtually all of the nicotinamide adenine dinuceotide pool is in the reduced state, assuming a NAD(P)H/[NAD(P)+NADP(P)H] ratio of 0.2.

It is difficult to say what caused this phenomenon. Several possible explanations are: (1) consumption of an unknown species, which had a direct effect on the cell's metabolism through the use of a secondary pathway; (2) the species partially blocked oxidation of NAD(P)H before it could be degraded; or (3) the species' degradation produced a fluorophore intermediate, which was subsequently degraded.

The next three fermentations, with one or two *E. coli* fermentations interspersed, demonstrated similar results. A long series of *A. eutrophus* fermentations prior to the *E. coli* fermentations showed no sign of this phenomenon.

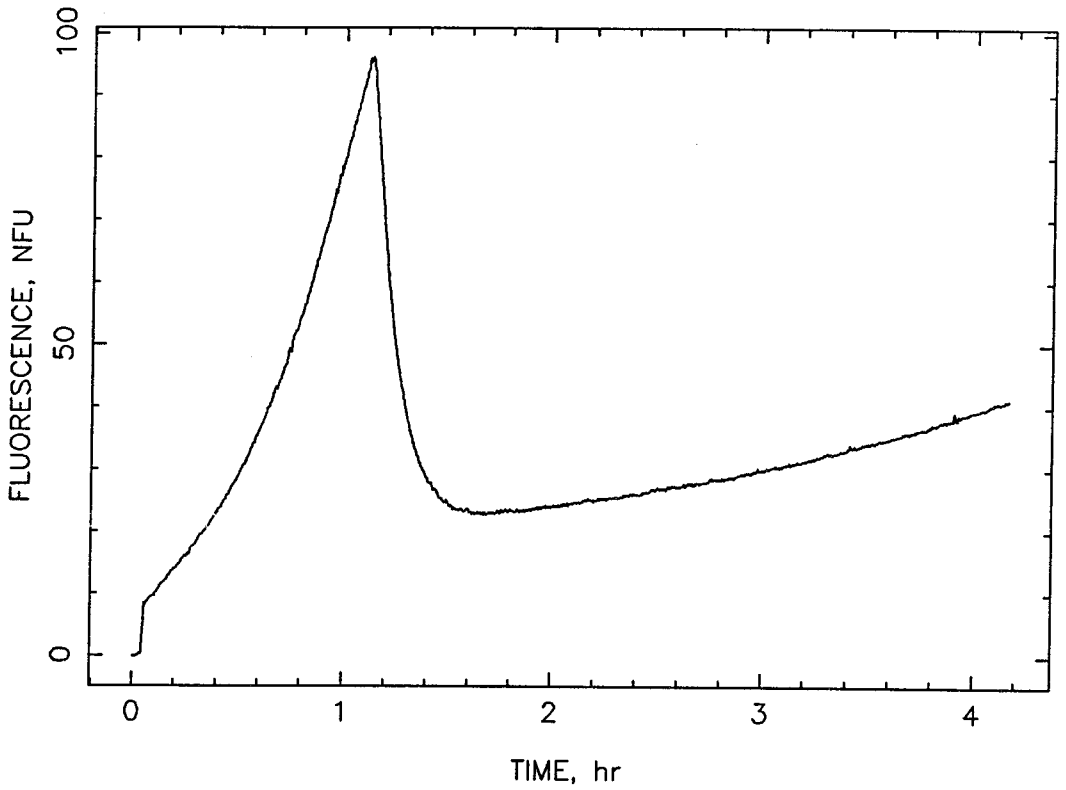

Figure 7.17: Influence of foreign substance experiment: raw, background corrected, unsmoothed culture fluorescence. Note that inoculation raises culture fluorescence from zero to almost 10 NFU shortly after time zero.

7.8 CONCLUSIONS

As Meyer *et al.*[3] have indicated, the use of culture fluorescence varies with each organism. In the case of *Alcaligenes eutrophus* H16, culture fluorescence, as an indicator of NAD(P)H levels, is uniquely related to PHB synthesis because of the relationship between elevated NAD(P)H levels and increased intrinsic PHB levels. In particular, the relationship between specific fluorescence and the intrinsic PHB concentration appears to be closely related in most cases.

From a process-monitoring standpoint, the use of the normalized rate of increase in culture fluorescence, μ_{NFU}, may have applicability as an on-line, *in situ* indicator of increased PHB synthesis activity as well as a monitor of undesirable fermentation conditions.

7.9 REFERENCES

1. Scheper, T., Lorenz, T., Schmidt, W., and Schügerl, K., *J. Biotechnol.*, **3**, 231 (1986).

2. Reardon, K.F., Scheper, T., and Bailey, J.E., *Biotechnol. Prog.*, **3**, 153 (1987).

3. Meyer, H.-P., Beyeler, W., and Fiechter, A., *J. Biotechnol.*, **1**, 341 (1984).

4. Luong, J.H.T., and Carrier, D.J., *Appl. Microbiol. Biotechnol.*, **24**, 65 (1986).

5. Scheper, T., and Schügerl, K., *Appl. Microbiol. Biotechnol.*, **23**, 440 (1986).

6. Zabriskie, D.W., and Humphrey, A.E., *Appl. Environ. Microbiol.*, **35**, 337 (1978).

7. Watteeuw, C.M., Armiger, W.B., Ristroph, D.L., and Humphrey, A.E., *Biotechnol. Bioeng.*, **21**, 1221 (1979).

8. Scheper, T., Gebauer, A., Sauerbrei, A., Niehoff, A., and Schügerl, K., *Anal. Chim. Acta*, **163**, 111 (1984).

9. Srinivas, S.P., and Mutharasan, R., *Biotechnol. Lett.*, **9**, 139 (1987).

10. Anders, K.-D., Müller, W., and Scheper, T. (in press).

11. Groom, C.A., Luong, J.H.T., and Mulchandani, A., *J. Biotechnol.*, **8**, 271 (1988).

12. Byrom, D., *TIBTECH*, **3**, 245 (1987).

13. Srinivas, S.P., and Mutharasan, R., *Biotechnol. Bioeng.*, **30**, 769 (1987).

14. Glaeser, H., and Schlegel, H.G., *Arch. Microbiol.*, **86**, 327 (1972).

15. Oeding, V., and Schlegel, H.G., *Biochem. J.*, **134**, 239 (1973).

16. Senior, P.J., and Dawes, E.A., *Biochem. J.*, **134**, 225 (1973).

17. Gottshalk, G., and Eberhardt, U., and Schlegel, H.G., *Arch. Mikrobiol.*, **48**, 95 (1964).

18. Schlegel H.G., Gottschalk G., and Bartha R., *Nature*, **191**, 463 (1961).

19. Pfennig, N., and Lippert, K.D., *Arch. Mikrobiol.*, **55**, 245 (1966).

20. Braunegg, G., Sonnleitner, B., and Lafferty, R.M., *Appl. Microbiol. Biotech.*, **6**, 29 (1978).

21. Lee, C., and Lim, H., *Biotechnol. Bioeng.*, **22**, 637 (1980).

22. Savitzky, A., and Golay, M.J.E., *Anal. Chem.*, **36**, 1627 (1964).

23. Steiner, J., Termonia, Y., and Deltour, J., *Anal. Chem.*, **44**, 1906 (1972).

24. Heinzle, E., and Lafferty, R.M., *Eur. J. Appl. Microbiol.*, **11**, 8 (1980).

25. Bowien, B., Cook, A.M., and Schlegel, H.G., *Arch. Microbiol.*, **97**, 273 (1974).

26. Siano, S.A., and Mutharasan, R., *Biotechnol. Bioeng.*, **34**, 66 (1989).

27. Mas, J., Pedrós-Alió, C., and Guerrero, R., *J. Bact.*, **164**, 749 (1985).

28. Pedrós-Alió, C., Mas, J., and Guerrero, R., *Arch. Microbiol.*, **143**, 178 (1985).

29. Blackkolb, F., and Schlegel, H.G., *Arch. Microbiol.*, **63**, 177 (1968).

30. Tunail, N., and Schlegel, H.G., *Biochem. Biophys. Comm.*, **49**, 1554 (1972).

31. Wilke, D., and Schlegel, H.G., *Arch. Microbiol.*, **105**, 109 (1975).

32. Richards, J.W., *Ind. Microbiol.*, **3**, 143 (1961).

33. Bailey, J.E., and Ollis, D.F., *Biochemical Engineering Fundamentals*, 2^{nd} ed., McGraw-Hill Book Company, New York (1986).

34. Silverman, M., Martin, M., and Engebrecht, J., *Genetics of Bacterial Diversity*, Hopfield, D.A., and Chater, R.F. eds., Academic Press, Harcourt Brace Jovanovich, Publishers, New York (1989), page 71.

35. Schlegel, H.G., and Vollbrecht, D., *J. Gen. Microbiol.*, **117**, 475 (1980).

36. Haywood, G.W., Anderson, A.J., Chu, J., and Dawes, E.A., *FEMS Microbiol. Lett.*, **52**, 91 (1988).

CHAPTER 8

THEORETICAL APPLICATION OF A METABOLIC MODEL — THEME AND VARIATIONS

8.1 INTRODUCTION

In previous chapters, a metabolic model for evaluation of *Alcaligenes eutrophus* H16's metabolism was proposed and used as a basis for analysis of the cell's growth and PHB synthesis metabolic responses to varying fermentation conditions. In this chapter, the model framework is extended to other applications. Focusing upon the associated intracellular balances on acetyl-CoA, ATP and NADH, a network linking the five metabolic pathways through the intracellular balances will be proposed and used to further analyze *Alcaligenes eutrophus* H16's metabolism as well as to provide a mechanism for confirming the validity of the overall pathway model. Finally, extension of this model for use in simulation of *A. eutrophus* metabolism will be discussed.

Beginning with the intracellular balances presented in Chapter 2, the associated undetermined metabolic parameters, such as the oxidative phosphorylation ratio (P/O), the ATP yield coefficient (Y_{ATP}^{max}), and the ATP maintenance coefficient ($m_{ATP,e}$), will be evaluated and average values proposed. Using the closed intracellular balances to simulate *A. eutrophus*'s metabolism under different fermentation conditions, the choice of metabolic parameters as well as the applicability of the intracellular balances will be evaluated relative to comparisons made with previous experimental results. The model will then be extended to include mathematical expressions for kinetics of selected pathways and used as a predictive tool; the result of this formulation again will be compared to

experimental results. Finally, some logical extensions of the model will be identified and discussed.

8.2 EVALUATION OF INTRACELLULAR METABOLIC BALANCE PARAMETERS

In Chapter 2, the metabolic, intracellular balances for acetyl-CoA, ATP, and NADH were derived; in this chapter, they form the foundation upon which the present development is based. Eq. (2.36) represents the intracellular balance on acetyl-CoA, Eq. (2.37) represents the intracellular balance on ATP, and Eq. (2.38) represents the intracellular balance on NADH for the metabolic pathways identified in the model.

$$\frac{dc_{AcCoA}}{dt} = \frac{1}{2}\left[\mathbf{v}_1 - \mathbf{v}_2 - \mathbf{v}_3\right] \tag{2.36}$$

$$\frac{dc_{ATP}}{dt} = \frac{1}{4}\mathbf{v}_1 + \frac{1}{2}\mathbf{v}_2 - \frac{1}{\mathrm{Y_{ATP}}}\mathbf{v}_B + (\mathrm{P/O})\mathbf{v}_R \tag{2.37}$$

$$\frac{dc_{NADH}}{dt} = \mathbf{v}_1 + 2\mathbf{v}_2 - \frac{1}{4}\mathbf{v}_3 - \mathbf{v}_R - \frac{1}{\mathrm{Y_{NADH}}}\mathbf{v}_B, \tag{2.38}$$

where $$\frac{1}{\mathrm{Y}_i} \equiv \frac{1}{\mathrm{Y}_i^{\max}} + \frac{\mathrm{m}_{i,e}}{\mu} \tag{2.39}$$

$$\equiv \frac{1}{(\mathrm{Y}_i^{\max})_{\mathrm{th}}} + \mathrm{m}_{i,g} + \frac{\mathrm{m}_{i,e}}{\mu}. \tag{2.40}$$

$\mathbf{v}_i$ represents the product production rate in the i^{th} pathway. Eqs. (2.39) and (2.40) identify the different representations of the yield coefficients used by most researchers.[1] The specific growth rate is symbolized by μ. For purposes of simplification, only Eq. (2.39) will be used in estimating the ATP and NADH yield

and maintenance coefficients. Therefore, five metabolic parameters require evaluation: the ATP and NADH yield coefficients, Y_{ATP}^{max} and Y_{NADH}^{max}, respectively, the ATP and NADH maintenance coefficients, $m_{ATP,e}$ and $m_{NADH,e}$, respectively, and the oxidative phosphorylation ratio, P/O.

As Stouthamer has noted,[1] these metabolic parameters are not generally growth-rate independent. Since the dependencies of these parameters relative to varying growth conditions are unclear, an attempt is made to obtain an average value for these parameters, suitable for a broad range of experimental data. To achieve this, a quasi-steady-state assumption is applied; *i.e.*, it is assumed that the time rate of change of the intracellular concentrations, $\frac{d\mathbf{c}_i}{dt}$, are small relative to all other terms in the balance. Experimental pathway flux data utilizing a least-squares approach is then implemented to evaluate the five metabolic parameters. Clearly, this is unnecessary for the acetyl-CoA balance since all the coefficients are stoichiometrically determined. However, the acetyl-CoA balance will be called into service later to facilitate evaluation of parameters in the ATP balance.

8.2.1 NADH Balance

From Eq. (2.38), two metabolic constants, Y_{NADH}^{max} and $m_{NADH,e}$ influence the calculated time derivative of the NADH intracellular concentration. Considering only the PHB storage phase, thereby eliminating the influence of Y_{NADH}^{max} ($\mathbf{v}_B = 0$), a direct determination of $m_{NADH,e}$ was made, assuming that $m_{NADH,e}$ did not vary between growth and PHB storage regimes. In investigating the appropriate fermentation data, an average value of 0.09 mmol NADH/((g

biomass)(hr)) was obtained, suggesting that $m_{NADH,e}$ was negligible. Applying the intracellular NADH balance to the growth phase of several experiments and forcing $m_{NADH,e}$ to zero resulted in a dramatic reduction in the previously observed Y_{NADH}^{max} oscillations when $m_{NADH,e}$ was freely adjustable; Y_{NADH}^{max} was bounded between 2 and 3.2 C-mol biomass/mol NADH with an average of 2.9 C-mol biomass/mol NADH. These results are consistent with previous metabolic models in which the contribution of NADH to maintenance activities is typically disregarded.

8.2.2 ATP Balance

Considering the ATP balance in Eq. (2.37), three parameters require evaluation, Y_{ATP}^{max}, P/O, and $m_{ATP,e}$. Four oxidative phosphorylation sites have been identified in *Alcaligenes eutrophus* H16, suggesting that P/O should be nonnegative and less than or equal to four.[2] Using a P/O ratio of 3.85, Drozd and Jones[3] calculated a Y_{ATP}^{max} of 13.0 g biomass/mol ATP, ignoring substrate-level phosphorylation. Under heterotrophic growth, complete degradation of fructose via the Entner-Doudoroff pathway[21] and the citric acid cycle results in the formation of 12 NADH and 3 ATP. Assuming a P/O of 3.85, the value of Y_{ATP}^{max} can be corrected to 12.2 g biomass/mol ATP. Considering a formula weight of 26 g/C-mol for *A. eutrophus* biomass, Y_{ATP}^{max} converts to 0.47 C-mol biomass/mol ATP. There was no indication as to whether the value of Y_{ATP}^{max} calculated by Drozd and Jones was corrected for PHB content. Typically, this correction is not made. Therefore, Y_{ATP}^{max} can be considered to be bounded between zero and 0.47 C-mol biomass/mol ATP.

No data for the ATP maintenance term, $m_{ATP,e}$, were found in the literature. An estimate of the bounds on $m_{ATP,e}$, however, can be made from PHB storage-phase data. No biomass synthesis occurs in the PHB phase, thereby eliminating the contribution by Y_{ATP}^{max}; *i.e.*, $\mathbf{v}_B = 0$. By assuming alternatively that P/O equals zero or 3.85, lower and upper limits of 1.3 and 17 mol ATP/((g biomass)(hr)), respectively, were calculated for $m_{ATP,e}$. This range is in good agreement with reported $m_{ATP,e}$ values for other organisms.[1,16]

A search was conducted to identify a technique in which the constrained metabolic ATP balance parameters could vary without any single parameter being consistently minimized or maximized. Closing the intracellular balances, *i.e.*, invoking the quasi-steady state assumption, allowed solution of any three dependent pathway rates, given any two independent pathway rates. Setting Y_{NADH}^{max} and $m_{NADH,e}$ equal to their previously determined values (see Table 8.1), the ATP balance metabolic parameters were determined for each experiment, based on the minimization of the sum of the squares of the residuals as follows:

$$\sum_n (\text{Residual})_{ij}^2 = \sum_n \left(\frac{|\Delta \mathbf{v}_k|}{\mathbf{v}_k} + \frac{|\Delta \mathbf{v}_l|}{\mathbf{v}_l} + \frac{|\Delta \mathbf{v}_m|}{\mathbf{v}_m} \right)^2, \qquad (8.1)$$

where $(\text{Residual})_{ij}$ represents the residual from the n^{th} observation calculated using pathways fluxes $\mathbf{v}_i$ and $\mathbf{v}_j$, and $\frac{|\Delta \mathbf{v}_k|}{\mathbf{v}_k}$ represents the absolute difference between the calculated $\mathbf{v}_k$ and the experimentally observed $\mathbf{v}_k$ normalized by the experimentally observed $\mathbf{v}_k$.

Relative to other techniques pursued, this approach yielded the most satisfactory behavior; all three parameters varied freely. Although cases existed where one of the ATP balance parameters was either maximized or minimized,

there were no consistent patterns of maximized or minimized parameter values as had been previously obtained by fitting the intracellular ATP balance alone. For each experiment, the three ATP metabolic parameters were calculated, using each of ten differing independent experimental pathway flux sets; metabolic parameters from each experiment calculated with the same pathway flux set; *e.g.*, $\mathbf{v}_R$ and $\mathbf{v}_2$ used to calculate $\mathbf{v}_B$, $\mathbf{v}_1$, and $\mathbf{v}_3$, were averaged. The averaged results from each pathway flux set calculation were then further combined and averaged. The results of this approach are included in Table 8.1

TABLE 8.1: Summary of averaged intracellular balance metabolic parameters

Metabolic Parameter*	Parameter Value
Y_{ATP}^{max}	0.34
Y_{NADH}^{max}	2.9
P/O	2.5
$m_{ATP,e}$	9.8
$m_{NADH,e}$	0

*$Y_i^{max} \equiv$ C-mol biomass/mol i; $m_{i,e} \equiv$ mmol i/((g biomass)(hr)); P/O $\equiv$ mol ATP/mol O.

8.2.3 Metabolic Parameter Validity Check

To briefly verify the validity of the determined metabolic parameters, a comparison with normal balanced growth conditions was considered. Selecting balanced growth pathway fluxes for $\mathbf{v}_B$ and $\mathbf{v}_3$ of 14.0 C-mmol biomass/((g biomass)(hr)) and 2.3 C-mmol PHB/((g biomass)(hr)), respectively, values of

17.7 mmol H_2O/((g biomass)(hr)), 9.2 C-mmol AcCoA/((g biomass)(hr)), and 6.9 mmol CO_2/((g biomass)(hr)) were calculated for $\mathbf{v}_R$, $\mathbf{v}_1$, and $\mathbf{v}_2$, respectively. These results compare quite well with those from balanced growth: 18.7 mmol H_2O/((g biomass)(hr)), 9.1 C-mmol AcCoA/((g biomass)(hr)), and 6.8 mmol CO_2/((g biomass)(hr)). Further adjustment in any of these metabolic parameter values does not significantly improve the calculated values of $\mathbf{v}_R$, $\mathbf{v}_1$, and $\mathbf{v}_2$. Only decreasing Y_{NADH}^{max} increases the value of $\mathbf{v}_R$ while decreasing both $\mathbf{v}_1$ and $\mathbf{v}_2$. Unfortunately, the relative changes in $\mathbf{v}_1$ and $\mathbf{v}_2$ are much larger than the change in $\mathbf{v}_R$, suggesting that adjustment of Y_{NADH}^{max} provides little or no benefit. It should be noted that although $\mathbf{v}_R$ appears to be low, it is well within one standard deviation of its balanced growth value (see Chapter 3).

Comparing early and late PHB storage pathway rates, an inadequacy surfaces in the model, given the constant parameter values listed in Table 8.1. Setting $\mathbf{v}_B$ to zero, thereby eliminating the contributions of Y_{ATP}^{max} and Y_{NADH}^{max}, and choosing 5.5/2.9 C-mmol PHB/((g biomass)(hr)) (early storage phase/late storage phase) for $\mathbf{v}_3$ result in calculated pathway flux values from the closed intracellular of balances 3.4/3.4 mmol H_2O/((g biomass)(hr)), 5.3/3.3 C-mmol AcCoA/((g biomass)(hr)), and -0.2/0.4 mmol CO_2/((g biomass)(hr)) for $\mathbf{v}_R$, $\mathbf{v}_1$, and $\mathbf{v}_3$, respectively. These values compare to the experimentally determined observed pathway rates of 5.8/3.0 mmol H_2O/((g biomass)(hr)) for $\mathbf{v}_R$, 5.6/3.0 C-mmol AcCoA/((g biomass)(hr)) for $\mathbf{v}_1$, and 0.6/0.4 mmol CO_2/((g biomass)(hr)) for $\mathbf{v}_2$. Except for $\mathbf{v}_1$, the agreement is not nearly so good as with the normal balanced growth example.

Two possible explanations for rationalizing the discrepancy between the PHB storage phase pathway flux values calculated from the closed intracellular balances and those calculated from the earlier pathway model. One is that P/O drops after the cessation of growth; the second is that $m_{ATP,e}$ increases. Both of these changes would dramatically increase $\mathbf{v}_R$ because of lower ATP formation efficiency or higher ATP demand while only increasing $\mathbf{v}_1$ and $\mathbf{v}_2$ a small amount. Of the two possibilities, the increase in $m_{ATP,e}$ is most probable from a physiological standpoint. As the cell accumulates PHB, there is an enormous increase in surface area. Mas *et al.*[4] have investigated this phenomenon and found an average increase in the surface area of *A. eutrophus* from 7.5 to 12.5 μm^2 with no volume change in the cell water as the cell accumulates from 0 to 96% PHB by dry cell weight. From a mass transfer standpoint, this change in cell surface area increases the area for passive proton flux across the membrane. Therefore, the cell must exert larger amounts of energy to maintain the proper membrane potential and ionic ratios. From a culture fluorescence standpoint (see Chapter 7), however, a decrease in P/O may be favored because of the accumulation of NADH; a lower P/O would allow higher consumption rates of NADH without producing glycolysis, citric acid cycle and pyruvate kinase pathway inhibition by ATP.[17–20]

The fact that $\mathbf{v}_R$ does not change and $\mathbf{v}_2$ increases, rather than both pathway rates decreasing during PHB storage phase, strongly suggests that other mechanisms are occurring that are not accounted for through closure of the intracellular balances with constant parameter values. $m_{ATP,e}$ or P/O may be changing independently or in concert for reasons previously mentioned. Alter-

natively, the cell may be expending energy to allow for restructuring within the cell to accommodate the large increase in intracellular PHB reserves. In any case the constant parameter model appears to be qualitative only with respect to its response to this metabolic regime. This is not very surprising, however, since the majority of the fermentation data used to determine the intracellular metabolic parameters involved varying degrees of cell growth rather than no cell growth as in the case of PHB storage.

8.3 VALIDATION OF INTRACELLULAR METABOLIC BALANCES

As a more sophisticated validation of the closed intracellular balance equations' predictive properties, an investigation was pursued utilizing the results gathered from a number of experiments. Choosing the time evolutions of any two pathway rates and evaluating the intracellular model on the basis of their experimental pathway flux data, the other three dependent pathway rates were calculated and compared to their observed values. This provided an evaluation of the appropriateness of the intracellular balance portion of the model, a further validation of the overall pathway network model developed in Chapter 2, and an evaluation of the invariance of the intracellular parameter values in Table 8.1 over differing cell fermentation environments. Also comparing computed pathway rates with observed pathway rates indicated circumstances under which other mechanisms within the *A. eutrophus* cells were operating, which were not

accounted for in the model formulation.

The five experiments utilized in this analysis have been previously described in detail in Chapters 2–7. These experiments are ammonium exhaustion, ammonium limitation, oxygen limitation, fructose exhaustion/limitation, and phosphate limitation/exhaustion. Refer to the appropriate chapters for a complete description of these experiments.

In order to assess sensitivity of the calculations to errors in the observed pathway rates, the method suggested by Liao[5] was employed. These calculations indicated that use of $\mathbf{v}_B$ and $\mathbf{v}_R$ as basis functions would be undesirable for calculation of the remaining pathway rates. The method was inconclusive with respect to suitability of other pairs of basis functions. Consequently, numerical calculations were conducted using different pairs of pathway rates as bases for determining the others. The qualitative results of these calculations may be summarized as follows:

$\mathbf{v}_B$ & $\mathbf{v}_R$: Consistently poor results: calculated $\mathbf{v}_1$, $\mathbf{v}_2$, and $\mathbf{v}_3$ values made observed rates appear as lines when plotted on the same axis.

$\mathbf{v}_B$ & $\mathbf{v}_1$: $\mathbf{v}_R$ grossly overestimated; $\mathbf{v}_2$ underestimated; $\mathbf{v}_3$ deviated noticeably.

$\mathbf{v}_B$ & $\mathbf{v}_2$: $\mathbf{v}_R$ dominated by $\mathbf{v}_B$ contribution; worst $\mathbf{v}_1$ calculation; $\mathbf{v}_3$ deviated noticeably.

$\mathbf{v}_B$ & $\mathbf{v}_3$: $\mathbf{v}_R$ dominated by $\mathbf{v}_B$ contribution; $\mathbf{v}_2$ underestimated.

$\mathbf{v}_R$ & $\mathbf{v}_1$: $\mathbf{v}_B$ dominated by $\mathbf{v}_R$ contribution; best $\mathbf{v}_3$ calculation.

$\mathbf{v}_R$ & $\mathbf{v}_2$: $\mathbf{v}_B$ dominated by $\mathbf{v}_R$ contribution.

$\mathbf{v}_R$ & $\mathbf{v}_3$: $\mathbf{v}_B$ dominated by $\mathbf{v}_R$ contribution; best $\mathbf{v}_1$ and $\mathbf{v}_2$ calculations.

$\mathbf{v}_1$ & $\mathbf{v}_2$: Good $\mathbf{v}_R$ calculation; good $\mathbf{v}_B$ calculation.

$\mathbf{v}_1$ & $\mathbf{v}_3$: Good $\mathbf{v}_R$ calculation; good $\mathbf{v}_B$ calculation.

$\mathbf{v}_2$ & $\mathbf{v}_3$: Good calculation of $\mathbf{v}_B$.

To examine the specific effectiveness of the use of the intracellar balances under different fermentation conditions, the previously identified experiments are analyzed in the following sections.

8.3.1 Ammonium Exhaustion

Figure 8.1 compares the best two calculated pathway rates to those observed for the ammonium exhaustion experiment described in Chapter 2. In virtually all cases the calculated biosynthesis activity underestimated the experimentally observed $\mathbf{v}_B$ value (0–30%). However, agreement during ammonium exhaustion was excellent.

All calculations utilizing $\mathbf{v}_B$ tended to overestimate $\mathbf{v}_R$ (0–50%), while calculations using some combination of $\mathbf{v}_1$, $\mathbf{v}_2$, or $\mathbf{v}_3$ tended to underestimate $\mathbf{v}_R$ (0–25%). Because of the values of P/O, Y_{ATP}^{max} and the relative magnitudes of $\mathbf{v}_B$ and $\mathbf{v}_R$, ATP production and consumption strongly link $\mathbf{v}_B$ and $\mathbf{v}_R$ via Eq. (2.37). The fact that calculations using $\mathbf{v}_R$ overestimated $\mathbf{v}_B$ and calculations using $\mathbf{v}_B$ underestimated $\mathbf{v}_R$ suggests that Y_{ATP}^{max} and/or P/O are/is too high. If Y_{ATP}^{max} and P/O are correct, there must be another mechanism that is a sink for ATP, indicating that an increase in $m_{ATP,e}$ may be appropriate.

Figure 8.1: Ammonium exhaustion experiment. All observed pathway rates denoted by ——— . **(a)** $\mathbf{v}_B$ calculated from $\mathbf{v}_R$ and $\mathbf{v}_2$, – – – ; $\mathbf{v}_B$ calculated from $\mathbf{v}_1$ and $\mathbf{v}_3$, ····· . **(b)** $\mathbf{v}_R$ calculated from $\mathbf{v}_B$ and $\mathbf{v}_2$, – – – ; $\mathbf{v}_R$ calculated from $\mathbf{v}_1$ and $\mathbf{v}_2$, ····· . **(c)** $\mathbf{v}_1$ calculated from $\mathbf{v}_B$ and $\mathbf{v}_3$, – – – ; $\mathbf{v}_1$ calculated from $\mathbf{v}_R$ and $\mathbf{v}_3$, ····· . **(d)** $\mathbf{v}_2$ calculated from $\mathbf{v}_B$ and $\mathbf{v}_3$, – – – ; $\mathbf{v}_2$ calculated from $\mathbf{v}_R$ and $\mathbf{v}_3$, ····· . **(e)** $\mathbf{v}_3$ calculated from $\mathbf{v}_B$ and $\mathbf{v}_1$, – – – ; $\mathbf{v}_3$ calculated from $\mathbf{v}_R$ and $\mathbf{v}_1$, ····· .

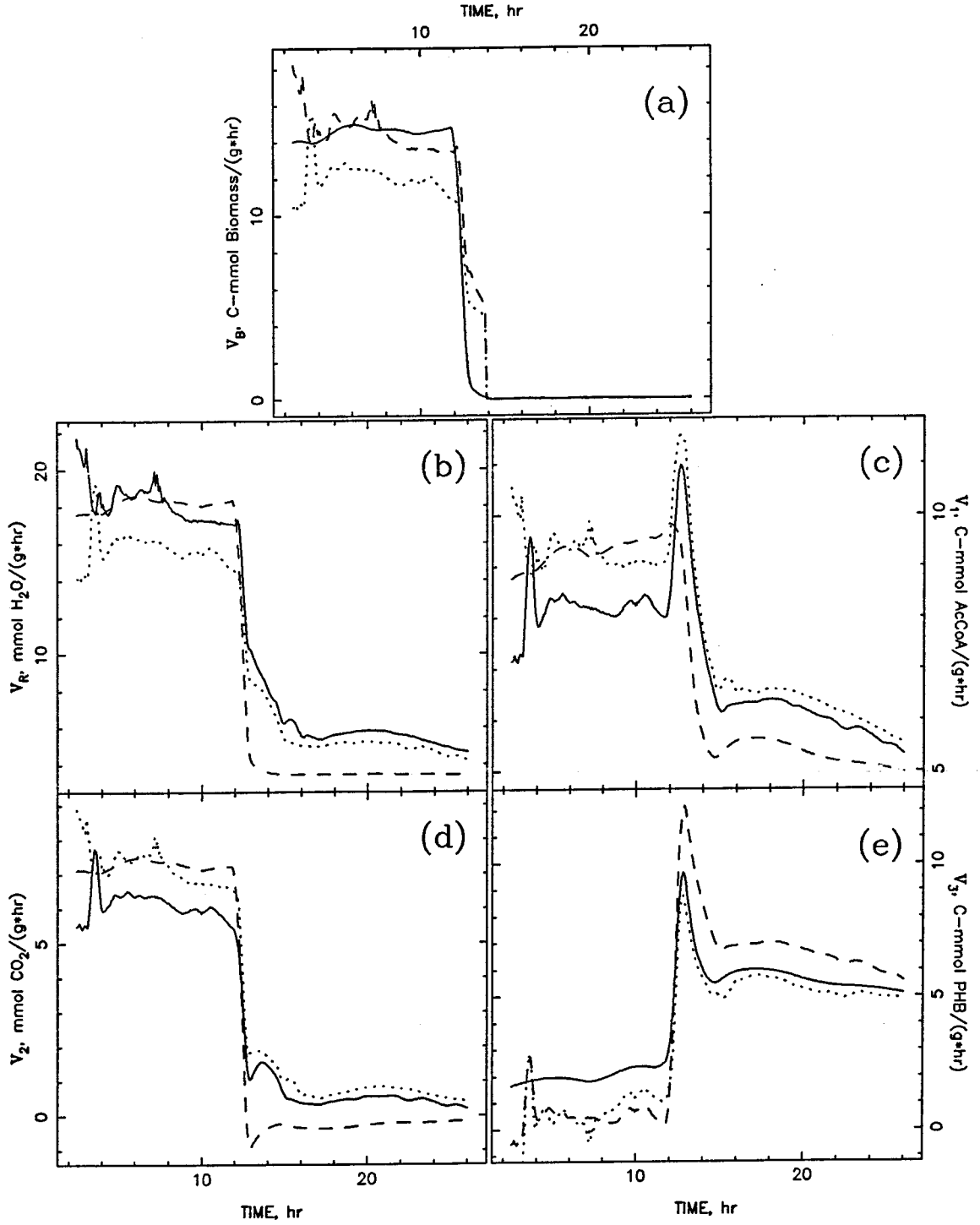
TIME, hr
10
20
(a)
V_B, C-mmol Biomass/(g*hr)
0
10
(b)
V_R, mmol H_2O/(g*hr)
20
(c)
V_1, C-mmol AcCoA/(g*hr)
5
10
(d)
V_2, mmol CO_2/(g*hr)
0
5
(e)
V_3, C-mmol PHB/(g*hr)
0
5
10
TIME, hr
10
20
TIME, hr

Figure 8.1

With regard to glycolysis activity, calculation using $\mathbf{v}_B$ and $\mathbf{v}_3$ gave qualitative results (0–25%), while both $\mathbf{v}_R$ calculations gave comparatively better results.

$\mathbf{v}_R$ and $\mathbf{v}_B$ dominated and overestimated all calculations of citric acid cycle activity. Calculations with $\mathbf{v}_R$ tended to overestimate $\mathbf{v}_2$ in storage phase, while calculations with $\mathbf{v}_B$ tended to underestimate $\mathbf{v}_2$. During growth, the $\mathbf{v}_R$ calculations approximated $\mathbf{v}_2$ to within 15%, while the $\mathbf{v}_B$ calculations were only within 30%.

Finally, none of the calculations of $\mathbf{v}_3$ resulted in very good fits during the growth phase. The fits were much improved during PHB storage phase, with the calculation from $\mathbf{v}_R$ and $\mathbf{v}_1$ being the best. The improved fits of all calculated pathways during PHB storage phase proved to be a common theme.

Clearly, the calculated pathway rates predicted the observed rates much better earlier in the growth phase than when ammonium exhaustion approached. This would seem to indicate the occurrence of a gradual shift in the cell's metabolism. Alternatively, as the next section indicates, the metabolism may be burdened by increased energy demand that is due to active ammonium transport, as the ammonium concentration decreases.

8.3.2 Ammonium Limitation

The most common trend in the calculations of the ammonium limitation experiment was the disparity between calculated pathway rates and observed pathway rates during the ammonium limitation portion of the experiment. Note

the sudden departure between the observed pathway rates and calculated pathway rates as ammonium becomes limiting at eight hours (Figure 8.2).

Given the fact that the *A. eutrophus* cells were ammonium-limited suggests that a larger fraction of the ATP energy generated was going to actively transport scarce extracellular ammonium resources.[6,7] Since the model does not specifically account for this mechanism, the model correlates a high respiration rate with a high biosynthesis rate. Similarly, since the actual biosynthesis rate was low, the model correlates this with a low respiratory rate. However, an approximate correction to Y_{ATP}^{max} can be made to incorporate this effect. From Chapter 2, for every C-mol of biomass, there is included 0.25 mol of nitrogen. Under balanced growth conditions, 2.92 mol ATP are required to synthesize one C-mol of biomass ($\equiv \frac{1}{Y_{ATP}^{max}}$). If for every nitrogen atom incorporated, one ATP molecule is required to actively transport one ammonium molecule, 2.92 $\times$ 1.25 mol ATP are required to produce one C-mol biomass. Therefore, the approximate Y_{ATP}^{max} under these conditions is 0.274 C-mol biomass/mol ATP — a 20% reduction. Using theoretical calculations, Stouthamer[1] estimates that over 12% of ATP consumed to form one gram of biomass is used for ammonium ion transport in a glucose and mineral salts medium. Jahns *et al.*[7] have indicated that *Alcaligenes eutrophus* H16's ammonium active transport system is induced at ammonium levels below 0.1 g/l ammonium chloride. As suggested in the ammonium exhaustion case, Y_{ATP}^{max} may be too high; this supports that assertion.

Using the value of Y_{ATP}^{max} from Table 8.1, the calculated value of $\mathbf{v}_B$ was overestimated during ammonium limitation, while the fits during unlimited

Figure 8.2: Ammonium limitation experiment. All observed pathway rates denoted by ——— . **(a)** $\mathbf{v}_B$ calculated from $\mathbf{v}_R$ and $\mathbf{v}_2$, – – – ; $\mathbf{v}_B$ calculated from $\mathbf{v}_1$ and $\mathbf{v}_3$, ····· . **(b)** $\mathbf{v}_R$ calculated from $\mathbf{v}_B$ and $\mathbf{v}_2$, – – – ; $\mathbf{v}_R$ calculated from $\mathbf{v}_1$ and $\mathbf{v}_3$, ····· . **(c)** $\mathbf{v}_1$ calculated from $\mathbf{v}_B$ and $\mathbf{v}_3$, – – – ; $\mathbf{v}_1$ calculated from $\mathbf{v}_R$ and $\mathbf{v}_3$, ····· . **(d)** $\mathbf{v}_2$ calculated from $\mathbf{v}_B$ and $\mathbf{v}_3$, – – – ; $\mathbf{v}_2$ calculated from $\mathbf{v}_R$ and $\mathbf{v}_3$, ····· . **(e)** $\mathbf{v}_3$ calculated from $\mathbf{v}_B$ and $\mathbf{v}_1$, – – – ; $\mathbf{v}_3$ calculated from $\mathbf{v}_R$ and $\mathbf{v}_1$, ····· .

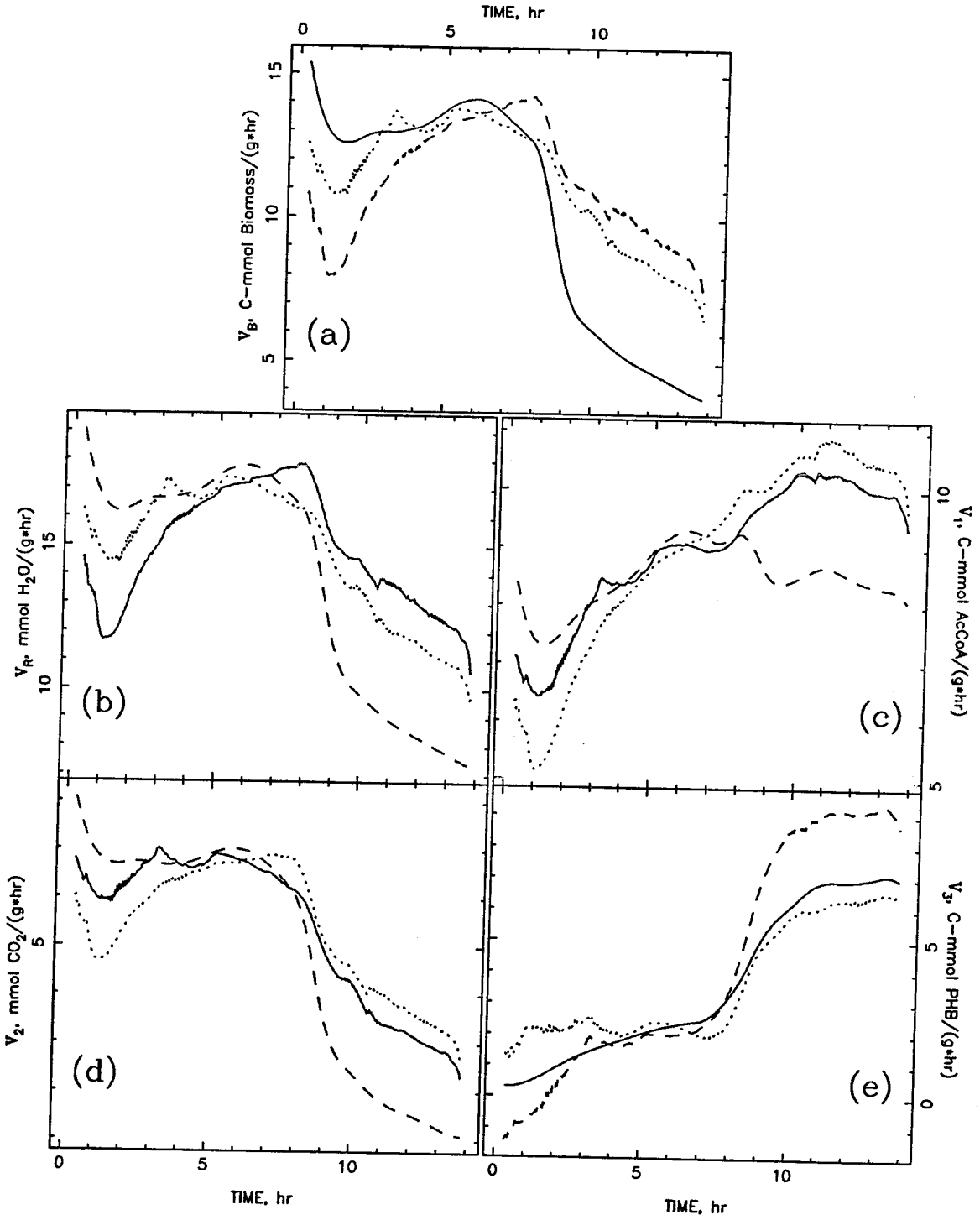
TIME, hr
0
5
10
15
10
5
V_B, C-mmol Biomass/(g*hr)
(a)
V_R, mmol H_2O/(g*hr)
(b)
V_1, C-mmol AcCoA/(g*hr)
(c)
V_2, mmol CO_2/(g*hr)
(d)
V_3, C-mmol PHB/(g*hr)
(e)
TIME, hr
TIME, hr

Figure 8.2

growth were very good. Likewise, calculations with $\mathbf{v}_B$ and $\mathbf{v}_2$ or $\mathbf{v}_3$ underestimated $\mathbf{v}_R$ (30%) during limitation while calculation with $\mathbf{v}_B$ and $\mathbf{v}_1$ overestimated $\mathbf{v}_R$ (5%, not shown), suggesting that $\mathbf{v}_1$ adequately compensated for the tendency of $\mathbf{v}_B$ to underestimate $\mathbf{v}_R$. Similarly, $\mathbf{v}_2$ and $\mathbf{v}_3$ together slightly overestimated $\mathbf{v}_R$ (5%, not shown), particularly during ammonium limitation. This can be attributed to the strong correlation between $\mathbf{v}_R$ and $\mathbf{v}_2$ through the NADH intracellular balance (Eq. (2.38)).

Calculation of $\mathbf{v}_1$ from combinations with $\mathbf{v}_B$ resulted in large underestimations — by as much as 50%. When $\mathbf{v}_B$ and $\mathbf{v}_2$ were used together, the result had the opposite trend (not shown), while calculations with $\mathbf{v}_B$ and $\mathbf{v}_3$ remained flat. Calculations with $\mathbf{v}_R$ had the same trend as the observed $\mathbf{v}_1$, beginning typically slightly below the observed value of $\mathbf{v}_1$ and ending slightly higher.

Although calculations of $\mathbf{v}_2$ using $\mathbf{v}_B$ were underestimated by as much as 65%, the trends were similar. Results with $\mathbf{v}_R$ and $\mathbf{v}_1$ or $\mathbf{v}_3$ were both very good through all portions of the fermentation.

In calculating $\mathbf{v}_3$, all results showed the correct trend except for $\mathbf{v}_B$ and $\mathbf{v}_3$ (not shown).

8.3.3 Oxygen Limitation

With regard to the calculation of biosynthesis activity under oxygen limitation conditions, generally the calculated value of $\mathbf{v}_B$ was overestimated; $\mathbf{v}_R$ and $\mathbf{v}_2$ or $\mathbf{v}_3$ gave the best results (Figure 8.3). Combinations of $\mathbf{v}_1$, $\mathbf{v}_2$, and $\mathbf{v}_3$

also overestimated $\mathbf{v}_B$ except during the first six hours, when $\mathbf{v}_B$ was underestimated.

Use of $\mathbf{v}_B$ and $\mathbf{v}_1$ as basis functions grossly overestimated $\mathbf{v}_R$ by as much as 50% (not shown). The other calculations with $\mathbf{v}_B$ qualitatively fit the observed $\mathbf{v}_R$ very well, with the fit being much better for the first oxygen limitation region than for the second limitation period. This may serve as an indication that the cell's metabolism is indeed shifting toward a more anaerobic regime as previously suggested in Chapter 4. $\mathbf{v}_1$ with $\mathbf{v}_2$ or $\mathbf{v}_3$ provides very good fits, underestimating $\mathbf{v}_R$ initially and slightly overestimating $\mathbf{v}_R$ throughout the rest of the experiment. Similarly $\mathbf{v}_2$ and $\mathbf{v}_3$ overestimate $\mathbf{v}_R$ with a flatter curve (not shown).

Calculations with $\mathbf{v}_2$ indicated trends in $\mathbf{v}_1$ that were generally opposite to those observed in $\mathbf{v}_1$ (not shown). $\mathbf{v}_B$ and $\mathbf{v}_3$ very generally followed the trend. $\mathbf{v}_R$ and $\mathbf{v}_3$ gave the best representation.

Except for the first six hours, calculations with $\mathbf{v}_B$ underestimated $\mathbf{v}_2$. In a similar fashion, calculations with $\mathbf{v}_R$ initially overestimated $\mathbf{v}_2$, while also underestimating $\mathbf{v}_2$ throughout the rest of the experiment.

Finally, trends from calculations with $\mathbf{v}_2$ were in the wrong direction when compared to $\mathbf{v}_3$. $\mathbf{v}_B$ and $\mathbf{v}_1$ along with $\mathbf{v}_R$ and $\mathbf{v}_1$ indicated the proper trends, although both began slightly negative.

8.3.4 Fructose Limitation/Exhaustion

Surprisingly, considering the large oscillations and changes throughout this

Figure 8.3: Oxygen limitation experiment. All observed pathway rates denoted by ——— . **(a)** $\mathbf{v}_B$ calculated from $\mathbf{v}_R$ and $\mathbf{v}_2$, − − − ; $\mathbf{v}_B$ calculated from $\mathbf{v}_1$ and $\mathbf{v}_2$, ····· . **(b)** $\mathbf{v}_R$ calculated from $\mathbf{v}_B$ and $\mathbf{v}_2$, − − − ; $\mathbf{v}_R$ calculated from $\mathbf{v}_1$ and $\mathbf{v}_2$, ····· . **(c)** $\mathbf{v}_1$ calculated from $\mathbf{v}_B$ and $\mathbf{v}_3$, − − − ; $\mathbf{v}_1$ calculated from $\mathbf{v}_R$ and $\mathbf{v}_3$, ····· . **(d)** $\mathbf{v}_2$ calculated from $\mathbf{v}_B$ and $\mathbf{v}_3$, − − − ; $\mathbf{v}_2$ calculated from $\mathbf{v}_R$ and $\mathbf{v}_3$, ····· . **(e)** $\mathbf{v}_3$ calculated from $\mathbf{v}_B$ and $\mathbf{v}_1$, − − − ; $\mathbf{v}_3$ calculated from $\mathbf{v}_R$ and $\mathbf{v}_2$, ····· .

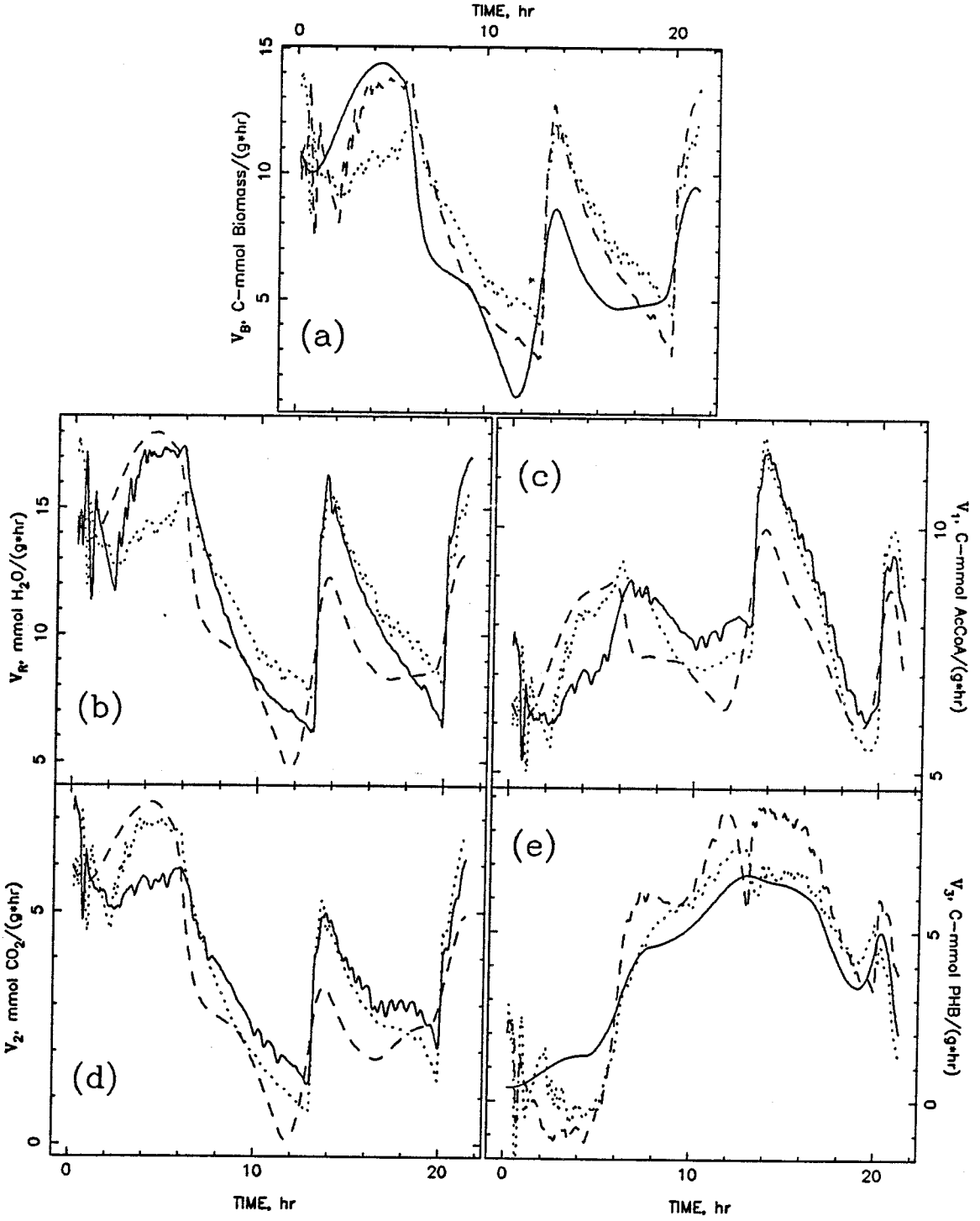
TIME, hr
0
10
20
15
10
5
V_B, C-mmol Biomass/(g*hr)
(a)
(b)
V_R, mmol H_2O/(g*hr)
(c)
V_1, C-mmol AcCoA/(g*hr)
(d)
V_2, mmol CO_2/(g*hr)
(e)
V_3, C-mmol PHB/(g*hr)
0

Figure 8.3

particular experiment, calculation of the various pathways yielded extremely good pathway rate values (Figure 8.4). Unlike ammonium transport, which is comprised of passive and active transport mechanisms, fructose is only actively transported into the cell.[8] Therefore, extra energy would not be required for fructose transport as the fructose concentration reached limiting levels.

When comparing calculated pathway rates with observed pathway rates, it should be remembered that the time evolution of $\mathbf{v}_B$ and $\mathbf{v}_3$ are smooth because of the off-line sampling required to determine these parameters, while $\mathbf{v}_R$, $\mathbf{v}_2$ and $\mathbf{v}_1$ reflect short-term changes that are due to the on-line contributions to these pathway rates. Therefore, "mental" smoothing is required when comparing an oscillating curve to a smooth curve.

In calculating $\mathbf{v}_B$, all calculated results were extremely good. Only the calculation utilizing $\mathbf{v}_2$ and $\mathbf{v}_3$ overestimated $\mathbf{v}_B$ slightly (10%).

Similarly, all calculated values of $\mathbf{v}_R$ were extremely good except for the value calculated from $\mathbf{v}_B$ and $\mathbf{v}_1$, which resulted in an overestimation (30%, not shown).

When $\mathbf{v}_R$ and $\mathbf{v}_2$ were used to estimate $\mathbf{v}_1$, the superposition of the oscillations in each of these measured quantities tended to give a result infused with random, sharp spikes. But, despite the spikes, the overall comparison of calculated and measured $\mathbf{v}_1$ values was very good. Similarly, $\mathbf{v}_B$ and $\mathbf{v}_2$ calculated $\mathbf{v}_1$ with spikes while following the correct trend. Unfortunately, the spikes in the calculated $\mathbf{v}_1$ are diametrically opposite those in the observed $\mathbf{v}_1$. This observation strongly suggests that the true $\mathbf{v}_B$ was not as smooth in actuality as determined by off-line sampling.

Figure 8.4: Fructose limitation/exhaustion experiment. All observed pathway rates denoted by ——— . **(a)** $\mathbf{v}_B$ calculated from $\mathbf{v}_R$ and $\mathbf{v}_2$, – – – ; $\mathbf{v}_B$ calculated from $\mathbf{v}_1$ and $\mathbf{v}_2$, ····· . **(b)** $\mathbf{v}_R$ calculated from $\mathbf{v}_B$ and $\mathbf{v}_2$, – – – ; $\mathbf{v}_R$ calculated from $\mathbf{v}_1$ and $\mathbf{v}_2$, ····· . **(c)** $\mathbf{v}_1$ calculated from $\mathbf{v}_B$ and $\mathbf{v}_3$, – – – ; $\mathbf{v}_1$ calculated from $\mathbf{v}_R$ and $\mathbf{v}_3$, ····· . **(d)** $\mathbf{v}_2$ calculated from $\mathbf{v}_B$ and $\mathbf{v}_3$, – – – ; $\mathbf{v}_2$ calculated from $\mathbf{v}_R$ and $\mathbf{v}_3$, ····· . **(e)** $\mathbf{v}_3$ calculated from $\mathbf{v}_R$ and $\mathbf{v}_1$, – – – ; $\mathbf{v}_3$ calculated from $\mathbf{v}_B$ and $\mathbf{v}_1$, ····· .

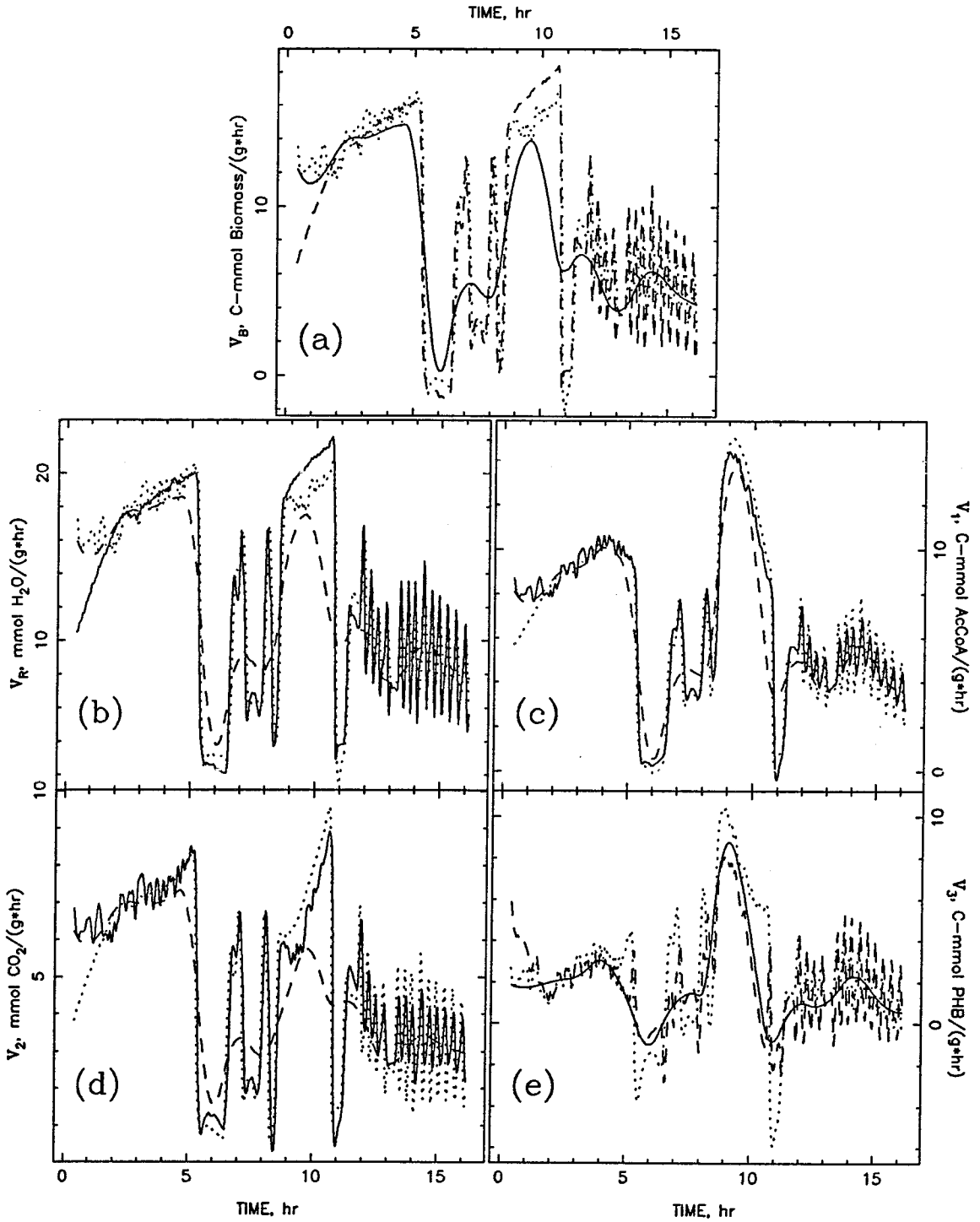
TIME, hr
0
5
10
15
V_B, C-mmol Biomass/(g*hr)
(a)
V_R, mmol H_2O/(g*hr)
(b)
V_1, C-mmol AcCoA/(g*hr)
(c)
V_2, mmol CO_2/(g*hr)
(d)
V_3, C-mmol PHB/(g*hr)
(e)
TIME, hr
TIME, hr

Figure 8.4

Not surprisingly, calculation of $\mathbf{v}_2$ from $\mathbf{v}_B$ and $\mathbf{v}_1$ resulted in a phenomenon similar to that described with the calculation of $\mathbf{v}_1$ from $\mathbf{v}_B$ and $\mathbf{v}_2$. The rest of the calculations compared quite well.

The trends calculated with $\mathbf{v}_B$ emulate the trends observed in $\mathbf{v}_3$; $\mathbf{v}_R$ with $\mathbf{v}_1$ or $\mathbf{v}_2$ gives very good results, although complicated with small, random spikes.

8.3.5 Phosphate Limitation/Exhaustion

Considering the case of phosphate limitation, one significant theme reoccurred (Figure 8.5). In virtually every case, the calculated pathway rate initially deviated significantly from the observed rate. This is attributable to the osmotic shock the cells first encountered upon inoculation (see Chapter 6 for details). The resulting extremely high respiratory rate significantly influenced the calculations.

Clearly, increased ATP demand, as signified by increased respiration activity, is not accounted for directly in the model formulation. If osmotic shock has significantly disturbed the ionic gradients associated with oxidative phosphorylation, presumably oxidative phosphorylation efficiency is reduced. This can then be incorporated into the calculations by lowering the P/O ratio and/or raising $m_{ATP,e}$, effectively reducing respiration ATP production and/or creating an increased ATP sink, accounting for the cell's need to adjust to its new environment. As time progresses, the agreement between calculated and observed pathway rates improves considerably.

Figure 8.5: Phosphate limitation experiment. All observed pathway rates denoted by ——— . **(a)** $\mathbf{v}_B$ calculated from $\mathbf{v}_R$ and $\mathbf{v}_1$, − − − ; $\mathbf{v}_B$ calculated from $\mathbf{v}_1$ and $\mathbf{v}_2$, ····· . **(b)** $\mathbf{v}_R$ calculated from $\mathbf{v}_B$ and $\mathbf{v}_1$, − − − ; $\mathbf{v}_R$ calculated from $\mathbf{v}_1$ and $\mathbf{v}_2$, ····· . **(c)** $\mathbf{v}_1$ calculated from $\mathbf{v}_B$ and $\mathbf{v}_3$, − − − ; $\mathbf{v}_1$ calculated from $\mathbf{v}_R$ and $\mathbf{v}_3$, ····· . **(d)** $\mathbf{v}_2$ calculated from $\mathbf{v}_B$ and $\mathbf{v}_3$, − − − ; $\mathbf{v}_2$ calculated from $\mathbf{v}_R$ and $\mathbf{v}_3$, ····· . **(e)** $\mathbf{v}_3$ calculated from $\mathbf{v}_B$ and $\mathbf{v}_1$, − − − ; $\mathbf{v}_3$ calculated from $\mathbf{v}_R$ and $\mathbf{v}_2$, ····· .

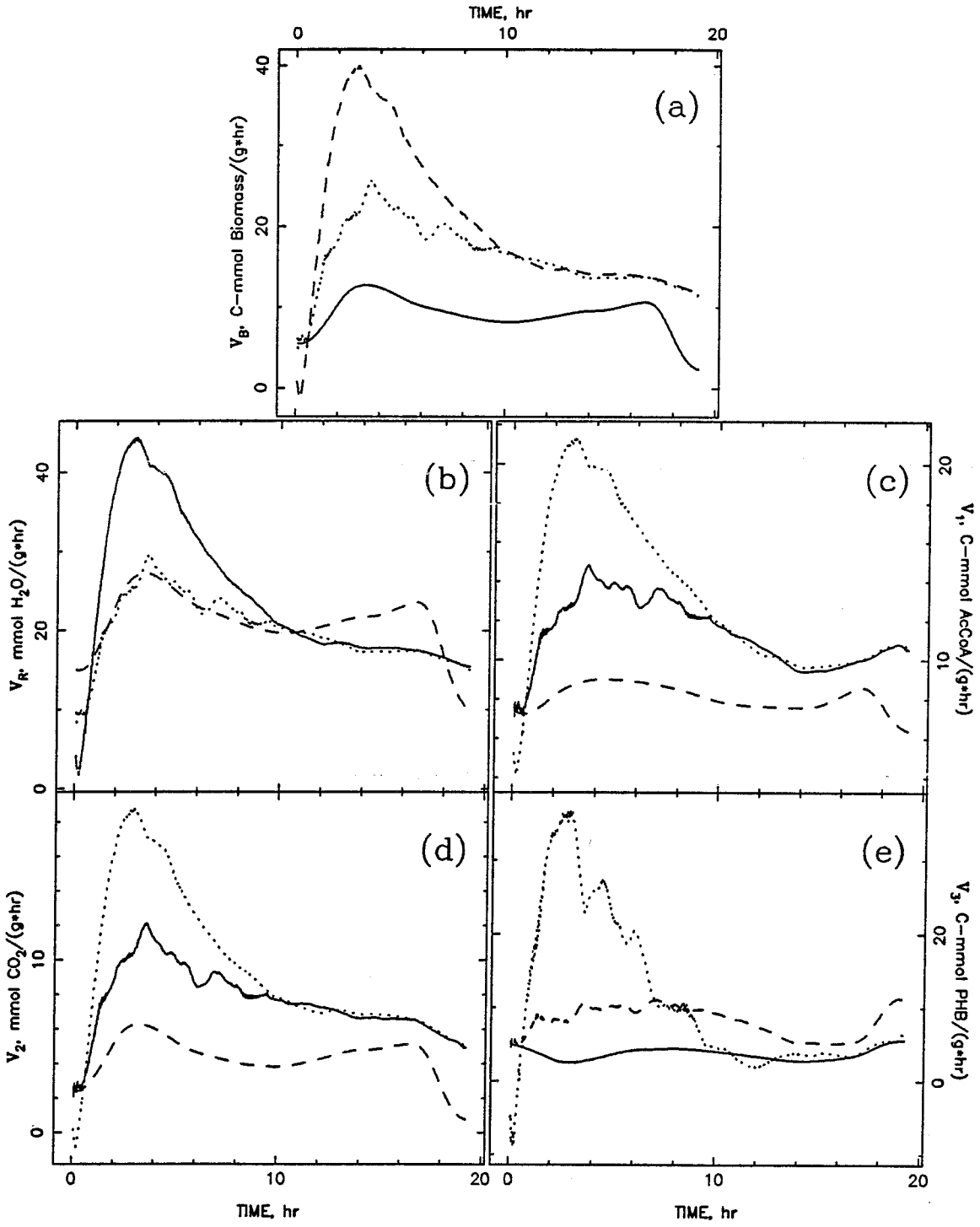
TIME, hr
0
10
20
(a)
V_B, C-mmol Biomass/(g*hr)
0
20
40
(b)
V_R, mmol H_2O/(g*hr)
(c)
V_1, C-mmol AcCoA/(g*hr)
(d)
V_2, mmol CO_2/(g*hr)
(e)
V_3, C-mmol PHB/(g*hr)

Figure 8.5

8.4 EXTENSION OF INTRACELLULAR METABOLIC BALANCE MODEL

From the previous section, it is clear that the use of the closed intracellular balance equations has great usefulness as a predictive tool. This property confirms the adequacy of the original model framework for many of the process conditions considered. The predictive property is further explored in this section by the incorporation of mathematical expressions for two pathways, with the subsequent calculation of the other three.

In Chapter 2, it was mentioned that Heinzle and Lafferty[9] developed a semi-empirical, structured model to describe batch growth and PHB production in autotrophically grown *Alcaligenes eutrophus* H16 cells under conditions of declining ammonium concentrations and ammonium exhaustion. Taking these equations and assuming that they provide a reasonable representation of kinetics in heterotrophic growth, expressions for $\mathbf{v}_B$ and $\mathbf{v}_3$ can be derived. The resulting expressions are substituted into the closed intracellular balances, thereby allowing calculation of $\mathbf{v}_R$, $\mathbf{v}_1$, and $\mathbf{v}_2$.

Heinzle and Lafferty described the time evolution of the residual biomass, R, relative to the cell dry weight, X, PHB concentration, P, and ammonium concentration, S, in the following manner:

$$X = P + R \tag{2.1}$$

$$\frac{dR}{dt} = r_R = \mu R, \tag{2.2}$$

where
$$\mu = \mu_1 + \mu_2 \tag{2.3}$$
$$= \mu_{m,1}\frac{S}{K_{S,1}+S} + \mu_{m,2}\frac{(S/K_{S,2})^n}{1+(S/K_{S,2})^n} \tag{2.4}$$
$$\frac{dS}{dt} = r_S = -\frac{1}{Y_{R/S}} r_R \tag{2.5}$$
$$\frac{dP}{dt} = r_P = r_{P,1} + r_{P,2}, \tag{2.6}$$

where
$$r_{P,1} = Y_{P/R} \cdot r_R \tag{2.7}$$
$$r_{P,2} = (k_2 R - k_1 P)\frac{K_I}{K_I + S}. \tag{2.8}$$

The specific growth rate, μ, is divided into an active transport term, μ_1, and a passive transport term, μ_2; μ is a function of the prevailing ammonium concentration. Furthermore, the decrease in the medium ammonium concentration is directly related through the ammonium yield coefficient, $Y_{R/S}$, to the increase in residual biomass (Eq. (2.5)). Finally, the change in the PHB concentration is considered to be the sum of a constitutive term (Eq. (2.7)), $r_{P,1}$, and a nongrowth associated term (Eq. (2.8)), $r_{P,2}$. $r_{P,2}$ is comprised of an ammonium inhibition component with inhibition constant K_I, a first-order biomass concentration component, $k_2 R$, and a first-order PHB self-inhibition component, $k_1 P$.

From the previous definition of $\mathbf{v}_B$ (see Chapter 2), μ and $\mathbf{v}_B$ are related in the following manner, for R with units of g/l:

$$\frac{dR}{dt} = \mu R = (\mathbf{v}_B \cdot MW_{Bio})\, R, \tag{8.2}$$

where MW_{Bio} is the single carbon formula weight of biomass. Therefore,

$$\mathbf{v}_B = \mu / MW_{Bio}. \tag{8.3}$$

Similarly, for P with units of g/l, $\mathbf{v}_3$ can be related to P in the following manner:

$$\frac{d\mathrm{P}}{dt} = \mathrm{Y_{P/R}} \cdot \mathrm{r_R} + (k_2\mathrm{R} - k_1\mathrm{P})\frac{\mathrm{K_I}}{\mathrm{K_I} + \mathrm{S}} = (\mathbf{v}_3 \cdot \mathrm{MW}_{PHB})\,\mathrm{R}. \tag{8.4}$$

Therefore,

$$\mathbf{v}_3 = \left[\mathrm{Y_{P/R}} \cdot \mathrm{r_R} + (k_2 - k_1[\mathrm{P}])\frac{\mathrm{K_I}}{\mathrm{K_I} + \mathrm{S}}\right] / \mathrm{MW}_{PHB}, \tag{8.5}$$

where [P] = P/R and MW_{PHB} is the single carbon formula weight of PHB.

To solve for the time evolution of $\mathbf{v}_B$ and $\mathbf{v}_3$, the time evolutions of S and [P] must be calculated. Substituting the left side of Eq. (2.2) into Eq. (2.5) and integrating directly relate S to R, leading to the following result:

$$\mathrm{R} = \mathrm{R_o} + \mathrm{Y_{R/S}}(\mathrm{S_o} - \mathrm{S}), \tag{8.6}$$

where $\mathrm{R_o}$ and $\mathrm{S_o}$ are the initial concentrations of biomass and ammonium, respectively. Substitution of the right side of Eq. (2.2) into Eq. (2.5) with subsequent substitution of Eqs. (2.7) and (2.8) allows computation of the time evolution of S:

$$\frac{d\mathrm{S}}{dt} = -\frac{1}{\mathrm{Y_{R/S}}}\left[\mu_{m,1}\frac{\mathrm{S}}{\mathrm{K_{S,1}} + \mathrm{S}} + \mu_{m,2}\frac{(\mathrm{S}/\mathrm{K_{S,2}})^n}{1 + (\mathrm{S}/\mathrm{K_{S,2}})^n}\right]\left(\mathrm{R_o} + \mathrm{Y_{R/S}}(\mathrm{S_o} - \mathrm{S})\right). \tag{8.7}$$

Noting that P = R[P], the time evolution of [P] can be calculated beginning with Eq. (2.6) and eventually substituting the right side of Eq. (2.2), leading to:

$$\frac{d\mathrm{P}}{dt} = \frac{d\mathrm{R}[\mathrm{P}]}{dt} \tag{8.8}$$

$$= [\mathrm{P}]\frac{d\mathrm{R}}{dt} + \mathrm{R}\frac{d[\mathrm{P}]}{dt} \tag{8.9}$$

$$= [\mathrm{P}](\mu R) + R\frac{d[\mathrm{P}]}{dt}. \tag{8.10}$$

Similar substitution of Eq. (2.2) into Eq. (2.6) with Eqs. (2.4) and (8.6) also substituted in leads to

$$\frac{dP}{dt} = Y_{P/R} \cdot r_R + (-k_1 P + k_2 R)\frac{K_I}{K_I + S} \tag{8.11}$$

$$= (\mu R)Y_{P/R} + (-k_1 P + k_2 R)\frac{K_I}{K_I + S}. \tag{8.12}$$

Equating Eqs. (8.10) and (8.12), dividing through by R, and rearranging yield an expression for the computation of [P] as a function of time:

$$\frac{d[P]}{dt} = \mu Y_{P/R} + (k_2 - k_1[P])\frac{K_I}{K_I + S} - \mu[P]. \tag{8.13}$$

Numerical solution of Eqs. (8.7) and (8.13), therefore, allows determination of the time-dependent behavior of $\mathbf{v}_B$ and $\mathbf{v}_3$ through Eqs. (8.3) and (8.5), respectively.

Following the approach taken by Heinzle and Lafferty, the required model constants were calculated from several ammonium exhaustion and ammonium limitation experiments. The values of these constant estimates are described in Table 8.2. $\mu_{m,1}$ and $\mu_{m,1} + \mu_{m,2}$ were determined from the slope of semilogarithmic plots of R versus time; $K_{S,1}$ and $K_{S,2}$ were estimated from a plot of μ versus S. n was calculated from an average of $\ln\left(\frac{\mu_2}{\mu_{m,2} - \mu_2}\right) / \ln\left(\frac{S}{K_{S,2}}\right)$ during growth. $Y_{R/S}$ was estimated from the slope of r_S versus r_R; $Y_{P/R}$ was estimated from the slope of r_P versus r_R, while S was still large and $r_{P,2}$ made a negligible contribution. k_1 and k_2 were evaluated from PHB storage data beginning with the equation $r_P (= r_{P,2}) = dP + kX$. Plotting r_P/P versus X/P allowed determination of d and k. Substitution of Eq. (2.1) allowed, therefore, calculation of k_1 and k_2 (*i.e.*, the S inhibition term is equal to one in Eq. (2.8)). Determination

of K_I required defining "a dimensionless rate of nongrowth-associated synthesis of PHB ($\bar{r}_P$):"

$$\bar{r}_P = \frac{r_P - Y_{P/R} \cdot r_R}{k_2 R - k_1 P} = \frac{K_I}{K_I + S}. \tag{8.14}$$

K_I was determined by plotting the reciprocal of $\bar{r}_P$ versus S and evaluating the inverse of the slope; *i.e.*,

$$\frac{1}{\bar{r}_P} = 1 + \frac{1}{K_I} \cdot S. \tag{8.15}$$

All values agreed reasonably well with Heinzle and Lafferty's calculations except for much smaller values of $K_{S,1}$, $K_{S,2}$, and n, indicating that heterotrophically grown *A. eutrophus* cells are less sensitive to ammonium concentration effects than autotrophically grown cells. In evaluating K_I, an exponentially increasing curve rather than a straight line was obtained when plotting the inverse of $\bar{r}_P$ versus S. This suggests that the inhibitory action of S on $r_{P,2}$ is more "on or off" than for autotrophic cells; *i.e.*, large S $\Rightarrow$ large slope $\Rightarrow$ small K_I; small S $\Rightarrow$ small slope $\Rightarrow$ large K_I.

Figure 8.6 describes the time evolution of dry weight, biomass, PHB, and ammonium chloride as well as the oxygen and carbon dioxide production rates. As a point of reference, these should be compared to the ammonium exhaustion experiment discussed in Chapter 2. Similarly, the model-calculated pathway rates for biosynthesis and PHB polymerization as well as the predicted respiration, glycolysis, and citric acid cycle pathway rates are presented in Figure 8.7. Clearly, the qualitative resemblance between these pathways and those described in Chapter 2 is striking.

TABLE 8.2: Heinzle and Lafferty model constants

Model Parameter	Parameter Value
$\mu_{m,1}$	0.25 hr^{-1}
$\mu_{m,2}$	0.115 hr^{-1}
$K_{S,1}$	0.005 g/l NH_4Cl
$K_{S,2}$	0.02 g/l NH_4Cl
n	1
$Y_{R/S}$	1.6 g biomass/g NH_4Cl
$Y_{P/R}$	0.135 g PHB/g biomass
k_1	0.041 $(g\ PHB)^{-1}$
k_2	0.201 $(g\ biomass)^{-1}$
K_I	0.03 g NH_4Cl

Attention should be called to a number of interesting points. First of all, an increase in $\mathbf{v}_1$ near the point of ammonium exhaustion has been observed qualitatively in a number of experiments. After ammonium exhaustion, $\mathbf{v}_1$ drops sharply and continues to decline to the end. As hinted before, both $\mathbf{v}_R$ and $\mathbf{v}_2$ drop sharply at the point of ammonium exhaustion. Unfortunately, $\mathbf{v}_2$ drops below zero, but gradually increases as PHB storage continues. After dropping sharply at the point of ammonium exhaustion, $\mathbf{v}_R$ continues at nearly the same level throughout the rest of the simulation rather than declines with time. Also note the sharp changes in the oxygen and carbon dioxide production rates relative to that observed for the experiment in Chapter 2 at the point of ammonium exhaustion. Clearly, the intracellular balance predictive model suggests much sharper changes in the cell's metabolism at the onset of ammonium exhaustion than was observed by analysis of the experimental data through the pathway model derived in Chapter 2. As suggested in Section 8.2.3, ATP consumption

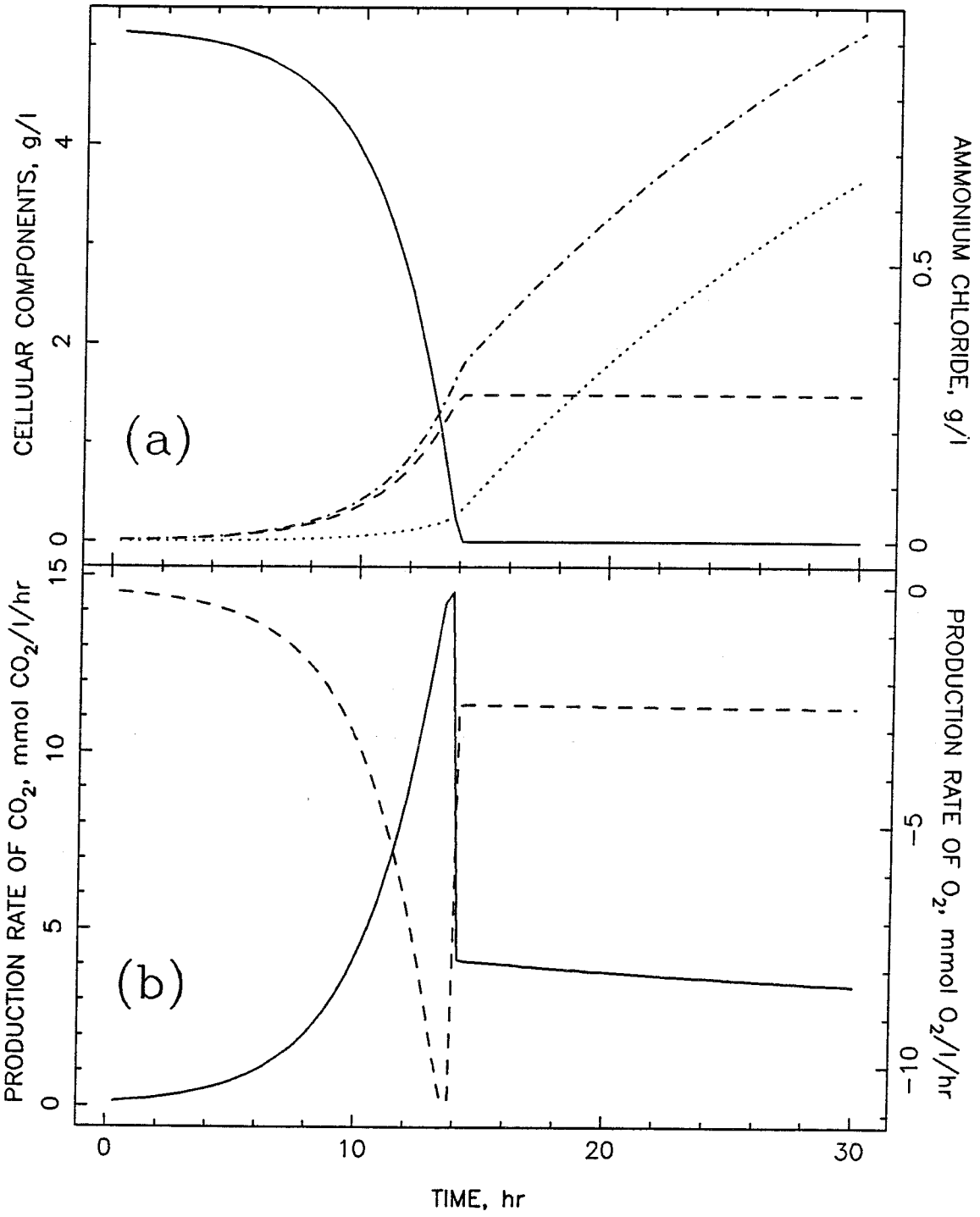

Figure 8.6: Model of ammonium exhaustion experiment: raw data. $R_o = 0.01$ g/l biomass and $S_o = 0.92$ g/l NH_4Cl. See text for other details. **(a)** Cell dry weight, — · — · ; biomass, — — — ; PHB, ····· ; ammonium chloride, ——— . **(b)** Carbon dioxide production rate, ——— ; oxygen production rate, — — — .

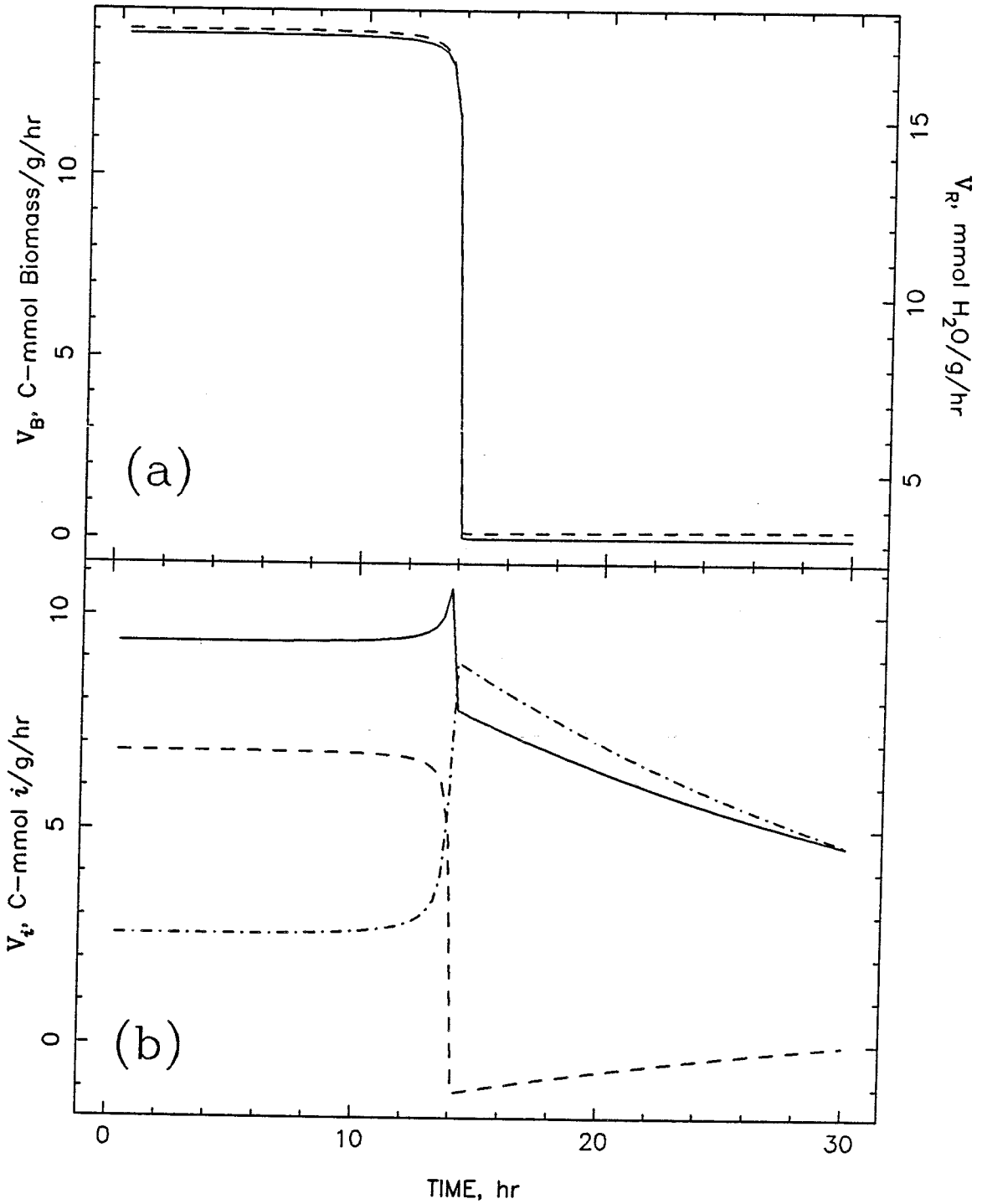

Figure 8.7: Model of ammonium exhaustion experiment: pathway fluxes. Biosynthesis and PHB polymerization activities calculated from adapted Heinzle and Lafferty model. $R_o = 0.01$ g/l biomass and $S_o = 0.92$ g/l NH_4Cl. See text for other details. **(a)** Biosynthesis activity ($\mathbf{v}_B$), ——— ; respiration activity ($\mathbf{v}_R$), − − − . **(b)** Glycolysis activity ($\mathbf{v}_1$), ——— ; citric acid cycle activity ($\mathbf{v}_2$), − − − ; PHB polymerization activity ($\mathbf{v}_3$), − · − · .

may be higher or ATP production is less efficient because of increases in $m_{ATP,e}$ or decreases in P/O, respectively; increasing $m_{ATP,e}$ or decreasing P/O effectively increases both $\mathbf{v}_R$ and $\mathbf{v}_2$. Presumably, after ammonium is exhausted, the cell still may have a number of biosynthetic precursors available within the cell, requiring further ATP consumption to finish any nonnitrogen-dependent biosynthetic manipulations. Therefore, the carbon dioxide and oxygen concentrations, $\mathbf{v}_R$ and $\mathbf{v}_2$ do not change as sharply as predicted by the model but "tail off" as these precursors are exhausted.

As a second example, a simulation of the ammonium limitation, fed-batch experiment was made (see Chapter 2). The equations are solved in the same manner except that a constant source term, $\alpha(t)$, is added to Eq. (2.5), signifying the constant addition of ammonium chloride to the theoretical reactor. Eq. (2.5) becomes

$$\frac{dS}{dt} = -\frac{1}{Y_{R/S}} r_R + \alpha(t), \tag{8.16}$$

where

$$\alpha(t) = \begin{cases} 0 & \text{if } t \leq t_o \\ \alpha_o & \text{if } t > t_o \end{cases}. \tag{8.17}$$

Recalling the analogous fed-batch macroscopic balance equation for ammonium,

$$\frac{d\mathbf{C}^l_{NH_3}}{dt} = -0.25\mathbf{X}\mathbf{v}_B + \frac{\mathbf{f}_{NH_3}}{\mathbf{V}^l}\mathbf{C}_{f,NH_3} - \frac{\mathbf{C}^l_{NH_3}}{\mathbf{V}^l}\frac{d\mathbf{V}^l}{dt}, \tag{2.32}$$

we see that Eq. (8.16) is nearly identical to Eq. (2.32), term for term, except for addition of the last term on the right-hand side, accounting for dilution that is due to addition of ammonium feed. For the ammonium limitation experiment

in Chapter 3, $\mathbf{V}^l \cong 12\ l$, $\left[\mathbf{C}^l_{\mathrm{NH_3}}\right]_{\max} \cong 0.3$ g/l, $\frac{d\mathbf{V}^l}{dt} \cong \mathbf{f}_{NH_3} \cong 0.015$ l/hr, and $\mathbf{C}_{f,NH_3} \cong 134$ g/l, ignoring volume changes during sampling. Therefore, the last term on the right-hand side of Eq. (2.32) is at most *ca* 0.2% of the second term on the right hand side. During ammonium limitation, $\mathbf{C}^l_{\mathrm{NH_3}} \rightarrow 0$, and the difference between these two terms is of even greater magnitude. We are justified, therefore, for reasons of simplification, in ignoring changes in the culture volume because of ammonium feeding. Consequently, Eq. (8.16) is a very good approximation of this system.

Following the previous development, Eqs. (8.6) and (8.7) then become

$$\mathrm{R} = \mathrm{R_o} + \mathrm{Y_{R/S}}\left[(\mathrm{S_o} - \mathrm{S}) + \alpha(\mathrm{t})(\mathrm{t} - \mathrm{t_o})\right] \tag{8.18}$$

$$\frac{d\mathrm{S}}{dt} = -\frac{1}{\mathrm{Y_{R/S}}}\left[\mu_{m,1}\frac{\mathrm{S}}{\mathrm{K_{S,1}} + \mathrm{S}} + \mu_{m,2}\frac{(\mathrm{S/K_{S,2}})^n}{1 + (\mathrm{S/K_{S,2}})^n}\right] \times \left[\mathrm{R_o} + \mathrm{Y_{R/S}}\left[(\mathrm{S_o} - \mathrm{S}) + \alpha(\mathrm{t})\,(\mathrm{t} - \mathrm{t_o})\right]\right]. \tag{8.19}$$

The equations for [P] remain the same.

The time evolution of the various cellular components, ammonium chloride concentration, and off-gas productions rates are described in Figure 8.8; the time evolution of the pathway rates are described in Figure 8.9. The constant rate addition term is defined as

$$\alpha(t) = \begin{cases} 0 & \text{if } t \leq 6 \text{ hr} \\ 0.17 \text{ g/hr/l } \mathrm{NH_4Cl} & \text{if } t > 6 \text{ hr} \end{cases}. \tag{8.20}$$

Clearly, these results compare very favorably with the ammonium limitation experiment. $\mathbf{v}_B$, $\mathbf{v}_R$, and $\mathbf{v}_2$ drop off asymptotically during ammonium limitation; biomass increases linearly and PHB increases nearly exponentially.

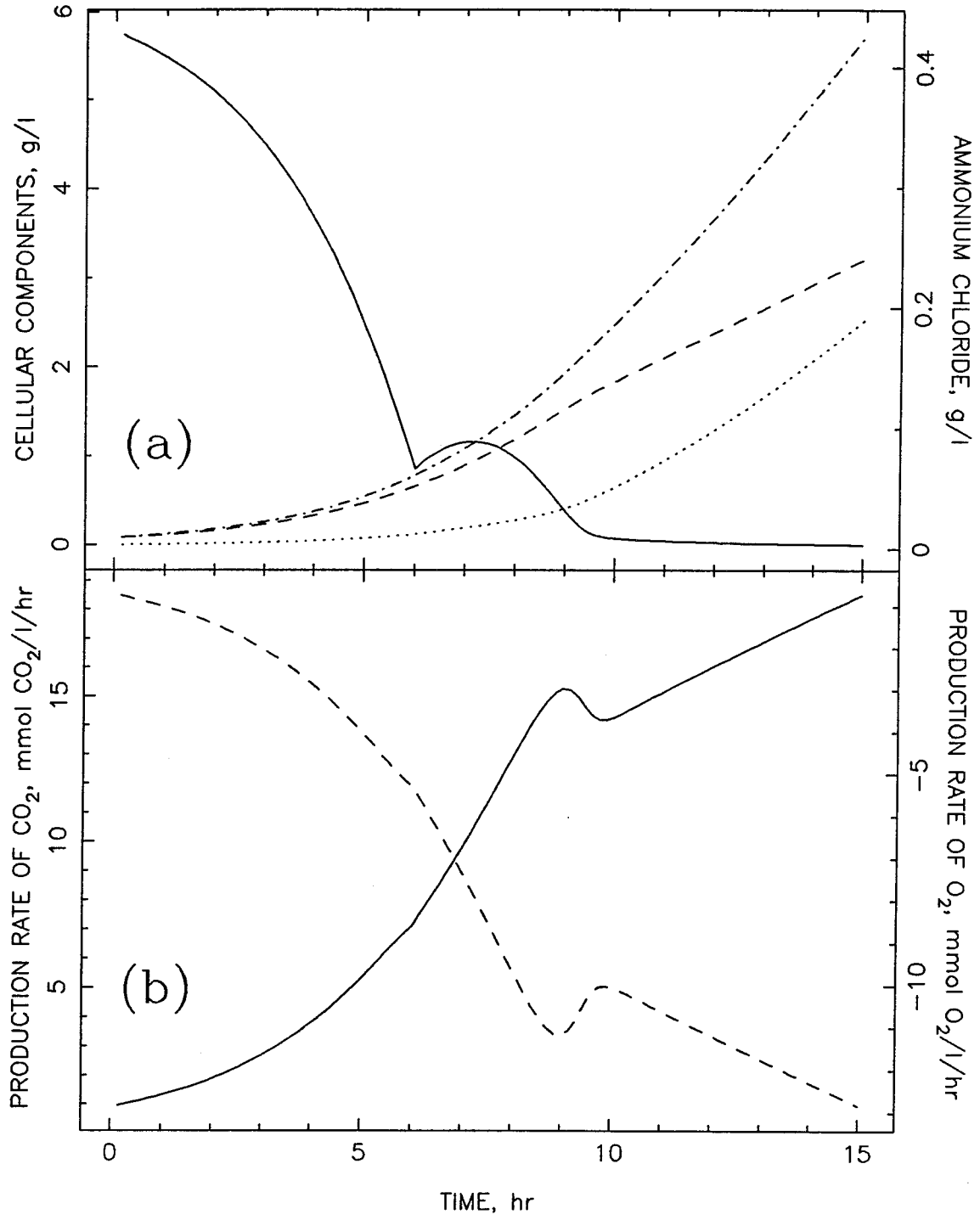

Figure 8.8: Model of ammonium limitation experiment: raw data. $R_o = 0.08$ g/l biomass and $S_o = 0.43$ g/l NH_4Cl. See text for other details. **(a)** Cell dry weight, $- \cdot - \cdot$; biomass, $- - -$; PHB, $\cdots\cdots$; ammonium chloride, ——. **(b)** Carbon dioxide production rate, ——; oxygen production rate, $- - -$.

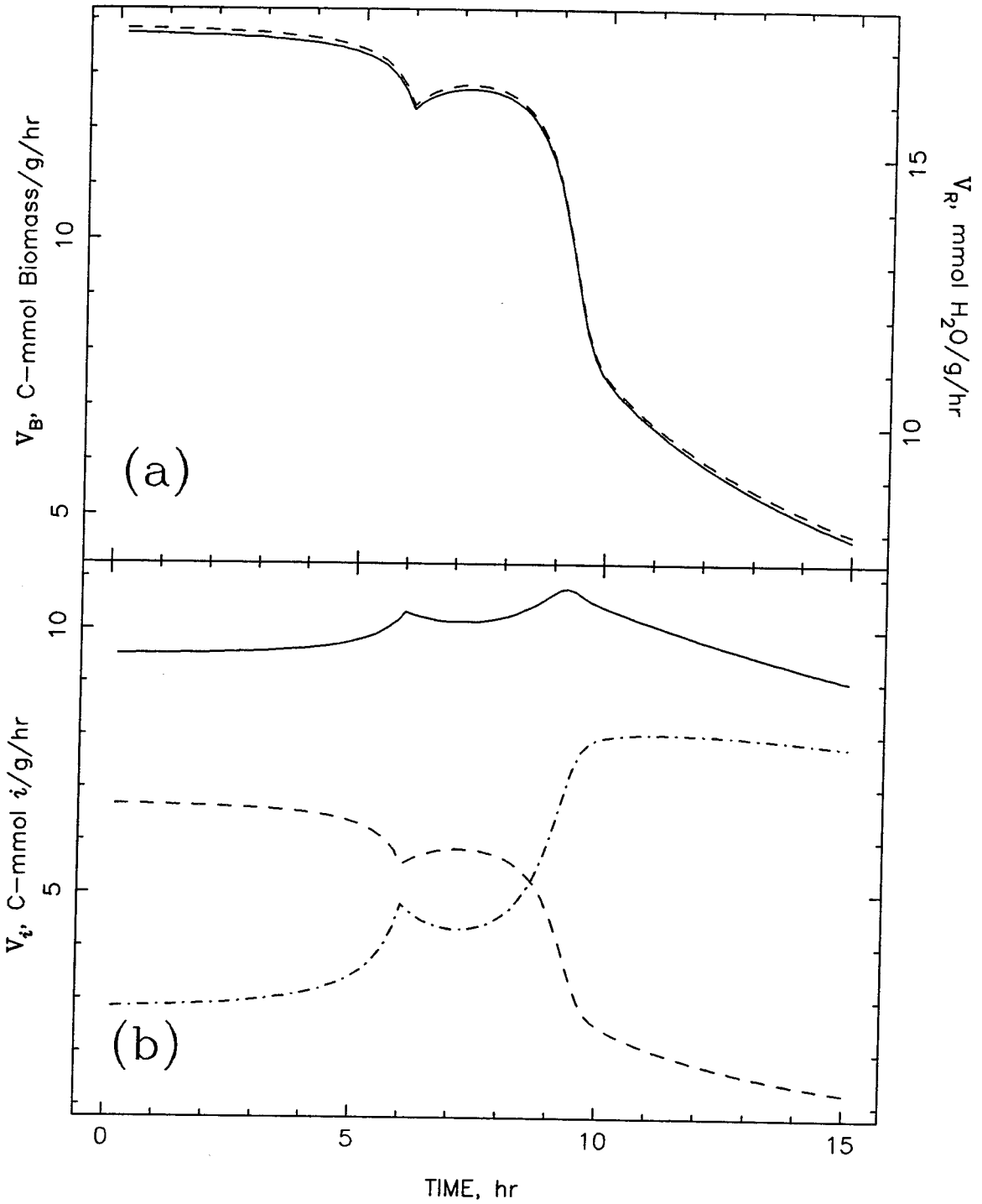

Figure 8.9: Model of ammonium limitation experiment: pathway fluxes. Biosynthesis and PHB polymerization activities calculated from adapted Heinzle and Lafferty model. $R_o = 0.08$ g/l biomass and $S_o = 0.43$ g/l NH_4Cl. See text for other details. **(a)** Biosynthesis activity ($\mathbf{v}_B$), ——— ; respiration activity ($\mathbf{v}_R$), – – – . **(b)** Glycolysis activity ($\mathbf{v}_1$), ——— ; citric acid cycle activity ($\mathbf{v}_2$), – – – ; PHB polymerization activity ($\mathbf{v}_3$), – · – · .

These two cases serve as excellent examples of the usefulness and predictive capabilities of this analysis framework.

8.5 FURTHER EXTENSIONS OF THE METABOLIC MODEL

As seen in the previous section, the intracellular balances provide a very good framework upon which *Alcaligenes eutrophus* H16's metabolism can be reasonably simulated. This also serves as a further validation of the overall metabolic pathway model presented in Chapter 2.

In the previous section, selected pathway rates were described by fairly empirical expressions. Building on this idea, the applicability of this model can be further extended by describing the pathway fluxes in each pathway by an appropriate kinetic expression that incorporates pertinent metabolic regulatory factors. Previous researchers have identified the key regulatory enzymes in the glycolytic, citric acid cycle and PHB polymerization pathways. These enzymes are glucose-6-phosphate dehydrogenase[10,11] and pyruvate kinase[12] in the glycolytic pathway, isocitrate dehydrogenase[13] in the citric acid cycle, and β-ketothiolase[14,15] in the PHB polymerization pathway. Each one of these enzymes has been isolated and kinetically characterized with respect to substrates, inhibitors, and enhancers, most notably ATP, NADH, acetyl-CoA and their associated counterparts.

Using this information, kinetic expressions and kinetic constants for each pathway can be derived for each of these three pathways. Since biosynthesis

and respiration are far more complicated pathways, general empirical regulatory expressions would have to be derived. These relationships could then be substituted into the appropriate macroscopic balances described in Chapter 2 and used to estimate/compare changes in biomass concentration, fructose consumption, etc. under various simulated fermentation conditions. Furthermore, the intracellular balances could be used to indicate changes in the intracellular concentrations of regulatory species such as ATP and NADH and could serve as a feedback mechanism for the regulation of the five metabolic pathways.

With such a working model in place, engineering decisions could be more intelligently made for identifying conditions of optimal growth and PHB production, identifying metabolic bottlenecks and proposing possible genetic modifications to enhance the cell's productivity.

8.6 CONCLUSIONS

Under most of the fermentation conditions considered, prediction of the pathway rates via the intracellular balance portion of the pathway model proposed in Chapter 2 proved to provide good results. Aside from indicating that the calculated intracellular parameters were reasonable as well as nearly constant (appropriate modifications to the metabolic parameters could be proposed to account for apparent deviations, *i.e.*, ammonium exhaustion and limitation) under a number of circumstances, this further confirms the validity and usefulness of the original proposed pathway network as a meaningful basis for understanding

Alcaligenes eutrophus H16 metabolism.

8.7 NOMENCLATURE

$\mathbf{c}_i$	mol i per unit weight biomass, mol/g
$\mathbf{C}_{f,i}$	nutrient feed concentration of i, mol/l
$\mathbf{C}_i^l$	liquid concentration of i, mol/l
$\mathbf{f}_i$	nutrient feed volumetric flow rate, l/hr
k_i	PHB synthesis rate constant, $i = 1$ or 2 (Eq. (2.8)), l/g/hr
K_I	PHB synthesis inhibition constant (Eq. (2.8)), g/l $(NH_4)_2\,SO_4$
$K_{S,1}$	active transport Michaelis-Menten constant (Eq. (2.4)), g/l $(NH_4)_2\,SO_4$
$K_{S,2}$	passive transport Michaelis-Menten constant (Eq. (2.4)), g/l $(NH_4)_2\,SO_4$
$m_{i,e}$	nongrowth associated maintenance coefficient, mol i/mol biomass
$m_{i,g}$	growth-associated maintenance coefficient, mol i/mol biomass
n	exponent, passive transport term (Eq. (2.4))
P	PHB concentration, g/l
[P]	intrinsic PHB concentration (=P/R), g/l
P/O	oxidative phosphorylation ratio, mol ATP/mol H_2O
$\mathbf{r}_i$	reaction rate of i (i = X, R, P, (P,1), (P,2), or S), g/l/hr
R	residual biomass concentration (R = X − P), g/l
S	$(NH_4)_2\,SO_4$ concentration; limiting nutrient, g/l
$\mathbf{v}_j$	rate through the j^{th} pathway, j = B (biosynthesis), R (respiration), 1 (glycolysis), 2 (citric acid cycle), and 3 (PHB polymerization), mol product/g/hr
$\mathbf{V}^l$	liquid culture volume, l

X	cell dry weight concentration, g/l
$\mathbf{X}$	(residual) biomass concentration, g/l
Y_i	yield coefficient of i, mol biomass/mol i
Y_i^{max}	maximum yield coefficient of i, mol biomass/mol i
$(Y_i^{max})_{th}$	maximum theoretical yield coefficient of i, mol biomass/mol i
$Y_{P/R}$	PHB yield coefficient, g PHB/ g biomass
$Y_{R/S}$	$(NH_4)_2\,SO_4$ yield coefficient, g biomass/g $(NH_4)_2\,SO_4$
α	ammonium source, g/l/hr
μ	specific growth rate of residual biomass, hr^{-1}
$\mu_{m,1}$	maximum active transport specific growth rate (Eq. (2.3)), hr^{-1}
$\mu_{m,2}$	maximum passive transport specific growth rate (Eq. (2.3)), hr^{-1}
μ_1	active transport specific growth rate (Eq. (2.3)), hr^{-1}
μ_2	passive transport specific growth rate (Eq. (2.3)), hr^{-1}

8.8 REFERENCES

1. Stouthamer, A.H., *Microbial Biochemistry*, **21**, 1 (1979).
2. Edwards, C., Spode, J.A., and Jones, C.W., *Biochem. J.*, **172**, 253 (1978).
3. Drozd, J.W., and Jones, C.W., *Biochem. Soc. Trans.*, **2**, 529 (1974).
4. Mas, J., Pedrós-Alió, C., and Guerrero, R., *J. Bact.*, **164**, 749 (1985).
5. Liao, J.C., *Biotechnol. Bioeng.*, **33**, 613 (1989).
6. Kleiner, D., *FEMS Microbiol. Rev.*, **32**, 87 (1985).
7. Jahns, T., Kaltwasser, H., and Kleiner, D., *Arch. Microbiol.*, **145**, 306 (1986).
8. Schlegel, H.G., and Eberhardt, U., *Adv. Microb. Physiol*, **7**, 207 (1972).
9. Heinzle, E., and Lafferty, R.M., *Eur. J. Appl. Microbiol. Biotechnol.*, **11**, 8 (1980).
10. Tunail, N., and Schlegel, H.G., *Biochem. Biophys. Res. Comm.*, **49**, 1554 (1972).
11. Blackkolb, F., and Schlegel, H.G., *Arch. Mikrobiol.*, **63**, 177 (1968).
12. Wilke, D., and Schlegel, H.G., *Arch. Microbiol.*, **105**, 109 (1975).
13. Glaeser, H., and Schlegel, H.G., *Arch. Mikrobiol.*, **86**, 327 (1972).
14. Oeding, V., and Schlegel, H.G., *Biochem. J.*, **134**, 239 (1973).
15. Ruhr, E.-M., Dissertation, Universität Göttingen, Göttingen (1977).

16. Stouthamer, A.H., *Symp. Soc. Gen. Microbiol.*, **28**, 285 (1977).

17. Glaeser, H., and Schlegel, H.G., *Arch. Mikrobiol.*, **86**, 327 (1972).

18. Blackkolb, F., and Schlegel, H.G., *Arch. Mikrobiol.*, **63**, 177 (1968).

19. Tunail, N., and Schlegel, H.G., *Biochem. Biophys. Comm.*, **49**, 1554 (1972).

20. Wilke, D., and Schlegel, H.G., *Arch. Microbiol.*, **105**, 109 (1975).

21. Entner, N., and Doudoroff, M., *J. Biol. Chem.*, **196**, 853 (1952).

CHAPTER 9

CONCLUSIONS

The major result of this work is that a reasonably simple model has provided a mathematical framework that adequately describes and simulates the metabolism of a very complicated organism over a wide range of growth and PHB polymerization conditions. This ability to relate macroscopic observations to microscopic phenomena is of great importance to the biochemical engineer with regard to design and control of any biological process. Clearly, the results of this work highlight the value of a modeling approach as well as suggest that a carefully chosen model basis can effectively achieve this macroscopic/microscopic relational objective.

As with any attempt at modeling a complex system with a simple model, there are always drawbacks. While the pathway model developed in Chapter 2 did an excellent job in identifying and quantifying intracellular metabolic activity, incorporation of the three intracellular balances in Chapter 8 met with somewhat less success. This is not to say that implementation of the intracellular balances as a predictive and simulatory tool was of any less value, but rather, indicates the inability of this approach to predict accurately the metabolic response under a certain circumstance, *i.e.*, ammonium limitation, served to identify fermentation conditions under which intracellular metabolic processes not explicitly included in the model are functioning, *i.e.*, active ammonium transport, as generally indicated by the apparent necessity to change or modify certain metabolic parameters. Certainly, this variability in metabolic parameters could be incorporated into the simulation model to improve simulation performance.

With regard to advancing the understanding of growth and PHB production regulation in *Alcaligenes eutrophus* H16, this model may be further extended by the incorporation of the intrinsic rate expressions for the key regulatory enzymes in each of the five pathways. If such an extended model could be made to function adequately, this would provide a test framework for determining the effects of eliminating various regulatory mechanisms through genetic or mutagenic manipulations in hopes of further optimizing the process.

APPENDIX 1

EXPERIMENTAL SETUP & TECHNIQUES AND DATA PROCESSING

A1.1 CULTURE CONDITIONS

A1.1.1 Strain Care and Maintenance

Alcaligenes eutrophus H16 cultures were stored long-term on test tube slants at 4°C. Slant medium consisted of 8 g/l nutrient broth (Difco Laboratories), 5 g/l NaCl, 10 g/l agar (Bactoagar), and 5 g/l fructose. Fructose was added to insure induction of the heterotrophic catabolic enzyme system.

Slant cultures were routinely streaked out *ca* every two months on plates consisting of the previously mentioned medium with 15 g/l agar instead of 10 g/l. Plates were incubated for one day at 30°C. Single colonies were picked off with a wire loop and streaked on fresh slants; slants were incubated one day at 30°Cand stored in the refrigerator.

A1.1.2 Medium Composition and Preparation

A. eutrophus fermentation cultures grew in mineral medium of the final composition shown in Table A1.1.[1,2] Solution (1) represents the final concentrations of the phosphate buffer components, solution (2) represents the final concentrations of the macronutrients, and solution (3) represents the micronutrients added from the described stock micronutrient solution.

In medium preparation for large-scale fermentation or small-scale inoculum/shake flask, two points were critical: (*i*) Solutions (1), (2), and (3) could

TABLE A1.1: Fermentation medium composition

Solution	*Nutrient*	*Concentration (g/l)*
(1)	$NaHPO_4 \cdot 6\ H_20$	6.74
	KH_2PO_4	1.5
(2)	Fructose	0–5
	NH_4Cl	0–1
	$MgSO_4 \cdot 7\ H_2O$	0.2
	$FeCl_3 \cdot 6\ H_2O$	0.004
	$CaCl_2 \cdot 2\ H_2O$	0.01
(3)	Supplemental Media	1 ml/l
Supplemental medium composition:		
	$ZnSO_4 \cdot 7\ H_2O$	0.1
	$MnCl_2 \cdot 4\ H_2O$	0.03
	H_3BO_4	0.3
	$CoCl_2 \cdot 6\ H_2O$	0.2
	$CuSO_4 \cdot 5\ H_2O$	0.01
	$NiCl_2 \cdot 6\ H_2O$	0.02
	$Na_2MoO_4 \cdot 2\ H_2O$	0.03

not be autoclaved together, thereby requiring separate autoclaving or sterile filtration, and (*ii*) the metal components of the medium required acidification prior to sterilization to assure solubility and proper oxidation state.

Inocula for fermentations were prepared in the following manner: Approximately 350 ml of medium (1 g/l NH_4Cl and 10 g/l fructose) were briefly acidified by the addition of 0.5 ml H_2SO_4. After correcting the pH to 8.1, *ca* 3 ml were sterile-filtered into each of two autoclaved test tubes and *ca* 300 ml were sterile-filtered into each of two autoclaved, one liter baffled shake flasks (Bellco).

Two days before the expected fermentation at 10:30 A.M., the test tubes were inoculated via a wire loop from a slant and placed in a rotary incubator at

30°C and *ca* 250 rpm. The following day at 1:30 P.M., each test tube culture was transferred to a baffled flask and placed in the 30°C rotary incubator. Each flask was then ready to inoculate the fermenter the next day at 7 A.M. Experience demonstrated that the final pH in each shake flask prior to inoculation was *ca* 6.8 — the desired fermentation pH.

Preparation of the fermentation medium called for a slight modification of the previous procedure. Phosphate components sufficient for 12 liters of medium were mixed into eight liters of distilled water and sterilized *in situ* in the fermenter. The rest of the medium components (12 liters worth) were mixed up in four liters, acidified with one ml of H_2SO_4, and sterile-filtered into the cooled fermenter.

All fermentations ran at 31°C ± 0.5°C. and pH 6.8 ± 0.02. The pH was maintained with addition of H_3PO_4 and NaOH and/or NH_4Cl. Air was sparged through the system at rates ranging from 1.75 to 2.5 l/min (0.14 to 0.2 vvm). The agitation speed varied according to the purpose of the fermentation.

A1.2 FERMENTER AND ASSOCIATED EQUIPMENT

A1.2.1 Fermenter

The fermenter utilized in this work was an 18 liter Bioengineering AG Laboratory Fermenter L1523. This fermenter provided a standard 25 mm Ingold mount for use with the Fluromeasure probe.

Temperature control was supervised by a temperature control unit in conjunction with a platinum resistance temperature sensor. Temperature control through a water recirculation loop allowed interaction between the fermenter's steam generator or an external heat exchanger and the heating/cooling mantle. The temperature control unit also controlled the *in situ* steam sterilization process.

The stirrer controller provided agitation ranging from 50 to 2500 rpm through a bottom drive stir shaft equipped with two disc turbine impellers. Special fermentation needs required special alloy mechanical seals (Crane Packing, Ltd.) to prevent fouling and leaking. The stirrer controller was modified to accept output from the dissolved oxygen controller input, thereby allowing both automatic and manual control of agitation.

The stainless steel fermentation vessel was configured with three 25 mm standard Ingold mounts around the base, 12 head plate ports, one top sight glass with viewing light and one side sight glass, four baffles, a loop sparger, and a mechanical foam breaker. In addition, the head plate was equiped with a safety release valve and pressure gauge. Inlet air was sterilized through a sterilizable ceramic filter. A similar ceramic filter for the outlet air was removed because of clogging and high back pressures.

A1.2.2 Dissolved Oxygen Probe

Monitoring of dissolved oxygen was accomplished with the Instrumentation Laboratories (IL) 531 Industrial Dissolved Oxygen Monitoring Sys-

tem. This system comprised a steam sterilizable Ingold polarographic oxygen sensor (25 mm Ingold flange fitting; 70 mm immersion length) and an IL amplifier. The amplifier featured temperature compensation (15 to 40°C), zero and gain potentiometers, and 4-position range selection (electronic zero, 0–100, 0–200, and 0–800). The analog output was modified to 0 to 2 volts.

A1.2.3 Dissolved Carbon Dioxide Probe

Dissolved carbon dioxide was monitored with an Ingold CO_2 monitor, Model 1230, and an Ingold dissolved carbon dioxide probe, Model 780. The monitor unit was a wall-mounted NEMA 4x display allowing observation of up to four decades of dissolved carbon dioxide concentration, two decades at a time (1 to 10,000 mbars). The monitor also featured a high-resolution $5\frac{1}{2}$ inch analog meter, and asymmetry, slope and temperature adjustments. High and low alarm settings, a 4 to 20 mA isolated output and automatic temperature compensation were also featured.

The probe was steam-sterilizable and fit a 25 mm standard Ingold mount with a 70 mm immersion length. The inner probe was retractable from the measuring position for calibration or sterilization. Easily accessible ports facilitated simple exchange of reference and calibration buffer solutions.

A1.2.4 On-line Optical Density

Lee and Lim[3] devised a flow cell suitable for cultures with high opti-

cal densities. A similar flow cell with an outside diameter of 1.2 cm and an outside diameter of the inner tube of 0.9 cm was constructed for the on-line monitoring of the culture optical density. A Bausch & Lomb Spectronic 20 was appropriately modified to accept the flow cell by the introduction of a hole in the bottom of the sample chamber. The flow cell was secured at the top of the instrument by string and then covered with a box to prevent stray light from entering the instrument. A flow loop from the fermenter sampling port leading to the flow cell and then returning to the fermenter provided a constant source of fresh sample. An in-line bubble trap prevented the signal from being corrupted by stray bubbles. The Spectronic 20 was modified to provide a 0 to 1 V output corresponding to 0 to 100% transmittance at 420 nm.

A1.2.5 pH Control

A Cole-Parmer pH controller, Model 5997-20 (no recording unit), facilitated extremely precise pH control in all fermentations. The controller featured an analog meter reading from 0 to 14 pH units or -700 to 700 mV in the NORMAL range and Δ 1.4 pH units or Δ 140 mV in the EXPANDED range. Typically, the EXPANDED range was used to maintain the pH at 6.8 ± 0.02. High and low adjustable set points activated separate power plugs used to control Masterflex peristaltic pumps (Cole-Parmer). Toggle switches allowed operation of the power plugs in OFF, MANUAL, or AUTOMATIC modes. The high set point activated addition of H_3PO_4. The low set point activated addition of

NaOH and/or NH_4OH, NH_4Cl, and fructose. The output normally reserved for the optional recorder was converted to a 0 to 2 V output for data logging.

The pH probe consisted of an Ingold Electrodes, Inc. glass combination electrode with an AgCl reference (part no. 10 405 3800) and immersion length of 100 mm. The pH probe was encased in a pressure housing equipped with a standard 25 mm Ingold fitting. Before acquisition of the dissolved carbon dioxide probe, the pH probe was inserted into one of the 25 mm fittings. Following the acquisition of the dissolved carbon dioxide probe, a special flow cell-type adapter was constructed for mounting of the pH probe in-line with the optical density recirculation loop. This modification had little effect on pH control performance.

A1.2.6 Fluorescence Probe

BioChemTechnology, Inc. (Malvern, PA), as part of the Fluromeasure System^{TM}, provided a fluorescence probe. The probe emitted light at 340 nm from a mercury lamp source and detected light at 460 nm, presumably from the fluorescence of NAD(P)H. Because 460 nm light is nearly within the visible range, all fermenter sight glasses were covered with foil to prevent room light (most notably fluorescent light) from corrupting the signal. The fluorescence probe fit a 25 mm standard Ingold mount and was steam-sterilizable. A transformer box supplied power to the probe as well as conditioning of the output signal through 6-pin and 5-pin shielded cables. The probe was cylindrical in shape with a length of 17 inches and a 2.25 inch diameter; the immersion length was 3.25 inches.

A1.2.7 Carbon Dioxide Gas Analyzer

Off-gas carbon dioxide quantification was performed by an Infrared Industries, Inc. (Santa Barbara, CA) Model #703-075 carbon dioxide gas detector. This instrument provided a dual range of 0–2% and 0–6% carbon dioxide displayed on an analog meter. A dual chamber detection system referenced the sample stream against air. A flow rate between 1000 and 3000 cc/min was required for operation. The analog output was modified to 0 to 2 V.

A1.2.8 Oxygen Gas Analyzer

Off-gas oxygen quantification was performed by a Leeds & Northrup 7863 Thermomagnetic Oxygen Analyzer. The 0 to 25 % range was displayed on an analog meter with a 0 to 10 V analog output for data logging. The instrument required a 0.25 to 1.0 l/min flow rate for proper operation.

A1.2.9 Off-gas Preparation System

The off-gas preparation system supplied the carbon dioxide and oxygen analyzers with dry fermentation gas and damped the gas flow rate fluctuations caused by foaming and other perturbations.

To assure a nearly constant gas flow rate, a Masterflex peristaltic pump with three #15 pump heads installed in the off-gas line maintained constant backpressure in the fermentation vessel while damping out flow rate surges from, for example, foam plugs in the off-gas line.

Foam removal and primary moisture removal were facilitated by a condensing column. Off-gas initially passed into a 500 ml round bottom flask, where foam was effectively removed from the gas stream and condensate was collected. A valve on the bottom of the flask allowed easy removal of foam and condensate. The gas stream next passed upwards through the condensing column. The condensing column was 15 inches long, had a $1\frac{1}{2}$ inch outside diameter and a $\frac{1}{2}$ inch inside diameter. An ethanol/water (*ca* 1:1) solution chilled to -5 to -8°C circulated inside the cooling jacket; cooling and circulation were provided by a Haake A80 recirculation bath. Column insulation was provided with cotton and cheese cloth.

Secondary drying was provided with two parallel Kimax drying columns. Each column had a capacity of 250 ml and was filled with Drierite, consisting of 1 part indicating Drierite to 4 parts nonindicating Drierite. The parallel design allowed one column to be in service while the other column was being charged with fresh Drierite. Possible dust from the Drierite columns was removed by a downstream paper filter (Whatman Filter tubes, Grade 12-10).

The dryed off-gas stream then split, part going to the carbon dioxide analyzer and part going to the oxygen analyzer. The flow rates to each analyzer were monitored by a 0 to 3 l/min rotameter for the carbon dioxide analyzer and a 0 to 2 l/min rotameter for the oxygen analyzer. The gas streams were then vented to the atmosphere, having passed through the gas analyzers.

A1.2.10 Dissolved Oxygen Controller

A homemade dissolved oxygen controller was designed to maintain a de-

sired set point, dissolved oxygen concentration through adjustment of the fermenter agitator. The controller was of a proportional type design: The output signal from the dissolved oxygen amplifier was compared to the dissolved oxygen set point, and the difference was multiplied by the gain. The resulting value was then added to the stirrer speed set point. The resulting signal then adjusted the stirrer speed appropriately.

The controller possessed the following features: dissolved oxygen set point, stirrer speed set point, amplification gain of 1 to 20, and attenuation gain of 0 to 1.

The agitation control unit was modified with a switch to allow either manual operator agitation control or automatic agitation control by the dissolved oxygen controller.

Although not fully automated, the dissolved oxygen controller was quite capable of "babysitting" the fermenter for long periods of time (*ca* 1 hour) depending upon the phase of the fermentation.

Once the dissolved oxygen set point was set and an appropriate agitation set point found, the controller was capable of maintaining the desired dissolved oxygen concentration at $\pm$ 2 mm Hg. Typically, as the fermentation progressed, the gain was gradually turned down for stability reasons. When the controller became less and less able to maintain the desired dissolved oxygen concentration (*i.e.*, tended towards the low side of the dissolved oxygen set point), the agitator set point was turned up slightly. The agitator set point was equipped with an RC-type circuit with a large capacitance to prevent readjustment of the set point from destablizing the controller.

A1.2.11 Data Acquisition System

The data acquisition system was constructed around BioChemTechnology's Flurometer System. This was a PC-based system built to be used in conjunction with the Flurometer probe. The system featured on-line data logging of culture fluorescence and five other parameters (pH, optical density/dissolved carbon dioxide, dissolved oxygen, off-gas carbon dioxide, and off-gas oxygen). Other features included linear calibration of input signals, one to 20 points/min sampling rates, on-line plotting and monitoring of fermentation parameters, off-line variable input and plotting, and plotting of off-line variables vs. on-line variables. The input interface box accepted a range of instrument inputs: 0–2 V, 0–5 V, 0–10V, and 0–20 mA.

Since the interface box used voltage dividers to achieve the necessary input voltage conversions and the range of resistors used was too low, often instrument analog outputs were "loaded down." For example, the Spectronic 20 was capable of delivering a 0 to 1 V signal (infinite resistance); but with the interface box's low resistances, the computer was able to "see" only 0 to 0.3 V. This resulted in a decrease in signal resolution as well as an increase in the signal-to-noise ratio. To circumvent the aforementioned problem, an amplifier box was built to "buffer" the instrument outputs, thereby providing enough power to the output signals to maintain the output voltage regardless of the interface box resistance. This also facilitated splitting of the dissolved oxygen signal for both data logging and input to the dissolved oxygen controller.

A1.3 FERMENTION PREPARATION AND RUN PROTOCOL

A1.3.1 Prefermentation Setup

Table A1.2 is a brief outline of the steps required in preparation of a fermentation run.

TABLE A1.2: Fermentation preparation outline

Day #1

Prepare inoculum medium, tubes and flasks.
Prepare fermenter medium.
Warm up instruments.
Inoculate test tubes.

Day #2

Calibrate pH and dissolved oxygen probes.
Assemble fermenter and sterilize.
Sterilize external tubing, nutrient reservoirs, etc. and assemble.
Filter-sterilize rest of medium.
Calibrate optical density flow cell, dissolved carbon dioxide probe, oxygen and carbon dioxide analyzers.
Perform instrument background run.

Day #3

Initialize data acquisition system.
Inoculate fermenter.

A1.3.2 pH-controlled Feeding

A pH-controlled feeding scheme was used to maintain a constant ammonium concentration in the fermentation broth. The principle behind the idea rested upon the fact that when ammonium was assimilated by cells, a proton

was ultimately ejected, which in turn caused the pH to fall. By neutralizing the ejected proton with hydroxide from NH_4OH, a constant ammonium concentration could be maintained. Unfortunately, theory and reality were not the same in this case. Predominantly because of the influence of dissolved carbon dioxide being solvated to H_2CO_3 and dissociating, the pH dropped faster than the actual ammonium uptake rate. Consequently, ammonium uptake was overcompensated when only NH_4OH was used for pH control.

This did not, however, discourage the use of pH control for the dispensation of nutrients. As a second attempt, NaOH was used to supplement NH_4OH, *i.e.*, to compensate for the carbonic acid contribution. Unfortunately, concentration determination of NH_4OH proved difficult, and an NH_4Cl/NaOH system was chosen instead. The pitfall, however, even though the concentration of NH_4Cl was known, was matching the proper feed ratios between NH_4Cl and NaOH.

At the same time an attempt to use pH-controlled feeding for fructose was also investigated. It had been reported that *A. eutrophus* was incapable of utilizing glucose because of the absence of the necessary active transport mechanism.[4,8] Tests confirmed that indeed growth could not be sustained on glucose alone and that glucose in the presence of fructose showed no toxicity effects. Since we were able to assay both fructose and glucose with the fructose assay, it was thought that by introducing a trace amount of glucose into the fructose feed, it could be determined how much fructose had been consumed during the course of a fermentation. Unfortunately, the passive diffusion of glucose into the cells proved to be higher than anticipated, forcing abandonment of this technique.

Fructose, NH_4Cl and NaOH were each added by pH-controlled feeding. Each substance had its own Masterflex peristaltic pump, allowing simple adjustment of the addition ratios. Pump flow rates were checked by how fast the meniscus dropped in separate 1 ml volumetric pipettes. Feed addition volumes were noted with time by the amount withdrawn from 50 ml pipette reservoirs.

A1.3.3 Sampling Procedure and Preparation

Samples were withdrawn from the same sample port used by the recirculation loop, thereby assuring fresh sample from the culture broth. Anywhere from 40 to 120 ml were withdrawn and immediately iced down. Two 10 ml aliquots were spun down at 18,000 rpm for 20 minutes at 4°C in a Beckman J2-21 centrifuge using a JA-20 rotor. From 7 to 80 ml samples were used for the dry weight determination. Following centrifugation of the two 10 ml samples, the supernatant was poured off into a 20 ml syringe with a 0.2 μm filter. The filtered supernatant was separated into two capped five-dram bottles; one was stored at 4°C and the other had 0.01 ml of concentrated H_2SO_4 added and was placed in a 37°C incubator. The pellets in the centrifuge tubes were placed in the −20°C freezer.

A1.4 ANALYTICAL TECHNIQUES

A1.4.1 Fructose Assay

The fructose assay was modeled after the Boehringer Mannheim GMBH Glucose/Fructose Assay Kit (Cat. No. 139106). The assay spectrophotometrically determines the concentration of glucose/fructose based upon the amount of reduced NADP (NADPH) in the following chemical reactions:

$$\text{Glucose} + \text{ATP} \xrightarrow{\text{HK}} (\text{G-6-P}) + \text{ADP} \qquad \text{(A1.1)}$$

$$\text{Fructose} + \text{ATP} \xrightarrow{\text{HK}} (\text{F-6-P}) + \text{ADP} \qquad \text{(A1.2)}$$

$$(\text{F-6-P}) \xleftrightarrow{\text{PGI}} (\text{G-6-P}) \qquad \text{(A1.3)}$$

$$(\text{G-6-P}) + \text{NADP} \xrightarrow{\text{G-6-P-DH}} (\text{Gluconate-6-phosphate}) + \text{NADPH} + \text{H}^+, \qquad \text{(A1.4)}$$

where HK = Hexokinase

PGI = Phosphoglucose isomerase

G-6-P-DH = Glucose-6-phosphate dehydrogenase.

The ATP/NADP buffer solution[5] began with a triethanolamine buffer base of 50 ml consisting of 13.93 g triethanolamine and 0.25 g $MgSO_4 \cdot 7\ H_2O$ in 50 ml water. To this were added 240 mg ATP and 600 mg NADP. This solution was brought up to 100 ml and pH corrected to 7.6. The buffer solution was good for *ca* two months when stored at 4°C.

The rest of the procedure was as described in the aforementioned kit. A Shimadzu UV-160 was used to make absorbance measurements at 365, 340, and 334 nm.

A1.4.2 PHB Assay

The procedure for the PHB assay was heavily based upon the work of Braunegg *et al.*[6]. Frozen, centrifuged fermentation pellets were first freeze-dried. Pellets were then carefully transferred to their respective development tubes (Kimax 45066, 16x100mm screw cape vials). To each centrifuge tube were added 2 ml of 3% v/v methanol in H_2SO_4 with 4.5 g/l benzoic acid added as an internal standard. The centrifuge tubes were briefly vortexed and the methanol transferred to the proper development tube. Two ml of chloroform were then added to each development tube, vortexed, and transferred to development tubes. The capped development tubes were incubated in an oven with occasional vortexing at 100°C for three and a half hours. Subsequently, the tubes were removed and allowed to cool to room temperature. Once cooled, one ml of water was added and the tubes vigorously vortexed. Two phases were formed: a top methanol/water phase and a bottom chloroform phase. Once both phases had adequately separated, the bottom phase was pipetted off and transferred to 1.5 ml GC sampling vials (Wheaton Scientific 255170).

For calibration purposes, 80 mg of the sodium salt of β-hydroxybutyric acid were weighed out in a development tube. Four ml of the above methanol solution and four ml of chloroform were added to the developing tube. The

standard was incubated for one hour at 100°C. Two ml of water were added to the room temperature standard and the chloroform phase transferred to a GC sampling bottle.

A Shimadzu GC-9A gas chromatograph equipped with a Shimadzu AOC-9 automatic sampler was used for sample analysis. This GC featured a double FID and temperature programming. The analysis conditions were as follows: 2 μl sample injection volume; injection port temperature = 200°C; oven temperature = 100°C for one minute, ramped up at 8°C/min to the final temperature of 150°C for one minute. Helium was used as the carrier gas at a flow rate of 50 ml/min. A Hamilton syringe (model 701N, 10 μl volume) was used for sample injection. An Alltech custom-made column was used for the separation. The metal column was 2 m long with a 5 mm outside diameter and a 3.4 mm inside diameter. The support consisted of 80/100 Chromosorb WAW with a liquid phase of 10% C20M-TPA. GC peak analysis was recorded on a Shimadzu C-R3A Chromatopac integrator.

A1.4.3 Total Protein Assay

Sigma Total Protein Kit No. P5656 was used for the wet chemistry portion of the protein assay. For cellular protein analysis, freeze-dried pellets were dissolved in 10 ml of a 1 g SDS/200 ml solution. Samples were then sonicated with a half-inch tip at "3" at 50 % duty for three minutes (Heat Systems Model W-375). Samples were then spun at 18,000 rpm for 20 minutes. The supernatant was separated from the pellet and the pellet was dis-

carded. For liquid fermentation broth samples, it proved necessary to precipitate the protein because of fructose interference. Spectrophotometric analysis was performed in either a Shimadzu UV-160 or a Bausch & Lomb Spectronic 21.

A1.4.4 Ammonium Assay

Initially, ammonium analysis was performed chemically, following the method outlined by Stainton *et al.*[7]. Unfortunately, this method proved to be too unreliable and inconsistent for this work's purposes. A far more reliable and quick method was found in the Ingold Electrodes, Inc. ammonium probe (Series 7500). The analysis procedure was modified as follows: A 50 ml culture test tube was shortened to *ca* 15 ml of volume. This size proved most adequate since the probe was only slightly smaller than the inside diameter of the tube, thereby reducing the exposed surface area for ammonia loss. One ml of sample was added to nine ml of water and vigorously stirred with a magnetic stirbar. The probe was inserted to just below the liquid surface prior to addition of 0.15 ml of a 40 g NaOH/100 ml solution. The probe's output was read by a Cole-Parmer Model 5997-20 pH controller on EXPANDED range and "mV" setting. The final value was recorded as well as data logged on the data acquisition system for later reference and calculation.

A standard NH_4Cl solution followed by serial dilutions was used to calibrate the probe. Calibration solutions were 10 ml final volume with one ml consisting of the salts portion (no NH_4Cl or fructose) of the fermentation medium.

Not only did temperature have a profound effect on the probe's output, but it also appeared that the ionic composition of the sample influenced the stability of the output reading. The logarithm of the output voltage versus the concentration provided the calibration curve against which all samples were compared.

A1.4.5 Dry Weight Assay

The dry weight assay followed the accepted dry weight membrane determination technique. Millipore filters (Cat. GSWP 047 00; 0.22 μm pores) were placed on individual numbered foil squares and placed in covered glass petri dishes before drying in an 80°C oven for one day. The petri dishes were then transferred to a dessicator to cool before weighing the filter and foil. Seven to 80 ml of fermentation broth were vacuum-filtered through each filter via a Millipore sintered glass filtration unit and a vacuum pump. Filters were then carefully returned to their respective glass petri dishes and placed in the 80°C oven for one to two days. The petri dishes were again removed and allowed to cool in a dessicator before final weighing.

A1.4.6 Biomass Composition Analysis

Compositional analysis of biomass was performed by the Chemistry Department's analytical laboratory. Fermentation samples were used for this purpose. Dry weight and PHB composition were noted; freeze-dried pellets were stored over Drierite prior to compositional analysis. Four different samples were analyzed for carbon, hydrogen, and nitrogen; the balance was assumed to be

oxygen. The analytical laboratory's results were then corrected for PHB content to arrive at the final reported biomass composition values.

A1.4.7 ^{14}C Assay

D-fructose-UL-^{14}C was used as the substrate in a series of radiochemical fermentation experiments. The ^{14}C-fructose was obtained from Sigma (product no. 29,755-0) with a specific activity of 268.7 mCi/mmol; each experiment used *ca* 20 μCi. Evolved $^{14}CO_2$ was trapped in an ethanolamine/methanol (1:2) filled gas washer. ^{14}C activities in various samples were assayed with a Beckman LS-5801 liquid scintillation counter. Sample vials (Beckman Mini Poly-Q vials; 6 ml; cat. no. 592928) contained one ml of sample and three ml of ScintiVerse I (Fisher Scientific, SX1-4). Sample activities ranged from 160,000 cpm to nearly zero cpm.

A1.5 INSTRUMENT CALIBRATION

A1.5.1 Dissolved Oxygen Probe

The dissolved oxygen probe was polarized for 24 hours while being stored in water. Prior to calibration, the probe was removed and dried. After setting "electronic zero," the amplifier was switched to the 200 scale. After accounting for humidity, atmospheric pressure, and temperature and making the necessary partial pressure calculations, the amplifier output for air calibration was noted

by the data acquisition system. Using a 40ml syringe to encase the probe's tip, high purity nitrogen gas was passed through the syringe at *ca* one l/min. When the probe output had stabilized, the data acquisition system again noted the amplifier output and made the corresponding calibration calculation.

Experience showed that sterilization normally had little effect on the probe's calibration. When not in use the probe was stored with its tip immersed in water to prevent drying of the internal reference solution.

A1.5.2 Dissolved Carbon Dioxide Probe

Sterilization of the dissolved carbon dioxide probe occurred in the presence of internal reference solution with the internal pH probe retracted from the probe membrane. After sterilization, the internal reference solution was first withdrawn through a special port via syringe, and then calibration buffer "A" was injected. Calibration buffer "A"'s partial pressure of carbon dioxide was known and the amplifier's output was noted by the data acquisition system. The process was then repeated with calibration buffer "A" being removed and calibration buffer "B" being injected; the probe output was again noted and the calibration calculations completed. Calibration buffer "B" was then removed and replaced by the internal reference solution. The internal pH probe was then inserted into the measuring position against the probe membrane.

During periods of nonuse, the internal pH probe was removed and stored in pH 4 buffer. It was found that the probe could not be stored "wet" since the steel mesh supporting the membrane had a propensity to oxidize.

A1.5.3 Optical Density Flowcell

Zero point calibration (0 % transmittance) was achieved without the presence of the flowcell in the Spectronic 21's sample chamber. (With the sampling chamber empty, a special shutter prevented light from reaching the photocell.) After data-logging the output, the flowcell was inserted, secured and covered with a shade hood. Uninoculated medium was then pumped through (bottom to top) with the pump rate being varied sporadically to dislodge any bubbles. The instrument was then adjusted to 100 % transmittance and the output data logged. The flowcell was found to provide a dilution factor of six, *i.e.*, six absorbance units culture = one absorbance unit recorded.

A1.5.4 pH Probe

When not in use, the pH probe was stored in pH 4 buffer. With the pH controller set on EXPANDED scale, the probe was immersed in pH 7.0 buffer and the offset adjusted so that the needle read "11." The probe was then placed in pH 6.0 buffer and the slope adjusted to a reading of "1." This procedure was repeated until no further adjustments of slope or offset were necessary and the corresponding outputs were recorded.

A1.5.5 Fluorescence Probe

When indicated by the software's internal checking routines, the Fluromeasure probe was recalibrated by BioChemTechnology Inc.

A1.5.6 Off-gas Carbon Dioxide and Oxygen Analyzers

After passing air through both instruments, the air calibration point (20.946 %) for the oxygen analyzer was data-logged. The gas was then switched to high-purity nitrogen and the zero calibration point for the oxygen analyzer recorded. While nitrogen was still flowing through both instruments, the zero calibration point was data-logged for the carbon dioxide analyzer. The gas source was finally switched to a 2.5% carbon dioxide/97.5% nitrogen mixture and the carbon dioxide analyzer calibration completed.

A1.6 FERMENTATION AND POST-FERMENTATION DATA MANIPULATION

A1.6.1 On-line Data Processing

Because of limitations inherent to the data acquistion system, special considerations had to be made to increase the resolution of the signals collected. When data-logging the on-line instruments, only four significant digits were stored to disk per input signal; the A/D converter processed 12 bits per channel, allowing only 4096 different values to be recorded over the complete measuring range. (If negative input voltages were possible, this number would essentially double. However, typical analog output signals usually range from zero to some maximum voltage.) Also, the on-line status display posted updated values with

only two significant digits to the right of the decimal place. These two considerations required a little ingenuity with regard to the calibration of instruments in order to maximize resolution of the recorded signals as well as to increase the sensitivity of the display on the status page to allow detection of small trends in the on-line observables.

This resolution problem and its solution can be clarified with the following example. With the off-gas oxygen analyzer, the detectable range was from one to 25 percent oxygen. Typically, the oxygen concentration would range from 20.946% (concentration of oxygen in air) to *ca* 17% for any given fermentation. With a normal calibration, air and oxygen-free nitrogen are used to achieve air saturation and zero oxygen calibration points. Therefore, the calibrated maximum range the computer sees is zero to 20.946% oxygen. Assuming that the output at 20.946% oxygen is at the maximum voltage that the data acquisition system can detect without saturating the computer input and that the output voltage at zero percent oxygen is zero volts, the smallest increment in the recorded signal is 0.0051(=20.946/4096)% oxygen. Unfortunately, since the computer can record only four significant digits and can display only two digits to the right of the decimal point, the effective resolution is reduced by a factor of two. For example, the numbers 19.0980% and 19.1031% would be displayed and recorded as 19.10%, since the computer is unable to distinguish between the two values.

To circumvent this problem, a pseudocalibration technique was developed. Instead of using 20.946 and zero percents for the high and low calibration points, the pseudovalues 1000 and zero, respectively, were used instead. Effectively, the

smallest detectable increment then becomes 0.24(=1000/4096). Using the same train of thought followed earlier, 19.0980 and 19.1031 become 911.77 and 912.01, respectively; these two points can be resolved by the system. Therefore, the resolution has been effectively maximized.

Following a fermentation run, stored data were converted from an unformated, stored form to a formated form after subtracting out any background, reconverting any pseudocalibration values to physically meaningful units, and performing simple mathematical transformations (*e.g.*, converting optical density to absorbance).

With certain runs further special manipulations were required. These runs involved wild oscillations in the off-gas carbon dioxide concentration that were due to addition of NaOH for pH control (see Appendix 2). The dramatic drops in off-gas carbon dioxide concentration were "clipped" when a pH control pulse was detected. Essentially, this entailed detection of the onset of NaOH addition and conversion of the off-gas carbon dioxide concentration to the last detected value prior to the onset of the pH control pulse. These data were later further modified by converting the imposed concentration plateaus to approximate linear ramps on the basis of the local trend of the off-gas carbon dioxide concentration.

Further manipulations of the on-line observables occurred on a VAX 11/780 or MicroVAX 3500. First, each on-line parameter was checked against a rejection tolerance. Following spurious data-point checking and elimination, the data were subjected to a three-point boxcar average. Using the method of Savitzky and Golay[9] with modifications by Steiner *et al.*,[10] the data were smoothed and derivatives calculated. Essentially, this technique is a modification of a linear

regression technique. A 25 point grouping size was used for both smoothing and derivative determinations. Smoothing was accomplished using a cubic weighting function, and derivatives were calculated with a quadratic-derivative weighting function. Every fifth point (every fifteenth point of the raw data) was selected for later pathway rate calculations. Since the culture volume was known at each sampling time via backcalculation, the volume and volume changes between sampling times were approximated by a linear expression.

A1.6.2 Off-line Data Processing

To make the off-line fructose, ammonium, PHB and dry weight data suitable for calculation with the on-line data, a number of adjustments and interpolations were necessary. In the case of fructose and ammonium chloride, additions of concentrated feed solutions had to be accounted for in the model. Also, since a fed-batch system was employed, PHB and dry weight concentrations were effectively diluted because of feed solution additions as were also the fructose and ammonium chloride concentrations.

To account for the effects of feeding and the associated volume changes, we begin with the previously presented general macroscopic balance (Eq. (2.23)), simplified for nongaseous liquid phase components only. There the "l" superscript will be dropped and all concentrations, volumes and rates of formation will be assumed to be liquid phase only. For a fed-batch reactor and nongaseous species i:

$$\frac{d(\mathbf{V}\cdot\mathbf{C}_i)}{dt} = \mathbf{f}_i\cdot\mathbf{C}_{f,i} + \mathbf{V}\cdot\mathbf{R}_{f,i}, \qquad \text{(A1.5)}$$

where $\mathbf{V} \equiv$ liquid culture volume, l

$\mathbf{C}_i \equiv$ mol i per unit liquid volume, mol/l

$\mathbf{C}_{f,i} \equiv$ mol i per unit liquid volume in the feed, mol/l

$\mathbf{R}_{f,i} \equiv$ rate of formation of i, mol/l/hr

$\mathbf{f}_i \equiv$ volumetric feed rate of i, l/hr.

Differentiating, dividing by $\mathbf{V}$, and rearranging Eq. (A1.5) lead to

$$\frac{d\mathbf{C}_i}{dt} + \frac{\mathbf{C}_i}{\mathbf{V}}\frac{d\mathbf{V}}{dt} - \frac{\mathbf{f}_i}{\mathbf{V}}\mathbf{C}_{f,i} = \mathbf{R}_{f,i}. \tag{A1.6}$$

This equation clearly demonstrates that unlike a constant volume batch fermentation in which $\mathbf{R}_{f,i}$ can be determined directly from the change in the concentration of i (second and third terms on the left hand side are zero.), we need to be aware of volume changes as well as feed additions in a fed-batch fermentation.

For the sake of mathematical convenience let us define Φ_i such that the derivative of Φ_i equals the left side of Eq. (A1.6):

$$\frac{d\Phi_i}{dt} = \frac{d\mathbf{C}_i}{dt} + \frac{\mathbf{C}_i}{\mathbf{V}}\frac{d\mathbf{V}}{dt} - \frac{\mathbf{f}_i}{\mathbf{V}}\mathbf{C}_{f,i}. \tag{A1.7}$$

Φ_i is, therefore, related to $\mathbf{R}_{f,i}$ through the following relationship:

$$\Phi_i = \int \mathbf{R}_{f,i}dt + \Theta_i, \tag{A1.8}$$

where Θ_i is an arbitrary constant. Essentially, Φ_i is a pseudoconcentration; the derivative of Φ_i gives $\mathbf{R}_{f,i}$. This relationship is analogous to the constant

volume reactor mentioned earlier. Eq. (A1.7) may be written in the alternate differential form

$$d\Phi_i = d\mathbf{C}_i + \frac{\mathbf{C}_i}{\mathbf{V}} d\mathbf{V} - \frac{\mathbf{f}_i}{\mathbf{V}} \mathbf{C}_{f,i} dt. \tag{A1.9}$$

For purposes of the following calculations, we should note that

$$d\mathbf{V} = \left(\sum_i \mathbf{f}_i \right) dt, \tag{A1.10}$$

when no samples are withdrawn from the fermenter. Integrating Eq. (A1.9) over the interval $[t_2,\ t_1]$ where $t_2 \geq t_1$ yields

$$\int_{t_1}^{t_2} d\Phi_i = \int_{t_1}^{t_2} d\mathbf{C}_i + \int_{\mathbf{V}(t_1)}^{\mathbf{V}(t_2)} \frac{\mathbf{C}_i}{\mathbf{V}} d\mathbf{V} - \int_{t_1}^{t_2} \frac{\mathbf{f}_i}{\mathbf{V}} \mathbf{C}_{f,i} dt, \tag{A1.11}$$

and

$$\Delta\Phi_i = \Phi_i(t_2) - \Phi_i(t_1) \tag{A1.12}$$

$$= \mathbf{C}_i(t_2) - \mathbf{C}_i(t_1) + \int_{\mathbf{V}(t_1)}^{\mathbf{V}(t_2)} \frac{\mathbf{C}_i}{\mathbf{V}} d\mathbf{V} - \int_{t_1}^{t_2} \frac{\mathbf{f}_i}{\mathbf{V}} \mathbf{C}_{f,i} dt. \tag{A1.13}$$

Equation (A1.13) is then applied to the time interval just after a sample has been taken and just before the next sample is withdrawn, *i.e.*, $[t_2^-,\ t_1^+]$. Note that for mathematical convenience the change in the culture volume is considered to be an instantaneous step function; the change in volume that is due to sampling does not affect the above calculation except in determining the starting and ending volume over the interval of interest. With some thought it is easy to convince ourselves that if $d\mathbf{V} \geq 0$ and if $\mathbf{f}_j \geq 0$ for all j over the interval $[t_2^-,\ t_1^+]$, the functional form of $\mathbf{V}$ and $\mathbf{f}_j$ is irrelevant as long as these functions are consistent with the previously mentioned relationship of Eq. (A1.10).

We then propose simple linear relationships for $\mathbf{C}_i$ and $\mathbf{V}$ over the interval $[t_2,\ t_1]$:

$$\mathbf{C}_i(t) = \mathbf{C}_i(t_1) + \left[\frac{\mathbf{C}_i(t_2) - \mathbf{C}_i(t_1)}{t_2 - t_1}\right](t - t_1) \tag{A1.14}$$

$$\mathbf{V}(t) = \mathbf{V}(t_1) + \left[\frac{\mathbf{V}(t_2) - \mathbf{V}(t_1)}{t_2 - t_1}\right](t - t_1). \tag{A1.15}$$

We note that over the interval $[t_2,\ t_1]$

$$f = \frac{\mathbf{V}(t_2) - \mathbf{V}(t_1)}{t_2 - t_1}, \tag{A1.16}$$

where f is the total average feed rate for all i. Similarly, for the interval $[t_2,\ t_1]$

$$d\mathbf{V}_{f,i} = f_i dt = \frac{\Delta\mathbf{V}_{f,i}[t_2, t_1]}{t_2 - t_1} dt, \tag{A1.17}$$

where $\mathbf{V}_{f,i} \equiv$ feed volume of i added, l

$F_i \equiv$ average volumetric feed rate of i, l/hr

$\Delta\mathbf{V}_{f,i}[t_2, t_1] \equiv \int_{t_1}^{t_2} \mathbf{f}_i dt.$

Making use of Eq. (A1.10) and substituting Eqs. (A1.14), (A1.15), and (A1.17) into Eq. (A1.13) and solving for $\Delta\Phi_i$ lead to

$$\begin{aligned}\Delta\Phi_i[t_2, t_1] &= \Phi_i(t_2) - \Phi_i(t_1) \\ &= 2(\mathbf{C}_i(t_2) - \mathbf{C}_i(t_1)) + \left[\mathbf{C}_i(t_1) - \left(\frac{\mathbf{C}_i(t_2) - \mathbf{C}_i(t_1)}{\mathbf{V}(t_2) - \mathbf{V}(t_1)}\right)\mathbf{V}(t_1)\right. \\ &\quad \left. - \left(\frac{\mathbf{C}_{f,i} \cdot \Delta\mathbf{V}_{f,i}[t_2, t_1]}{\mathbf{V}(t_2) - \mathbf{V}(t_1)}\right)\right] \ln\left(\frac{\mathbf{V}(t_2)}{\mathbf{V}(t_1)}\right).\end{aligned} \tag{A1.18}$$

Using this expression in conjunction with the off-line experimental data, we have effectively consolidated into one parameter the effects of concentration changes, volume changes and feed additions.

At this point the question of why we have proceeded in this manner may arise. Simply put, it is much better, computationally speaking, to integrate the data, fit the pseudoconcentration, Φ_i, with a smooth function for interpolation and calculation of derivatives than to try to fit the actual concentration data and assume a linear profile for feed additions. The latter method introduces larger uncertainties in the derivative calculations simply because the concentration of species i fluctuates up and down from point to point throughout the fermentation, giving both positive and negative slopes. With the pseudoconcentration method, calculation of derivatives is dramatically improved, since the pseudoconcentration is almost always monotonically increasing or decreasing.

Pseudoconcentrations were smoothed and interpolated using IMSL cubic spline routines ICSSCU or ICSSCV; interpolations and derivative calculations were made at points corresponding to the smoothed on-line data.

A1.7 REFERENCES

1. Schlegel H.G., Gottschalk G., and Bartha R., *Nature*, **191**, 463 (1961).
2. Pfennig, N., and Lippert, K.D., *Arch. Mikrobiol.*, **55**, 245 (1966).
3. Lee C. and Lim H., *Biotechnol. Bioeng.*, **22**, 639 (1980).
4. Cook, D.W., Tischer, R.G., and Brown, L.R., *Canadian Journal of Microbiology*, **13**, 701 (1967).
5. Friehs, K., Personal communication.
6. Braunegg G., Sonnleitner B., and Lafferty R.M., *Appl. Microbiol. Biotech.*, **6**, 29 (1978).
7. Stainton M.P., Capel M.J., and Armstrong F.A.J., *The Chemical Analysis of Fresh Water*, Miscellaneous Special Publication No. 25 (2^{nd} ed.), Freshwater Institute, Winnepeg, Manitoba.
8. Schlegel, H.G., *Adv. Comp. Physiol. Biochem.*, **2**, 185 (1966).
9. Savitzky, A., and Golay, M.J.E., *Anal. Chem.*, **36**, 1627 (1964).
10. Steiner, J., Termonia, Y., and Deltour, J., *Anal. Chem.*, **44**, 1906 (1972).

APPENDIX 2

CLOSING THE CARBON BALANCE

A2.1 INTRODUCTION

Early in the evolution of this project, there were strong indictations that something was amiss with the application of the model to the experimental system. This necessitated scrutiny of the experimental system and the calculated results derived from the experimental data. The two most common occurrences were:

- Under normal exponential, balanced growth conditions, high citric acid cycle activity would be expected to fulfill the cell's high reductive energy demand during energy-intensive biosynthesis. Therefore, $\mathbf{v}_2$ would be expected to be very close to $\mathbf{v}_1$, particularly if PHB polymerization were very low. The results of a number of experiments, however, suggested that, on average, $\mathbf{v}_2$ was only 20% of $\mathbf{v}_1$.
- Through the majority of the fermentation experiments, large oscillations in the off-gas carbon dioxide concentration were observed in the last half of the fermentation. The magnitude of these oscillations often ranged from one to two percent relative to a four to five percent average off-gas carbon dioxide concentration.

Given these two observations, it became apparent that a reevaluation of the experimental system with respect to the carbon balance was necessary.

A2.2 INVESTIGATION OF THE CARBON BALANCE

In the majority of the fermentations performed, a discrepancy of 25–30% in the overall carbon balance was observed. In other words, 25–30% of the carbon consumed as fructose could not be accounted for as biomass, PHB or carbon dioxide. A number of factors suggested that the estimate of dissolved carbon dioxide gas was too low. The medium used was highly buffered with phosphate. Secondly, the oscillations in the off-gas carbon dioxide were synchronized with pH additions of sodium hydroxide. Since hydroxide can react with dissolved carbon dioxide in the following manner,

$$CO_2 + OH^- \longrightarrow HCO_3^-, \qquad \text{(A2.1)}$$

conversion of dissolved carbon dioxide to bicarbonate with subsequent reduction in the mass transfer desorption driving force appeared as a real possibility. From a model calculation standpoint, if the carbon dioxide production rate by the cells was higher than reflected in the off-gas carbon dioxide measurement, $\mathbf{v}_2$ would be larger and closer in magnitude to $\mathbf{v}_1$.

Secondly, accumulation of dissolved carbon dioxide in the culture liquid appeared to be a possibility. Unlike oxygen, which was transferred from gas to liquid, dissolved carbon dioxide must migrate through the liquid to a gas bubble before being transported out of the fermenter. If the mass transfer resistance is large enough, carbon dioxide can accumulate in the liquid, thereby reaching very high levels. Typically, most researchers have used Henry's Law as an estimate of the dissolved carbon dioxide concentration. Smith and Ho[1] disputed

the validity of this approximation by presenting data which gave an absorption coefficient for carbon dioxide of 360, suggesting that a large accumulation of dissolved carbon dioxide was possible. If Henry's Law held, the absorption coefficient should be about one. (The adsorption coefficient relates the ratio of the partial pressure of a gas species in the liquid phase to the partial pressure of the same gas species in the gas phase.)

The conditions under which Smith and Ho performed their experiments were virtually identical to those used in our experiments except that the volumetric flow rates used in our experiments were nearly seven times lower and the medium used was a defined salts medium relative to Smith and Ho's complex medium. Based upon Smith and Ho's reported data, the underestimation of the dissolved carbon dioxide concentration and associated underestimation of carbonic acid, bicarbonate and carbonate along with the observed oscillations in the off-gas carbon dioxide gas concentration strongly suggested that this might be the source of the missing carbon.

Subsequently, an Ingold dissolved carbon dioxide probe was purchased to fully investigate this question. Contrary to Smith and Ho's results, the data confirmed that Henry's Law held under virtually all conditions except during sharp transitions in fermenter conditions or in cellular metabolism. Also, no large oscillations in the dissolved carbon dioxide concentration were observed upon the addition of sodium hydroxide. Thus, the question of dissolved carbon dioxide gas concentration was answered, although the observation of the off-gas carbon dioxide oscillations was as yet unresolved.

A2.3 TOTAL ORGANIC CARBON (TOC) EXPERIMENT

Although it had been suggested that *Alcaligenes eutrophus* H16 grew with little or no excreted products under normal conditions,[2] it was decided to confirm these observations. Therefore, a TOC experiment was constructed to examine cellular carbon excretion under early, mid and late exponential growth as well as under PHB storage conditions.

The experiment was set up in the following manner: Four baffled one liter flasks were filled with 300 ml of standard medium composition[3,4] with 1 g/l ammonium chloride as a nitrogen source. Differing amounts of fructose were added to each flask: 1, 2.5, 4, and 13 g/l. The initial pH was set at 7.3 (previous experience showed that the pH quickly fell to the neighborhood of 6.8 shortly after growth began). Each flask was inoculated with 0.5 ml from a inoculum tube containing cells grown on standard medium, 1 g/l ammonium chloride and 8 g/l fructose. All four baffled flasks were incubated in a rotary shaker at 30°C and 250 rpm.

The time course of each flask was closely monitored; at or near the point of fructose exhaustion, each flask was iced down. The contents of each flask was analyzed for PHB, protein, fructose, and dry weight concentrations. For purposes of obtaining samples suitable for TOC analysis, the medium in each flask was spun down for 20 minutes at 4°C and 14,000 rpm . The resulting supernatant was filtered through a prerinsed 0.2 μm filter and stored at 4°C. TOC analysis was performed by Brown and Caldwell Laboratories in Pasadena.

(TOC analysis entails acidification of the sample followed by aeration with nitrogen to drive off any dissolved carbon dioxide species. The sample is then injected into a TOC analyzer, where any carbon present is oxidized, usually on a platinum catalyst, to carbon dioxide and calculated as TOC.)

After correction for residual fructose, the results of the TOC analysis indicated that only 0.6 to 2.1% of the fructose consumed showed up in the medium, thereby suggesting that excreted products were not a major factor in the unresolved carbon balance. One surprising consistency, however, did arise from these results. In all four flasks, after substracting the fructose consumed to produce biomass, PHB and TOC, approximately 42% of the consumed fructose was presumably evolved as carbon dioxide, regardless of the relative proportions of PHB to biomass. In the composite of all fermentations run up to this point, the average ratio of detected carbon dioxide evolved relative to fructose consumed on a per C-mol basis suggested that only 25% of the fructose was evolved as carbon dioxide. This suggested either that the carbon dioxide portion of this calculation was in error, implying an inaccurate carbon dioxide off-gas analyzer, an incorrect estimate of dissolved carbon dioxide species, or that the calculated fructose consumption rate was in error.

A2.4 DISSOLVED CARBON DIOXIDE SPECIES EXPERIMENT

Carbon dioxide in its solvated gas state can react reversibly with water to

form carbonic acid:

$$CO_2 + H_2O \rightleftharpoons H_2CO_3. \qquad \text{(A2.2)}$$

Carbonic acid then spontaneously and reversibly dissociates to bicarbonate and then carbonate, depending upon the prevailing pH:

$$H_2CO_3 \rightleftharpoons H^+ + HCO_3^- \rightleftharpoons 2H^+ + CO_3^{2-}. \qquad \text{(A2.3)}$$

Although the equilibrium constants for the above reactions are reported, there appears to be some discrepancy.[5,6] Furthermore, equilibrium values reported are usually for a pure water system.

In an attempt to dispense with some of this confusion, a determination was made of the approximate concentration of dissolved carbon dioxide species under conditions similar to those observed under typical *A. eutrophus* fermentations. To accomplish this two similar experiments were performed: one with distilled water and one with fermentation medium without added ammonium chloride and fructose.

In the first experiment, 12 liters of distilled water were added to the fermenter and maintained at 31°C. For two hours the system was maintained at pH 4 and flushed with pure nitrogen gas at 1.5 l/min to remove any carbon dioxide. Prior to beginning the experiment, the pH was raised to the fermentation condition of 6.8. With the agitation speed set at 600 rpm, 2.5% carbon dioxide gas (balance nitrogen) was introduced at approximately 1.5 l/min. Dissolved carbon dioxide, off-gas carbon dioxide and pH were data-logged. Sodium hydroxide was used to maintain the pH. After *ca* four hours, the system was very near equilibrium. The carbon dioxide gas was turned off and the pure nitrogen gas turned

on to desorb the dissolved carbon dioxide. Again the pH was maintained at 6.8 by sulfuric acid addition.

This same sequence of events was also carried out with the fermenter filled with fermentation medium minus ammonium chloride and fructose. Unlike the distilled water case, saturation and complete desorption were achieved in about half the time.

Performing an overall carbon dioxide balance, the amount of carbon dioxide dissolved in the liquid phase as gas/ionic species for the prevailing carbon dioxide partial pressure could be determined. Beginning with Henry's Law,

$$p_{CO_2} = Hx_{CO_2} = \frac{H}{C_T} C_{CO_2}, \qquad \text{(A2.4)}$$

where p_{CO_2} ≡ partial pressure of carbon dioxide in the gas phase

H ≡ Henry's Law coefficent for carbon dioxide

x_{CO_2} ≡ mole fraction of carbon dioxide in liquid phase

C_T ≡ total moles per liter in solution (*ca* 55.5 M)

C_{CO_2} ≡ liquid phase dissolved carbon dioxide gas concentration.

A modified Henry's Law relationship can be defined, assuming constant pH, appropriate dissociation equilibrium relationships, and a total concentration of carbon dioxide species, $C^T_{CO_2}$, given by

$$C^T_{CO_2} = C_{CO_2} + C_{H_2CO_3} + C_{HCO_3^-} + C_{CO_3^{2-}}, \qquad \text{(A2.5)}$$

as follows:

$$p_{CO_2} = Hx_{CO_2} = \frac{H}{C_T} C_{CO_2} = \frac{H'}{C_T} C^T_{CO_2}. \qquad \text{(A2.6)}$$

From Eq. (A2.6), H′ is related to H in the following manner:

$$HC_{CO_2} = H'C^{T}_{CO_2} \tag{A2.7}$$

$$= H'\left(C_{CO_2} + C_{H_2CO_3} + C_{HCO_3^-} + C_{CO_3^{2-}}\right) \tag{A2.8}$$

$$= H'(C_{CO_2} + K_1C_{CO_2} + K_2C_{CO_2} + K_3C_{CO_2}) \tag{A2.9}$$

$$= H'(1 + K_1 + K_2 + K_3)C_{CO_2}. \tag{A2.10}$$

The K_i are the appropriate equilibrium constants between dissolved carbon dioxide gas and the various ionic carbonate species at constant pH, and H′ is the modified Henry's Law constant. H is related to H′ in the following manner,

$$H = H'(1 + K_1 + K_2 + K_3). \tag{A2.11}$$

Therefore, Eq. (A2.7) can be used to relate the total dissolved carbon dioxide species to the carbon dioxide partial pressure at constant pH.

For the distilled water experiment, $H' = 1 \times 10^4$ mm Hg, and for the fermenter medium experiment, $H' = 2 \times 10^5$ mm Hg. The higher value for H′ in the fermenter medium experiment is due to what is commonly referred to as the "salting out" effect;[7] *i.e.*, the solubility of a gas is reduced by a higher ionic content in the liquid phase.

Using the modified Henry's Law expression and the new value for the Henry's Law coefficient, H′, improved the carbon balance by 4 to 5%.

A2.5 REEVALULATION OF ASSAY PROCEDURES

Attention was next turned to a reevaluation of the various analytical tech-

niques employed in hopes of identifying any systematic errors or inherent inaccuracies.

A2.5.1 Fructose Assay

The fructose assay was checked for accuracy with regard to the linearity of the absorbance/concentration relationship as well as the accuracy of dilutions. A standard solution was prepared and diluted to varying concentrations covering the full range of absorbance differences (*i.e.*, final absorbance minus initial absorbance). Calculated fructose concentrations were compared to expected fructose concentrations with an average discrepancy of -2.3% and a variance of 1.3% for five determinations. The conclusion, therefore, was that the fructose assay was quite accurate.

On a similar note, the fructose feed solution was checked for hygroscopic properties. That is to say, if the fructose feed solution absorbed significant amounts of water, the volume would expand, the effective concentration would decrease and the amount added as indicated by the 50 ml buret would overestimate the absolute amount of fructose added during pH-controlled feeding. The fructose solution was exposed to air in a beaker overnight. The measured fructose concentration increased, indicating that the feed solution was not hygroscopic under those conditions. However, this did not rule out absorption of water from autoclaved reservoir bottles and tubing, although care was taken to dry tubing and reservior bottles before addition of all feed solutions. It is highly unlikely that any residual water had a significant effect on the feed concentrations.

A2.5.2 Dry Weight Assay

The membrane filtration technique was compared to drying cells in an aluminum pan. A dense, late storage-phase culture was grown in a shake flask (1 g/l ammonium chloride, 12 g/l fructose, standard salts medium). Four predried, preweighed membranes were used to vacuum-filter 10 ml of medium each and were rinsed with *ca* 3 ml water. The membranes were placed in covered glass petri dishes and dried in an 80°C oven to constant weight. Ten milliliters of culture were placed in each of four centrifuge tubes plus 2 ml of methanol (to prevent growth) and spun down in a centrifuge. The supernatant was removed, and the pellet was reconstituted and rinsed out of each centrifuge tube with 4 ml water and 1 ml methanol and put into one of the four predried, preweighed aluminum pans. The aluminum pans were placed in covered glass petri dishes and dried to constant weight in the 80°C oven. Differences between final and initial weights were compared between the membranes and the pans, with the membranes averaging 34.8 mg and the pans averaging 37.1 mg; the membranes averaged 6% lower than the pans. However, recalling that the cells in the pans were not resuspended and washed, this weight difference is actually too large. Considering that there are *ca* 8.44 g of salts added to each liter of medium not including residual fructose and estimating that 0.25 ml of medium was retained in the pellet, the weight difference in the pans would be 2.1 mg too high because of retained medium salts. Since the weight difference between the membranes and the pans is only 2.3 mg, this would suggest that the membrane technique is accurate relative to the discrepancies in the carbon balance.

A2.5.3 PHB Assay

The PHB assay was checked for repeatability of the same sample, variance between identical time samples from the same culture, and losses that were due to transferring the freeze-dried pellet from the centrifuge tube to the incubation tube. Four centrifuge tubes filled with 10 ml of culture from the same late storage phase culture were spun down and the pellets freeze-dried in their respective centrifuge tubes. Four more samples of Sigma-supplied PHB were used to check the transfer losses. Although the Sigma PHB was not pure, it was assumed to be homogeneous. Two samples of Sigma PHB, one high concentration and one low, were added to two centrifuge tubes, and two other samples of similar concentration were added directly to two incubation tubes. The hydroxybutyric acid standard was prepared as per usual, *i.e.*, added directly to an incubation tube. All samples were prepared as previously described in Appendix 1.

For the four culture samples, the repeatability of the same sample gave a variance of less than 1% (Average = 0.4%); among the four samples the variance was *ca* 2%, suggesting that the repeatability of the same sample and the variance between identical samples were very good.

With regard to the transfer losses investigation, it was found that the Sigma PHB was not pure, as evidenced by the cell debris at the chloroform/methanol interface. To correct for this impurity, the GC-measured PHB concentration was normalized by the weighed concentration. (The Sigma PHB, based on this ratio, was only 92% pure.) To compare losses that were due to the transfer of the freeze-dried pellet from the centrifuge tube to the incubation tube, the

ratio of the normalized incubation tube values were taken with respect to each normalized centrifuge tube value. This ratio averaged 1.05, with a standard deviation of 0.03. This result indicated that GC-determined PHB concentrations as determined by the standard assay technique were on average 5% below the true value. Correction of the PHB concentrations by a factor of 1.05 had only a small effect on the carbon balance, leaving a deficiency of 20 to 25%.

As a final note, it was discovered that the biomass concentration sometimes increased in late storage-phase fermentations even though ammonium was exhausted and the protein concentration was constant. This result suggested that the PHB concentration was too low. For PHB concentrations above 3 g/l, regular vortexing of the incubating PHB pellets was necessary to insure complete reaction of the PHB pellet.

A2.6 REEVALULATION OF OFF-GAS SYSTEM

All the assay procedure inaccuracies did not lead to enough errors to account for the discrepancies in the carbon balance. Attention was turned next to the off-gas system. Of particular interest was a check of the linearity of the off-gas carbon dioxide analyzer and the calibration check of the off-gas system rotameters.

A2.6.1 Off-gas Carbon Dioxide Analyzer

In checking the linearity of the off-gas carbon dioxide analyzer, four cali-

bration gases were used: high-purity nitrogen (zero gas), 1.5% carbon dioxide (balance nitrogen), 2.5% carbon dioxide (balance nitrogen), and 9.6% carbon dioxide (balance nitrogen). It should be noted that the off-gas carbon dioxide analyzer's maximum range was 0 to 6% carbon dioxide. Unfortunately, 6% calibration gas was not available, and, because of the considerable expense, was not purchased.

To allow the 9.6% carbon dioxide gas to register on scale, the instrument slope was reduced. Each gas was allowed to flow through the off-gas analyzer at the same flow rate until the analog output stabilized. The output was then recorded. For the 0%, 1.5% and 2.5% gases, a correlation coefficient of 0.9999 was obtained. Using the line created by these three points, it was found that the output for the 9.6% gas was 21% below its predicted value. Again, the instrument was not designed to extend to this range, but it did suggest that part of the carbon balance error might lie here. However, one observation refuted this idea. Under near-exponential growth conditions, the majority of the recorded carbon dioxide concentrations were within the range of 0 to 2.5%. A running carbon balance indicated that the carbon balance was still an average of 20 to 25% off even in this range. Therefore, the carbon balance was still off during the off-gas carbon dioxide analyzer's "good" range, suggesting that another source was at fault.

A2.6.2 Off-gas Rotameters

The off-gas detection system comprised of the off-gas carbon dioxide and off-gas oxygen detectors, several valves and a rotameter for each off-gas detector

was designed to fit into a modular framework. This unit was inherited from another researcher and was assumed (erroneously) to be in complete working order. While checking the calibration of the rotameters using an in-line wet test meter, it was discovered that two of the Swagelok fittings had previously undetected gradual leaks and that the backpressure in the system was higher than expected, leading to erroneously low flow rate readings. A calibration of the rotameters with line leaks in place resulted in a simple linear correction to previously recorded flow rates. These corrections resulted in a 15 to 20% increase in all flow rates. Subsequently, the carbon balance was improved to an average 10% missing carbon.

A2.6.3 ^{14}C Experiment

Although a carbon balance error of 10% is not uncommon, given the many assays required, this had a rather profound effect on the pathway calculations, particularly with respect to v_2, where fructose consumption and carbon dioxide evolution counteract each other strongly. Also this had further implications with regard to influencing the estimation of such parameters as the oxidative-phosphorylation rato (P/O). With this in mind, an effort to further improve the carbon balance discrepancy was pursued.

From the TOC experiment, an average of 42% of the fructose carbon unaccounted for by biomass, PHB, TOC, and residual fructose was assumed to be carbon dioxide. However, with the flow rates corrected, only 36% of the consumed fructose was showing up as carbon dioxide in the majority of the fermentations performed. With the reliability of the off-gas carbon dioxide analyzer

not completely verified, an experiment using ^{14}C-labeled fructose was performed with trapping of the evolved $^{14}CO_2$

Using a baffled one liter flask equipped with a stir bar and placed in a 31°C water bath, inoculum cells were introduced to 300 ml of typical media containing 1 g/l ammonium chloride and 10 g/l fructose with *ca* 20 μCi of ^{14}C-labeled fructose added. Sterile air was pumped into the system with the exit air passing first through an ethanol/dry-ice trap before passing through two chilled gas washers in series filled with ethanolamine-methanol (1:2). The ethanolamine-methanol mixture stripped the exit gas of carbon dioxide.[8]

After running liquid scintillation counts on the final culture broth, the initial pre-inoculation media and the ethanolamine-methanol solution, it was found that indeed 42% of the initial radioactivity was found in the ethanolamine-methanol solution. This confirmed the assumption made, based on the TOC results as well as again implicated carbon dioxide as one of the possible culprits of missing carbon in the carbon balance.

A2.6.4 Other Corrections

In the course of investigating the off-gas system, a few improvements were employed in hopes of pushing the carbon balance closer to closure. Because of the physical constraints of the system, the off-gas system was physically removed from close proximity to the fermenter, thereby imposing a time lag between events occurring within the fermenter and the acknowledgement of those events by the off-gas system. Therefore, gas concentration step responses were introduced into the fermenter off-gas line to determine the residence time distribution.

The analysis showed that the off-gas line's response could be approximated as plug flow. Because of the difficulties entailed in trying to perform the same analysis on the fermenter filled with liquid, the head space was assumed to resemble a CSTR. Using this information, the time lag in the off-gas concentrations was eliminated during computer analysis of the off-gas data.

A2.6.5 Off-gas Carbon Dioxide Oscillations

A problem that plagued this work from the very beginning involved the previously mentioned large, pH-synchronized, off-gas carbon dioxide concentration oscillations. Particularly perplexing (at the time) was the sudden and distinct disappearance of this phenomenon in later fermentations. Only after a number of somewhat inaccessible factors fell into place did this observation find an explanation.

Because of extensive foaming, which oftentimes threatened the off-gas instruments, a number of techniques were tried to minimize foam production. Antifoam was initially sought as a solution until it was realized that the integrity of the dry weight analysis was impaired. Finally, a paddle was added to the end of the stirrer shaft (in the head space above the liquid in this bottom drive agitator system) to act as a mechanical foam breaker. On a few rare occasions (typically all sight glasses were covered with aluminum foil to prevent the fluorescence probe from picking up stray room light.), the action of the foam breaker could be observed through the top sight glass. Although the foam breaker did an admirable job of controlling the foam level, the foam layer

exhibited surprising mechanical properties, oftentimes preferring to be rapidly stirred rather than to be disrupted.

Early pH-control schemes called for the dropwise addition of sodium hydroxide (or phosphoric acid) through the head plate. After some time it was noticed that pH control appeared to be disrupted by the presence of a foam layer in that after the pH controller stopped adding sodium hydroxide, the pH continued to rise for some time (Figure A2.1. Later, this scheme was modified by adding the acid/base and nutrient feed solutions directly to a recirculating culture broth stream which emptied into the head space). Although not immediately recognized, the wild oscillations in the off-gas carbon dioxide concentration diminished dramatically.

On the basis of this knowledge — the active stirring of the foam layer and the delayed/overshoot pH response — it was realized that the reaction described in Eq. (A2.1) was occurring. In essence, as sodium hydroxide was being added, it was being thoroughly mixed up in the foam layer before gradually passing on into the bulk culture broth. In a sense the foam layer and the bulk culture broth were acting like two different phases. Since a typical foam is approximately one part liquid to three parts gas or higher,[9] the amount of sodium hydroxide added to adjust the pH of *ca* 12 liters was being concentrated in less than one liter, resulting in a sharp localized increase in the pH, resulting in the stripping of evolved carbon dioxide gas. Slight oscillations were also observed after the pH addition system was modified, attesting to the mechanical properties and vigorous stirring of the foam layer.

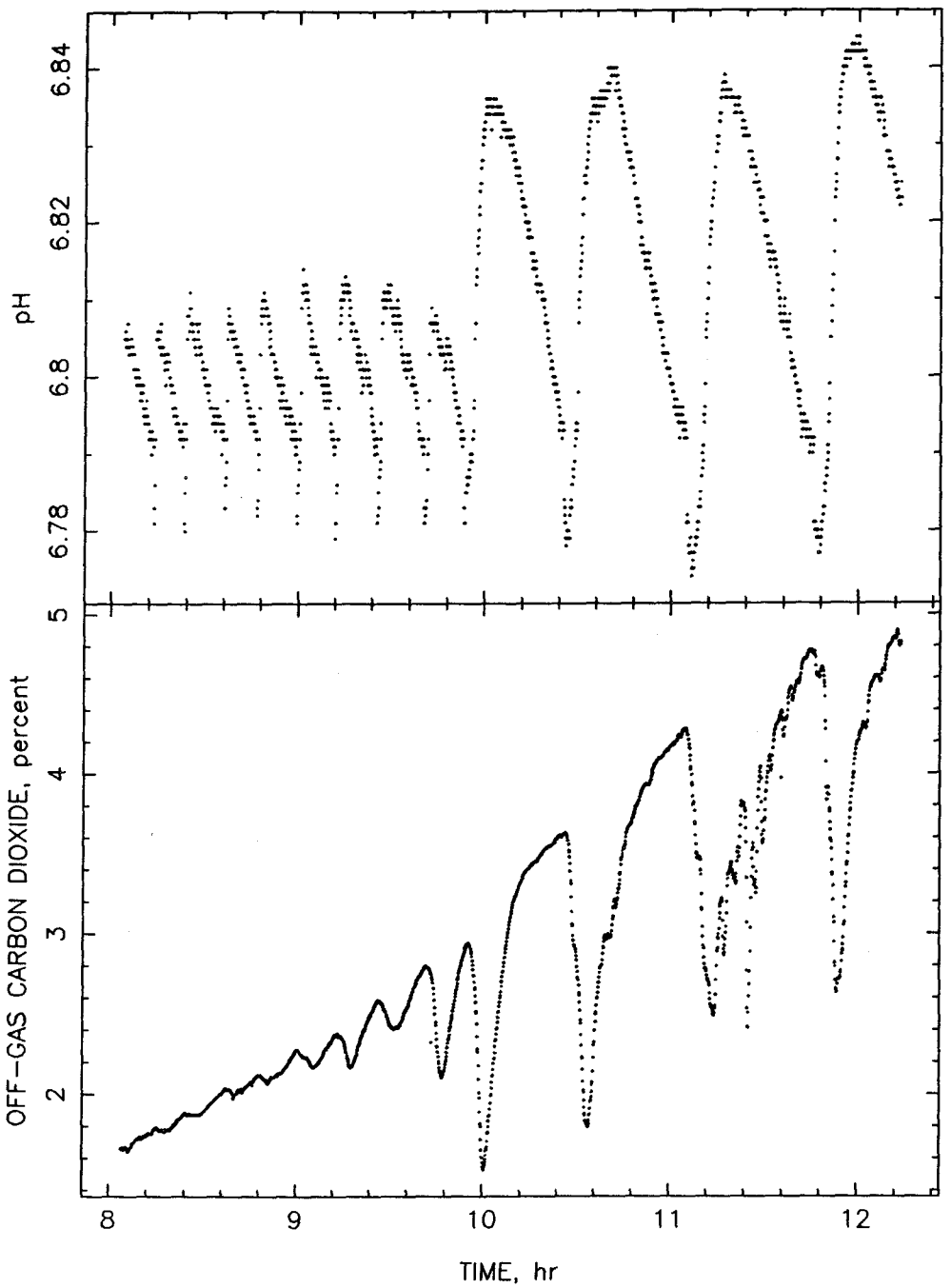

Figure A2.1: Influence of foaming on pH control and the off-gas carbon dioxide concentration. **(a)** Raw pH data; **(b)** raw off-gas carbon dioxide concentration data. pH "drops" or "jumps" approximately 0.01 units when pH control is switched on or off, respectively. At eight hours foaming begins to become excessive. Note that as pH control switches off, the pH initially jumps up and continues to rise even though no sodium hydroxide is being added; the off-gas carbon dioxide concentration drops as carbon dioxide is stripped out of the gas stream.

Close inspection of the time evolution of the carbon dioxide off-gas oscillations revealed that under typical exponential-type growth, the carbon dioxide concentration would continue increasing with an overall exponential character (Figure A2.2). When the pH-control pulses were far enough apart, the off-gas carbon dioxide concentration would increase exponentially until pH control was exerted. Upon introduction of sodium hydroxide, the carbon dioxide concentration would plummet until the pH-control pulse ceased. The carbon dioxide concentration would then increase until it reached the expected extrapolated exponential curve and would continue increasing along that curve until the next pH-control pulse was encountered. In cases where the pH-control pulses occurred more frequently, not allowing complete recovery of the carbon dioxide concentration, the peaks of the curve would increase in an exponential manner.

The pH-induced oscillations not only disrupted the carbon balance by effectively incurring a time lag in the carbon dioxide evolution rate as carbon dioxide was "stockpiled" in the foam layer, but also created a smoothing inconvenience. Therefore, the off-gas carbon dioxide concentration was modified to provide what was deemed to be an appropriate representation of the off-gas carbon dioxide concentration *sans* disruption by pH control.

The off-line modification of the off-gas carbon dioxide concentration entailed two steps. The first called for "clipping" the sharp drops that were due to pH control. The pH was monitored until control action was detected, usually indicated by a disjointed drop in the pH meter output that was due to the activation of the pump relay. At this point the carbon dioxide concentration was monitored with the most recent highest value being retained. When the

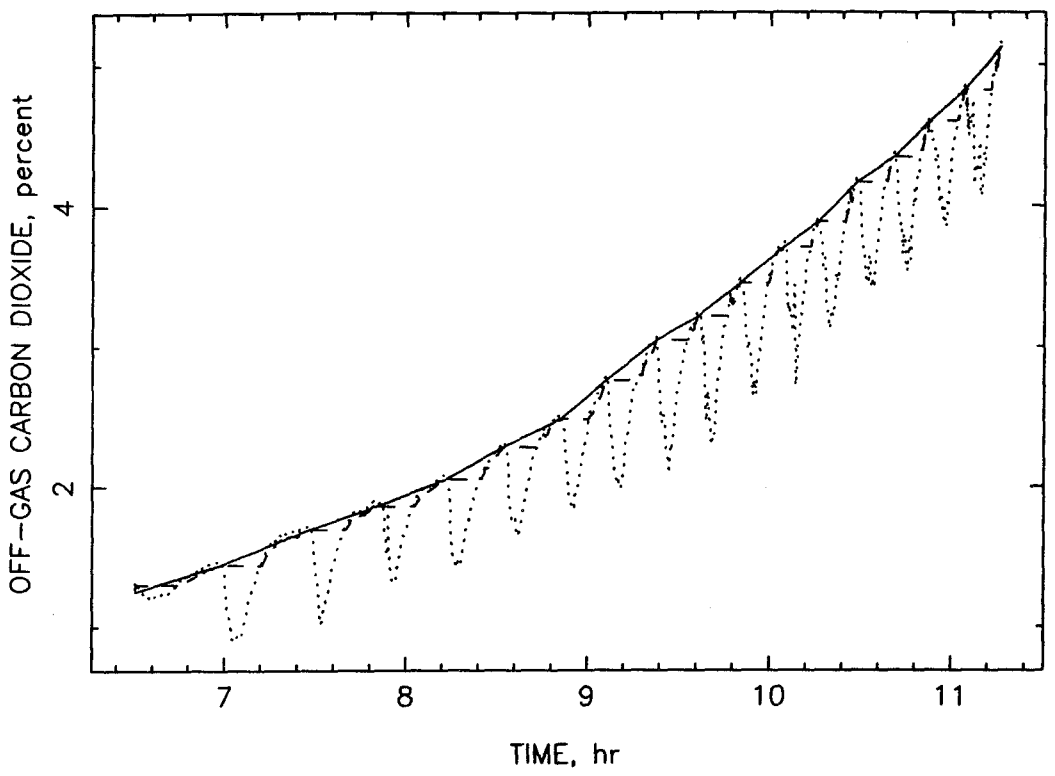

Figure A2.2: Approximation of pH-control influenced off-gas carbon dioxide concentration. Raw off-gas carbon dioxide data, ····· ; "clipped" carbon dioxide oscillations, – – – ; local linearization of carbon dioxide concentration, ——— .

carbon dioxide concentration dropped below this value, the lower concentration was replaced. This process continued until the carbon dioxide concentration rose above the high set point and the "flag" was turned off until the next incidence of pH control. This converted the oscillations into stairsteps — an improvement but still a smoothing problem.

The second step of the off-line modification approximated the curve by drawing a line from the beginning of one "stairstep" to the beginning of the next. All points in the interval falling below the line were replaced, while all points falling above the line were retained. In this way the off-gas carbon dioxide concentration was approximated. Although this may seem to be an overestimation, it must be remembered that the foam phase, based upon the pH overshoot data, was at a higher pH than the bulk culture broth. This effect increased the dissolved carbon dioxide species concentration, while reducing the effective carbon dioxide gas concentration.

A2.7 ERROR ESTIMATION

Given the ideas presented by Liao,[10] an error estimation technique was applied to identify once and for all the most probable source of missing carbon. By constructing a theoretical reaction space based upon the following single carbon, balanced stoichiometric equations for biosynthesis* (Eq. (A2.11)), res-

* Oxygen contribution calculated as residual balance in compositional analysis without correction for ash.

piration (Eq. (A2.12)) and PHB polymerization (Eq. (A2.13)), the extents of reaction as well as the overall production or consumption of any two experimental parameters may be calculated from overall production or consumption of three other experimental parameters.

$$CH_2O + 0.25NH_3 + 0.046O_2 \longrightarrow CH_{1.66}O_{0.55}N_{0.25} + 0.55H_2O \quad \text{(A2.12)}$$

$$CH_2O + O_2 \longrightarrow CO_2 + H_2O \quad \text{(A2.13)}$$

$$CH_2O + 0.25O_2 \longrightarrow 0.33CO_2 + 0.67CH_{1.5}O_{0.5} + 0.5H_2O \quad \text{(A2.14)}$$

For example, on the basis of the total evolution of carbon dioxide, the total production of PHB and the total consumption of fructose, the extent of PHB polymerization, biosynthesis and respiration can be calculated as well as total production of biomass and total consumption of oxygen. (Liao originally developed this technique for use with singular value decomposition techniques to reduce the reaction space basis for application as a predictive tool.)

Using the experimental fermentation data, the time-integrated fluxes of $\mathbf{v}_1$ ($\mathbf{v}_1$'), $\mathbf{v}_2$ ($\mathbf{v}_2$'), $\mathbf{v}_3$ ($\mathbf{v}_3$'), and $\mathbf{v}_B$ ($\mathbf{v}_B$') were calculated as well as the time integrated fructose consumption rate normalized by biomass (FCR'). The following ratios were calculated: $\mathbf{v}_1$'/FCR', $\mathbf{v}_B$'/FCR', $\mathbf{v}_2$'/$\mathbf{v}_1$', and $\mathbf{v}_3$'/$\mathbf{v}_1$'. Upper and lower bounds for these ratios were calculated on the basis of two separate assumptions: (1) Lower bounds were calculated for these ratios, ignoring the carbon balance discrepancy, thereby causing FCR' and $\mathbf{v}_1$' (when in the denominator) to be as large as possible and the numerators as small as possible being calculated using only carbon dioxide, PHB and biomass, as appropriate. (2)

Upper bounds were calculated by closing the carbon balance and by including the missing carbon, effectively increasing the numerator; the denominators did not change.

Using the theoretical reaction space, these same ratios were calculated for every possible combination of three observables. When all four ratios fell within the respective upper and lower limits, the two calculated observables were noted and compared with the actual observable values. The implications were that (1) if the four ratios fell within the respective bounds, the calculation represented a valid reaction state, and (2) an estimate of the error in the parameter would be given by the difference between the calculated value and the observed value.

Four consistent cases were found for virtually every experiment. These suggested that the erroneous observables (with the corresponding average fractional difference between the value calculated with the theoretical reaction space and the value observed) were: biomass (0.39) and oxygen (0.33); carbon dioxide (0.41) and oxygen (0.83); fructose (-0.14) and oxygen (0.31); and fructose (-0.23) and carbon dioxide (-0.22). Clearly, oxygen is a reoccurring observable, but since it is not important to the carbon balance and because its stoichiometric interaction in the theoretical reaction space model is questionable, it will be ignored.

Given the accuracy of the dry weight and PHB assays, it is highly unlikely that the biomass concentration is off by nearly 40%. Similarly, it is highly unlikely that the carbon dioxide evolution rate could be off by 40%; this would suggest that either the off-gas analyzer was off 40%, the flow rate would need to be increased by nearly 40%, or the dissolved carbon dioxide concentration

was considerably higher than expected. Each one of these has been investigated with the results suggesting that the error is much less than this level. The fourth case suggests considerable decreases in both carbon dioxide and fructose — a possibility, but not likely, given the accuracy of the both the carbon dioxide off-gas analyzer and the fructose assay. Also, given the small oxygen contribution to the biomass composition, using the oxygen consumption rate to predict fructose consumption and carbon dioxide evolution further increases the unreliability of this result. An error of 14% in the fructose concentration is far more probable and within the range of consideration, given the possibility of error accumulation (see Chapter 1 for calculation) in the FCR calculated directly from the fructose concentration and fructose feed addition rate.

A2.8 RESOLUTION AND CONCLUSION

If the evolved carbon dioxide evolved averaged approximately 42% of the fructose consumed, then the total of biomass and PHB produced must average 58% as suggested by the TOC and ^{14}C experiments. In nearly all the fermenter experiments, the ratio of biomass plus PHB produced per fructose consumed was considerably less than 0.58. The implication, again, is that the calculated fructose consumption rate is too high.

In assessing this discrepancy, a number of mathematical techniques were employed. One involved closing the intracellular AcCoA balance separately for PHB, carbon dioxide, biomass and fructose. In closing the balance for fructose,

the average ratio of carbon dioxide evolved per fructose consumed averaged 40% — none of the other attempts came near this result.

On the basis of all the previous information, it was decided that the solution to the carbon balance problem was to close the AcCoA balance for fructose. And indeed, a number of earlier problems, such as a low or negative citric acid cycle activity, disappeared. The question remained, however, as to what happened to the missing fructose and why the fructose consumption rate was overcalculated. The best explanation is that part of the fructose feed was retained in the foam layer, or that the foam layer at least delayed its physical addition to the bulk culture broth. There are a number of observations that support this notion. For one, the lag in pH control and continued rise in pH after the pH control pulse had stopped strongly suggested that the foam layer had a propensity to retain dropwise added solutions. Secondly, it was observed that fermentations run with dropwise addition of the fructose feed tended to have higher carbon balance discrepancies than those in which the fructose feed was added directly to the recirculating stream. Finally, it was observed that the ammonium yield coefficient was approximately 20% too low; *i.e.*, the theoretical yield coefficient based on the biomass composition was *ca* 2 g biomass/g ammonium chloride while a value of 1.6 g biomass/g ammonium chloride was typically observed. This strongly suggests that the added feed solutions were impeded, presumably by the foam layer, from reaching the bulk culture broth. In the case of ammonium chloride, the discrepancy is larger than that observed with fructose because at pH 6.8, one ammonia molecule is in equilibrium with approximately every 280 ammonium molecules and can be desorbed into the gas phase and removed.

A2.9 REFERENCES

1. Smith, M.D., and Ho, C.S., *Chem. Eng. Commun.*, **37**, 21 (1985).

2. Brown, L.R., Cook, D.W., and Tischer, R.G., *Dev. Ind. Microbiol.*, **6**, 223 (1964).

3. Schlegel H.G., Gottschalk G., and Bartha R., *Nature*, **191**, 463 (1961).

4. Pfennig, N., and Lippert, K.D., *Arch. Mikrobiol.*, **55**, 245 (1966).

5. Knoche, W., *Biophysics and Physiology of Carbon Dioxide*, Bauer, G., Gros, G., and Bartels, H., eds., Springer-Verlag, Berlin, FRG, 3 (1980).

6. Ho, C.S., Smith, M.D., and Shananhan, J.F., *Adv. Biochem. Biotechnol.*, **35**, 83 (1987).

7. Schumpe, A., Quicker, G., and Deckner, W.-D., *Adv. Biochem. Engin.*, **24**, 1 (1982).

8. Medinsky, M.A., *J. Anal. Toxicol.*, **10**, 24 (1986).

9. Prins, A., and van't Riet, K., *TIBTECH*, **5**, 296 (1987).

10. Liao, J.C., *Biotechnol. Bioeng.*, **33**, 631 (1989).